Advanced Characterisation Techniques for Battery Safety Assessment

Drasti Patel

Submitted in part fulfilment of the requirements for the degree of

Doctor of Philosophy at University College London

2023

Declaration

I, Drasti Patel confirm that the work presented in this thesis is my own. Where information has been derived from other sources, I confirm that this has been indicated in the thesis.

Signature

Date

Acknowledgements

work, which she did so graciously – it was not easy given how over-confused a PhD student I was! I am grateful also for her research guidance and friendship and in parallel for Becky for her enthusiasm and dedication to various projects and for encouraging me to explore my body and its limits: thank you both for the intro to trail running. Thank you also for the conversations on inequality, I hope you continue to challenge yourselves and others. I am grateful to have shared this space with you and am excited to see where you lead. To Alice Llewellyn for her humour, reliability, and for laminating my birthday cards. To 'off-grid' Lara and Dina for your collective smoking area chats, and Rema and Fabiola for their encouragement and advice. To Zahra for her joyous and carefree energy, in contrast to Max, whose opposite nature created an entertaining balance for our trio. I am grateful for the friendship of Theo Suter, for his humour and for always challenging my approaches, and to Harry Michael, Aaron Wade, Alex Dimitrijevic, and the many others that formed the EIL community.

I am grateful for the friendship of Almuth Schwarz who sat through numerous video calls, more than anyone should be obliged to, while I externally processed every feeling from excitement to dread. I look forward to mirroring this support as you complete your PhD. Housing instability has been a constant, difficult and personal struggle throughout the duration of this work and I am thankful for the friendships of Michael High and Diane Croskin, especially during our stint at Jackson Rd. Thanks for being present and grounded, and for making Highbury a home. These thanks extend to the support from numerous and various housemates. I am grateful for the friends who carried me in all the different ways over the years, Halan Gloy, Vikash Gondalika, Anna Tomaszewska, Umair and Roger, Uma Mitra, Sarah Guzman and particularly for future Dr Alisha Dua, for encouraging me to pursue this PhD. A special thanks to Salma Begum, for appreciating the small things with me when I needed to most. Thanks to Bilaal, Yan, Hannah, Jian and Sam for your friendship and support.

Parts of this work were conducted in the midst of a global pandemic. This journey was bleak and isolating at times, and I am grateful for the inspiration, love and encouragement from Laurence Baker during this period.

I am thankful also for Lucy Todd, Oli, Mike, Jie, Elias, Christian and the 'plastics' in TCR90 whose support during the write-up stage has been immeasurable.

A special thank you to my sister, Hani, for seeing me, and together with Heren, for opening the doors to your home. Thank you both for your patience and support. The latter parts of this thesis were written while supporting baby Ivaan's troubled journey to Earth. Your strength during this time extended to and inspired the final stages of this work. Further thanks to my extended family (who if I were to begin to name would take this thesis over its word limit), my uncles and aunts for their sacrifices, and to each of my cousins for their encouragement and support. I am forever grateful to my grandparents and parents for their resourcefulness and resilience carried forward to me from each of their individual and incredible journeys, and particularly to my dad for encouraging creativity, curiosity and independence.

A final thanks to this thesis for providing a temporary, focused purpose and for the learnings it reflected, for humbling me and reminding me that I have courage, perseverance and this language to express. Thanks always to baby me for her intuition and guidance.

<div align="center">⁂</div>

Abstract

The need to shift to cleaner energy sources is imperative. Battery technology is considered a highly promising technology to successfully bring about this shift. It has already been implemented in numerous ways and features in our day-to-day lives; from mobile phones to homes. Recently, concerns regarding their safety have increased and as a result, governments have boosted research efforts in this area, with the added urge to work collectively with industry partners and regulatory bodies. These cells are prone to undergo catastrophic failures as a result of a series of exothermic reactions (thermal runaway) that can be triggered by several methods. Many research efforts have been made to understand this phenomenon from various perspectives: material selection, mechanical design, mitigation or preventative measures. This thesis shows how we can begin to comprehend this complexity and apply it to advancing existing battery safety assessment techniques. Through thermal analyses and multi-scale X-ray CT imaging, the correlations between heat generation and battery architecture are addressed. In this work, for the first time, differential scanning calorimetry was used to measure heat signals from full cells, high aspect ratio battery samples were imaged and a custom-built calorimeter chamber was developed to provide operando images and heat measurements of cells undergoing thermal failure. The results obtained from the methodologies and techniques established in this work have advanced our understanding of how various battery material morphologies and architectures behave under certain stresses. In turn, these findings can aid not only in the development and manufacture of safer lithium-ion batteries but also in the standardisation of testing standards, and improvement of failure mitigation strategies.

Impact Statement

Lithium-ion batteries have seen a significant uptake across the globe in the last two decades with the increasing adoption of clean energy technologies. Alongside this, their rapid implementation in day-to-day activities has given rise to numerous concerns regarding their safety. The work in this thesis considers the wide number of stakeholders in the development and use of such batteries: industry representatives, regulatory bodies, customers and the public. It expands on early findings of battery failure and safety assessment and addresses them from a fundamental engineering perspective, with a particular focus on materials, design and methodology.

Several new methodologies and analysis tools have been developed. From the use of novel thermal measurement techniques, advances in the characterisation of battery materials through imaging and improvements to failure testing methodology, the findings presented in this work can be utilised by several specialists in academia and industry. The understanding of battery material and structural morphology is a fundamental step in improving battery performance, thermal management and safety. By correlating electrochemical, thermal and image analyses, this work has provided new insights to the Johnson Matthey Battery Materials team, who have gained vital counsel on material morphology and degradation, failure mechanisms and methods for post-mortem analyses. The importance and limitations of imaging battery failure have been widely discussed. This work addresses the need to focus on slower degradation mechanisms and improve the accessibility to such measurements. Furthermore, this work provides a full experimental dataset that allows existing mathematical simulation models to be comprehensively validated to predict and guide further research.

The topic of battery safety has academic, industrial and governmental and public relevance. To address this, the findings in this work have been disseminated through peer-reviewed journal publications (Journal of The Electrochemical Society focus issue on Battery Safety, Reliability and Mitigation and the Johnson Matthey Technology Review), posters and oral

presentations at both national and international conferences. Collaborations have also been forged across various institutions; from work carried out in the UK at Johnson Matthey and in Europe at the European Synchrotron Radiation Facility. Additionally, these findings are expected to guide science and climate policymakers. Outreach efforts through UCell involving giving talks, demonstrations and workshops in electrochemical energy storage systems at science festivals and a range of schools have expanded the reach and social impact of this work. Furthermore, through additional engagement activities such as writing blog posts and hosting a podcast related to the STEM field, this research has accessed audiences that are traditionally underrepresented and in doing so addressed the wider issues surrounding inclusivity and diversity in UK higher education.

Contents

List of Tables

List of Figures

List of Symbols

Symbol	Definition
ΔG	Change in Gibbs free energy [J mol^{-1}]
n	Number of electrons per mole of reactants
F	Faraday constant, [96,487 C mol^{-1}]
E	Electromotive force
Q_{SEI}	Heat output from SEI layer decomposition [J]
Q_{PE}	Heat output from positive electrode reaction [J]
Q_E	Heat output from electrolyte decomposition [J]
Q_{NE}	Heat output from negative electrode reaction [J]
Q_B	Heat output from binder decomposition [J]
Q_{TOTAL}	Total heat output from decomposition reactions [J]
$T, \Delta T$	Temperature and change in temperature [°C]
q	Heat flow [W m^{-2}]
R	Resistance (of the thermoelectric disk) [Ω]
I_d	Detected intensity [W m^{-2}]
I_0	Incident intensity [W m^{-2}]
μ	Property of the beam energy and material density [cm^{-1}]
D_{eff}	Effective diffusion coefficient [m^2 s^{-1}]
D	Intrinsic diffusivity of the transporting phase [m^2 s^{-1}]
φ	Volume fraction of the conductive phase
$\tau, \tau_c, \tau_x, \tau_y, \tau_z$	Tortuosity factor; characteristic, and in directions x, y, z.
dQ	Change in heat output [J]
dW	Total work done [J]
H	Enthalpy [J]
U, dU	Internal energy and change in internal energy [J]
P	Pressure [Pa]
V	Volume [m^3]
I	Current [A]
U_{OCV}	Open circuit voltage [V]
m	Mass [kg]
c_p	Specific heat capacity [J kg^{-1} °C^{-1}]

V_{cell}	Cell voltage [V]
ΔS	Entropy change [J K^{-1} mol^{-1}]
Q_{total}	Total heat output during charge/discharge [J]
Q_{irr}	Total irreversible heat output [J]
Q_{rev}	Total reversible heat output [J]
x	Molar fraction
$\eta, \eta_{Ohmic}, \eta_{kinetic}, \eta_{diffusion}$	Overpotential; Ohmic, kinetic and diffusion, respectively [V]
$\dot{Q}$	Total volumetric heat generation [mW]
R_{Ohm}, R_D, R_{CT}	Resistance: pure Ohmic, diffusion and charge transfer, respectively [Ω]
i, i_0	Exchange current density [A m^2]
α	Charge transfer coefficient
R	Universal gas constant [8.314 J K^{-1} mol^{-1}]
I_0	Initial radiation intensity
I_p	Primary intensity after absorption
μ	Linear attenuation coefficient
d	Penetration distance [m]
σ	Photon noise
ω	Anuglar frequency [radian s^{-1}]
$Z(\omega)$	Frequency dependent impedance [Ω]

List of Abbreviations

Abbreviation	Definition
AC	Alternating Current
AFM	Atomic Force Microscopy
ARC	Accelerating Rate Calorimetry
BEV	Battery Electric Vehicle
BMS	Battery Management System
CAD	Computer Aided Design
CBD	Carbon Black/binder Doman
CCCV	Constant-Current Constant-Voltage
CCD	Charged-Couple Device
CID	Current Interrupt Device
CNR	Contrast to Noise Ratio
CT	Computed Tomography
DEC	Diethyl Carbonate
DMC	Dimethyl Carbonate
DOD	Depth of Discharge
DSC	Differential Scanning Calorimetry
EC	Ethylene Carbonate
EDX	Energy Dispersive X-ray
EIL	Electrochemical Innovation Lab
EIS	Electrochemical Impedance Spectroscopy
EMC	Ethyl-methyl Carbonate
EMF	Electromotive Force
ESRF	European Synchrotron Radiation Facility
EV	Electric Vehicle
FBP	Filtered Back Projection
FIB	Focused-ion Beam
FOV	Field of View
GC or GC-MS	Gas Chromatography Mass Selective
HART	High Aspect Ratio Tomography
HEV	Hybrid Electric Vehicle
HF	Hydrogen Fluoride

HSAL	High Surface Area Lithium
IEC	International Electrotechnical Commission
IEEE	Institute of Electrical and Electronic Engineers
ISC	Internal Short Circuit
LCO	Lithium Cobalt Oxide, $LiCoO_2$
LFOV	Large Field of View
LFP	Lithium Iron Phosphate, $LiFePO_4$
LIB	Lithium-ion Battery
LMO	Lithium Manganese Oxide, $LiMn_2O_4$
LNO	Lithium Nickel Oxide
MCMB	Mesocarbon Microbeads
NCA	Lithium Nickel Cobalt Aluminium, $LiNiCoAlO_2$
NIST	National Institute of Standards and Technology
NMC	Lithium Nickel Manganese Cobalt Oxide, $LiNiMnCoO_2$
NMO	Lithium Nickel Manganese Oxide, $LiNiMnO_2$
NMP	N-Methyl-2-Pyrrolidone
NMR	Nuclear Magnetic Resonance
OCV	Open-Circuit Voltage
PC	Propylene Carbonate
PE	Polyethylene
PID	Proportional-Integral-Derivative
PP	Polypropylene
PSD	Particle Size Distribution
PTC	Positive Temperature Coefficient
PTFE	Polytetrafluoroethylene
PVDF	Polyvinylidene Fluoride
ROI	Region of Interest
RTD	Resistance Temperature Device
RVE	Representative Volume Element
SEI	Solid Electrolyte Interphase
SEM	Scanning Electron Microscopy
SOC	State of Charge
UCL	University College London
VC	Vinylene Carbonate
XRD	X-ray Diffraction

Chapter 1

1. Introduction

1.1. Research Motivation

The past 20 years have seen record change in the world's energy resource consumption. Since 2000, global primary energy consumption via hydrocarbons has grown by nearly 37,000 TW h[1]. However, encouraged by rising concerns over climate change and the depletion of fossil fuel reserves, the World Energy Outlook 2021 projects that this will begin to decline from 2025 to 2050[2], while energy consumption by renewables will increase. As industry initiatives and government policies[3][4] push to support investments in renewable electricity, energy applications such as portable electronics, hybrid electric vehicles (HEVs), battery electric vehicles (BEVs) and grid power storage are seeing a surge in market size and growth rate[5]. Electrochemical energy storage in the form of rechargeable batteries is widely used in such applications and is key to enabling the integration of intermittent renewable energy technologies such as wind and solar power. Lithium-ion batteries (LIBs) are considered one of the fundamental technologies to lead a clean and sustainable energy future[6].

The development of LIBs began in the late 1950s and continues today in response to a range of new applications requiring high power densities, higher energy densities, lighter weights and lower volumes. Today, the nominal voltages of LIBs can range between 3.0 - 4.2 V depending on the chemistry of the cathode material. The US Department of Energy's (DoE) goal for high-energy battery systems in EVs is to reach an energy of roughly 500 Wh kg^{-1}[7], it is currently at 350 Wh kg^{-1}[8]. As energies increase, so do the safety concerns associated with them[9]. It has been and continues to be, widely reported that the thermal stability of battery materials decreases at higher capacities, making them liable for failure as a direct consequence[10][11].

The current design, manufacturing and testing of batteries require greater insights and standardisation concerning safety[12][13][14]. The most common cause for LIB failures is latent defects, especially during manufacturing, which are often difficult to detect[15]. Although examples in the media emphasise failures as a result of manufacturing defects, the cause and extent of LIB failures are equally dependent on the batteries' fundamental design such as; separator thickness, electrolyte flammability, the electrical and thermal conductivity of materials and/or the battery configuration i.e. pouch cell, cylindrical[16].

The current estimated failure rate of rechargeable LIBs is 1 in 10 million[9]. While commercial cells currently undergo rigorous testing standards, it is clear that failure is a statistical process in which the prediction of failure remains a challenge[22][23]. There are several widely recognised safety standards developed through a consensus process based on participation by representatives from industry, regulatory and insurance bodies, and recently consumer advocacy[19]. Some widely known stakeholders in safety standards include the Underwriters Laboratories (UL1642 or SU2580), the Institute of Electrical and Electronic Engineers (IEEE), the United Nations (UN) for transportation and the International Electrotechnical Commission (IEC). There have been numerous battery safety studies, all of which can be categorised into three fundamental types; mechanical, thermal or electrical[20]. Examples include thermal abuse tests where the cell is heated up to critically high temperatures, or electrical abuse tests involving abnormal charging at high rates or voltages. Other standards include external short circuit, crush, penetration and forced internal short circuit tests. However, despite the coordination of various abuse tests across the existing safety standards, they largely remain inconsistent[21]. Along with this, as more failure modes are identified, research results must be both quickly and easily translated into new safety standards to aid the commercialisation of the LIB.

Lithium ion battery technology: a multi-scale approach.
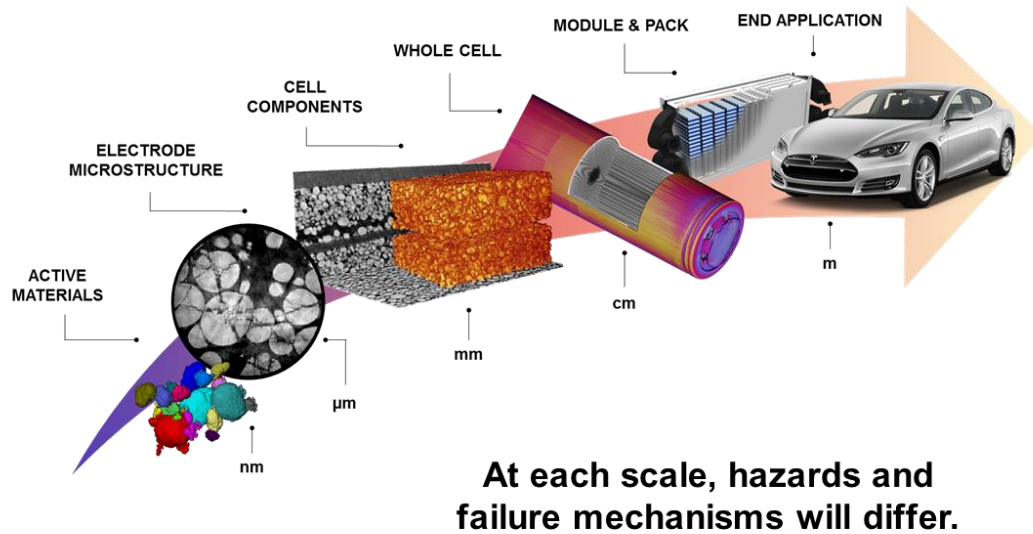
Figure 1.1 Schematic showing the multi-length scale features of the lithium-ion battery from its active material components in the nanoscale to its end application, such as electric vehicles; and therefore the complexity of investigating their failure mechanisms and safety.

1.2. Thesis Objectives and Structure

Today, the LIB is the state-of-art power source for many electronic devices. Given the drastic change in the battery market over the last decade and assessing the current and future trends, it is evident that there are still many changes projected in this field. Rising demands for newer applications require battery design to quickly adapt and scientific research to accommodate alongside. The LIB combines highly energetic and flammable materials making them naturally liable to suffer from failure when subjected to unfavourable conditions. The effects of material morphology on the likelihood and extent of failure as well as mechanical design, existing safety features, failure mechanisms and the limitations of current safety assessments are well-researched but not yet correlated or standardised[22]. This provides the framework for the investigations in this thesis.

Chapter 2 provides the fundamentals of battery technology, and, heat generation, battery failure mechanisms and materials characterisation and reviews the existing literature in areas concerning LIB safety assessment, including safety regulations, testing standards, methodologies to induce failure and thermal analysis. Furthermore, existing literature for battery materials characterisation using a host of imaging techniques is also detailed in the same chapter.

Chapter 3 introduced the methods utilised for the scientific investigation in this work. Battery abuse conditions are created and evaluated using techniques such as calorimetry, including accelerated rate calorimetry (ARC) to determine the onset temperature for thermal runaway and rate of heat generation of various commercial cells. Differential scanning calorimetry (DSC) is used to further characterise material reactivity and heat generation during normal operation and failure. Building on traditional characterisation techniques such as optical microscopy, atomic force microscopy (AFM) and scanning electron microscopy (SEM) this thesis utilises a multi-scale and operando X-ray computed tomography (CT) approach to characterise several failure mechanisms in LIBs[23].

Chapters 4, 5, 6 and 7 of this thesis make up the main results of this work. First, techniques for thermal analysis are evaluated in the context of heat generation. Second, multi-scale imaging of battery materials and formats is investigated with suggestions for advancements. Chapter 6 expands on these findings and begins to establish areas where the techniques can be correlated. Chapter 7 introduces a novel operando technique that was developed to image the architectural changes to electrodes during a battery failure and correlates it with findings from thermal analyses.

Results from this work provide useful and new insights for researchers in academia and industry alike. Chapter 8 concludes the main findings from this work that are useful in the context of battery safety assessment, and outlines areas for future work. Supplementary data are provided in the appropriate appendices.

Chapter 2

2. Literature Review

2.1. Fundamentals of the Lithium-ion Battery

In a basic electrochemical cell, the electrons that transfer between a positive and negative terminal are the outcome of a series of chemical reactions that convert chemical energy into electrical energy. It takes one pair of electrochemical reactions to operate a battery – one that yields electrons (oxidation) and one that gains electrons (reduction). The maximum work, or energy, that can theoretically be achieved from this type of reaction is defined in thermodynamic terms as the change in Gibbs free energy (ΔG in J mol^{-1}). For a specific amount of material, the possible energy that can be converted to electrical energy is given by the following relationship.

$$\Delta G = -nFE$$

<div align="right">Equation 2.1</div>

Where n is the number of electrons being transferred per mole of reactants. F, the Faraday constant, is the quantity of electrical charge in coulombs per mole of electrons (96,487 C mol^{-1}), and E is the electromotive force (EMF) of the cell. The electrochemical reactions of the reactive materials must proceed spontaneously i.e. with a positive EMF and negative ΔG for the battery to produce energy. The theoretical energy given by this relationship, however, cannot be practically achieved. It is limited by polarisation losses including activation losses and concentration losses from the uneven depletion of reactants and products that result in concentration gradients.

The fundamental functions of a battery are dependent on three active components – the negative electrode, positive electrode and electrolyte. In the LIB, the negative electrode is normally an electron donor group that is electropositive in nature like lithium metal. The positive electrode is usually an electron acceptor which is strongly electronegative such as $LiMO_2$ compounds, where M represents Co, Ni, Mn, etc. The generalised

electrochemical reactions occurring in the electrodes during charge and discharge processes can be expressed as follows.

The positive electrode:

$$LiMO_2 \leftrightharpoons Li_{1-x}MO_2 + xLi^+ + xe^-$$

Equation 2.2

The negative electrode:

$$C + xLi^+ + xe^- \leftrightharpoons Li_xC$$

Equation 2.3

Full cell reaction:

$$LiMO_2 + C \leftrightharpoons Li_xC + Li_{1-x}MO_2$$

Equation 2.4
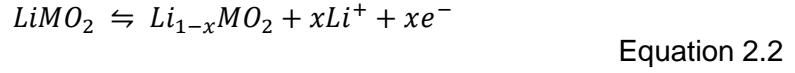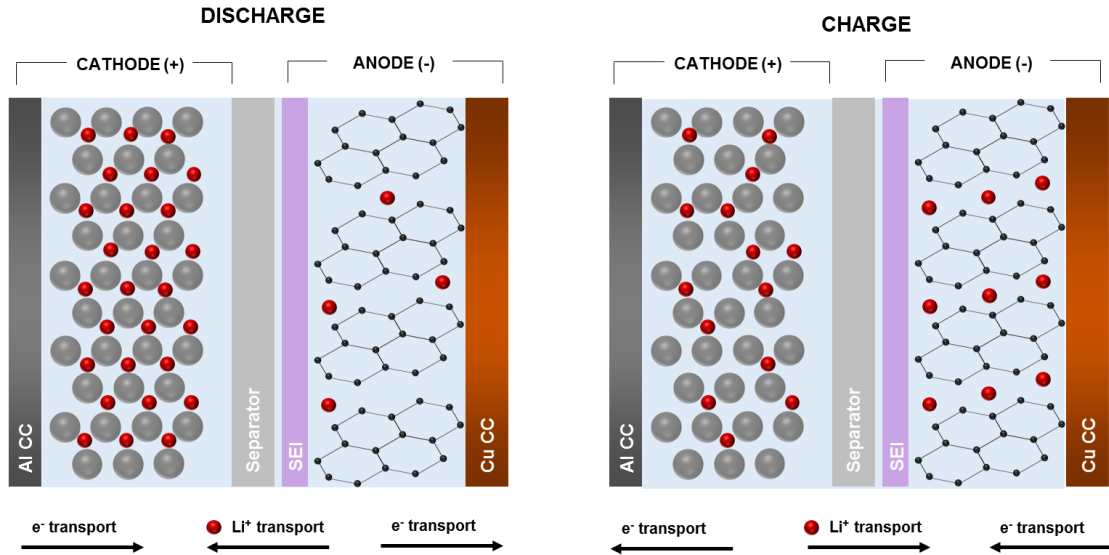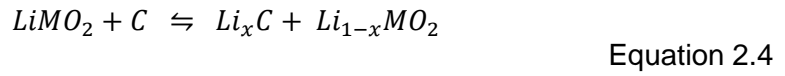
Figure 2.1 Schematic of the lithium-ion battery illustrating the movement of ions and electrons during charge and discharge.

A schematic of LIB operation in Figure 2.1 illustrates the battery operation during discharge. During discharge, the negative electrode is oxidised and yields an electron in the process. This electron moves along an external circuit to the positive electrode, which accepts the electron. The Li^+ ions move from the negative electrode to the positive electrode (reverse during charge) through the electrolyte. The electrolyte, a medium for the transfer of ions between electrodes, is typically a lithium salt dissolved in an organic solvent in LIBs. The electrolyte must be a good lithium-ion conductor and electronic insulator. Common parameters used to validate the quality of an

electrode material are cell voltage, conductivity, specific capacity, coulombic efficiency[24], capacity retention i.e. stability and cycle life[25], gravimetric and volumetric energy density, power density as well as cost, toxicity and safety.

2.1.1. Applications

Table 2.1 summarises the properties of common positive electrode materials used in present-day commercial LIBs, as well as their advantages, disadvantages and applications. Raw material costs and battery pack prices drive the LIB materials markets now. The overall battery pack price was reduced by nearly 97 % from 1991 to 2020[26]. Increases in charge density and developments in materials and chemistry are thought to be the main drivers for this trend. More recently, investments in LFP have seen a new surge in application and production since NMC (and other higher energy density cathode materials) that originally dominated the market in 2016. In 2020, the production of LFP surpassed NMC for the first time in three years[27] and electric vehicle (EV) companies such as Volkswagen and Tesla announced switches to LFP for their standard range vehicles[28][29][30]. It is predicted that the rising price of Li, Co and Ni caused the adoption of low-cost cathode chemistries such as LFP which is ~ 30 % cheaper than NMC[31]). Another driving factor is the decreased use of Co in Ni-based cathodes due to the health, safety and environmental risks of its extraction and mining[32].

Table 2.1 Comparison of common positive electrode materials. N.B. specific capacities are those used in typical commercial applications.

Positive electrode material	Average voltage vs. Li	Specific capacity (mAh g^{-1})[33]	Advantages	Disadvantages	Applications
LCO	3.9	155	High capacity and cycle life	High cost and low thermal stability at high charge rates	Smaller portable electronics

LMO	4.0	100 - 120	Low cost High thermal stability	Low capacity Low cycle stability	Higher power applications, such as power tools
NCA	3.7	150 - 180	High capacity and cycle life	High sensitivity to moisture	Portable and high-power applications, such as low to mid-range EVs, e-bus and e-bicycles premium electronic and/or energy storage applications
NMC	3.8	140 - 180	High energy density Low-temperature performance High power	High material costs Lower thermal stability	
LFP	3.4	160	Low cost High thermal stability	Low energy density Weight	

The overall reduction in physical size and increases in energy density and range have seen increases in concerns over the safety of batteries; which in turn have created widespread challenges in their design and manufacture[9]. During operation outside of their normal (or safe) operating window, LIBs can ignite and initiate fires or release toxic gases[34]. Although statistically rare[35], some LIB failures are heavily publicised: firstly due to the speed at which they're becoming a ubiquitous technology in modern society, but also because of their unique failure behaviour in terms of initiation, spread, and duration when compared to other fire hazards[21]. An example of LIB safety in the media is a product recall by Sony, Japan in 2006 of 9.6 million LIBs powering laptops of well-known computer manufacturers[36] that were deemed fire hazards due to faulty crimping and the introduction of microscopic metal contaminants during manufacture. Similarly, ten years later, Samsung, South Korea, recalled 2.5 million Note 7 mobile phones[13] because of the use of thinner than normal separators and poor alignment of components[14]. More recent headlines include fires within EVs such as several Tesla Model S cars (Tesla Inc., USA) between 2013 – 2021[37][38] and a Jaguar I-Pace (Jaguar Land Rover, UK) in 2021[39].

These recent events have highlighted the numerous variables that can shape a battery safety incident; from the cause of failure, application type, and therefore battery format, management system, and extent of the damage. As a result, research efforts are categorised from the cell/chemistry level and the

manufacturing to the battery management systems level. For example, the development of ceramic coatings on the separator or positive electrode has proved effective in preventing failure due to internal short circuits (ISC)[40]. Furthermore, various microstructural developments in electrode[41] and current collector thicknesses[42], particle morphology and orientation[43] and structural/thermal stabilities of electrodes[44], separators and electrolytes[45]–[47] have made breakthroughs for battery safety at the cell/materials level. On a whole-cell level, the placement and alignment of electrodes, tabs[48], pressure release vents such as the positive temperature coefficient (PTC) and current interrupt devices (CIDs)[49][34], and battery management system (BMS) devices have also seen an increase in research efforts[50]. Outside of academic efforts, additional quality control testing in factories and modified production steps (slurry mixing, coatings, and packaging) and advanced monitoring and software solutions to identify faulty cells have been implemented[21].

2.2. Materials, Components and Design

2.2.1. Positive electrode

The positive electrode in the LIB has intercalative abilities that can store the Li^+ ions. These stored ions can be reversibly inserted and removed from the host structure. The host structure can be a network of compounds consisting of metal chalcogenides, transition metal oxides or polyanion compounds, each of which can be categorised into different crystal structures; layered, spinel, olivine, and tavorite as shown in Figure 2.2.
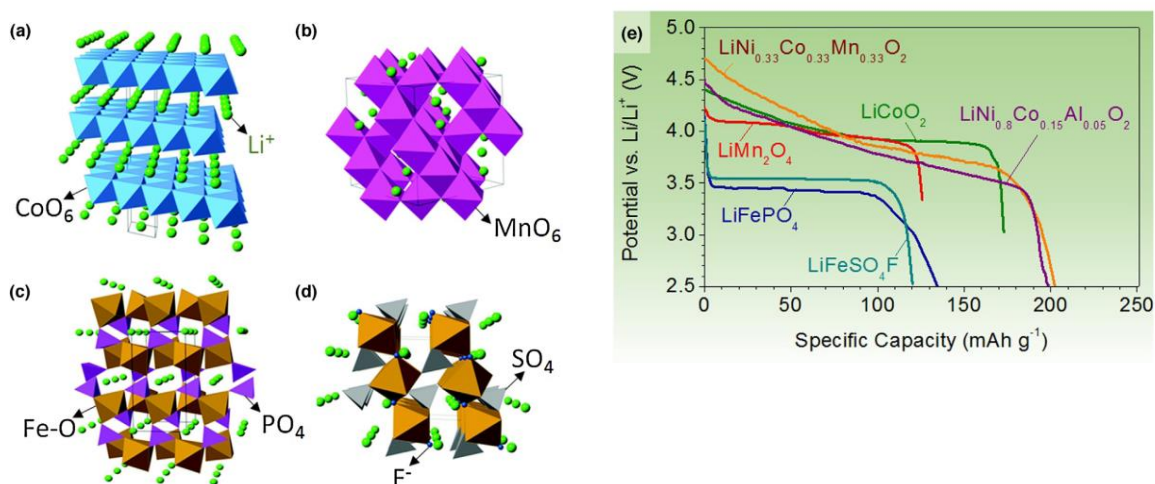
Figure 2.2 Crystal structures of intercalation cathodes and their respective discharge profiles: (a) layered ($LiCoO_2$), (b) spinel ($LiMn_2O_4$), (c) olivine ($LiFePO_4$), and (d) tavorite ($LiFeSO_4F$) and (e) typical discharge curves of intercalation cathodes (adapted from [51]).

LCO is recognised as the first and most commercially successful intercalative positive electrode material form. Its alternating layered structure hosts octahedral sites for Co^{3+} and Li^+ occupancy in cubic arrangements, forming hexagonal symmetries. LCO is an attractive cathode material due to its relatively high theoretical specific capacity (274 mAh g^{-1}), low self-discharge rate and cycle performance[52].

$LiNiO_2$ (LNO), which exhibits the same structure, achieves a similar theoretical specific capacity as LCO but has a higher energy density and lower cost compared to cobalt-based materials. Due to the tendency of Ni^{2+} to substitute Li^+ sites during material synthesis, pure LNO is unfavourable as a positive electrode material. The largest limitation of this chemistry is its low thermal stability (lower than that of LCO), because of Ni^{3+} having a higher reduction potential than Co^{3+}. Substitution of Ni with small amounts of Co and Al has proven to improve thermal stability and electrochemical performance. This development lead to the $LiNiCoAlO_2$ (NCA) cathode, which has seen large commercial demand in recent years owing to its high discharge capacity (approximately 200 mAh g^{-1}) and storage life when compared to traditional cobalt-based positive electrode materials. However, operation at elevated temperatures, i.e. > 40 °C, causes rapid capacity fade due to solid electrolyte interphase (SEI) layer growth and micro-scale cracks[51][53][54].

LMO transition metal oxide cathodes exhibit lower toxicity when compared with cobalt and nickel-based electrodes. During early LIB development, LMO improved upon the performance of many chemistries of the time. For present-day energy demands, however, it has an unsatisfactory cycling performance because of structural changes during lithium ion extraction. Additionally, Mn^{2+} ions leach out of the LMO at high voltages[55] and react with the electrolyte, resulting in the decomposition of the protective SEI layer and crossover to the counter electrode. Although LMO stability can be improved by cationic doping (for example, Al, Co, Cr, Mg, Zn etc.)[56], its poor cycle stability compared with newer chemistries is what largely limits its commercialisation.

Continuous research efforts in developing a cheaper positive electrode material lead to the synthesis of $Li(Ni_{0.5}Mn_{0.5})O_2$ (NMO). The addition of cobalt further enhanced structural stability and as a result, NMC with the following $LiNi_{0.33}Co_{0.33}Mn_{0.33}O_2$ (NMC111) formulation is used extensively in commercial applications. The formation of macroporous NMC has shown specific capacities as high as 234 mAh g^{-1} and good stability at temperatures up to 50 °C[57]. More recently, Sun et al. reported a novel expansion to this material whereby each particle (of the bulk material) is surrounded by a concentration gradient outer layer[58]. The bulk material has a high nickel content for higher energy density, with a composition of $Li(Ni_{0.8}Co_{0.1}Mn_{0.1})O_2$, while the outer layer is $Li(Ni_{0.46}Co_{0.23}Mn_{0.31})O_2$ for better cycle life and safety. It is suggested that the stability of the material is due to the Mn^{4+} of the surface layer, delaying any gas evolution from reactions between the nickel ions and the electrolyte.

2.2.2. Negative electrode

In the early 1980s Yoshino et al. reported the benefits of a low-temperature carbon such as petroleum coke. In a patent, a combination of this negative electrode material with a modification of LCO suggested by Goodenough showed that the petroleum coke was more resistant to the solvent molecules when compared to graphite[59]. Furthermore, findings by Dahn et al., showed the addition of ethylene carbonate (EC) to propylene carbonate (PC) based electrolytes, further improved this resistance[60]. Sony

developed a hard carbon second-generation negative electrode and later mesocarbon microbeads (MCMB) which gave higher specific capacities. Using ethylene carbonate with a linear dialkyl carbonate and $LiPF_6$ salt of high purity, together with a nonwoven polyethylene (PE) separator, the initial LIB achieved energies of 155 Wh kg^{-1}[61][62].

Over 30 years ago, petroleum coke was used as a negative electrode material achieving roughly 180 mAh g^{-1} specific capacity, enabling the first rechargeable LIB to be successfully commercialised. Before this, the commercial breakthrough of batteries based on metallic lithium failed due to safety concerns associated with the negative electrode[63][64]. During charging, the deposition of lithium was inhomogeneous, creating high surface area lithium (HSAL) - or dendrites of different structures[65]. This phenomenon resulted in safety risks as it increased the probability of reacting with electrolyte, as well as its tendency to grow towards the positive electrode and cause an ISC. It was clear that the metallic lithium negative electrodes had to be replaced by a more reliable and safer material for widespread commercialisation[66].

Forms of carbon are now used for the negative electrode due to its low potential vs Li/Li$^+$. Electrochemical activity in carbon is a result of lithium intercalation between layers of graphene. One lithium for every six carbon atoms can be stored in this way, providing good lithium transport and mechanical stability. Graphitic carbon can achieve close to the theoretical specific capacity of 372 mAh g^{-1}, however, it does not combine well with PC-based electrolytes (which are preferred due to their low melting points). The SEI layer forms as a result of lithium intercalation at the basal planes[54]. During lithium intercalation, the large graphitic grains undergo 10 % strain along the edge planes. These may damage the SEI layer and in return, deteriorate the cycle life. Recently, graphitic carbons have been coated with amorphous carbon as a means to protect the edge planes from electrolyte interaction[67].

2.2.3. Electrolyte

The third vital component of a battery following the positive and negative electrodes is the electrolyte. The electrolyte must be ion-conducting whilst being electronically insulating. Most batteries are designed using a liquid electrolyte solution, either aqueous or nonaqueous. The LIB, highly reactive in the presence of water, uses nonaqueous, gel, or solid electrolytes. While solid electrolytes may increase the cyclability and design flexibility of cells, they suffer from high resistance for ion conductivity, limiting the maximum power output of the cell[68]. Nonaqueous electrolytes offer higher performance with regard to conductivity, cost, safety and thermal stability. An organic electrolyte based on a combination of linear and cyclic alkyl carbonates is widely used as a solvent in the forms of ethylene carbonate, dimethyl, diethyl, and ethyl-methyl carbonates (EC, DMC, DEC, EMC respectively) and $LiPF_6$ as the electrolyte salt. These offer good stability for positive electrode materials that achieve up to 4.0 V[69].

$LiPF_6$ decomposes to LiF and PF_5 at high temperatures[70], where the latter hydrolyses to form HF and PF_3O, both of which are highly reactive and affect the performance of the electrodes in the LIB[71][69]. The hazards associated with conventional $LiPF_6$/carbonate-based electrolytes include high gas decomposition products, large combustion enthalpy, and high flammability of the solvent[72]. There are several established lithium salts including $LiAsF_6$, $LiClO_4$, $LiBF_4$ or $LiSO_3CF_3$. However, suffering from disadvantages such as high toxicity or low ionic conductivity, these salts are generally avoided and $LiPF_6$ is used as a compromise[69]. There are intensive efforts to develop new solvents, salts and additives that may improve overall performance and more importantly, the safety of these systems[73][74][34].

2.2.4. SEI Layer

The negative electrode SEI layer is composed of precipitates from the decomposition of solvents, lithium ions, salts and any impurities present in the electrolyte. It initially forms during the first charge and gradually grows (albeit at a slower rate) after the first cycle until it fully develops. An ideal SEI layer should have negligible electrical conductivity and high resistance to electrolyte diffusion, as well as high lithium ion selectivity and permeability. An SEI-like

layer also forms on the positive electrode, however, its influence on cell operation is negligible[54]. The SEI layer impacts battery performance, influencing capacity loss, self-discharge, cycle life and safety[75]. When the negative electrode is fully passivated, the SEI layer protects lithium plating and dendrite formation at the negative electrode during charging. However, while its presence is vital, it is difficult to control its growth, chemical composition and stability[54], all of which influence battery safety.

It is recognised that during failure, the thermal decomposition of the SEI layer is the most easily triggered reaction[76], playing a critical role in determining the safety of a cell. The entire negative electrode must be covered by a protective SEI layer to prevent further undesired reduction of the electrolyte (by lithium ions) during degradation or failure.

2.2.5. Separator

In a nonaqueous, liquid electrolyte cell, the separator is an ionically conductive but electrically resistive porous electrolyte-filled medium. It is placed between, and in contact with the positive and negative electrodes. It is essential that while the separator is porous and as thin as possible that it is simultaneously physically strong enough to keep the electrodes both mechanically and electrically separate. Additionally, the separator must have high chemical stability to resist degradation as well as good electrochemical stability for the highly oxidative/reductive environment within the cell. With regard to battery safety, one primary challenge for the separator is to harness the full theoretical power density while suppressing the growth of metallic structures, called dendrites, on the surface of the negative electrode upon charging[77]. Dendrites are detrimental to the performance and overall life of the battery and after long cycling; they penetrate the separator leading to the possibility of an ISC or catastrophic failure.

A widely used separator that is utilised in commercial LIBs is the Celgard tri-layer PP/PE/PP separator, where PP is polypropylene. The multilayer design functions as a safety mechanism due to the different melting points of the PE and PP layers, 135 °C and 165 °C, respectively. Initially, the inner PE layer melts and fills the pores at a temperature lower than that

associated with uncontrollable thermal runaway. From this temperature, up to the melting point of PP, the outer PP layers provide mechanical strength. Shutdown separators are reliable[78] and increasingly being incorporated into modern battery designs[34].

2.2.6. Whole-cell design

While the chemistry makes the battery work, physical design plays a crucial role in determining its performance efficiency, safety and reliability for the application type. Commercial cells are manufactured in a variety of geometries, and the energy versus power trade-off is an essential consideration for defining electrode thickness and layout[50]. Typically, electrodes are made using active material powders mixed with a binder, conductive carbon and a solvent to create a paste. This provides the porous properties for better electrolyte soaking and higher surface area for greater power. The paste is applied to both sides of a current collector (Al foil for the positive electrode and Cu foil for the negative electrode). These coated electrode sheets are then arranged in various formats depending on the application type.

The four most commonly used LIB formats are cylindrical, prismatic, coin/button or pouch. The coin cell has a single positive electrode layer and a negative electrode layer pressed into a can. They are small and inexpensive to build, and most coin cells used today are non-rechargeable and used for medical purposes and small devices such as watches and car keys. A cylindrical cell, such as the 18650 has a diameter of 18 mm and a height of 65 mm. It is manufactured by winding the positive and negative electrodes (divided by a separator and soaked with electrolyte) into a spiral or "jelly roll". The spiral is placed inside a cylindrical case, typically made of steel or aluminium. Although it boasts high mechanical strength and cost-effectiveness when compared to cells of similar formats, under extreme conditions, the cylindrical case may behave as a pressure vessel leading to violent ruptures and explosions. In a pouch cell electrodes are cut into multiple sheets and layered. They are placed inside a foil casing (typically Al) with tabs and heat-sealed, and have a lightweight and flexible design. While they offer better

volumetric energy density and packing abilities[79], pouch cells are cased in aluminium-plastic composite films which make them more susceptible to deformations such as piercing, bulging or swelling. On the other hand, the smaller physical size of cylindrical cells makes it easier to assemble them into packs (for example, with gaps between cells) to integrate cooling systems. Several safety features are integrated into these designs to prevent and mitigate undesired states of charge and thermal runaway. The previously mentioned shutdown separator is one of many safety features, others include cell vents, CIDs, PTCs and BMSs extensively reviewed by Balakrishnan et al.[34].

2.3. Heat Generation

As outlined, the generation of heat is critical in the understanding of battery performance and safety. This section introduces the thermodynamics of a LIB during normal working conditions and thermal runaway which occurs during battery failure. The thermal stability of the various cell components and associated decomposition reactions are also outlined.

2.3.1. Thermodynamics

Heat generation in a battery can be derived from the first law of thermodynamics. In a closed system, any change in internal energy is equal to the sum of heat generated or dissipated and the work done by the system. It can be expressed as the following, where dU is the change in internal energy, dQ is a change in the heat that can be added to/or removed by the system, and dW is the total work done by the system.

$$dU = dQ - dW$$

Equation 2.5

Often reactions will induce pressure and volume changes in the system, as a result, the total heat exchange is no longer equal to the change in internal energy (because some of the heat is converted to work). This limitation can be expressed by enthalpy, expressed as the sum of internal energy and the product of pressure and volume.

$$H = U + PV$$

Equation 2.6

Under conditions where the pressure, volume and temperature are constant, the change in internal energy can be expressed as the change in enthalpy. Furthermore, the change in enthalpy for the LIB can be expressed via several terms: reaction, heat capacity, phase change and the enthalpy of mixing.

$$\frac{dH}{dt} = IT^2 \frac{d}{dT}\left(\frac{U_{OCV}}{T}\right) + mc_p \frac{dT}{dt} + phase\ change + enthalpy\ of\ mixing$$

Equation 2.7

Overall, Equation 2.7 can be combined with the first law and expressed with regard to the total heat transfer to the surroundings, dQ/dt

$$\frac{dQ}{dt} = \frac{dW}{dt} - IU_{OCV} + IT\frac{dU_{OCV}}{dT} + mc_p \frac{dT}{dt}$$

Equation 2.8

The electric power of the battery is expressed as dW/dt and is the product of the current and voltage of the cell. For an isothermal process, it is assumed that the rate of heat dissipated from the system is equal to the heat generation rate of the battery. As a result, the sign for heat transfer rate changes to positive, to express the heat released from the battery. Bernardi et al. presented a generic energy balance equation for a cell in Equation 2.9, which shows a combination of heating effects, some reversible, such as heat generation from electrochemical reactions, and some irreversible, such as Joule heating and side reactions[80]. The heat produced from mixing and the term for phase changes within the battery are neglected.

$$Q_{total} = \sum_j I_j \left(U_j^{avg} - T\frac{\partial U_j^{avg}}{\partial T} \right) - IV_{cell}$$

Equation 2.9

A simplified form shown in Equation 2.10 is often cited in literature when evaluating the heat generation in a LIB, where the first term is the irreversible electrical power of that battery and the second term is the sum of producible reversible work and entropic heating from reactions within the battery. I is the

current passing through the cell, U_{OCV} is the open circuit voltage of the cell, V_{cell} is the cell voltage, T is the temperature, ΔS is the entropy change, n is the number of electrons transferred during an electrochemical reaction and F is the Faraday constant.

$$Q_{total} = Q_{irr} + Q_{rev} = I \cdot (U_{OCV} - V_{cell}) - \left(I \cdot T \frac{\Delta S}{n \cdot F} \right)$$

<div align="right">Equation 2.10</div>

During the charge and discharge of cells, an oxidation and reduction process is taking place: as a result, ions and electrons are moving between the anode and the cathode. The migration and diffusion of these are driven by gradients in the potential and concentration within the cell's internal structure. During normal operation, heat in a battery is generated from energy losses that can be categorised as three fundamental losses: Ohmic, activation, and diffusion. The losses occur when a current that accompanies the electrochemical reactions, flows through the electrodes. The heat generation rate, therefore, depends on the current and potential characteristics of the battery, as well as its rate of charge and discharge. Thus, in Equation 2.10, the first term refers to the overpotential due to Ohmic losses, charge transfer at the interface and mass transfer limitations. The second term is the entropic heat coefficient. The internal processes during discharge are summarised as a schematic diagram in Figure 2.3.

The entropy change of the reversible reaction can be determined by the following equation, where x is the molar fraction.

$$\Delta S(x, T) = F \cdot \left(\left. \frac{dU_{OCV}(x, T)}{dT} \right|_x \right)$$

<div align="right">Equation 2.11</div>

As a result, the total volumetric heat generation rate in the LIB can be written in terms of the overpotential η, under a specific current load as follows.

$$\dot{Q} = \frac{I}{V_{cell}} \left(\eta - T \frac{\Delta S}{n \cdot F} \right)$$

<div align="right">Equation 2.12</div>

The total overpotential η, is the sum of the Ohmic losses, charge transfer resistances and mass transport limitations due to diffusion limits and can be expressed as the following.

$$\dot{Q} = \frac{I}{V_{cell}}\left(\eta_{Ohmic} + \eta_{kinetic} + \eta_{diffusion} - T\frac{\Delta S}{n \cdot F}\right)$$

Equation 2.13

The Ohmic losses, η_{Ohmic}, are a result of flow limitations, for example resistances to electron and ion flow. Kinetic or activation losses, $\eta_{kinetic}$, are due to kinetic limitations, where resistances to the activation of the chemical reactions occur. They are also affected by the availability of reaction species and reaction sites. Diffusion or mass transport losses, $\eta_{diffusion}$, often referred to as 'concentration polarisation' due to the mass transport limitations associated with any temporary existence of concentration gradients[43]. Each of these loss mechanisms can be represented by a resistance or impedance over which the overpotential occurs. The Ohmic and diffusion overpotentials can be expressed as a function of resistance by Equations 2.14 and 2.15, respectively, where R_{Ohm} is the pure Ohmic resistance and R_D is the diffusion resistance.

$$\eta_{Ohmic} = I \cdot R_{Ohm}$$

Equation 2.14

$$\eta_{diffusion} = I \cdot R_D$$

Equation 2.15

In the case of the kinetic losses, the relationship between the overpotential and the current density it given by the Butler-Volmer equation (Equation 2.16). Where i_0 is the exchange current density of the reaction, α is the charge transfer coefficient, and R is the universal gas constant. The charge transfer resistance R_{CT} can therefore be expressed as shown in Equation 2.17.

$$i = i_0 \cdot \left\{ exp\left[\frac{\alpha nF\eta_{kinetic}}{RT}\right] - exp\left[\frac{(1-\alpha)nF\eta_{kinetic}}{RT}\right]\right\}$$

Equation 2.16

$$R_{CT} = \frac{\eta_{kinetic}}{i}$$

<div align="right">Equation 2.17</div>

Overall, from Equation 2.13, the heat generation rate will vary according to the changes in the overpotentials (which are influenced by the operating conditions of the LIB). In Chapter 4, coin cells are studied by DSC whereby changes to the overpotentials are induced to evaluate the implications this has on the rate of heat generation in the cell during cycling.
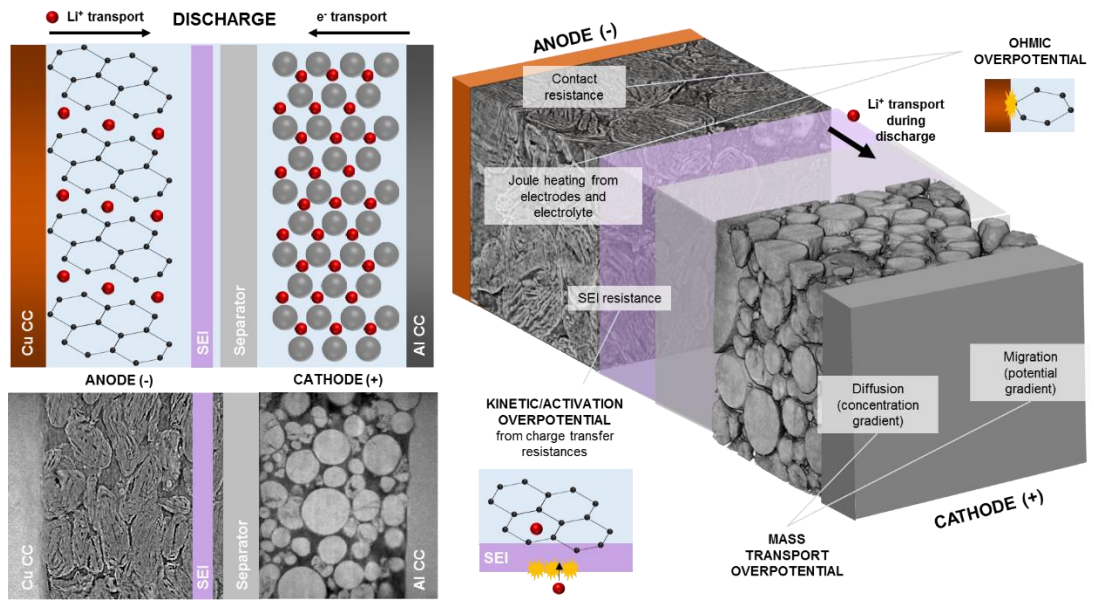
Figure 2.3 Schematic showing the discharge process in a Lithium-ion battery. The microstructures of the anode and cathode are shown to illustrate their link to the internal behaviour of the cell and the components associated with the irreversible heat effects (Ohmic, kinetic/activation and diffusion/mass transport).

2.3.2. Thermal runaway

Aside from the highly oxidising and reducing materials present in LIBs, their safety is compounded by their design having an inherent drawback of poor heat dissipation[81]. When a cell is heated above a certain temperature, exothermic reactions between the electrodes and electrolyte are triggered, raising the internal temperature of the cell. If the cell is adequately designed to dissipate this heat, its temperature will not rise abnormally. However, poor heat dissipation will facilitate exothermic processes to continue under adiabatic-like conditions - this is known as thermal runaway[81]. The safety

limit of a cell is often quantified in literature by the temperature at which these exothermic reactions are initiated, i.e. the onset temperature. Any pressure generated by this process can cause mechanical deformations, trigger short circuits, and swell or rupture cell casings; all of which are considered battery failure mechanisms. On the other hand, any scenarios such as overcharge/discharge, dendrite formation, or electrode misalignment can also trigger the onset of these exothermic reactions. Overall, several events are common among all types of batteries and the generation of heat is the most dominant response of a battery to abusive conditions[82][49].
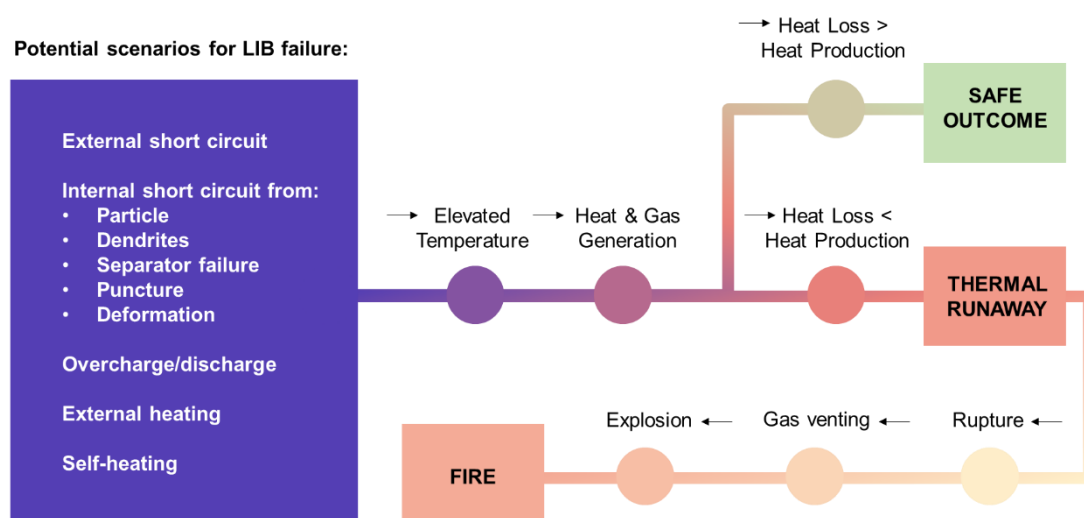
Figure 2.4 Flowchart depicting the possible outcomes of a typical lithium-ion battery failure sequence adapted from Total Battery Consulting[83].

2.3.3. Thermal stability of battery components

The cathode material has the largest influence on cell safety[9]. In this case, 'cell safety' is discussed regarding onset temperature: the temperature at which materials begin to thermally decompose either outside of or within a full working cell. $LiCoO_2$, being the cathode of choice for many consumer-level LIBs, remains one of the most reactive and least thermally stable materials when compared to other cathode materials (such as NMC or LFP)[84]. For example, Jiang et al. compared the onset temperatures of $LiCoO_2$, $Li(Ni_{0.1}Co_{0.8}Mn_{0.1})O_2$ and $LiFePO_4$ cathode chemistries which were 150, 220 and 310 °C, respectively. Zhong et al. investigated the thermal stabilities of

$Li(Ni_{0.5}Co_{0.2}Mn_{0.3})O_2$, $LiMn_2O_4$, and $LiFePO_4$ and concluded that the NMC cathode chemistry was the least thermally stable of the three (when comparing the temperature at which it begins to self-decompose)[85]. Furthermore, Bak et al., using a combination of X-ray diffraction and mass spectrometry compared the structural changes and oxygen release of NMC cathodes of varying nickel contents (i.e. NMC433, NMC532, NMC622 and NMC811). It was found that the higher the nickel content (and therefore less cobalt and manganese), the lower the onset temperature for decomposition reactions[44]. For NMC samples, a higher energy density can be achieved when the cut-off voltage is increased, however, the structure is prone to instabilities when large fractions of lithium are removed[44][86]. Furthermore, higher voltages can lead to faster degradation of materials (for example, transition metal dissolution and electrolyte oxidation). Recent developments in NMC cathode materials have shifted the focus to Ni-rich NMC. They allow for larger amounts of lithium to be extracted while keeping the structure more stable (within the same voltage range) than at more traditional NMC ratios, such as NMC111. However, Ni-rich NMC can suffer from shorter cycle life as their ability to retain capacity diminishes as shown by Noh et al.[11]. On the other hand, at high temperatures (> 170 °C), Ni-rich NMC is still thermally less stable than LCO or LFP. As their structures change from layered to spinel and eventually to rock-salt structure, oxygen is released. This has been extensively studied by Jung et al. for varying Ni-content NMC materials[87]. Released oxygen from the cathode lattice reacts exothermically with electrolyte and sustains thermal runaway. The research focused on high nickel content cobalt-free cathode chemistries[88][89] such as $LiNi_{0.7}Mn_{0.25}Al_{0.05}O_2$ (NMA70)[90] has revealed noticeable improvements in thermal stability when compared to existing high-Ni content cathodes. When compared to an NMC sample, the NMA70 had a higher onset temperature (252.9 °C compared to 232.1 °C) and lower overall heat generation (319.2 J g^{-1} compared to 454.4 J g^{-1})[90]. The presence of Al can greatly improve the thermal stability of high-Ni content and cobalt-free cathodes[91][92].

Alongside the cathode chemistry, several other components and their chemistries will influence cell safety (for example, the negative

electrode[46][81], separator structure[93] and the chemical makeup of the electrolyte[94]). Geng et al. found that the presence of electrolytes can accelerate the thermal and structural decomposition of cathode materials; for example, almost all the layered phases transformed to a rock-salt phase for cathode material tested with electrolyte versus without[95]. These phase changes are accompanied by gas release, which can influence the occurrence and rate of exothermic reactions during thermal runaway. For LIBs that use liquid electrolytes, for example, carbonates and ethers, and salts such as lithium hexafluorophosphate ($LiPF_6$), the cell design becomes inherently thermally unstable as these organic solvents are highly flammable. Furthermore, the thermal decomposition of $LiPF_6$ in various solutions of dialkyl carbonates will lead to the release of several products that will sustain reactions when the conditions are favourable for further decomposition such as high temperatures[94] – a detailed review of such reactions is provided in the following sections. Electrolyte additives have also been widely researched and implemented in commercial cells to improve thermal stability and overall battery safety[74].

The separator, often made from polypropylene and/or polyethylene, is a porous medium that is used to facilitate ion transport within a cell while preventing electrical conductivity between the anode and the cathode. The porous structure of various separator materials allows a high electrolyte wettability enabling the diffusion of lithium ions. The separator may become mechanically unstable if it is pierced by lithium metal dendrites. The only other time their influence on battery safety is discussed is when the temperature within a cell reaches the melting point of the separator material. Generally, at temperatures above 120 °C, the separator material is expected to melt. The material will begin to shrink and contact between the anode and cathode may occur. Advancements in separator design have led to the tri-layer separator made up of PE|PP|PE layers (Celgard 2325, Celgard, LLC.) which has an intrinsic 'shutdown' mechanism due to the different melting points of PP and PE, 165 °C and 135 °C, respectively. As the PE layer melts, ionic transport between electrodes ceases, to potentially delay or prevent an internal short circuit[96].

2.3.4. Thermal decomposition reactions

Several thermal decomposition reactions occur during LIB operation under normal conditions and others occur under failure-prone conditions such as high temperature. The thermal behaviour of LIBs during failure conditions has been widely researched. Figure 2.5 shows a schematic of the various thermal degradation responses occurring within a typical LIB during thermal failure. The heat generated by various reactions is also widely documented, both using models[97][98] and experimentally[99], however, due to the large variations in cell formats and chemistries, it is often difficult to determine the reaction sequence and to what extent each is contributing to the overall heat generated. Nonetheless, for the cells tested in this thesis, there is sufficient literature to understand some of the material reactions that may be occurring during thermal failure.
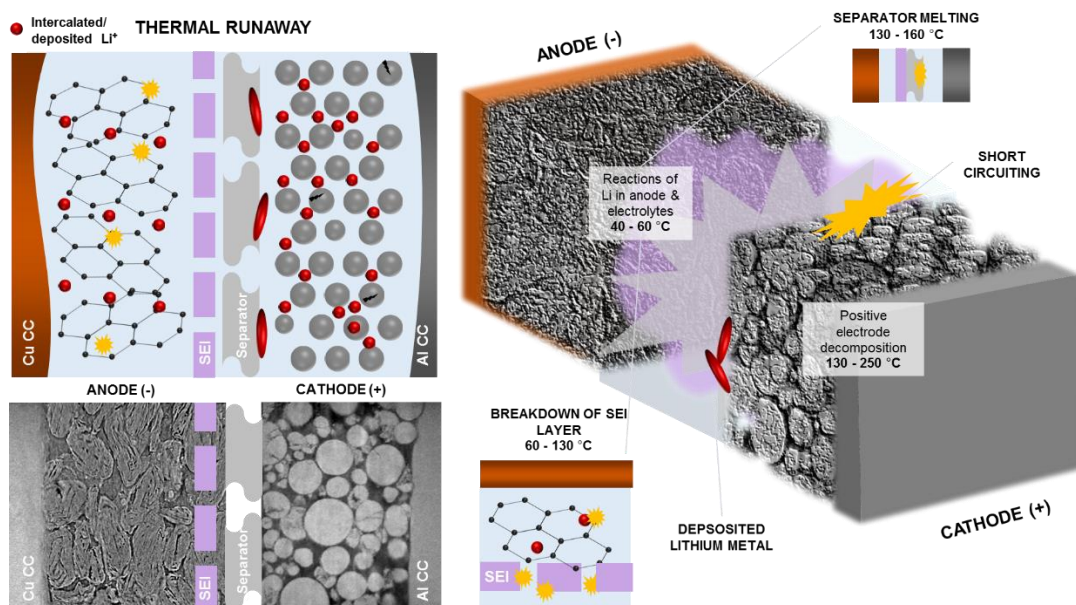
Figure 2.5 Schematic showing the degradation of lithium-ion battery components during thermal runaway. The microstructures of the anode and cathode are shown to illustrate their link to the internal behaviour of the cell and the components associated with the heat and gas generated in the cell as it undergoes thermal runaway.

Reduction of the electrolyte is one of the first decomposition reactions to occur in LIBs. The working potential of the negative electrode lies below the stability window of the electrolyte and lithium metal is thermodynamically unstable in the presence of electrolyte components (salts and solvents). During the first charge and discharge (or formation) of the battery

decomposition products precipitate to form a passivating SEI layer on the negative electrode surface[100][101]. Lithium ions can still diffuse or migrate across this layer and any freshly plated lithium will continue reacting with the electrolyte[102]. The rate at which this happens is dependent on the composition of the electrolyte. The formed SEI layer consists of two parts; one being dense and the other diffused within which a variety of insoluble chemical compounds will be present. Some of these include $LiOCH_3$, $(CH_2OCO_2Li)_2$, or $LiCH_2CH_2OCO_2Li$ which is often presented by Equation 2.18 where R can be CH_3 or C_2H_5.

$$ROCO_2Li \longrightarrow ROLi + CO_2$$
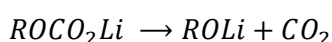
Equation 2.18

Further compounds such as Li_3N, Li_2CO_3, Li_2S, $Li_2S_2O_4$, $LiOH$, LiF, or $LiCl$, and gases CH_4, CO_2, C_2F_6, H_2, CO, $CH_2 = CH_2$, $CH_3 = CH\text{-}CH_2$, etc. may also be formed. Since the composition of the SEI is dependent on the electrolyte composition and potential of the cell, it is often difficult to measure its thickness, chemical makeup and resulting thermal behaviour[103]. However, there is literature available on the effects that electrolyte compositions and salt concentrations have on the thermal stability of the SEI layer using techniques such as DSC[104]. Ryou et al. found that the presence of $LiPF_6$ is the main cause of the thermal decomposition of lithium alkyl carbonates in the SEI layer[103]. The decomposition reaction of $LiPF_6$ produces PF_5, which is a strong Lewis acid, as shown in Equation 2.19.

$$LiPF_6 \Longleftrightarrow PF_5 + LiF$$
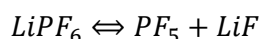
Equation 2.19

The PF_5, reacts with the oxygen atom of carbonyl groups and any other compounds with a high electron density. The dominant component of the SEI layer is $(CH_2OCO_2Li)_2$ which would indicate C-O groups. Some investigations propose that the presence of PF_5 damages the SEI (in a $LiPF_6$ system), at approximately 69 °C[105]. During longer cycle operation at room temperature, the composition of the SEI may change[106] which can alter the electrochemical behaviour of a cell. Furthermore, at elevated temperatures, around 100 – 150 °C[81][107], the SEI layer decomposes exothermically.

The thermal decomposition of various LiPF$_6$ concentrations in solutions of ethyl- and methyl-carbonate have been investigated using DSC. The mixtures typically produce a large exothermic peak below 100 °C where the peak height increases as the concentration of LiPF$_6$ increases. Interestingly, thermal decomposition investigations using DSC for pure LiPF$_6$ salts showed a small endothermic peak occurring in the range between 57.3 °C[103] and 75 °C[108], while no peaks occur below 100 °C for the thermal decomposition of pure ethyl- and methyl- carbonate solutions (without LiPF$_6$). The endothermic peaks occurring below 100 °C for LiPF$_6$ salts alone are predicted to be from hydrogen fluoride (HF) removal[108] and thermal decomposition by trace amounts of moisture as shown by the following two reactions (Equation 2.20 and 2.21):

$$LiPF_6 - HF \rightarrow LIPF_6 + HF$$

Equation 2.20

$$LiPF_6 + H_2O \rightarrow LiF + OPF_3 + 2HF$$
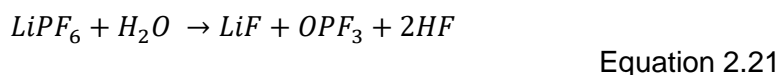
Equation 2.21

The endothermic reactions from pure LiPF$_6$ do not play a significant role in triggering the exothermic reaction of the SEI layer. However, the thermal decomposition reaction occurring in mixed solutions as shown in Equation 2.22 (where R can be CH_3 or C_2H_5), is significant.

$$ROCO_2Li + HF \rightarrow LiF + ROH + CO_2$$

Equation 2.22
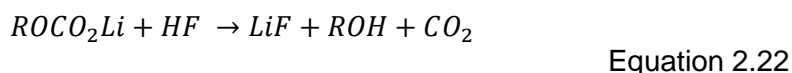
Ravdel et al. investigated the thermal stability of 1M LiPF$_6$ in solutions of dimethyl carbonate (DMC), diethyl carbonate (DEC) and ethyl methyl carbonate (EMC) up to 85 °C. Decomposition was detected at approximately 70 °C upon heating and occurred more rapidly at temperatures above 85 °C. Some of the decomposition products observed by gas chromatography with mass selective detection (GC-MS) and nuclear magnetic resonance (NMR) spectroscopy included phosphorus pentafluoride (PF$_5$), phosphorus oxyfluoride (OPF$_3$), and CO$_2$ for all three carbonate solutions. It is believed that the highly reactive PF$_5$ solids and OPF$_3$ initiate solvent decomposition to form several other liquid and gaseous products[94] and that the thermal decomposition of LiPF$_6$ in DMC is slower than in DEC.

After the breakdown of the primary SEI layer, the electrolyte has easier access to the lithiated graphite surface. Intercalated lithium ions move to the edge of the graphite (from the inner structure) at high temperatures, which is accelerated by the presence of PF_5 which is removing electrons from the graphite. The lithium reacts with the electrolyte exothermically. Pure graphite has high thermal stability, greater than 600 °C, however, this is lowered after lithium intercalation. Edstrom et al. found that the decomposition of the SEI layer (when using graphite, $LiPF_6$/EC+DMC) starts at 102 °C[109], while other studies[110] using MCMB, $LiPF_6$/EC+DMC or MCMB, $LiPF_6$/EC+DEC[111] measured this temperature to be 130 °C and 100 °C, respectively. These temperatures vary largely due to the variations in SEI formation on the anode layer, which are a function of the electrolyte composition. Furthermore, the onset temperature and rate at which heat is produced by the exothermic anode-electrolyte reactions are controlled by the SEI layer. Using DSC, Yamaki et al. found that upon further heating of a graphite and $LiPF_6$/EC+DMC electrolyte sample, mild heat generation continued from 140 °C until a large exothermic peak appeared at 280 °C[112]. The mild heat generation within this temperature range is due to a series of consuming exothermic reactions: the rate of which positively correlates to the exposed surface area of the graphite particles[113]. The reaction products that are formed during these reactions begin to accumulate and form a secondary SEI film. The reaction between lithiated graphite and electrolyte gets obscured by the lithium-consuming/secondary SEI layer formation and is often difficult to differentiate in a DSC profile. An example of a lithium metal and electrolyte reaction is shown in Equation 2.23.

$$6Li + LiCF_3SO_3 (LiTFS) \rightarrow 3LiF + Li_2S + Li_2CO_3$$
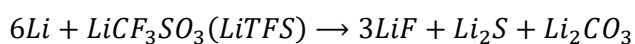
Equation 2.23

Furthermore, some of the energy released from the initial thermal decomposition reactions may be absorbed by the evaporation of the electrolyte (~ 140 °C) or melting of the separator (between 130 °C and 190 °C). As the new SEI layer thickens, however, it prevents further reaction of the electrolyte and intercalated lithium. At temperatures above 200 °C, an exothermic peak occurs when the secondary SEI layer decomposes. This

peak is also often obscured by a number of other simultaneous reactions which involve the polyvinylidene fluoride (PVDF) binder, lithiated graphite, Li-alkyl carbonates and the electrolyte. Alone, the anode-electrolyte reaction does not have as much energy (as a cathode-electrolyte reaction) to sustain the exothermic reaction series during thermal runaway, however this heat release becomes more important in larger cells[113].

At temperatures above 200 °C, the electrolyte may combust if there is a presence of oxygen. Oxygen typically begins to evolve from the positive electrode from anywhere as low as 225 °C up to 400 °C (depending on the composition), examples of which are given in Equations 2.24 and 2.25.

$$4MnO_2 \longrightarrow 2Mn_2O_3 + O_2$$

<div align="right">Equation 2.24</div>

$$LiClO_4 \longrightarrow LiCl + 2O_2$$

<div align="right">Equation 2.25</div>
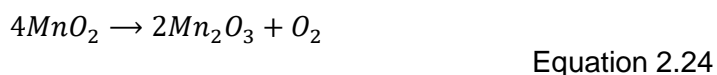
It is understood that de-lithiated NMC811 samples release larger amounts of O_2, CO_2, and heat at lower onset temperatures[95]. Geng et al. studied the thermal stability of NMC811 at different degrees of lithiation: $Li_{0.75}NMC811$, $Li_{0.5}NMC811$, $Li_{0.3}NMC811$, and $LiNi_{0.8}Mn_{0.1}Co_{0.1}O_2$ (pristine, or uncycled sample) using DSC. The dry NMC811 samples were tested with 1.5M $LiPF_6$ in EC electrolyte and sealed in stainless steel capsules inside an Ar-filled glove box. The start temperature was 50 °C and ramped up to 400 °C, step-wise at a rate of 5 °C min^{-1}. The pristine sample was stable up to 300 °C, whereas the most de-lithiated sample ($Li_{0.3}NMC811$) began to decompose and release O_2 much sooner, at 245 °C. Bak et al. on the other hand reported that traces of O_2 were released as early as 130 °C at a lower state of lithiation (~ $Li_{0.22}NMC811$).

Generated oxygen will begin to participate in several combustion reactions, some examples are given in Equations 2.26 and 2.27.

$$2H_2 + O_2 \longrightarrow 2H_2O$$

<div align="right">Equation 2.26</div>

$$CH_4 + 2O_2 \longrightarrow CO_2 + 2H_2O$$

<div align="right">Equation 2.27</div>
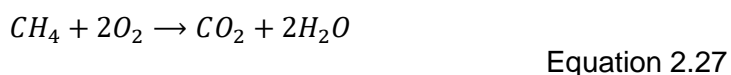
Furthermore, a commercial battery will contain several other combustible materials such as the separator (PE or PP), binder (polytetrafluoroethylene, PTFE), tapes and adhesives (e.g. silicone or acrylic). Examples of the separator combustion reactions are given in Equations 2.28 and 2.29.

$$(-C_3H_6-)_n + 9/2 \, nO_2 \rightarrow 3nCO_2 + 3nH_2O$$

Equation 2.28

$$(-CH_2 - CH_2-)_n + 4nO_2 \rightarrow 2nCO_2 + 4nH_2O$$

Equation 2.29
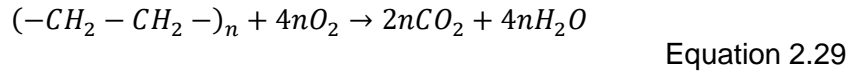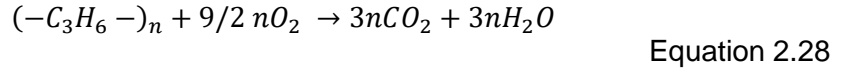
Furthermore, at higher temperatures, approximately 600 °C, combustion of the graphite/carbon anode:

$$C + O_2 \rightarrow CO_2$$

Equation 2.30

Lithium metal may react with the water produced by the oxidation of the organic solvents. It can also react with the PTFE binder and produce lithium fluoride which will contribute to the heat release.

$$(-CF_2 - CF_2-)_n + 4nLi \rightarrow 4nLiF + 2nC$$

Equation 2.31
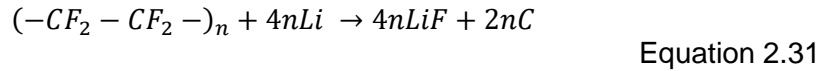
2.3.5. Investigations in literature

Among the several reactions taking place during thermal failure [114], the primary sources of heat can be categorised into five dominant reactions[66][67]; the decomposition of the SEI layer, Q_{SEI}, reaction between electrolyte and the positive electrode, Q_{PE}, decomposition of the electrolyte, Q_E, reaction between the electrolyte and the negative electrode, Q_{NE} and the reaction between the binder material and negative electrode, Q_B. Hence, the total heat released can be expressed as;

$$Q_{TOTAL} = Q_{SEI} + Q_{PE} + Q_E + Q_{NE} + Q_B$$

Equation 2.32

This relation considers heat generation from decomposition reactions only, i.e. heat output during operation, such as Joule heating is not included. It should be noted that a rise in temperatures because of overcharging, for example, would have a significant contribution to the failure of the cell. The kinetic

parameters outlined by the Arrhenius Law play a critical role in determining the onset temperature of each of the five sources contributing to Q_{TOTAL}. The rate at which each occurs and the contribution to the amount of heat generated by each differs and depends on several factors, such as SOC, electrode thickness, particle size and many more that are discussed in the scope of this thesis.

Reactions and their associated kinetic parameters have been extensively modelled to understand and predict thermal runaway[116][115][117]. Hatchard et al.[116], and Kim et al.[115], model thermal runaway and report that heat generation follows an exponential function (Arrhenius Law) while heat dissipation exhibits a linear function (Newton's Law of Cooling). The maximum contribution to heat generation by different components has been modelled[118] with the assumption that each component undergoes complete reaction and/or combustion. The onset temperature of each reaction is different. Similarly, the quantity of heat generated by each reaction varies.

Heat generation, along with gas evolution, occurs between 90 – 120 °C due to the exothermic decomposition of the metastable SEI layer. The highly exothermic breakdown of the graphite phase (on the negative electrode) occurs as the electrolyte encounters exposed lithium ions. The subsequent reaction mechanisms that follow are dependent on both the temperature and the degree of lithiation[46][111][119][120]. Studies of this phenomenon have enabled a comprehensive survey of material morphology and the role of electrolyte additives in lowering the onset temperature of the exothermic reaction[121]. The widely used $LiPF_6$ electrolyte solution exhibits an onset for thermal reactions between 150 °C and 200 °C[69].

At the positive electrode, beginning at ca. 230 °C, oxygen is released from the delithiated material. Once the onset potential for oxygen release is reached, exothermic chemical oxidation of the electrolyte is accelerated forming water and CO_2, increasing the risk of thermal runaway. The amount of oxygen that may be released from the positive electrode is limited, and only if there is a further supply of oxygen can the complete combustion of

components occur[76]. Several safety features integrated into the cell design play a role in introducing external oxygen, facilitating the thermal runaway process. Generally, the amount, rate and temperature at which this phenomenon occurs are highly dependent on the morphology of the positive electrode material. For example, the release temperature for LMO<NMC<NCA[120][122] while there is little oxygen release for $LiFePO_4$[123]. The characteristic thermal behaviours of various positive electrode materials are determined through techniques such as ARC and gas chromatography (GC)[10][47]. Various studies indicate that the more energy dense a material, the higher the rate at which it heats[124]. Similar to the negative electrode, the reduction process of the transition metal oxide electrode is influenced by electron availability in the electrolyte; however, it is predominantly controlled by its crystal structure and composition[125]. Thus, the thermodynamic stability of the material directly influences the onset temperature of the exothermic reduction[124].

During thermal runaway, it is recognised that a higher maximum temperature is reached for a fully charged cell when compared to a cell at nominal voltage, as well as it having a significantly lower onset temperature[80][81]. Additionally, it has been reported that charging beyond a cell's full SOC results in extremely low lithium content in the positive electrode material, this increases the resistance to lithium removal and subsequently increases the Joule heating[78]. Further to understanding the effects of electrode material morphology on battery safety, studies have revealed how surface-dependent features, such as the specific surface area, determine the degree of heat generation during failure[128]. Jiang and Dahn[129] demonstrated that a reduction in particle size of LCO from 5 μm to 0.8 μm resulted in a lower onset temperature for thermal runaway. Furthermore, it has been demonstrated that additional surface area as a result of particle cracking can further decrease the thermal stability of an electrode (due to the increase surface area available for reactions). Despite this, there are a limited number of studies to understand the role of particle size on thermal stability. Although it is evident that particle microstructure plays a critical role in electrode

behaviour (heat generation) during failure[130][131], this area is not yet well understood.

2.4. Failure and Safety Assessment

In a comprehensive review of LIB fire safety studies, Ruiz et al. report that most literature focuses on single-cell and component scales as opposed to module or pack scales[132]. The failure behaviour of larger-scale battery packs is different to individual cells and so the outcome of investigations also differs depending on the scale at which they are studied. Investigations can therefore be categorised by order of 'layer of protection' starting from prevention, compartmentation, and detection to suppression of the fire[132]. The prevention layer aims to avoid the failure scenario altogether and is the category for most single-cell and component scale investigations. For this, the fundamental mechanisms that trigger and sustain the failure need to be understood; which is also where the focus of this thesis lies.

2.4.1. Failure modes and testing standards

The underlying causes for battery failure vary across different chemistries, physical designs and sizes. Failure modes can be categorised into four broad categories based on when they occur during the battery life. Early failures occur soon after manufacturing and are often a result of poor handling, fundamental design flaws, missing components, or contamination[133]. Latent failures or random defects such as seal failure or internal short circuits may occur anytime during battery life (i.e. storage or in use). The rate of these failures is usually relatively low and constant. Degradation, or slow but steady loss of active materials within the battery, may result in the premature end of life[53]. These generally occur later in battery life but can be accelerated via excessive self-discharging, chemical breakdown of the electrolyte, dendrite formation and various other complications depending on individual components. Over time, active materials may eventually be fully consumed or internal resistances may increase to a critical level and the battery can no longer supply power.

Although this is not a "failure mode" for safety assessment, it is important to note that the deterioration of cells is not only a function of time and the number of cycles, but also influenced by the environmental conditions in which they are stored or operated.

Various failure modes in literature are replicated to understand their magnitude and associated risk of thermal runaway. Aurbach et al. reviews failure mechanisms which arise in LIBs upon fast charging[134]. For applications that require high charging rates, for example, powering portable electronic devices, passivation is considerably worsened: the higher the rate of charging, the higher the rate of lithium deposition. This leads to dendrite formation and depletion of active reactants; lithium and solvent species[53]. First reported *ca.* 1980, structures of metallic lithium or dendrites form at the negative electrode and grow towards the positive electrode, resulting in direct contact between electrodes (internal short circuit)[135][136], leading to rapid overheating and discharge of the cell. Thus, understanding the occurrence of short circuits inside the cell is vital when assessing battery safety. As a result, numerous studies exist in attempting to replicate internal short circuits induced externally or internally[132][137][16]. Similarly, thermal failure is induced via extreme (or "abuse") conditions, which can be thermal (overheating), electrical (overcharge, high pulse power) or mechanical (crushing, internal or external short circuit). Common abuse studies and standards for LIB are reviewed and summarised by Ruiz et al.[132] and Chen et al.[133].

Despite standardisation efforts across LIB manufacturers, organisations, and battery researchers, current LIB safety testing standards have different guidelines for different battery formats, applications and failure trigger scenarios. For example, heating tests are used to analyse the LIBs' thermal stability and heat distribution. Some standards[133] deem a battery as 'safe' if it does not leak or combust after it is placed in a hot box and heated to 130 °C at 5 °C min^{-1} and kept at this temperature for 30 min, whereas others heat to 150 °C (at any heating rate) and hold for 60 min before classifying it as safe. For nail penetration (or ISC) tests, the battery should be at 100 % SOC before it is penetrated by a high-temperature-resistant stainless steel nail (with a diameter between 5 – 8 mm) at a speed of 25 mm s^{-1}. The penetration

position should also be as close to the geometrical centre of the cell and the nail should reach 100 % of the depth of the battery for some, while for others the nail positioning and depth are not controlled. Several research efforts have been made to compare the results of varying the battery SOC and capacity when heating as well as the depth and position of the nail during penetration tests. For example, Mendoza-Hernandez et al. report that thermal runaway is triggered much sooner and at a lower onset temperature in a cell at 100% SOC compared to 50 % SOC[138]. The severity of reactions is reported to be greater when a cylindrical cell is penetrated at the centre as opposed to the top and bottom, while higher nail penetration speeds decreased the uniformity of temperature distribution within the cell[139]. Therefore, it is crucial to consider how such variations can affect the extent of failure and interpretation of LIB safety.

2.5. Thermal Analysis

The exothermic nature of LIB reactions means calorimetry is suitable for studying these mechanisms under controlled conditions. In literature, adiabatic calorimetry (e.g. ARC and DSC) has been used to investigate the decomposition of LIB materials as individual components as well as components within a complete cell[140][141][142][143]. Several investigations to predict battery failure behaviour and the thermal runaway mechanism have been conducted both on the component and cell level, using accelerating rate calorimetry (ARC). Based on kinetic parameters determined from ARC tests, Dahn et al.[144] developed models to study reaction mechanisms and thermal stabilities of small amounts of various materials at a component level. Furthermore, Spotnitz and Franklin surveyed various abuse behaviours on LIB materials by combining DSC with ARC[114]. It was reported that the decomposition of the binder on the negative electrode (anode) plays an inconsequential role during thermal runaway. Furthermore, the combined technique revealed the advantages of both techniques for LIB thermal analysis: providing an insight into reaction rate and the sequence in which they occur, as well as their overall and individual contributions to heat generation during failure.

This has been extended to cell-level investigations by Hatchard and Kim[116][115] who established a model to predict the behaviour of large format cylindrical Li-ion batteries. Roth et al. used a combination of ARC and DSC to measure the thermal response of high-power commercial 18650 cells when subjected to temperatures up to 400 °C. The technique allowed the individual contributions of the positive and negative electrodes to thermal abuse response to be determined[141]. Golubkov et al. reported thermal behaviours of various positive electrode materials during thermal ramping tests[124]. Ren et al. investigated thermal runaway mechanisms through DSC tests on individual components and their mixtures[117]. Robinson et al. used a combination of ARC and post-mortem image characterisation to analyse the thermal failure properties of a fully charged commercial pouch cell[96].

The effects of cell geometry and configuration were studied by Lopez et al. who found that a prismatic shape had a slower temperature response and failure reaction kinetics than a cylindrical shape[145]. Several models exist for thermal runaway triggered by various mechanical loadings and crash events, however, Zhu et al. conclude that due to the inhomogeneity between the numerous behaviours such as temperature, pressure-dependence, anisotropy, or ductile fracture, each component (current collector, coating, separator, shell casing) exhibits, models that accurately predict thermal behaviour are currently limited to the microscale[146].

2.6. Structural Characterisation

The performance and reactions occurring within LIBs are highly dependent on the microstructures of the materials present such as the positive and negative electrode. For example, internal structures including particle shape, distributions and arrangements all influence conductivity, charge capacity, and degradation rates of various electrodes. SEM has been used extensively to image LIB electrode material surfaces[147]. High magnification results reveal the fine structures of pores and particles and the presence of nanoscale pores. While the SEM data demonstrates the multi-scale nature of the electrode, the data is often limited to 2D information, preventing the study of inter-particle pore networks (3D), for example[148]. SEM is often combined

with energy-dispersive X-Ray (EDX) analysis to determine chemical compositions. Furthermore, the removal of thin slices by the focused-ion beam (FIB) and subsequent SEM imaging allows the construction of 3D models of electrodes. Measurements of phase volume fractions (particle and porosity), surface area and tortuosity had initially been demonstrated for lithium-ion electrode materials, such as $LiFePO_4$[147] and $LiCoO_2$[149] using 3D reconstructed data from FIB-SEM imaging. However, these methods require the battery to be discharged to 0 V and then opened for the removal and handling of the electrode samples which is disruptive to the cell environment[150].

Shearing et al. successfully demonstrated ways in which 3D data obtained via X-ray tomography enables direct assessment of phase connectivity within electrode materials[151], unachievable by previous stereological approaches[152][153]. The technique was non-destructive and provided resolutions that could quantify pore networks and sub-particle defects. Ebner et al. applied X-ray tomography to NMC cathode materials and reported that smaller particles influenced packing within interfaces of the separator and current collectors, consequently revealing porosity distributions throughout the electrode[154]. Quantitatively studying pore geometry (e.g. tortuosity) enabled the effective diffusivity of porous materials and subsequently the link between Li^+ ion transport through electrodes and performance to be determined[155][156]. Maire and Withers review the use of X-ray CT images for numerical modelling based on realistic microstructures such as predicting flow through a porous sample or mechanical properties of composite materials[157][158].

It is known that the generation of heat and other common failure mechanisms are inherently linked to material morphology and behaviour during operation and failure[15][53]. While the heterogeneous microstructure of battery electrodes and their porous nature often determine the electrochemical performance of a cell, it is common that any defects within such materials can behave as causes for macroscopic failures[53][159]. For example, the expansion and contraction of active electrode materials during operation can lead to particle cracking[160] or SEI layer

deformation[161][162]. Hence, understanding microstructures are essential to failure assessment and development towards safer batteries[22].

2.6.1. Multi-scale imaging
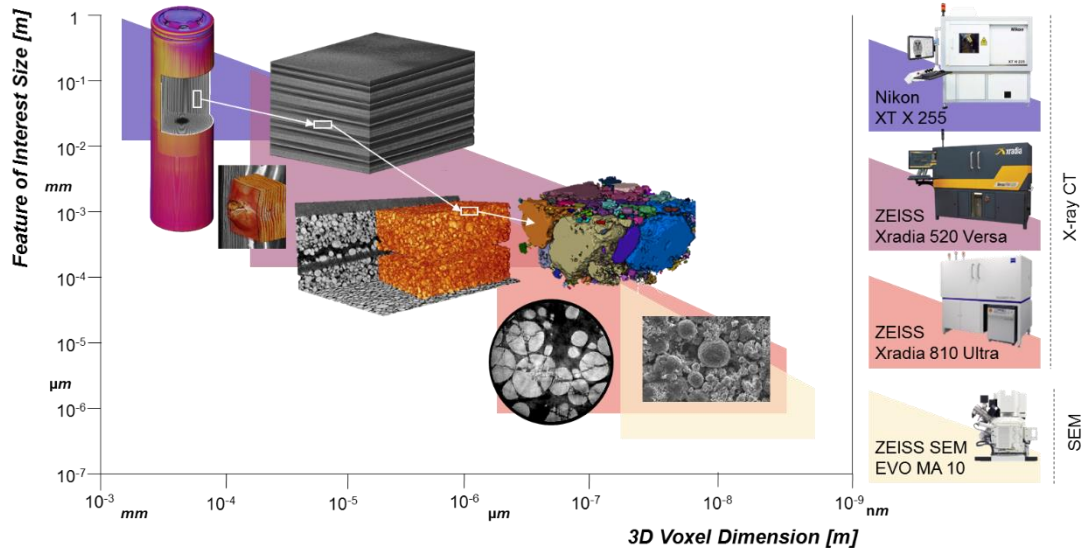
Figure 2.6 Comparison of lab-based X-ray CT systems and SEM as a function of the feature of interest size in (LIB materials) and 3D voxel dimensions.

The multi-length scale aspect of the LIB is investigated by a variety of imaging instrumentation, including optical and electron microscopy and 3D X-ray microscopy[163], each with unique strengths. Depending on the sample preparation technique used, the imaging of battery materials can be categorised as either 'destructive' or 'non-destructive'[130]. The minimum feature size that can be detected is dependent on the operating length scale of the imaging instrumentation[23]. The suitability of a technique to understand the multi-length scale structures within battery electrode materials is determined by the feature size of interest and the resolution offered by the equipment. Furthermore, the composition of a sample and its size, for LIB materials, will determine the achievable spatial resolution[164].

The thickness of electrodes, alignment of assembled batteries, or placement of safety features are all design parameters that can be examined on a centimetre or millimetre length scale. A commercial LIB typically has an electrode thickness that is approximately 100 µm and active particle diameters

ranging from 5 to 25 µm, thus X-ray tomographic instrumentation with resolutions in the order of 500 nm to 1 µm is used for microstructural studies. Several parameters can be used to describe the structure-performance relationship of porous electrode materials; porosity, tortuosity, particle size distribution (PSD) and the specific surface area. Comparative studies examining how well a single 2D image section represents inherently 3D microstructural parameters in battery electrodes report that stereological approaches are often ambiguous and lead to under- or over-estimation of parameters such as particle size, porosity or tortuosity[17][159]. Historically, the microstructural data of electrode materials were extracted using this approach, and with electrochemical methods that considered only the average behaviour of the electrode, limiting any investigation of inhomogeneity within bulk structures (e.g. particle packing). Shearing et al. reported local inhomogeneities in a commercial 18650 negative electrode using lab-based X-ray tomography[151]. Eastwood and Taiwo[165][166][159] investigated the application of phase contrast X-ray techniques for imaging LIB electrodes. The micro-CT resolution allowed for key features of the bulk properties of electrodes containing thousands of particles to be quantified. For example, larger bulk particles correlate to an increase in the quantity of intercalated Li[167], and smaller particles facilitate decomposition reactions[168].

Layered transition metal oxides (typical cathode materials such as NMC and NCA) consist of spherical particles with diameters of ~ 10 µm densely packed with smaller particles (0.1 – 1 µm)[169]. These are often referred to as primary and secondary particles, respectively. Several structural degradation mechanisms such as surface reconstruction and micro-cracks[170][171] have been reported to affect the reaction capability of a LIB cathode material. Heenan et al. utilised the low spatial resolutions of lab-based nano-CT to identify microstructural defects in NMC811[172].

2.6.2. Image-based modelling

Some of the microstructural parameters most commonly reported for LIB materials are phase volume fraction, surface area, geometric tortuosity and pore radius[159]. While several empirical relationships like porosity, ε and

tortuosity, τ exist (such as the Bruggeman relation[173]), modern X-ray tomography directly and more accurately quantifies real-life pore geometries[174]. Initial simulation techniques assumed tortuosity to be isotropic and homogeneous throughout the electrode material. However, the validity of the Bruggeman relation has been questioned for its application to LIB electrodes where broad PSD[175] or varying pore types (open or closed) exist[17]. Local inhomogeneities are expected to cause variations in tortuosity[176]. Cooper et al. quantified the effect of electrode tortuosity on the resistance to diffusion through a material by a heat transfer analogy using a LiFePO$_4$. Using computational fluid dynamics, the measured tortuosities were shown not to correlate with the widely used Bruggeman relation.

Understanding particle shapes and distributions as well as their orientation within an electrode can all aid in accurately investigating the key phenomena that define battery performance. For example, the influence of particle arrangements on battery performance was investigated by Ebner et al.[174]. An analysis of direction-specific tortuosity within NMC, LCO, and graphite electrodes revealed that while the NMC (spherical particles) showed isotropic tortuosity, the LCO and graphite electrode showed a higher tortuosity value for the direction perpendicular to the current collector than for the values parallel to the current collector. Xuekun et al. developed a 3D microstructural-resolved electrochemical model that showed that the gradients of electrolyte concentration and the state-of-lithiation increased with the depth of discharge in the direction from the current collector to the separator. Furthermore, as the discharge rate increased, the impact of particle size on state-of-lithiation heterogeneity became more pronounced. A graded-microstructure electrode design was proposed and demonstrated that it better utilised the active material[43]. Furthermore, Daemi et al. presented a technique that combined compression and in-situ X-ray nano-CT to emulate calendaring during electrode fabrication. The movement of particles through the electrode as a function of the applied load was introduced to aid models of crack initiation and propagation[177].

A critical limitation of image-based modelling is the sensitivity of parameters to the resolution of the image[165][151]. Phase volume (particle

and pore) are relatively insensitive to spatial resolution, as demonstrated by Shearing et al.[155] when comparing a cathode material at three different resolutions (15 nm, 65 nm, and 597 nm). Specific surface areas on the other hand were often underestimated due to features being unresolved at low resolutions. It was reported that the carbon black/binder domain (CBD) present between active particles and pore structures played a critical role in accurately modelling conductivity within electrode materials. The nanometre length scale of the CBD phase requires imaging techniques such as FIB-SEM[178][179] or X-ray nano-CT[180][181]. In a study by Daemi et al.[181], the inactive CBD was examined within an NMC electrode using a combination of both high-resolution FIB-SEM and X-ray nano-CT data. FIB-SEM data reduced uncertainties present in multi-scale CT image processing by confirming porosity at nanoscale and the distribution of macro-pores at a larger scale. The combined technique confirmed an increased tortuosity value when a two-phase scenario was compared to one which considered the CBD as a third phase.

Zhu et al. review the safety-focused mechanical modelling of LIBs[146]. The structural mechanics of cells undergoing various failure types are modelled at multiple length scales. At the whole-cell level, there are limitations with regard to homogenising models to characterise multiple phenomena occurring together. In-situ X-ray micro-CT and X-ray diffraction (XRD) for real-time monitoring of material behaviour during failure are suggested to provide information for existing models of whole-cell failure. Radhakrishnan et al. developed a processing toolbox for capturing the displacement of electrode structures at the onset of battery failure initiated by nail penetration[182].

2.6.2.1. Failure characterisation: In-situ/operando, ex-situ and post-mortem analysis

Several dynamic electrochemical, thermal, and structural phenomena occur inside a battery as it undergoes failure. Waldmann et al. reviews state-of-art methods by which aged cells are disassembled and investigated after failure[150]. However, each method is limited to a single measurement (i.e. only electrochemical) making it difficult to characterise failure mechanisms[183]. Imaging techniques such as SEM[184], X-ray

radiography[185][16][186], X-ray CT[187][188][189] and neutron tomography[190] have been proven to be useful methods to obtain structural and dynamic parameters of materials during and after a failure incident.

Ebner et al. first introduced an operando tomographic investigation of an operational LIB, where the lithiation of individual particles was tracked under normal operation[161]. In-situ and operando X-ray imaging methods in combination with various accelerated stress tests, particularly thermal runaway, have been conducted to track degradation (particle fractures, SEI formation, lithium plating, and delamination of material) in LIBs. Finegan et al. combined thermal imaging, high-speed radiography and tomography to track the mechanical degradation of a commercial cylindrical cell that underwent thermal runaway[185]. The internal structure of the cell: electrode architecture, safety features and vents were examined for multiple samples and it was concluded that the failure behaviour of cells can vary greatly. Yufit et al. introduced the first post-mortem analysis of a failed lithium polymer pouch cell[191], and since then, multiple methods for post-mortem analyses for LIB failure characterisation have been introduced. Mao et al. compare the anode extracted from a cylindrically wound cell after nail penetration with that of a pristine graphite anode and finds that the layered structure is still intact but has some additional fragments and voids where flammable materials may have been consumed by the thermal runaway reactions[139]. Micro-CT was used in combination with XRD by Zhang et al. to visualise the cross-section of a jelly-roll pouch cell. A buckling behaviour was observed at the folded edges of the electrode layers as a function of extreme cycling. Ripples created by this posed a high chance of ISCs. As a result, the authors' proposed optimised anode layer structures that controlled the distribution of stress and constraint in a jelly-roll cell[192].

The impact of low-temperature charging on the degradation of LIB materials was conducted by We et al. using a cell-opening method where the jelly-roll structure was unwound and separated into a cathode, anode and separator. They were visually inspected for surface smoothness, detachment of active material and regions of exfoliation from the current collectors. Lithium

plating on the anode was observed, and later SEM scans revealed cracks between primary particles when compared with fresh cell materials[193].

Finegan et al. investigated the effects of an overcharge-induced thermal runaway on LIB materials using operando X-ray CT. A post-mortem multi-scale approach was introduced whereby significant morphological and phase changes in a $LiCoO_2$ pouch cell after failure were examined using X-ray CT at the whole cell, bulk electrode structure and particle scales. The post-mortem battery architecture, bulk electrode, and particle degradation revealed how failure mechanisms propagated across multiple spatial resolutions[131].

2.7. Summary

When assessing battery safety it is important to understand the fundamentals of the technology as well as its application. The core theory of the LIB has not changed much over the years since its discovery; however, its materials, components and design have seen significant improvements to meet the growing demands on their performance and safety. While performance improvements was once the key driver of such technological advancements, the need for safe and failure proof operation has grown as an area of interest. The primary risk of LIB technology is thermal runaway and the associated generation of heat and gas. The reactions and conditions in which these phenomena may occur were reviewed and the fundamental thermodynamics and temperature ranges within which key features occur were outlined; from the mildly exothermic decomposition of the SEI layer starting at 60 °C up to the larger exothermic events such as the breakdown of cathode materials at > 200 °C. While a number of BMS and safety features are integrated into the design of the battery, there is still a lack of standardisation across multiple stakeholders (manufacturers, governing bodies to standards) regarding the processes by which safety is tested and defined.

Safety assessment in LIBs is commonly analysed by purposefully inducing failure via multiple methods; for example, using calorimetry to analyse the behaviour of a battery undergoing thermal failure, or using imaging techniques

such as X-ray radiography and tomography to capture dynamic battery degradation across multiple length and time scales. This literature review has revealed that there remains a lack of standardisation across current safety assessment techniques. This thesis advances the current understanding of battery failure and the methods by which it is analysed.

Chapter 3

3. Methodology

This thesis aims to provide a toolbox for battery safety assessment by combining existing characterisation techniques for the LIB and its materials before and after failure. The experimental sections of this thesis can therefore be split into three distinct categories: thermal, failure and image analysis. A coin-cell differential scanning calorimeter (DSC) is utilised to investigate the thermal behaviour of different LIB electrode materials (e.g. NCA, NMC) under normal and abnormal conditions, while an accelerating rate calorimeter (ARC) and nail penetration instrument are used to induce thermal and mechanical failures in commercial cells of different geometries. Commercial cells and lab-built single-layer pouch cells are used for the development of a multi-scale imaging analysis technique with a focus on characterising failure mechanisms. These are summarised in Figure 3.1.
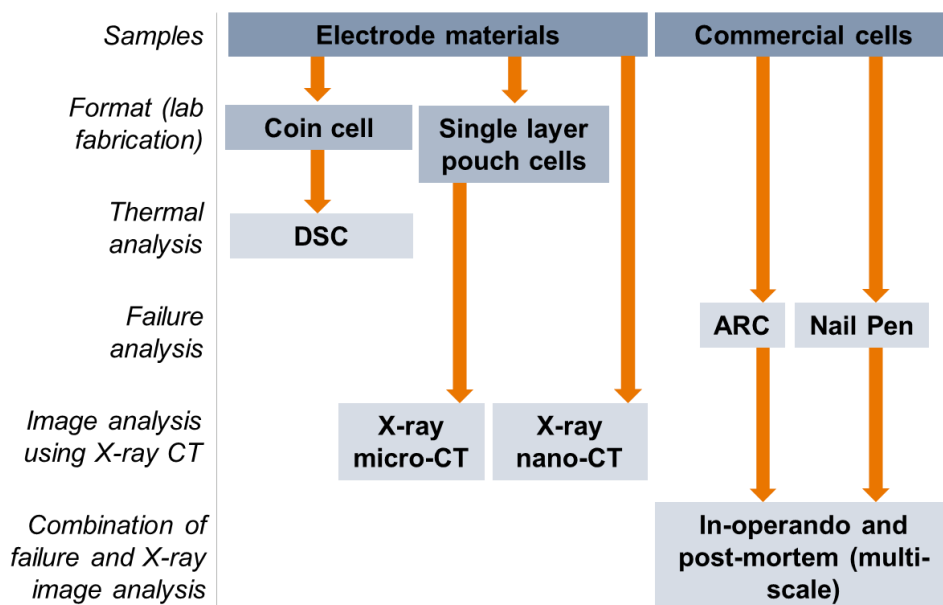
Figure 3.1 Summary and workflow of sample types and techniques used in this thesis.

3.1. Electrochemical Characterisation

3.1.1. Coin cell assembly

The cathode material for all coin cells in this work is either NCA or NMC of differing compositions. While this section describes the coin cell fabrication process, the specific chemistry of the cathode material is made clear in the relevant results sections. All electrode discs were dried for 12 h under vacuum at 120 °C in a glass drying oven (B-585, BUCHI Ltd.) before being assembled into coin cells (CR2032, Hohsen Corp.). For full cells, the cathode was arranged as the working electrode and the anode as the counter electrode. For half cells, lithium foil with an 18 mm diameter was used for the counter electrode. A tri-layer polyolefin membrane was used as a separator (Celgard 2325, Celgard, LLC.) and the electrolyte used was 1.0 M lithium hexafluorophosphate in ethylene carbonate and diethyl carbonate (1.0 M $LiPF_6$ in EC: DEC (1:1 v/v), Soulbrain MI). All cells were assembled in a glove box with an argon atmosphere (O_2 and H_2O < 0.5 ppm, MBraun, Germany). The overall coin cell configuration is illustrated in Figure 3.4.

3.1.2. Pouch cell assembly

Lithium nickel manganese cobalt oxide (NMC111, NMC622, and NMC8111, NEI Corporation) and Graphite (NEI Corporation) were used as respective positive and negative electrode materials for single-layer pouch cell fabrication in this work. (found in the appendices) lists the materials, electrodes and cell design parameters. Single-sided electrode sheets were punched into electrodes with tabs. The negative electrode overhung the edges of the positive electrode by 0.5 mm on all sides to accommodate electrode alignment imperfections and prevent lithium plating[194]. Active material was carefully removed from each tab using N-Methyl-2-Pyrrolidone, NMP (anhydrous, Sigma Aldrich) to expose the current collector for welding. The total active areas for the positive and negative electrodes were therefore 13.19 cm^2 and 14.71 cm^2, respectively. 1 M $LiPF_6$ in a 1:1:1 by wt EC:EMC:DMC and 1% vinylene carbonate (VC) electrolyte was used. The theoretical reversible capacity of the positive electrodes NMC111, NMC622, NMC811

were 2.01, 1.81, 1.86 mAh cm^{-2}, respectively, and 2.23 mAh cm^{-2} for the Graphite negative electrode. The reversible negative to positive capacity ratio (N: P ratio) was set at 1.11, 1.24, and 1.20 for a C/10 rate for the operating cell voltage window of 3.0 – 4.2 V.

Cells were assembled in a dry room at the Johnson Matthey Labs (Oxford) and formed at the Electrochemical Innovation Lab (EIL) at UCL (London) before image analysis. The average dimensions of the cells measured on the outside of the aluminium case (excluding the tabs) were 10 cm x 5.5 cm as shown in Figure 3.2 (c).
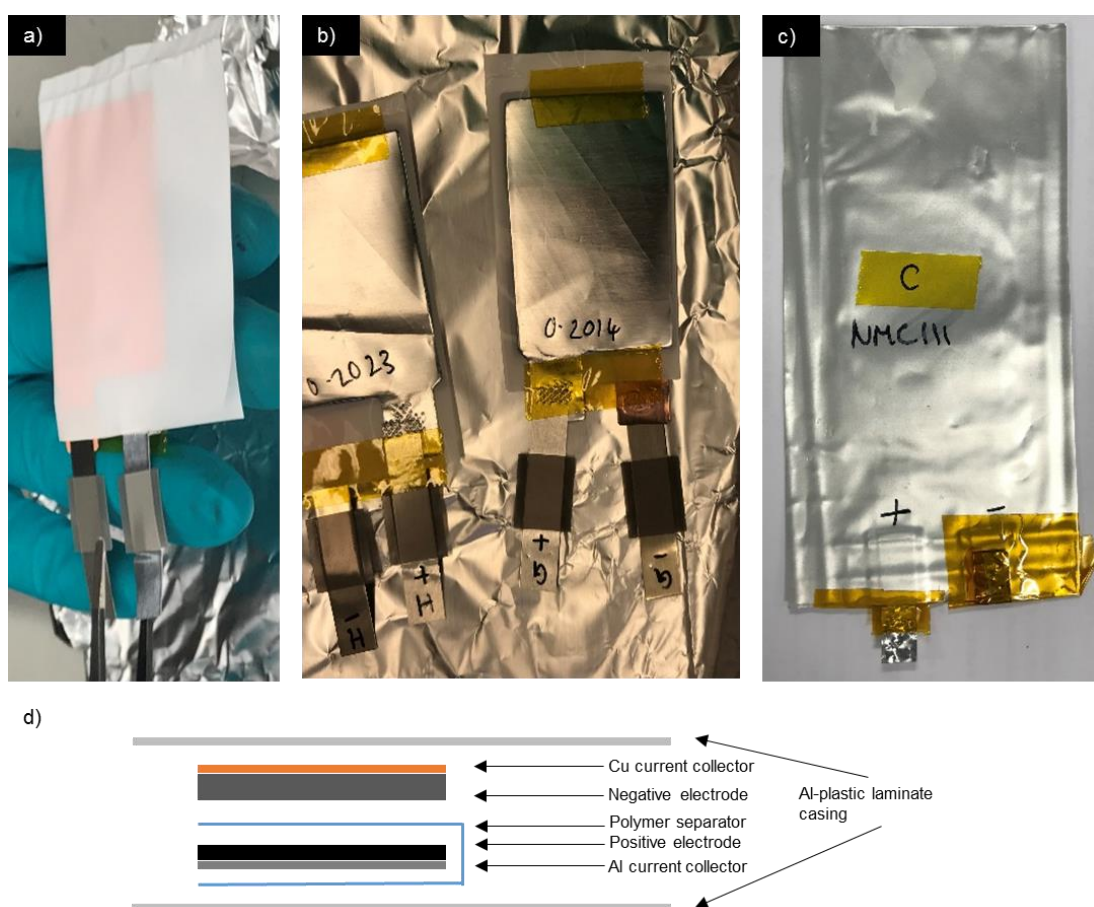
Figure 3.2 Photographs of pouch cell fabrication where (a) shows the negative electrode assembled inside a separator envelope, (b) shows the positive electrode secured onto the separator envelope with polyamide tape and (c) shows the final pouch cell assembly sealed using a vacuum heated seal inside an argon-filled glovebox.

3.1.3. Cycling protocols

The battery cycling in this thesis was performed on three types of multi-channel battery cyclers: 1. Novonix: a high-precision coulomb instrument (model UHPC-10A, NOVONIX, Canada, measurement current accuracy up to 0.005 % FSR, and source current and voltage range between 100 µA – 10 A and 0 – 5 V, respectively), 2. Biologic: ultra-precision with EIS (model BCS-805, BioLogic, France, measurement current accuracy up to 0.015 % FSR with a source current and voltage range between 10 µA – 150 mA and 0 – 10 V, respectively), and 3. Maccor: high-precision test system (model 4300 Desktop Automated System, MACCOR, USA, measurement current accuracy up to 0.02 % FSR, with a source current and voltage range between 300 µA – 5 A and 0 – 5 V, respectively). The system used for each test varied depending on the current and voltage requirements for the cell that was being tested, for example, larger pouch cell cycling was conducted using the Novonix system owing to its greater current and voltage range maximum, whereas coin cell samples were cycled on systems with higher resolution and accuracy. The make of the battery cycler that was used for the tests in this thesis is highlighted in the relevant results chapters. Furthermore, a Gamry potentiostat (Interface 1000E, Gamry Instruments, USA, with a maximum current and voltage of 1 A and 12 V, respectively, and EIS frequency between 10 µHz – 10 kHz) was connected to a coin cell calorimeter (MMC 274 Nexus, Netzsch Geratebau GmbH, Germany) to electrochemically analyse cells alongside measurements of heat flux.

The theoretical capacities of coin cells were calculated based on their mass loadings, specific capacity, and electrode areas. The cells underwent two initial formation cycles using a constant-current-constant-voltage (CCCV) charge and constant-current (CC) discharge protocol. The current used during the constant current steps were equivalent to a C/20 rate with a cut-off condition of 4.2 V for charge and 3.0 V for discharge. For the constant-voltage charge step, the cells were held at 4.2 V until the current dropped to C/50.

Pouch cells underwent two initial formation cycles using a CCCV charge and CC discharge protocol. This was performed in a multi-channel

Novonix battery cycler (NOVONIX Limited, Belford, Canada). The current used during the constant current steps were equivalent to a C/20 rate with a cut-off condition of 4.2 V for charge and 3.0 V for discharge. For the constant-voltage charge step, the cells were held at 4.2 V until the current dropped to C/45.

3.1.4. Differential capacity analysis and phase transition

The intercalation mechanism exhibited by lithium-ion insertion into cathode material occurs by diffusion of the lithium-ion into a crystal with no significant changes occurring to the structure of the host material. However, the term 'intercalation system' refers to a system that intercalates over a range of compositions and temperatures. First-order phase transitions occur when host structures are energetically favoured at different lithium-ion concentrations. Intercalation materials depend on the voltage at different contents of the intercalating material, x, this is shown in dx/dV, where V in dx/dV is the cell voltage. The charge, Q is equal to the charge on the Li$^+$ ions that have been intercalated into the cathode material; hence, Q is directly proportional to x. Therefore, the differential capacity, dQ/dV can be measured experimentally by a standard electrochemical CCCV protocol. Characteristic feature changes in the differential capacity plots in this work are used to provide information regarding the underlying thermodynamics and kinetics of coin cells during heat flux measurements. The phase transitions, which are assessed by the changes to peak heights and positions across the voltage range, are corroborated with findings in the literature values of comparable materials undergoing similar protocols.

3.1.5. Electrochemical impedance spectroscopy (EIS)

EIS is a useful non-destructive technique that provides both in-situ and ex-situ measurements during battery cycling and at various states of charge and discharge. A small alternating current (AC) signal is applied to the battery over a wide frequency range and the response is measured, most commonly with a frequency response analyser (FRA). The make-up of the battery is complex and contains several impedance elements such as bulk layers and interfaces, to which EIS is suitably sensitive. Impedances can arise from several

mechanisms from loss of active material and/or deterioration of ion transport. Middlemiss et al. summarise some of how EIS can be used to characterise degradation mechanisms in LIBs using EIS[195].

In this work, EIS was used to correlate thermal analysis investigations of various coin cells and conditions (e.g. high temperature) in Chapter 4. Coin cells were placed inside a novel heat-flux type DSC coin cell calorimeter and correlative EIS was performed on the coin cells using the AC-impedance measurement function of a Gamry potentiostat (Interface 1000E, Gamry Instruments, USA) which was connected using four wires; two for cell potential and two for current. EIS was used in a potentiostatic (constant voltage) mode where a voltage was chosen and applied at each frequency and the resulting current was measured. Specific currents and frequency details can be found in relevant sections throughout this thesis.

3.1.5.1.   Analysis of EIS data

EIS utilises the AC analogue of Ohm's Law, where the impedance dependence on frequency is accounted for according to Equation 3.1, where $Z\,(\omega)$ is the frequency dependent impedance measured in Ohms, and $V\,(t)$ and $I\,(t)$ are voltage and current, respectively.

$$Z\,(\omega) = \frac{V\,(t)}{I\,(t)}$$

Equation 3.1

The generated impedance spectra consist of a combination of electronic and ionic resistances. The impedance can be separated into real (Z_{real}) and imaginary (Z_{imag}) components which can be represented by three plots: the Bode phase, a Bode magnitude and a Nyquist plot. The latter Nyquist plot is characterised by its arc-shaped curves where resistance is along the x-axis (Z_{real}) and capacitance is displayed on the y-axis (Z_{imag}). The multiple components and processes present within the LIB are separated and assigned to models in the form of equivalent electrical circuits. These circuits are comprised of resistors, capacitors and constant phase elements (CPE).

Four common features relating to the LIB can be distinguished in the Nyquist plot of a typical metal-ion battery EIS measurement as shown in Figure

3.3. The first element, R_1, is a non-zero Ohmic resistance where the curve intersects with the x-axis at high frequency. It is represented in the equivalent circuit by a resistor. The second and third features are each represented by a resistor and capacitor in parallel. These represent characteristic arc-shaped curves, which are usually different in size. Oftentimes these curves are distorted or non-ideal semi-circles; therefore, a CPE is added in parallel with the resistor and capacitor to account for this. The impedance of the CPE depends on the angular frequency (ω) given by $\omega = 2\pi f$. The fourth feature, at a low frequency, is a tail, which can be a non-ideal capacitor (represented as a CPE) or a Warburg element if the tail is at approximately 45 ° to the real Z_{real} axis. The Warburg element represents a diffusion-controlled process adding additional impedance to the overall battery response. Not shown in Figure 3.3 is a tail that may occur below the Z_{real} axis at high frequencies. It often represents the inductive effects of the battery or experimental set-up.
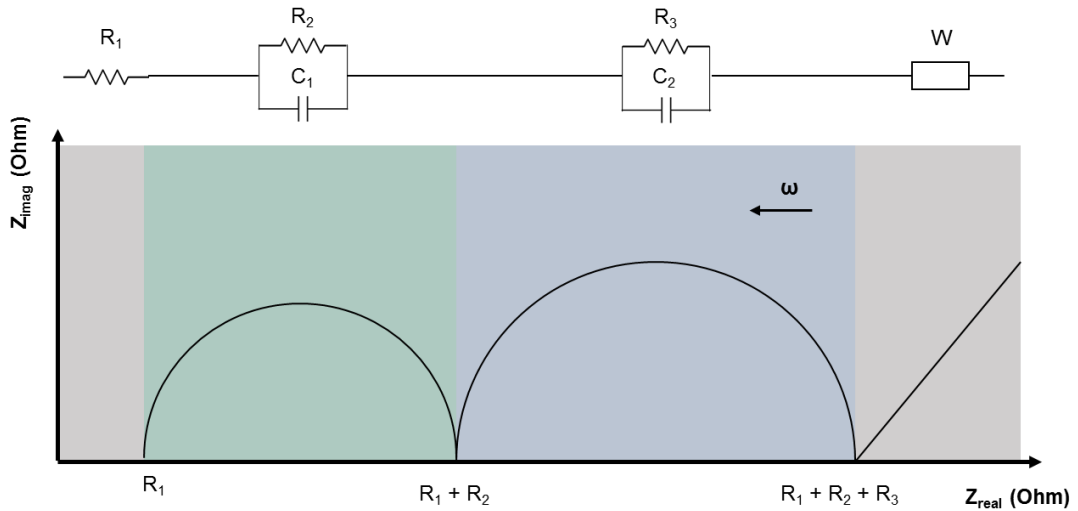
Figure 3.3 Schematic of the equivalent circuit elements for various components in a typical metal-ion battery and the related characteristic Nyquist curve showing four distinct features comprised of resistors and capacitors.

3.2. Thermal Analysis using DSC

Heat generation in a battery can be directly measured by obtaining kinetic and thermodynamic data of the various materials and complex reaction processes that make up a single cell. In this work, calorimetry is used to measure the thermal properties of various LIBs. In this technique, the enthalpy

associated with specific material reactions is directly determined by connecting temperature and the specific physical property of a substance. Further details regarding the energy balance for the LIB and the overall contributions of reversible and irreversible heat can be found in Chapter 4.

3.2.1. Coin cell differential scanning calorimetry (DSC)

Differential scanning calorimetry (DSC) is amongst the various thermal analysis apparatus that is routinely used in battery materials research. It determines the heat flow associated with exothermic and endothermic transitions as a function of temperature or time. The heat quantity released and absorbed by a material is measured by calculating the difference between the sample material and a reference. DSC can be categorised into two types: heat-flux and power-compensated. In a heat-flux DSC, the sample material is enclosed in a vessel and an empty reference vessel is placed on a thermoelectric disk surrounded by a furnace. Heat is transferred to the vessels from the furnace through the thermoelectric disk. Due to the heat capacity of the sample, the resulting temperature difference between the vessels, ΔT (measured by thermocouples) can be used to determine the heat flow, q via Ohm's law, where R is the resistance of the thermoelectric disk.

$$q = \frac{\Delta T}{R}$$

Equation 3.2

In a power-compensated DSC, the sample and reference are placed in separate furnaces which are heated by a heater and the difference in the power required to maintain the samples at the same temperature is determined as a function of time or temperature. As a result, the structural-phase transitions, melting, crystallisation, and thermal stability of electrode materials and electrolytes separately in LIB materials can be characterised.
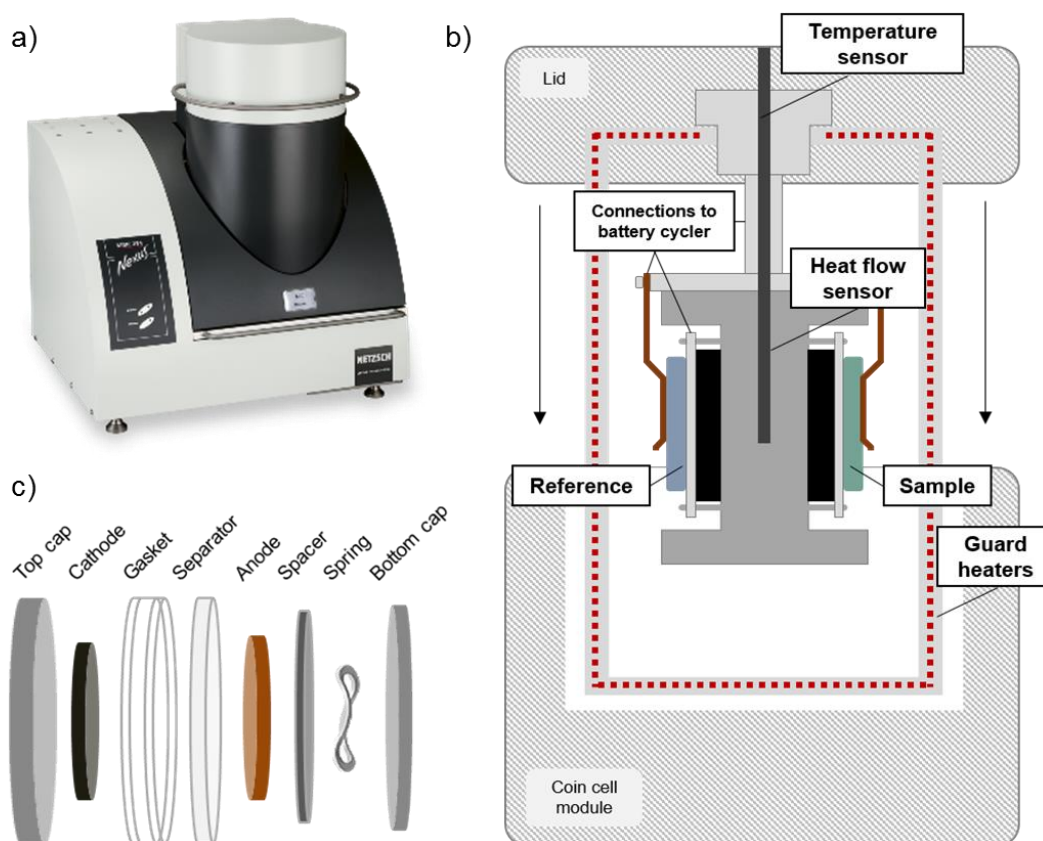
Figure 3.4 Photograph of (a) heat-flux type DSC coin cell calorimeter (MMC 274 Nexus, Netzsch Geratebau GmbH, Germany), and illustrations of (b) the module showing the reference and sample sides, connections to the battery cycler, guard heaters, heat flow and temperature sensors, and (c) the coin cell assembly protocol: top cap, cathode, gasket, separator, anode, spacer (0.5 – 1 mm), spring and bottom cap (with the electrolyte not shown).

In this work, a novel heat-flux type DSC coin cell calorimeter (MMC 274 Nexus, Netzsch Geratebau GmbH, Germany) is used in combination with a potentiostat (Interface 1000E, Gamry Instruments, USA). It allows for reversible and irreversible heat generation during cycling, and the formation and decomposition of heat from high-temperature failures to be determined in a working cell. Two coin cells are placed on either side of a carrier (see Figure 3.4) the sample cell and a reference. The heat flow between the coin cell of interest and a reference is measured by a resistance temperature device (RTD) sensor placed inside the carrier and in close proximity to the two cells. The whole carrier is enclosed in a thermally isolated chamber fitted with heating elements and the instrument can be operated from room temperature up to 250 °C. For all tests, an empty CR2032 cell sealed with a polypropylene

gasket inside an argon-filled glovebox (O_2 and H_2O < 0.5 ppm, MBraun, Germany) was used as a reference. Thermal measurements taken during charge/discharge were carried out in the isothermal mode where the internal heaters adjust their temperature to keep a constant temperature. For tests at different temperatures, time was given to the cell to reach thermal and chemical equilibrium before the cycling protocol started. The cells were also held at an open-circuit voltage (OCV) for 1 h before heat flux signals were measured. The cells followed a CCCV charge and CC discharge protocol. The cells underwent a chosen number of cycles while their heat flux signals were recorded by the calorimeter software.

Calibration of the DSC sensitivity and temperature was a regular procedure carried out throughout the timescale of the experiments conducted in this thesis. The Netzsch Geraetebau GmbH DSC was calibrated with four different standards: Gallium, Indium, Tin and Bismuth. The melting behaviours of the reference materials were assessed and their calibration polynomials for temperature and sensitivity were calculated and the validity of the calibration was confirmed by comparing the same curves for naphthalene ($C_{10}H_8$).

3.3. Failure Analysis

3.3.1. Accelerating rate calorimetry (ARC)

Thermal abuse tests in this work were performed using ARC inside a calorimeter (Phitec Battery Test Calorimeter, HEL Group, Herts., UK), shown in Figure 3.5, using the heat-wait-search method. Once an initial control temperature is reached for the sample being tested, the following procedure is initiated: the calorimeter increases the temperature in discrete steps (e.g. 5 °C), waits for any thermal transients to decay and monitors the sample temperature. If within this time (e.g. 5 min) the temperature remains unchanged, up to a threshold value (e.g. 0.02 °C min^{-1}), the calorimeter continues to increase the temperature by 5 °C until self-heating is detected. Temperature rate profiles are extracted from the built-in programme where temperature recordings from thermocouples placed on various areas of the sample and calorimeter are provided.
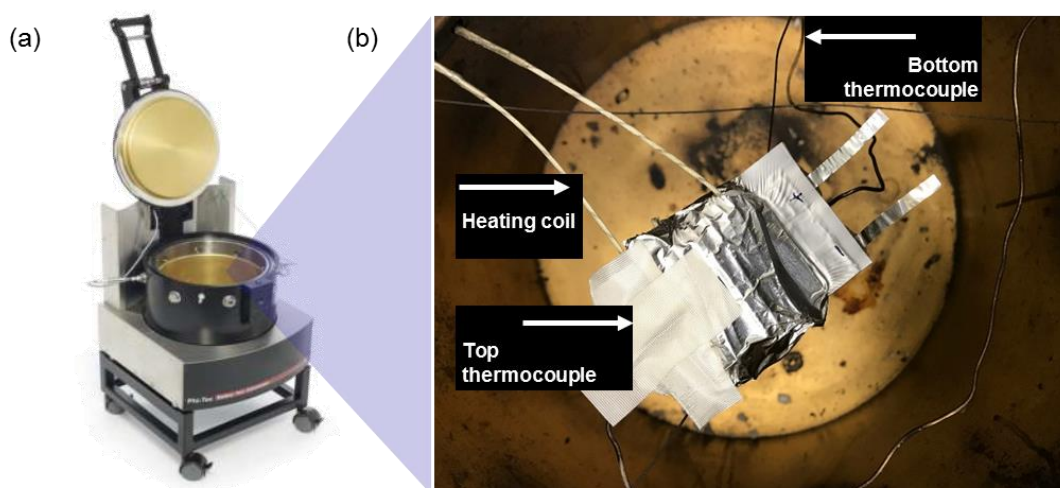
Figure 3.5 Photographs of (a) accelerating rate calorimeter (Phitec Battery Test Calorimeter, HEL Group, Herts., UK) and (b) set up of a pouch cell inside the calorimeter showing the heating coil and thermocouple positions. The cell is secured with glass fibre and aluminium tape.

3.3.2. Nail penetration

Nail penetration tests were conducted using a battery penetration instrument (Pneumatic Nail Penetration Tester, MSK-800-TE9002, MTI Corp. CA, USA) shown in Figure 3.6. The instrument is a large fire-proof chamber fitted with an air vent, clamps to hold the sample in place and a stainless steel nail with a 4 mm diameter. Cells were fully charged to the maximum rated voltage, (e.g. 4.2 V) and were mounted horizontally. The nail was positioned so it would penetrate the centre of the cell and the penetration depth was chosen to fully pierce through all the layers at a speed of 30 mm s^{-1}. After penetration, the nail is slowly reversed out of the cell. Heat and voltage measurements were not recorded for cells during failure. The nail-penetrated battery and unit are left to rest for 24 hours to allow for any electrolyte to evaporate.
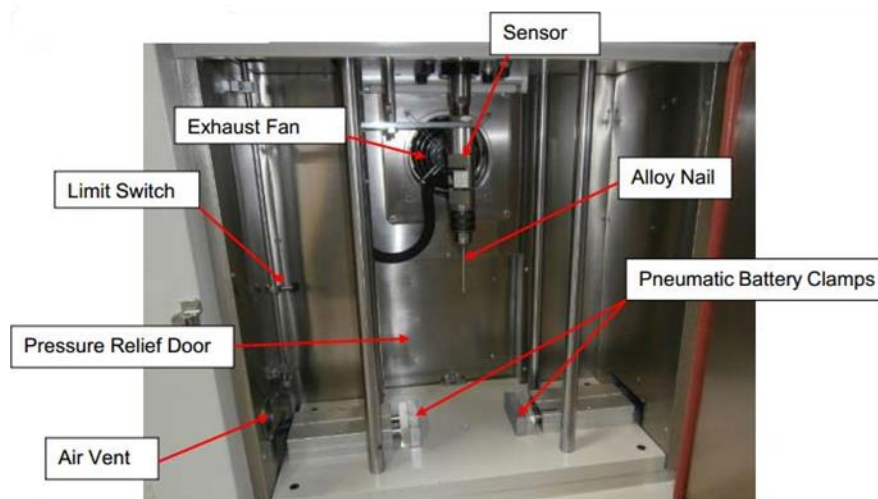
Figure 3.6 Photograph showing the inside of the battery nail penetration instrument by Pneumatic Nail Penetration Tester, MSK-800-TE9002, MTI Corp. CA, USA.

3.3.3. Cell disassembly

The procedure for cell disassembly varies depending on the cell type (e.g. cylindrical or pouch cell). The tools used for the cells in this work were a pair of ceramic scissors (to avoid short circuits), pliers, pipe cutters and various equipment for safely separating and storing disassembled components, such as ceramic tweezers, dishes and glass beakers.

First, the cells for disassembly are discharged to the manufacturer's safe voltage limit (2.5 V or 2.7 V) at a specified discharge rate (typically C/2 or C/5) and rest for several hours (at least 4 hours). For any cylindrical cell, upon opening, the cell voltage was checked to ensure it had been discharged to the manufacturer's safe voltage limit. The cells in this work were dismantled inside an argon-filled glovebox (where sometimes, the circulation was turned off). Using a pipe cutter, a cut was made around the rill of the cell top. The cell top was then lifted off to reveal the top of the positive current collecting tab (which travels down into the spiral wound layers). Kapton tape was applied around this tab to mitigate the chances of a short circuit. Using the pipe cutters, the outer casing was removed by an 'orange peel' method without damaging the inner spiral wound layers. In some cases, sparking occurred; this is due to some electrolyte not having fully evaporated from deep inside the wound layers. The removal of the outer case reveals the spiral wound layers

consisting of the positive current collecting tab (Al), separator, negative current collecting tab (Cu) and a steel cylindrical tube, which were slowly unravelled. The components were separated and placed on dishes for 24 hours for any remaining electrolyte to evaporate. Sample sections from the positive and negative electrodes were cut and washed using DMC in a beaker. These were left to dry for another 24 hours before being removed from the glovebox for further preparation (e.g. for SEM or X-ray CT).

For pouch cells, a similar procedure to the cylindrical cells was followed, whereby the cells were discharged to the manufacturer's safe voltage limit (if provided, otherwise ~ 2.7 V). The pouch cells were cut open from the most convenient point (often the seal edge) and left to dry for 24 hours for electrolyte evaporation. The tabs were cut through using ceramic scissors before the stack consisting of the positive current collector (Al), separator, and negative current collector (Cu) was removed. Sample sections from the positive and negative electrodes were cut and washed using DMC in a beaker. These were left to dry for another 24 hours before being removed from the glovebox for further preparation (e.g. for SEM or X-ray CT).

3.4. Scanning Electron Microscopy & Energy Dispersive X-ray Spectroscopy

SEM is a useful imaging technique for investigating material surfaces. An electron beam is rastered across the surface of a sample under vacuum conditions. As a result, electrons emitted from the sample, which are subsequently collected by a detector that generates an image. The sample can release three types of electron emission during the acquisition by SEM; secondary, backscattered and X-ray. Secondary electrons are released directly from atoms in the sample, whereas backscattered are incident electrons that have been deflected back from the sample. The electron beam voltage can therefore be tuned to optimise the number of electrons released by each method to ensure sharp and focused images. Furthermore, a variable called the working distance, which is the distance between the top of the sample surface and the electron filament, can be adjusted to further improve

image acquisition and/or quality. A focused ion beam (FIB) can be used to prepare a cross-section of the sample and together with SEM; an additional z-axis image can be created. FIB-SEM is a technique used widely in battery materials research to gain a 3D understanding of samples[196]. The widespread use of the technique however is limited by its slow imaging speeds and lack of system stability[197].

The third type of emission, X-rays, emits when higher energy electrons interact with the sample. These electrons cause higher energy states in the material. When the atoms relax to lower states, the excess energy from this process dissipates as X-rays. Since each element in the material has a unique set of energy levels, the emitted X-rays are characteristic and can be used to determine the elements that are present in the form of an elemental map across a chosen field of view. This technique is referred to as energy dispersive X-ray spectroscopy (EDX or EDS) and has been used particularly for understanding thermal runaway mechanisms in LIBs in the form of determining the distribution of elements such as cobalt in post-mortem cell failure analysis[131].

While SEM provides a good understanding of surface morphologies, and further when combined with EDX, the distribution of elements, the technique is limited to the 2D surface of the material. Additionally, it is destructive to the sample in two ways; firstly, sample preparation, especially when investigating battery materials in working cells, requires cell disassembly and can only offer ex-situ investigations. Secondly, for EDX analysis, higher energy beam voltages can damage sample surfaces. X-ray CT is a technique that allows for 3D understanding of materials and in-situ investigations that can be acquired without destroying the sample. The details of this technique are discussed in the following section.

3.5. Image analysis using X-ray characterisation

Imaging battery materials via advanced tomography require well-defined beams of radiation i.e. electrons, neutrons or X-rays. Each radiation source has varying characteristics, from the way it is produced to the way it interacts

with matter. This ultimately determines its field of view for imaging. Electrons are most suited to small samples with high resolutions and neutrons are for imaging thick samples at low resolution; X-rays take an intermediate position. In this thesis, computed tomography using X-rays provides a multi-length scale and non-destructive imaging technique that relies on the interaction of X-rays with various battery materials. The fundamentals of X-ray characterisation are discussed in detail in this section from X-ray interaction with materials to 3D imaging via X-ray CT. Furthermore, X-ray sources are discussed from lab-based to synchrotron facilities as well as their benefits and limitations with a particular focus on the instruments, uses and parameters relevant to the work in this thesis. Sample preparation methods used for X-ray characterisation in this thesis are detailed, and finally, the image processing approaches and methods are outlined.

3.5.1. Fundamentals of X-ray characterisation

3.5.1.1. X-ray interaction with materials

In X-ray radiography, 2D image projections are generated by measuring the intensity of X-rays that are transmitted through a sample. As the X-ray beam penetrates the sample, it is attenuated due to its interaction with the electrons of the material. X-rays pass through the sample and are absorbed according to the composition and density of the material they encounter. The intensity, i.e. the number of photons per second is reduced for a linear attenuation coefficient, μ. The linear coefficient is not uniform but has some spatial variation that can be expressed as μ (x,y,z) for a 3D structure. The attenuation coefficient equation is expressed in Beer-Lambert's law as follows.

$$I_d(x, y) = I_0 e^{-\mu x}$$

Equation 3.3

For a monochromatic X-ray beam, I_d is the detected intensity, I_0 is the incident intensity that is known and generally held constant, and μ (cm^{-1}) is a property of the beam energy and material density. As a result, the suitability of the system to image a particular material will depend on its' emission spectrum as shown in Figure 3.7.
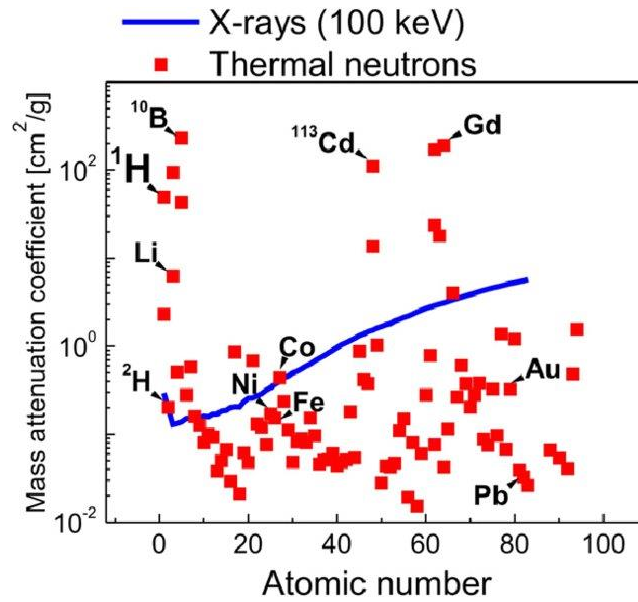
Figure 3.7 Comparison of absorption coefficients of various elements for 100 kV X-ray radiation and thermal neutrons reproduced from Strobl et al[132].

A database of attenuation coefficients for materials across a range of wavelengths is documented by the National Institute of Standards and Technology (NIST)[198][199]. The difference between the attenuation coefficients of various materials in one sample can be considered as the contrast. Image contrast is improved when the difference between material attenuation coefficients is greater.

3.5.1.2. Computed Tomography

Absorption X-ray tomography is a widely used method which is based on a physical process that reduces intensity as radiation or particles pass through a sample. It uses digital geometry processing to reconstruct a 3D image of a sample via a series of radiographs. Traditionally, the sample is rotated around an axis through 180° perpendicular to the X-ray beam. The X-rays are either adsorbed, transmitted or scattered when incident upon the sample. To obtain 3D data, several radiographs (usually several hundred) are recorded as the sample is rotated. Transmitted X-rays are recorded by a detector and/or converted to visible light by a scintillator creating a visible image that can be digitised for further processing. Data is combined using reconstruction algorithms to spatially resolve information obtained from the instrument. A common algorithm is the filtered back projection (FBP) procedure[200].

3.5.2. Lab-based X-ray computed tomography

3.5.2.1. X-ray sources

X-rays are waves that lay within the 0.005 – 10 nm range on the electromagnetic wavelength scale. They can be created either by replacing core electrons from atoms with higher energy electrons to emit X-ray photons or by accelerating or decelerating free-charged particles. Lab-based X-ray tomography equipment utilises an X-ray tube within which electrons are accelerated and released from a cathode by thermionic emission (i.e. from a hot filament). The electrons are directed onto a metal target (anode) that can result in two types of emissions. The first is Bremsstrahlung which occurs when electrons are decelerated within the magnetic field, and the second, is the characteristic fluorescence radiation. The accelerating voltage of the cathode tube affects the energy interval of the Bremsstrahlung spectrum. The greater the voltage, the more kinetic energy is transformed into radiation. The anode material is chosen based on its specific characteristic X-ray emission spectrum which contains peaks overlaid on the Bremsstrahlung. Common anode materials include Copper, Chromium, Tungsten, Molybdenum and Silver. Some lab-based systems will make use of these distinctive peaks such as the Zeiss Xradia Ultra 810 (Carl Zeiss XRM, Pleasanton, CA, USA) which uses a quasi-monochromatic beam of around 5.4 KeV (a characteristic emission from its Chromium target).

Once generated, the X-rays are refined into beams that have controlled temporal and spatial coherence, typically determined by their degree of monochromaticity and collimation. Lab-based X-ray beams can be categorised into two geometries: cone or parallel. Cone beams require less refinement since beams are naturally divergent, however generation of a parallel beam involves the use of condensers or other collimation instruments such as zone plates or lenses.
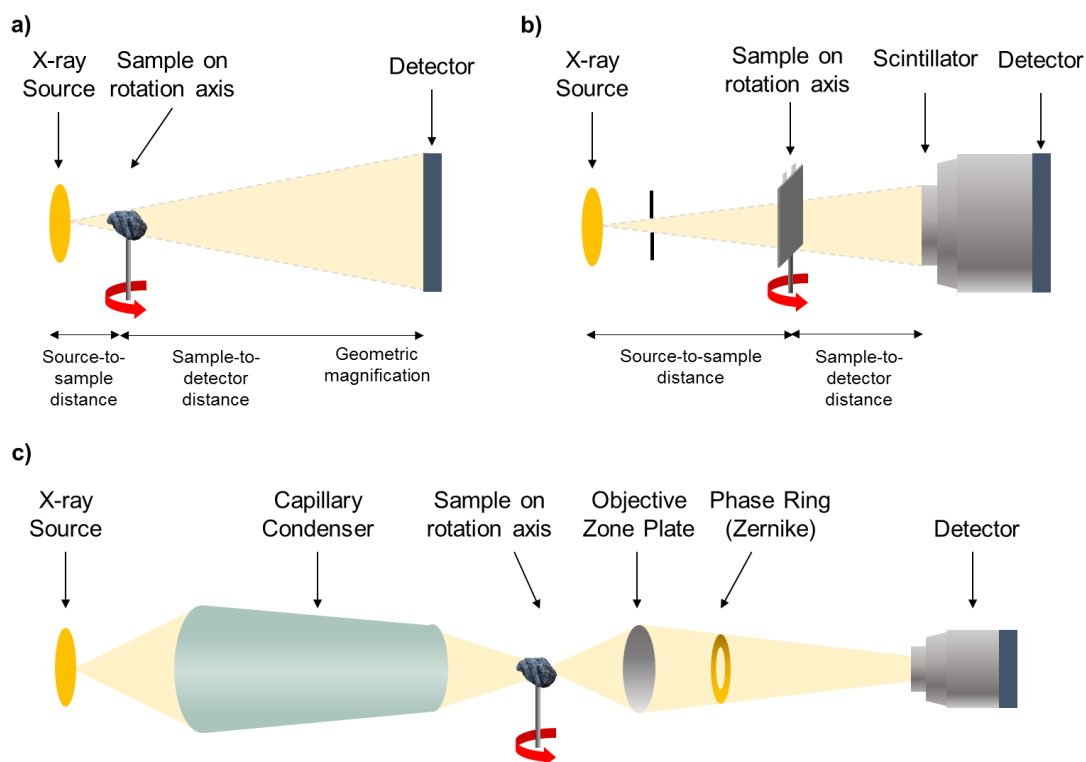
Figure 3.8 Set-up for X-ray production and refinement within the lab-based X-ray CT systems used in this work. (a) Nikon XT H225 (b) Zeiss Xradia 520 Versa, and (c) Zeiss Xradia 810 Ultra.

3.5.2.2.   X-ray instruments

Macro-scale imaging can be achieved using the Nikon XT 225. This equipment can be operated with a transmission target which utilises a beam energy of up to 180 kV, achieving a minimum pixel size of 1 µm, or with a reflection target with a beam energy of up to 225 kV, attaining a pixel size of 3 µm. For certain samples, i.e. those with sizes greater than 1 mm, using a lower energy X-ray emission is beneficial. These can be achieved using the multi-metal targets provided: Tungsten, Silver, Molybdenum, and Copper. Copper filters of varying thickness can be placed between the source and sample to filter out low-energy photons and reduce beam hardening artefacts. The system operates with a cone beam geometric magnification and a 16-bit flat panel detector (PerkinElmer 1620) with 2000 x 2000 pixels and 200 µm pixel size, offering a frame rate of up to 3.75 fps at 1 x 1 binning.

Micro-scale imaging, decreasing in the length scale of the feature of interest can be achieved using the Zeiss Xradia Versa 520 which uses a

tungsten target with a tube voltage ranging between 30 – 120 kV. It has three objective lenses for optical magnifications; 4x, 20x and 40x, which can provide pixel resolutions down to < 0.2 µm. Different magnifications have different fields of view (FOVs) as shown in Table 3.1. To optimise the resolution of the image, it is important to match the sample size to that of the FOV (i.e. keep the sample within the beam path). The cone beam enables the geometric magnification to be adjusted by changing the source-to-sample and sample-to-detector distances. The system operates with a two-stage magnification in which the sample is first exposed to the X-rays and subsequently projected onto a scintillator. The X-rays are then converted into visible light and exposed onto a 2048 x 2048 charged-couple device (CCD) detector. A spatial resolution down to 0.7 µm can be achieved. The rotation angles for this set-up range between - 180° and + 180°. Various filter materials can be placed between the source and sample to filter out low-energy photons in the case of highly attenuating samples. Filters can also aid in the reduction of artefacts caused by beam hardening. 3D reconstructions of data are carried out using the Zeiss XMReconstructor software (which utilises a FBP algorithm). The centre shift and beam hardening corrections are defined and applied in this process depending on the geometry of the sample and chosen imaging parameters.

Table 3.1 The field of views for a chosen magnification/objective lens of the Zeiss Xradia 520 Versa X-ray imaging instrument.

Magnification / objective lens	Field of View (FOV)
0.4X	40 mm
4X	3 – 4 mm
20X	800 µm
40X	400 µm

High-Aspect Ratio Tomography (HART) is a feature of the Zeiss Xradia Versa 520 instrument. It is a modification that allows samples that are thin and wide, (such as single-layer pouch cells), to be imaged with significantly minimised beam hardening effects. HART acquires projections at a higher angular density for the 'long' view (along the width of the sample/ or the longer 'beam path' through the sample), but keeps the total number of projections the

same. Overall, the effects are an improved image quality (less noise and beam hardening) and/or a reduced scan time (due to the variable exposure capability). Each projection of the tomography can have a unique angular span. The strength of the angular density increases at the centre of the HART region, i.e. the long view (as shown in Figure 3.9).
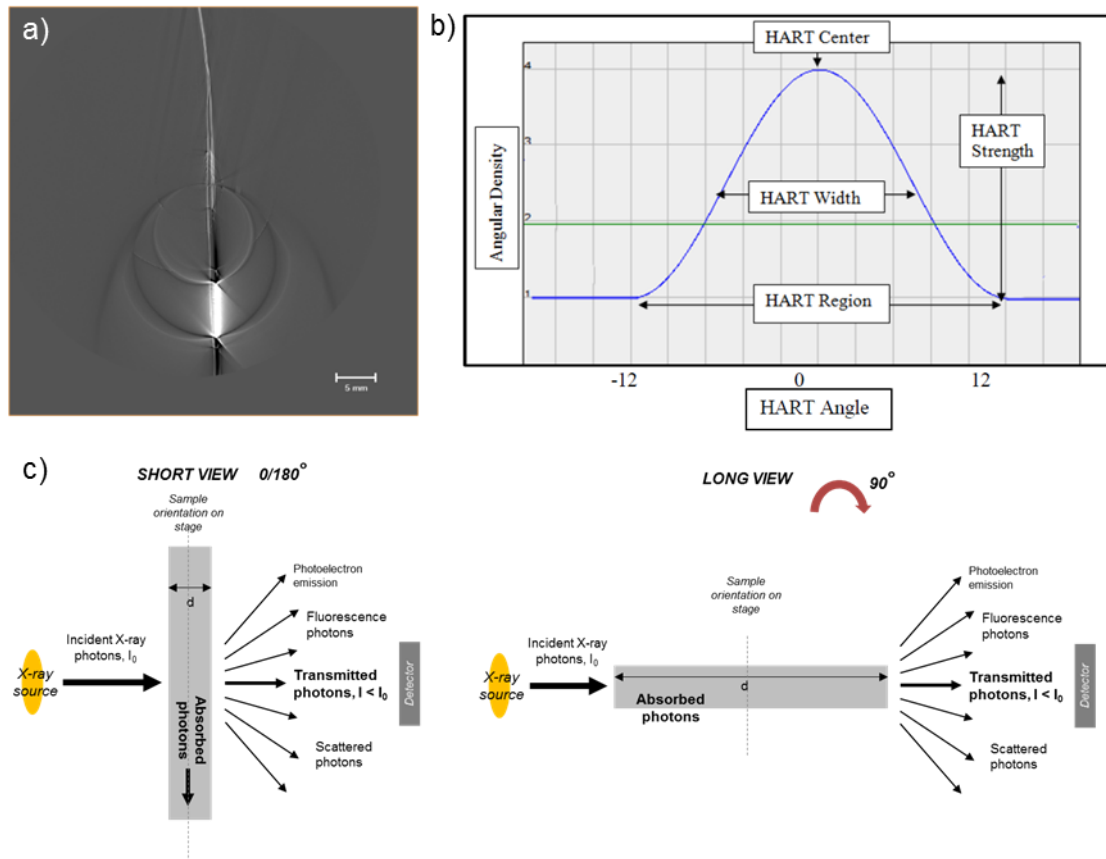
Figure 3.9 (a) 2D orthoslice of a tomogram of a single layer pouch cell showing the beam hardening artefacts caused due to the high aspect ratio of the sample. A (b) graph, and (c) illustration depicting how the HART angular speed of the theta stage can be adjusted to achieve variable angle scans. The theta stage slows down in the HART region and reaches a minimum.

Imaging features in the nanoscale can be carried out using the Zeiss Xradia Ultra 810 which utilises a quasi-monochromatic beam around the K-edge of its chromium target, 5.4 keV. It offers a tube voltage and current of 35 kV and 25 mA, respectively. Two energy-selective optics are used to achieve the quasi-monochromatic beam. Firstly, a capillary condenser placed between the X-ray source and the sample focuses as much light as possible on the sample. Secondly, a Fresnel zone plate, placed between the sample and

scintillated CCD detector focuses a single photon energy (5.4 keV) to a point. The sample stage rotation is 180° and the detector is 1024 x 1024 pixels. This lab-based X-ray nano-CT instrument can be operated in two imaging modes: Large Field of View (LFOV) which achieves a pixel size of 64 nm and High Resolution (HRes) which achieves a pixel size of 16 nm. 3D reconstructions are carried out using the Zeiss XMReconstructor software package which utilises the FBP algorithm. The centre shift and beam hardening corrections are defined and applied to this process depending on the sample geometry and imaging parameters specific to the sample.

3.5.2.3.   *Imaging Parameters*

The reconstructed 3D dataset obtained from X-ray CT is composed of voxels each with an assigned number correlating to its X-ray attenuation at that particular location. Lab-based systems differ according to their imaging capabilities such as length scale, spatial resolution and methods. The suitability of an X-ray CT instrument for material characterisation is often determined by the energy and brilliance of the X-ray beam. For example, a low brilliance beam requires both a higher exposure time and an increased number of projection angles to achieve a sufficient signal-to-noise ratio, increasing the overall scan time. Image quality can be improved further by various sample preparation techniques[166]. FIB milling has previously been used to prepare small samples[201], and recently micro-machining with lasers has shown considerable improvements in obtaining optimal sample geometries[202]. Thus, a trade-off between various imaging parameters such as exposure time, the number of projections and sample size exists for optimal X-ray imaging. Common imaging parameters used for lab-based X-ray CT systems are summarised in Table 3.2.

Table 3.2 Lab-based X-ray CT imaging parameters and their definitions.

Imagining Parameter	Definition
Tube Voltage (kV)	Sets electrode potential across X-ray tube source. Determines the acceleration of the electrons that bombard the sample. The intensity of the spectrum, as a result, determines the transmission through the sample. A lower voltage correlates to a greater number of X-rays being absorbed by the sample. At lower energies, the intensity spectrum shifts towards lower energy photons. Oftentimes, filters are used to reduce beam hardening artefacts caused by lower energy photons. A suitable voltage is chosen based on the sample material and desired image contrast.
Camera Binning	Represents the method by which the CCD groups its pixels. For example, in the 1 x 1 binning mode, each pixel on the CCD is defined as a single pixel and in the 2 x 2 binning mode, a 2 x 2 matrix is defined as a single pixel.
Exposure time	Defines how long the detector shutter remains open. A higher exposure time exposes the sample to the X-ray source for a longer time. This increases the number of counts and reduces the signal-to-noise ratio. However, the overall scan time and the risk of recording sample shifts are increased.
No. of Projections	Defines the number of radiographs recorded for every angular increment that the sample is rotated. A higher number of projections reduces the signal-to-noise ratio and improves image quality, but increases the scan time. Often the sample size exceeds the size of the detector; as a result, the minimum number of projections can be determined for an instrument based on its detector size. The number of pixels across the longest axis of a detector, for example, 2000 pixels would give the appropriate number of projections to be 3180 based on the approximation $2000\pi/2$[203].

3.5.3. Synchrotron imaging

In synchrotron facilities, high-energy electrons are accelerated close to the speed of light. They are then released into a primary storage ring where electrons are directed in a polygonal path by the use of magnets. The magnets are arranged in a closed space at angles to create the polygonal shape of the

storage ring. This accelerates the electrons while also changing their direction of travel. In this process, some kinetic energy is lost by the electrons as they are slowed down in the magnetic field in the form of high-intensity X-ray radiation (Bremsstrahlung). The energy of the electron travelling within the ring influences the emission spectrum while the current determines the X-ray flux. An advantage of working with high-brilliance beams is that they provide large distances between the source and the detector. These large distances are housed in areas known as the experimental hutch that are easily accessible and provide a large working area for experimental rig set-ups. The beam exiting the electron ring can be refined using filtering, focusing or monochromatising in the optics hutch, before it enters the experimental hutch. For example, a white beam consisting of the full spectrum of wavelengths can be utilised on its own or with a filter where low-energy photons are filtered out. Alternatively, a monochromatic beam may also be used to reduce the attenuation of lower-energy X-rays. The brilliance of beams from synchrotron radiation is about 10 orders of magnitude higher than those from rotating target systems such as those based in laboratories.

Synchrotron investigations in this thesis were performed at the ESRF in Grenoble, France using beamline ID19. This beamline offers high flux at high energies for high spatial and temporal imaging. Specific parameters such as beam energies and experimental set-ups are described in detail for relevant results sections. The experiments were all conducted with a scintillator and complementary metal-oxide-semiconductor (CMOS) detector. Reconstruction of 3D CT images was carried out with a standard FBP algorithm, beam hardening and centre shift corrections.

3.5.4. Radiography and high-speed imaging

Several X-ray systems exist, each differing in design, properties and system capabilities. For example, synchrotron radiation can provide a sufficiently high photon flux for high-resolution images over short periods. Laboratory sources on the other hand have a much lower flux and are slower in terms of time taken for tomogram acquisition; however, they can provide a comparably high spatial resolution as synchrotron facilities. Synchrotron

imaging is more expensive and can involve lengthy application processes or waiting times for short usage times. Whereas lab-based systems are more readily accessible and cost much less to operate. When considering battery failure (occurring within seconds), the ability to capture the evolution of the internal architecture over short periods requires a high temporal resolution. The European Synchrotron Facility (ESRF) can achieve real-time CT down to ~ 0.01 s per series of projections. However, especially for uses such as material imaging, where high temporal resolution is not required, then lab-based systems such as the Xradia Ultra become a competitive alternative offering comparably high spatial resolutions to synchrotrons.

In this thesis, two such methods are used for in-situ imaging of cell failure. The lab-based system, Nikon XT 225, discussed in earlier sections of this thesis offers a frame rate of up to 3.75 fps using its 2000 x 2000 pixels 16-bit flat panel detector (PerkinElmer 1620). The ID19 beamline at ESRF offers a frame rate of up to 20,000 fps using its 1024 x 1024 pixels CMOS model SA-Z detector (Photron, Japan). The ultra-high speed of the synchrotron detector is limited by the number of frames stored per recording of in-situ data storage chips that often limits the length of time over which images can be captured, however, both systems provide comparable spatial resolutions of ~ 20 µm. Hence, the suitability of the system depends more on its application and feature of interest.

3.5.5. Materials and preparation methods

In this work the whole battery and its electrodes, in the form of a current collector and active material, are investigated using multiscale X-ray CT. Whole battery scans, conducted using the Nikon XT 225 instrument require the least preparation in the sense that the whole battery without interference needs to be placed on the sample stage. What is important however is to ensure that the sample is clear of any obstructions such as wires as it rotates on the sample stage. Furthermore, in some cases where the sample is symmetrical, such as in a cylindrical cell format, it is important to ensure that the cell is aligned to the centre of rotation as this will influence the later reconstruction of the 3D image. For example, a whole cell that is placed slightly

off-centre will skew the reconstruction and introduce errors where centre shift and potential beam hardening corrections may not be sufficient.

Sample preparation for X-ray micro- and nano-CT is more complex depending on the feature of interest and is discussed considering sample treatment, size, preparation and mounting in the following sections. Some electrode materials were obtained after disassembling a whole battery as discussed in previous sections. For the X-ray instruments used in this thesis, the collected samples are secured to a chuck on a sample platform provided by Zeiss. The sample platform is placed on the rotation stage of the Versa 520 or Ultra 810 systems.

3.5.5.1. *Manual and laser preparation*

Battery electrode samples intended for X-ray micro-CT were prepared by cutting the material into sizes that would fit within the FOV of the chosen objective lens. For example, Figure 3.10 (a) shows a triangular shape (approximately ~ 3 mm in height and width) mounted onto a pin using a quick setting epoxy (5-minute epoxy, ITW Devcon, USA) with its tip facing up. The tip would fit the FOV for a 40 X objective lens (0.4 mm). Some samples were cut with greater precision using a Series/Compact Laser Micromachining System (Oxford Lasers, Oxford, UK) with an embedded Class 4, 532-nm-wavelength laser. Figure 3.10 (b) shows the laser cutting process whereby squares that are 0.8 by 0.8 mm are cut to fit the 20 X FOV (0.8 mm). Figure 3.10 (c – g) shows the sample preparation, mounting and scan set-up stages. The double-sided electrodes after being cut to the right size are mounted onto a 3D-printed stacker using Kapton tape. The stacker is then attached to the sample platform provided by Zeiss and placed inside the X-ray micro-CT instrument (Zeiss Xradia 520 Versa, Carl Zeiss XRM, Pleasanton, CA, USA). This procedure ensured that samples were held upright (as shown in Figure 3.10 (h)) throughout the scan to reduce the overall signal-to-noise ratio and scan time. This method produced 3D images with a 0.375 μm voxel size as shown in Figure 3.10 (i).
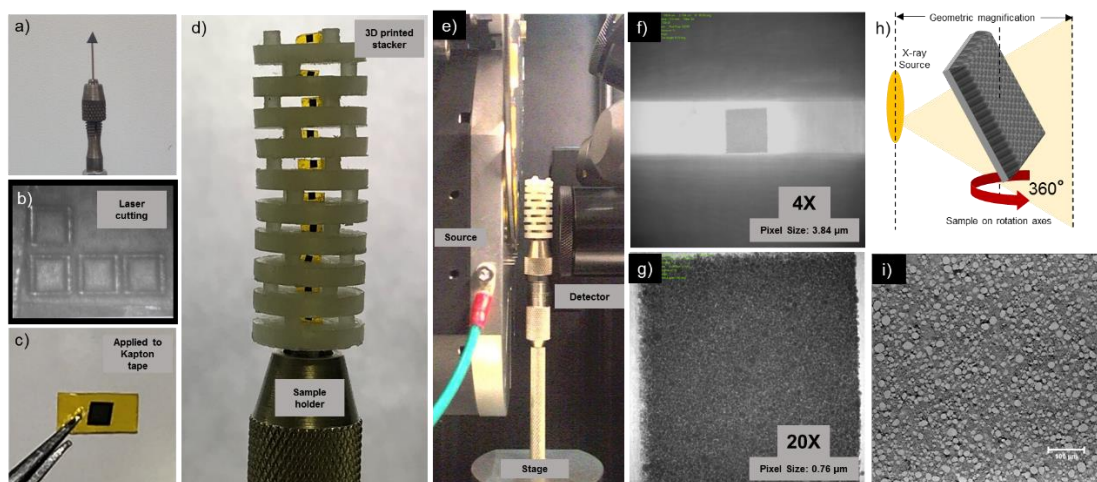
Figure 3.10 Sample preparation techniques for electrode samples for X-ray micro-CT where (a) shows a triangular cut-out, ~ 3 mm, mounted onto a pin with Epoxy, and (b) shows the precision by which a laser cuts electrode samples to sizes under 1 mm to fit the FOV of the desired magnification. Samples are mounted onto (c) Kapton tape which acts as an adhesive as well as strengthens the electrode to keep it upright during the scan duration and placed on a (d - e) 3D printed stacker. The radiograph view of the sample at two objective lenses is shown for comparison in (f) and (g). The theory by which signal-to-noise is reduced is illustrated in (h) and a final orthoslice view in the XY plane for an NMC cathode is shown in (i).

Recent developments in laser lathes have shown considerable improvements in achieving optimal sample geometries for lab-based nanoscale X-ray CT[202]. A cylinder with a diameter and height equal to the instrument FOV sufficiently minimises the volume of the sample external to the FOV which interferes with beam attenuation through the sample. All samples intended for nano-CT are prepared using a Series/Compact Laser Micromachining System (Oxford Lasers, Oxford, UK) with an embedded Class 4, 532-nm-wavelength laser. Laser preparation used a pulse energy of 1 mJ, a power of 2.4 W, and a 5000 Hz pulse frequency. Figure 3.11 (a) illustrates the laser preparation procedure in four stages. An initial sample with a 1 mm diameter is cut from the sample material using a doctor blade and secured onto a dowel using epoxy (5-minute epoxy, ITW Devcon, USA). The dowel is then attached to a rotary chuck that moves under a fixed laser beam. The edges of the sample are machined to reduce the sample size to a suitable fine pillar diameter for micro- or nano-CT FOV as described by Bailey et al.[202] and shown in Figure 3.11 (b – e).
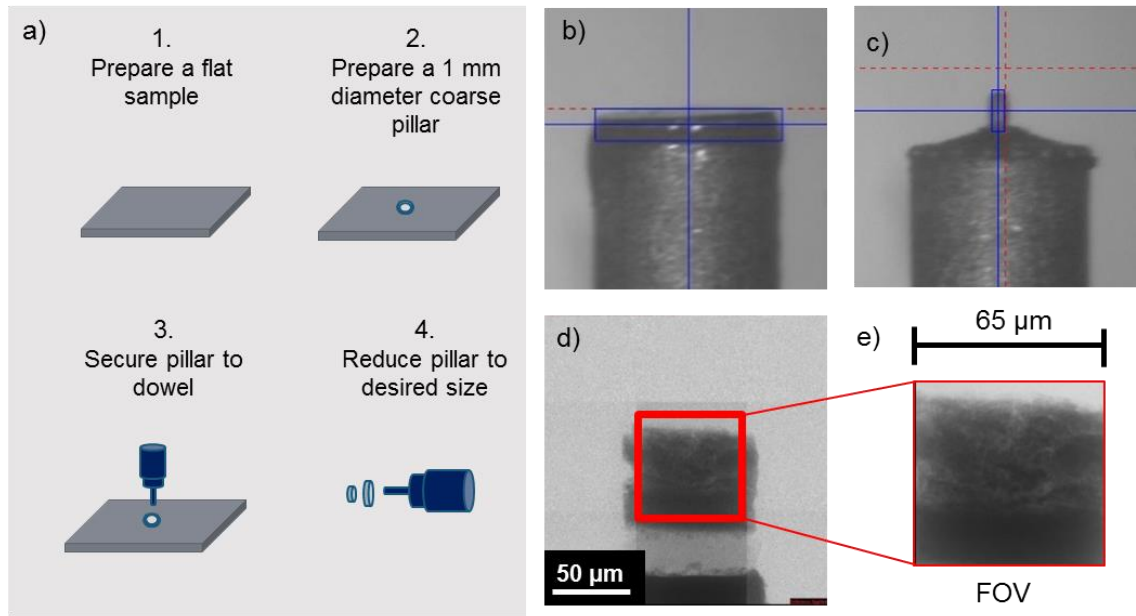
Figure 3.11 (a) Schematic showing the four stages of sample preparation using the micromachining laser method. Optical image of a laser-prepared sample showing a) a 1 mm diameter course pillar mounted onto a dowel and b) 63 µm diameter fine pillar mounted onto a dowel. The corresponding mosaic radiograph of the sample is shown in (c) and a single radiograph with a FOV equal to that used for X-ray nano-CT (Ultra 810, LFOV) is shown in (d).

3.5.6. Image processing

Imaging using X-ray CT enables 3D quantification of several microstructural and transport properties of battery materials. Reconstructed datasets obtained from X-ray CT contain a 3D volume in which each voxel (the volume equivalent of a pixel) is given a value that correlates to its X-ray attenuation at a point in space. Different materials display different attenuation signals i.e. darker regions attribute to weakly attenuating materials and lighter to highly attenuating materials. This difference in greyscale allows images to be separated and labelled as different materials, phases or segments of data. Effective data analysis by this method is highly dependent on scan resolution, including beam hardening and ring artefacts[164]. For X-ray CT of LIBs that contain features smaller than the resolution of the instrument, the resulting attenuation signal can often represent a combination of multiple materials i.e. particle as pore or pore as a particle. This can lead to under- or overestimation of key parameters such as porosity or PSDs. Several image processing

techniques can mitigate the effects of such errors and improve the quality of data.

3.5.6.1.   Filters

The use of filters, particularly the non-local means filter, is one such technique that enhances the quality of datasets by reducing the noise in images. A filter transforms an image to emphasize or stress a specific feature of its structure. A common filter used throughout this thesis is the non-local means filter. It operates by assigning an averaged value taken from a group of pixels to a target pixel, using a weighting strategy whereby the surrounding pixels are weighted depending on their similarity to the target pixel. While this, along with other filter types, preserves boundaries and smooths image textures, errors remain particularly when important details may be overlooked by user-chosen filter settings. While various filters can detect sharp transitions to enhance, contrast or detect edges, a common limitation with filtering is to estimate a signal mixed with noise and local changes in intensity present another common problem[204]. When using filters settings and types are considered carefully to ensure important details are preserved.
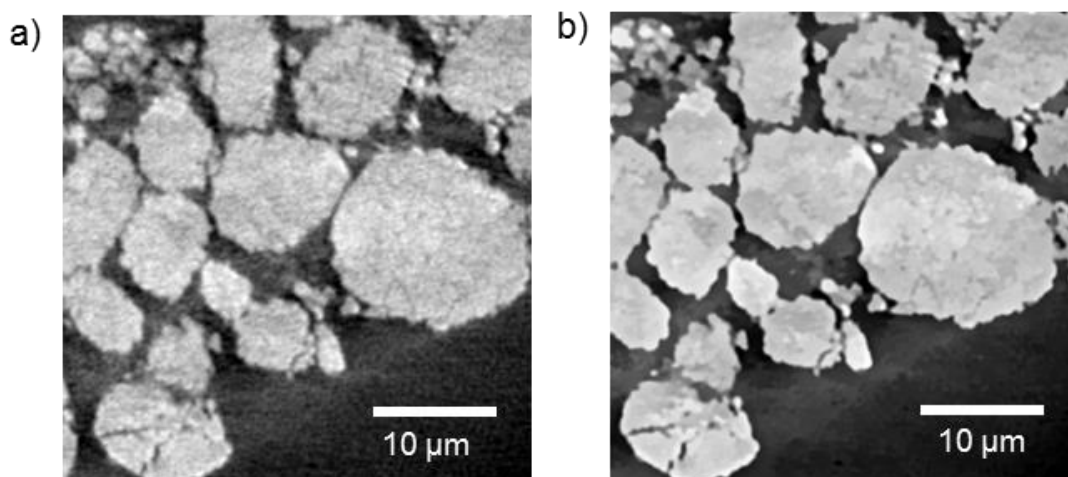
Figure 3.12 2D orthogonal slices showing an unprocessed grayscale image of cathode material particles (a) before filter application, and (b) after applying a non-local means filter, where some image features such as cracks are enhanced and some textures are smoothed.

3.5.6.2. Segmentation

LIB batteries and their materials are composite structures made up of several phases. For example, the cathode material is comprised of three phases: active particle, pore, and binder. Each of these phases is represented by a differing greyscale value. Highly attenuating materials, like the active particles, will appear as brighter regions (bright white or shades of light grey), whereas those with lower attenuation will appear as darker regions (black or dark grey). The segmentation of materials and phases is mostly based on the differences between their grayscale values which can be easily visualised as distinct peaks on the associated histogram for the image. The segmentation process involved assigning a label to each pixel of the image, which describes the region or material associated with the pixel (e.g. particle or pore). The segmentation fields are stored as separate data objects called Labels. In this work, segmentation and associated labels are often the prerequisite for volume fraction, particle size or tortuosity measurements. Generally, the segmentation of 3D datasets can be automatic, or interactive depending on the desired output. The segmentations in this work have been interactive where peaks were separated and assigned by the user. As a result, the extent to which the segmentation accurately represents a dataset is oftentimes dependent on the user.

3.5.6.3. Parameter extraction: bulk electrode and particle morphology

Parameters such as the electrode thickness can be extracted from images of the bulk electrode. For example, in scans of the whole battery segmentation; the differing greyscale values of the electrode layers can be used to segment the layers. Two types of quantification can be carried out: the thickness of the electrode measured across the 3D volume and/or if the resolution allows the particle size distribution. An example of this parameter extraction is represented as steps in Figure 3.13 (a – c), where the initial greyscale image is shown, and then the segmented binary image (where the positive electrode particles are assigned and shown in blue). Using the binary image, a built-in thickness measurement tool in Avizo Fire 9.5 image

processing software (FEI VSG, France) is used to measure the thickness of the bulk electrode across the extracted 3D sub-volume. A volume rendering of the segmented layers is shown in Figure 3.13 (d) where the copper current collector of the anode and positive particles of the cathode electrode is shown as an example. The resolution of the image can be a significant source of error when extracting this parameter as the intensity of a pixel represents a mix of the attenuation coefficients of various materials within that region. Therefore, the electrode thickness measurement is highly sensitive to pixel resolution, especially when the exact boundary location needs to be distinguished.
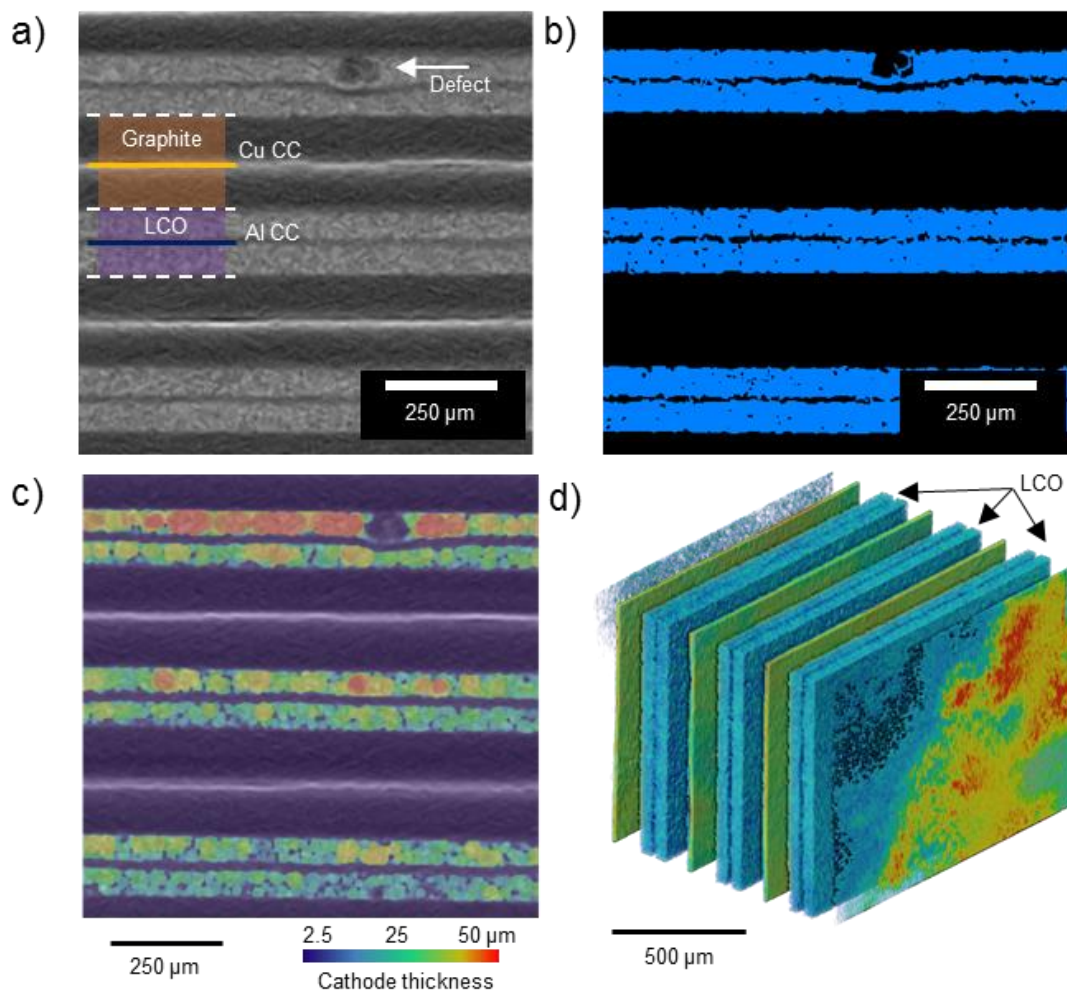
Figure 3.13 (a) 2D orthoslice from a tomogram of a commercially available layered pouch cell, showing the greyscale differences between materials and electrode layers. The white materials are highly attenuating, for example, the copper current collector, while the less attenuating materials are in black, for example, graphite. A defect is also highlighted. (b) A binarised image where the positive electrode material is segmented, and (c) after a thickness map is applied to the layers. (d) A volume rendering of the layered structure showing the positive electrode and highly attenuating copper current collector layer.

In this work, both open-source and commercially available software packages are used to quantify porosity, pore and particle size distributions and tortuosity. Before this, a sub-volume of data (e.g. X x Y x Z voxels) is selected from a region of interest (ROI) within a dataset. The analysis is carried out on this chosen sub-volume. A representative volume element (RVE) analysis must be performed on this to ensure the data is representative of the bulk material[159][22]. The minimum RVE data sizes for the results in this work are determined using a method that considers the maximum relative error threshold of the desired property measured as the sub-volume size increases. This continues until the whole sample is analysed. The first volume size that returns an error below the threshold is defined as the RVE[159]. An example of this workflow is shown in Figure 3.14 (a – d); first the image is enhanced by the application of filters (features are smoothed), and then particles are assigned and labelled via a simple threshold segmentation. A 'label analysis' is carried out in Avizo imaging software that separates the assigned labels according to the openings/spaces between the various amalgamated 3D volumes (i.e., separate particles). Figure 3.14 (e – h) shows a similar workflow using 3D volume renderings; here a typical dataset for a cathode material is shown for a sample prepared using laser milling (as discussed in detail in section 3.5.5.1. Manual and laser preparation of this thesis) and imaged using the Ultra X-ray CT at a nanometre resolution. A sub-volume is extracted from the dataset; this reduces computation time and reduces errors, which may arise from the laser milling technique. For example, the high-power laser could cause damage to the outer edges of the milled pillar and extracted a sub-volume from the centre of the pillar reduces the chances of analysing particles damaged from sample preparation. Lastly, especially when extracted parameters such as PSD, it is important to remove those particles that are touching the edges of the sub-volume box. These are oftentimes not whole particles and can skew datasets. A built-in 'border kill' tool in Avizo software is applied that removes such particles before subsequent measurements of particle size.
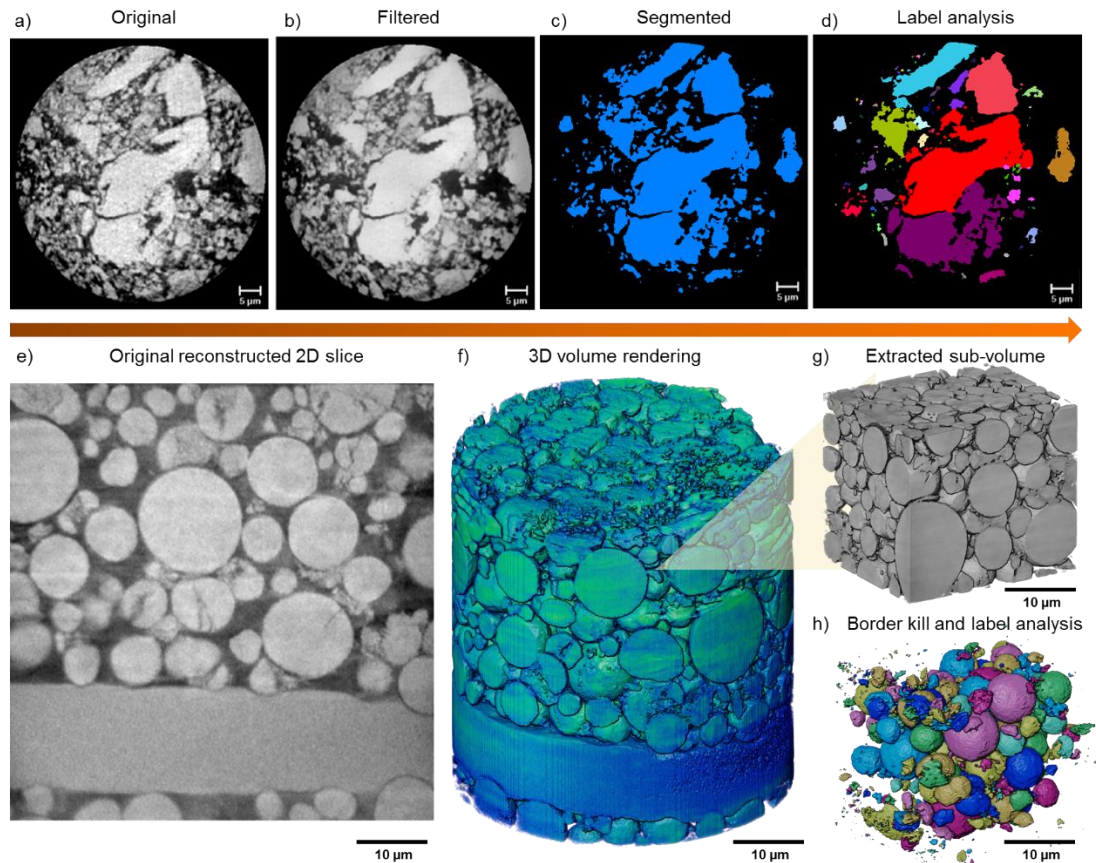
Figure 3.14 Workflow from the (a) unprocessed dataset, (b) after filtering, (c) segmentation of the active particles, and (d) separate labelling of individual particles. (e – h) shows the data processing steps from the raw data, to the 3D volume rendering, sub-volume extraction to the separation of particles and label analysis. Comparison between (g) and (h) shows the result of applying a 'border kill' module accessed in Avizo Fire 9.5 image processing software (FEI VSG, France).

3.5.6.4.   Volume fractions and porosity

After filtering and processing, parameters such as volume fraction and porosity can be extracted. The ratio of voxels which represent each phase to the total number of voxels in a chosen sub-volume is determined after segmentation of either a micro- and/or nano-CT dataset. The ratio of void volume to the total volume is defined as the porosity and is calculated using a built-in tool in Avizo Fire 9.5 image processing software (FEI VSG, France). Caution is taken when choosing a suitable bounding box size; the edges should be carefully chosen so that data occupies the total volume, as opposed to void space, which may interfere with segmentation if the attenuation of the material is similar to that of void space.

3.5.6.5.   Particle Size Distribution

PSD calculations are carried out by identifying isolated objects i.e. separating particles from one another. This work is performed using a 'separate objects' function in the Avizo Fire 9.5 software (FEI VSG, France). The function combines a watershed algorithm with a distance map and identifies gradients in greyscale values that may represent boundaries between particles in a given volume. Once identified, a 'label analysis' feature calculates the 'equivalent diameter' (diameter of a sphere of equal volume to the identified particle) of each isolated particle, given by the following equation.

$$EqDiameter = \sqrt[3]{\frac{6 \times Volume3d}{\pi}}$$

Equation 3.4

Before calculating this value, a 'border kill' module is applied to remove any particles touching the sub-volume boundaries that can skew the distribution and introduce errors.

3.5.6.6.   Tortuosity Factor

Tortuosity describes the convolution of a path between two points; i.e. the paths through electrodes that lithium ions need to travel. It can be defined as the ratio of the actual path length to the Euclidean distance between the two points. The tortuosity factor, a transport parameter within electrode materials in this work, was determined using a MATLAB plugin, TauFactor[205]. X-ray CT image data is processed into binarized image stacks before TauFactor simulates diffusion through the structure of a phase of interest (e.g. pore volume) by applying a fixed potential on two opposite sides of a volume. A steady-state diffusion equation between two Dirichlet boundary conditions[181] is solved and the effective diffusion coefficient, D_{eff} is calculated based on Equation 3.5.

$$D_{eff} = D \frac{\varphi}{\tau}$$

Equation 3.5

Where D is the intrinsic diffusivity of the transporting phase and D_{eff} is the effective diffusivity through the conductive phase of interest. φ is the volume fraction of the conductive phase and τ is the tortuosity factor. The tortuosity factor is determined by comparing the steady-state diffusive flow in a fully porous volume to the flow through a porous network in a volume of the same size. For electrode material analysis, the diffusive flow is considered to occur exclusively via the porous network, thus φ is replaced by the porosity, ε of the material.

3.6. Summary

In this chapter, the basics of electrochemical characterisation from cell assembly to cycling to parameter extraction were introduced. Thermal analysis of cells using calorimetric techniques was discussed using DSC and ARC. Thermal analysis using coin cell DSC was described in detail and will be referred to in Chapter 4. Methodologies for conducting thermal failure and nail penetration tests on LIBs were outlined and will be referred to in Chapters 5 – 7. Post failure cell disassembly methods were also introduced for two types of cell formats (cylindrical and pouch).

The basic theory behind microscopy, X-ray imaging and computed tomography was discussed and their applications for characterising whole battery architecture and materials was discussed. Multi-length scale imaging techniques were introduced and their applications and uses are discussed and demonstrated further in Chapters 5 – 7. Synchrotron radiation sources and the ability to image at higher frame rates was discusses in the context of capturing high speed thermal failure in LIBs; their advantages and disadvantages were discussed and this is explored further in Chapter 7. Multiple material preparation methods (manual and laser milling) are described from imaging to resolve the electrode bulk layer features down to the individual particle. Finally, the image processing techniques and the typical parameters extracted from image-based quantification techniques were outlined. These are referred to in all chapters involving X-ray CT. The following sections of this thesis are the results chapters.

Chapter 4

4. Thermal Analysis

4.1. Introduction

LIB operation involves many complex processes from various chemical reactions, and charge transport, to the intercalation or de-intercalation of lithium ions. The processes are influenced by heat generation from various internal processes and external temperatures that govern the overall performance of the cell regarding its cycle life, efficiency and safety. For example, the cycle life of a LIB may be reduced by the presence of side reactions such as lithium plating due to the consumption of Li^+ and electrolyte over time. At higher temperatures and C-rates these side reactions are more likely to occur and alter the electrochemical behaviour of the cell. Chemical reactions and charge transport (i.e. conductivity or diffusivity) are also temperature dependent, where the speed of reactions will impact the overall efficiency of the cell performance[206]. Furthermore, at extremely high temperatures, above ~ 80 °C, a series of exothermic reactions may be initiated where materials (the SEI layer, electrolyte and electrodes) will begin to degrade and decompose. This phenomenon is commonly referred to as thermal runaway where the cell may generate large amounts of heat and gas. The extent to which the cell fails (whether it leads to rupture or fire) is predominately governed by the rate of heat dissipation throughout the cell, which should be higher than the rate of heat generation for a less catastrophic outcome. Therefore, understanding material reactivity and heat generation within LIBs is vital for the design of safer batteries.

4.1.1. Reactions and expected observations

A high-energy storage density can be achieved when a large electrochemical potential difference exists between the anode and cathode. In the following sections, unless otherwise stated, the cathode is made of $LiNiMnCoO_2$ (of varying stoichiometries) which behaves as an intercalation

host for Li⁺ ions and graphite as the anode. The two are separated by a porous permeable membrane which is ionically conductive but electrically resistant separator (Celgard 2325, Celgard, LLC). Upon charging, the Li⁺ ions de-intercalate from the lithium metal oxide, pass through the lithium ion conductive electrolyte and intercalate into the graphite. Electrons travel through an external circuit to couple with Li+ to maintain charge neutrality shown by Equation 4.1. During discharge, the reverse mechanism occurs (Equation 4.2). The electrolyte is a polar organic solvent with a lithium salt dissolved in it such as LiPF₆.

Anode:

$$LiNiMnCoO_2 \leftrightarrow Li_xNiMnCoO_2 + Li + xe^-$$

Equation 4.1

Cathode:

$$6C + xLi^+ + xe^- \leftrightarrow Li_xC_6$$

Equation 4.2
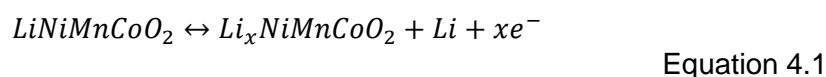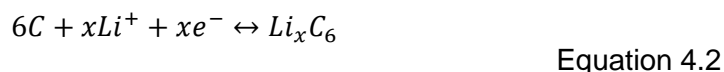
A number of additional reactions take place as the battery reaches temperatures outside of its recommended or optimal operating temperature. These have been extensively outlined in the literature review in section 2.3.4. While the reagents and products of the reactions vary depending on the chemical make-up of materials such as the electrolyte, salts, or the cathode, through extensive experimental tests (such as DSC and ARC), we can categorise some of the main observations that are likely tlo occur during thermal failure. The main features are summarised in the following list and are referenced in other sections of this chapter.

Observation 1: The first exothermic event that occurs at the lowest temperature is the decomposition of the least-stable components of the SEI layer. The layer is formed during electrochemical cycling and can show signs of an exothermic decomposition (under normal operating conditions) as early as 69 °C[105]. This is visible in both de-lithiated and lithiated graphite.

Observation 2: The second and largest heat release reaction is the reaction between electrolyte and lithium stored in the graphite anode after the primary

SEI breaks down, usually around 100 °C. The reaction rate is positively correlated to the surface area of graphite particles that are exposed.

Observation 3: The heat released by the electrolyte-anode reaction is inhibited by the accumulation of reaction products that make up with secondary SEI layer. This is expected to last up to about 200 °C and in DSC, this often shows up as a plateau in the heat release rate[113].

Observation 4: At temperatures above 200 °C, a rapid increase in heat release is expected in which several major reactions have been recognised: both exothermic and endothermic in nature (such as oxygen release reactions or the separator melting).

The electrochemical and thermal behaviour of LIBs depends on their chemical makeup and microstructures. These are often characterised by techniques such as differential capacity analysis and DSC. The objective of this chapter is to provide insight into the thermal behaviour of LIB cathode materials under various working cell conditions. DSC is used to characterise the thermal stability of various cathode chemistries (NMC111, NMC622 and NMC811) and the influence of electrolyte on the thermal behaviour of working cells. Later, DSC results are correlated with electrochemical data from a battery cycler to evaluate the rates of irreversible heat generation under various operating conditions (standard and more aggressive testing at higher temperatures, C-rates and upper cut-off voltages). The methodology presented provides heat generation maps where the influence of changes in operational variables, such as temperature, C-rate, and, the upper cut-off voltage can be easily compared. The protocols for coin cell fabrication intended for DSC studies are described in detail in Chapter 3, Section 3.1., however, specific cell chemistries are defined for each result in their respective sections.

4.2. Experimental

The experimental procedure in this section extends from Chapter 3, Section 3.2. The cells in this chapter underwent initial formation cycling using

the Biologic ultra-precision battery cycler system (model BCS-805, BioLogic, France, measurement current accuracy up to 0.015 % FSR with a source current and voltage range between 10 μA – 150 mA and 0 – 10 V, respectively). The cell heat generation rate $\dot{Q}$, in mW, was measured using a novel heat-flux type DSC coin cell calorimeter in combination with a potentiostat (Interface 1000E, Gamry Instruments, USA, max. current and voltage of 1 A and 12 V, respectively), with EIS capabilities (rated frequency between 10 μHz – 10 kHz). For the tests studying the heat generation under normal operating conditions analyses, a temperature of 25 °C was chosen at either 0.5 or 1 C-rate. The first set of cells consisted of NMC111 cathode chemistry from various manufacturers and the anode material varied, these are summarised in Table 4.3. The second set of cells, used for studying heat generation under more aggressive testing analyses, consisted of NMC811 cathode chemistry and graphite anode, summarised in Table 4.4.

For all cells, an OCV measurement was taken at the beginning and at the end of each test, to verify that there was no change to the initial SOC.

1. First, the sample coin cell (after formation) and a reference cell were placed inside the calorimeter module.
2. The isothermal temperature of the DSC would be set once the cell had been placed inside the module and left to 'rest' for 1 h at the intended temperature for the test.
3. A CCCV charge-discharge protocol would then be implemented for 10 cycles.

A total of 52 tests were conducted across 24 test cells and references, some of these underwent the following (numbered list) cycling conditions and sequence. The cells were cycled using a battery cycler (Interface 1000E, Gamry Instruments, USA). The CCCV protocol was implemented for charging and CC for discharging, which meant the cells were charged with a constant current, followed by charging with the upper voltage limit until the current decreased to C/20. Afterwards, the cells were discharged with the respective C-rate until the lower voltage limit was reached.

1. Constant current discharge with a suitable voltage limit.

2. Constant current charge with a suitable voltage limit.

3. Steps 1 and 2 were repeated several times (e.g. five cycles).

4. For some cells, a constant current discharge to 50 % SOC based on voltage (i.e. 3.8 V) followed.

5. The impedance was measured at 50 % SOC after a relaxation period of approximately 3 hours with frequencies ranging from 1000 kHz to 0.01 Hz.

4.2.1. Data processing

The cycling and heat flux data, although measured for a single cell, were obtained using two different software. For example, battery cycling data from the Gamry potentiostat software (Echem Analyst version 7.07, Gamry Instruments, USA) and thermal data from the calorimeter software (Proteus, Netzsch Geratebau GmbH, Germany). As a result, some datasets included a start time offset, this was corrected for during electrochemical data processing. The heat flux value ΔT, when positive represents an exotherm and when negative represents an endotherm. For analyses where heat generation was analysed, heat flux vs. time results was normalised to zero (in the y-axis), however, for datasets where no further calculations were made, and only the peak characteristic was compared, the heat flux (y-axis) was kept at non-zero values.

EIS measurements were collected for various conditions for the NMC811 vs. Graphite cells. The resulting data was fitted using the equivalent circuit model shown in Figure 4.1. Where R1 is the series resistance, R2 and CPE1 represent the charge transfer resistance occurring at the interface, R3 and CPE2 represent the charge transfer of the active materials, and CPE3, in this case, is used to fit the low-frequency tail. EIS data was collected for 50 % SOC and the exchange current density was calculated using the Butler-Volmer equation (Equation 2.16).
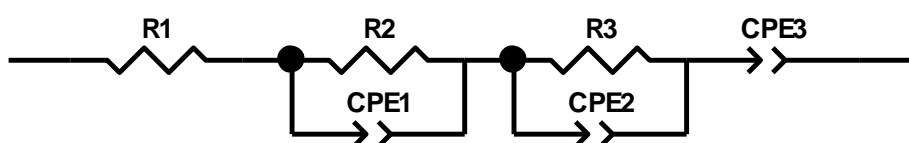
Figure 4.1 Schematic showing the equivalent circuit model used to fit the EIS data.

4.3. Results

4.3.1. Material decomposition tests

In this section, the temperature at which thermal decomposition begins (onset) of NMC111, NMC622 and NMC811 cathodes in full-cell configuration is measured. The thermal behaviour of the cycled NMC811 is compared to that of an uncycled NMC811 cell. Later, the behaviour of NMC811 without the presence of electrolyte is measured and compared.

4.3.1.1. Thermal stability of varying NMC stoichiometry and SOC

Three cells were designed and prepared, as outlined in Table 4.1, charged to 100 % SOC and heated at a constant rate under adiabatic conditions in the coin cell calorimeter (MMC 274 Nexus). Similarly, three empty CR2032 cells sealed with a polypropylene gasket inside an argon-filled glovebox (O_2 and H_2O < 0.5 ppm, MBraun, Germany) were used as the reference. Repeat tests were not conducted for this analysis, as it was a proof of concept test to establish a baseline for later, more rigorous analyses.

Table 4.1 Summary of coin cell samples and their components for thermal stability of components tests.

Sample/Coin cell number	1	2	3	4
Positive electrode	90 wt % $Li(Ni_{0.33}Mn_{0.33}Co_{0.33})O_2$ (NMC111, NEI), 15mm, 12.55 mg/cm^2	90 wt % $Li(Ni_{0.6}Mn_{0.2}Co_{0.2})O_2$ (NMC622, NEI), 15mm, 10.63 mg/cm^2	90 wt % $Li(Ni_{0.8}Mn_{0.1}Co_{0.1})O_2$ (NMC811, NEI), 15mm, 9.77 mg/cm^2	90 wt % $Li(Ni_{0.8}Mn_{0.1}Co_{0.1})O_2$ (NMC811, NEI), 15mm, 9.77 mg/cm^2
Negative electrode	92 wt % Graphite (NEI), 16 mm, 6.75 mg/cm^2			
Separator	Polypropylene–polyethylene–polypropylene (Celgard 2325, Celgard, LLC.), 18mm			
Electrolyte	1 M $LiPF_6$ in EC:DEC 1:1 v/v (Soulbrain MI), 60 µL			
Measured capacity (mAh)	2.5	3.1	2.8	2.6

Testing mode and temperature	Constant heating, 1 °C min^{-1} to 170 °C & dq/dV @ 25 °C	
Operating voltage	3 – 4.2 V	N/A
Cycling protocol (C-rate)	Formation: 2 cycles at C/20, followed by 10 cycles at 0.1 C	N/A

The DSC heat flux responses for the NMC-graphite full cells with varying nickel content are presented in Figure 4.2 (a) within the 120 °C and 160 °C temperature ranges. The sharp endothermic peaks observed between 135 °C and 145 °C may be associated with the melting of the PP layer within the composite separator material. The heat-absorbing reactions (at the point of inflection) shortly after what is assumed to be the separator melting are measured to begin at 138 °C for NMC111, 140 °C for NMC811, and 142 °C for NMC622. While the width of the endothermic peak remains similar for all three samples the heights differ.. It is expected that the variation in the cell capacities plays a role in the amount of heat that is absorbed[140][207]. The cell capacities in the order of highest capacity to lowest were NMC622>NMC811>NMC111, which correlate with the trends observed for the onset of heat-absorbing temperatures and the height of the endothermic peaks. Here, the higher the discharge capacity, the higher the onset temperature and lower the heat absorbed. Although, it should be noted that the reactions depend strongly on the degree of lithiation, particle size and the specific surface areas of the electrode materials (which are not measured here). In addition to the capacity of the cell, Zheng et al. report that the thermal stability of the layered NMC structure can be tuned by the most unstable oxygen (see reference [208]), suggesting that the lithium content, the stoichiometry of Ni, Mn and Co, the Ni and Li ordering can affect the temperature at which the most unstable oxygen is released.

Some exothermic decomposition reactions shortly after the main endothermic peak for NMC111 and NMC622 can also be observed. As the separator melts, its structural stability reduces as it shrinks, and the lithiated anode surface/as well as the secondary SEI are left exposed to react further with electrolyte salts and solvents. Furthermore, any water released from the PP and PE combustion reactions will exothermically react with lithium in the secondary SEI layer[114]. The effects of the subsequent heat release

reactions (observations 3 and 4) are expected to occur at temperatures greater than 200 °C, which are outside of the temperature range of this study. It is assumed that as the temperature exceeds 150 °C, CO_2 may have been released for the NMC111 and NMC622 cells from reactions between the electrolyte and lithiated anode (observations 2 and 3).
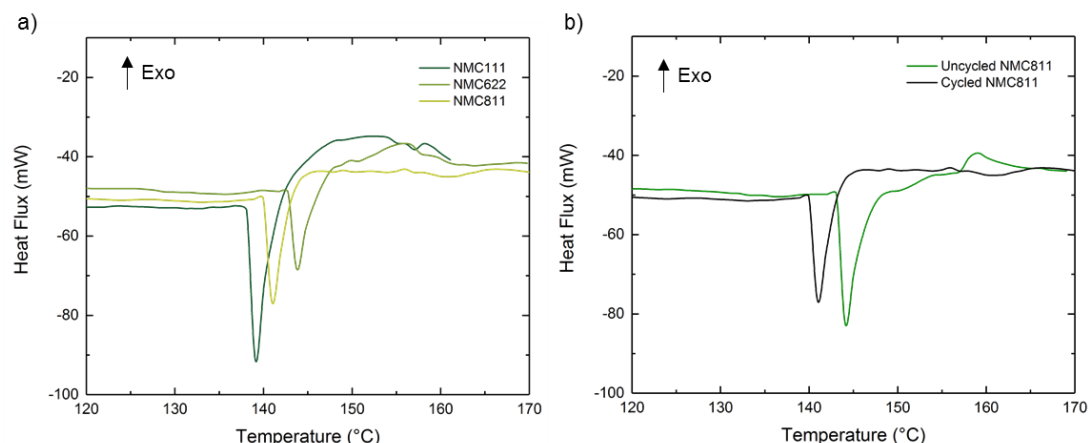
Figure 4.2 Heat flux signals obtained for the thermal decomposition (a) of NMC111, NMC622 and NMC811 full cells heated up to 170 °C at 1 °C min^{-1}, and (b) two NMC811 cells; one cycled cell which has undergone formation and 10 charge-discharge cycles and the other, uncycled cell, which has not undergone formation (e.g. de-lithiated graphite, no SEI layer).

An additional uncycled NMC811 cell (Sample 4 in Table 4.1) was tested using the same parameters and compared with an identical cycled cell (Sample 3 in Table 4.1). Figure 4.2 (b) shows how the cycled cell has a lower onset temperature when compared with the uncycled equivalent. Generally, the thermal stability of a cell is lower with a higher the degree of lithiation of graphite, whereas the amount of heat generation is lower for lithiated graphite compared to a graphite sample that has not been lithiated[81]. Some exothermic peaks can be observed for the uncycled NMC811 which correlate to the findings in literature. To investigate this further, two identical cells (NMC811, cycled and uncycled) were tested inside an ARC to measure the thermal response of the cells at a higher temperature up to 250 °C.The cells were heated at the same rate (1 °C min^{-1}) as those that were tested using DSC. It is difficult to predict the onset temperatures from the temperature profiles obtained from the ARC measurements because the ARC chamber is much greater in size compared to the DSC chamber and designed for larger samples than a coin cell. While the equipment type is not well suited to

measure the temperature changes within the coin cell to an accurate degree, it does provide a preliminary test to ascertain the suitability of the cells for DSC. The red lines highlighted in the temperature rate profiles (Figure 4.3) show the temperature at which the gasket inside the cells melted and the seal failed (i.e. the coin cells opened). This can't be observed in the DSC profile (Figure 4.2 (b)) due to the nature of the experimental set-up where the maximum temperature was 170 °C for the DSC measurement, which is below the melting point of the coin cell gasket material. There is a distinct gap in the data where the measured temperature rate jumped from below 1 °C min^{-1} to approximately 2 °C min^{-1} for both the charged and uncharged cells in Figure 4.3. The temperature at which the cell opened for the charged cell is lower, at ~ 185 °C compared to that of the uncharged cell which opened at ~ 220 °C. The charged NMC811 cell had a lower onset temperature than the equivalent uncharged NMC811. This was a similar observation to the samples tested using DSC in Figure 4.2 (b). The DSC profile in Figure 4.2 (b) shows the initial thermal responses at lower temperatures, such as the melting of the separator and subsequent reactions, while the ARC profile gives an indication of how quickly heat generation accelerates for the cycled cell vs. the uncycled cell.

Considering the trends observed between the four cells and the two techniques, and those in the literature for NMC811[11], these results show that lithiated NMC811 is more thermally stable than de-lithiated NMC811. Future work should include repeats of these experiments, to accurately conclude these findings, building on the viability studies carried out here.
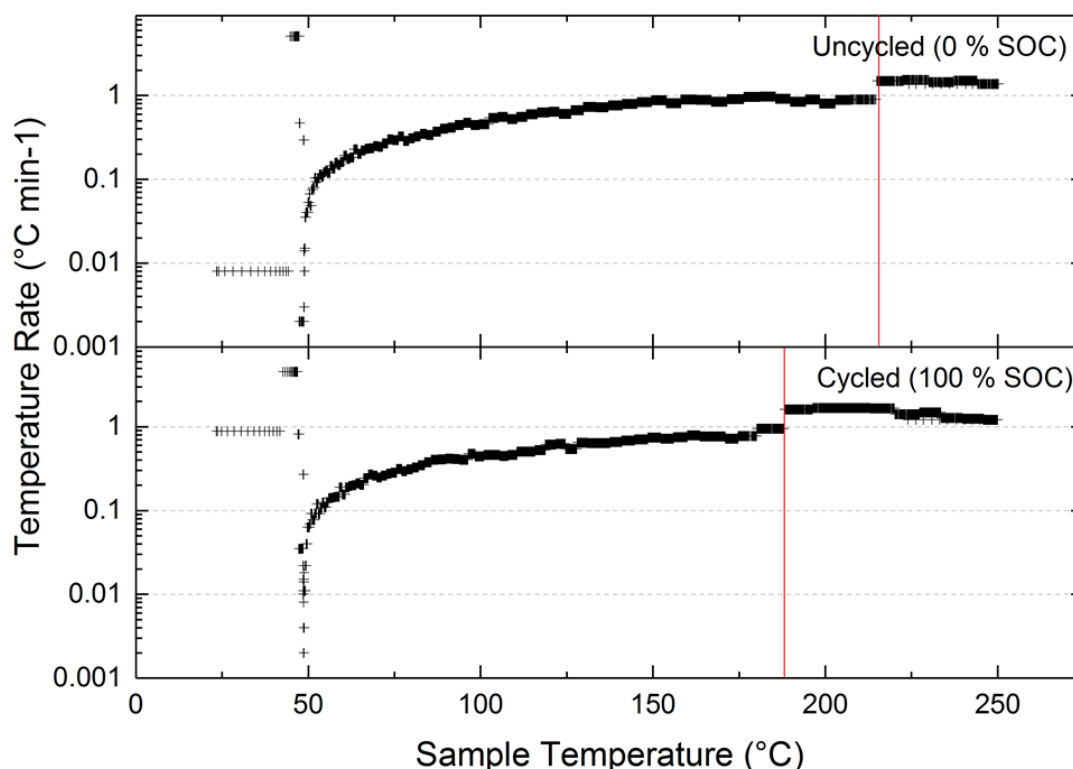
Figure 4.3 ARC self-heating rate profiles of NMC811 coin cells. Beginning at a start temperature of 50 °C, the temperature was increased step-wise by 2 °C until a self-heating rate greater than 0.01 °C min^{-1} was measured up to 250 °C. The temperatures at which the O-ring seal failed and the cell opened were measured. TOP: The cycled cell at 100 % SOC (4.2 V) this temperature was 220 °C. BOTTOM: The uncycled cell at 0 % SOC (0 V), this temperature was 185 °C.

4.3.1.2.   Decoupling heating effects from various components

Three cells were designed and prepared as outlined in Table 4.2. The full cell (sample 5) was charged to 100 % SOC and all three samples were heated at a constant rate under adiabatic conditions in the coin cell calorimeter (MMC 274 Nexus, Netzsch Geratebau GmbH, Germany). Similarly, three empty CR2032 cells sealed with a polypropylene gasket inside argon-filled glovebox (O_2 and H_2O < 0.5 ppm, MBraun, Germany) were used on the reference side for each test.

Table 4.2 Summary of coin cell samples and their components for testing cathode stability with and without the presence of an electrolyte.

Sample/Coin cell number	5	6	7
Description	Full cell	Without electrolyte	Electrolyte only
Positive electrode	90 wt % Li(Ni$_{0.8}$Mn$_{0.1}$Co$_{0.1}$)O$_2$ (NMC811, NEI), 15mm, 9.77 mg/cm^2		N/A

Negative electrode	92 wt % Graphite (NEI), 16 mm, 6.75 mg/cm^2		N/A
Separator	Polypropylene–polyethylene–polypropylene (Celgard 2325, Celgard, LLC.), 18mm		N/A
Electrolyte	1 M LiPF$_6$ in EC:DMC 3:7 v/v (Soulbrain MI), 60 µL	N/A	1 M LiPF$_6$ in EC:DMC 3:7 v/v (Soulbrain MI), 60 µL
Measured capacity (mAh)	2.7	N/A	N/A
Testing mode and temperature	Constant heating, 1 °C min^{-1} to 160 °C		

*Formation: 2 cycles at C/20, followed by 10 cycles at 0.1 C

The heat flux signal obtained from the three tests is shown in Figure 4.4. The full cell sample (black line) showed the greatest number of peaks, whereas the cell sample without electrolyte (blue line) did not show any distinct features. For the full cell, the first event observed is a small exothermic peak at ~ 142 °C followed shortly after by a large endothermic peak. At this temperature, it is expected that the SEI layer has already begun decomposing and the presence of PF$_5$ will begin to damage the SEI and generate heat anywhere between 100 – 150 °C[81][107]. Some of the energy released by these reactions is absorbed by the evaporation of the electrolyte[98] or partial melting of the tri-layer separator[93]. A similar endothermic peak is also observed for the electrolyte only cell at ~ 146 °C. The evaporation may occur at a higher temperature for the electrolyte only cell since the full cell had undergone cycling and have a less thermally stable SEI layer (and components). Interestingly an endothermic peak is not observed in the NMC811 cell without electrolyte – it would be expected since it has the same separator material as the full cell. The separator in the cell without electrolyte would be less thermally conductive than a separator membrane soaked in electrolyte[209]. As a result, the internal temperature distribution in the cell with electrolyte vs. the cell without electrolyte would differ and alter the overall heat effects in terms of characteristic endothermic or exothermic peaks.

Above 150 °C, both the curves for the full cell and the 'electrolyte' cell show two exothermic peaks in the range approximately between 153 °C and 158 °C. The maximum peak height and the peak width for the full cell are much greater than that of the electrolyte. A greater heat generation is expected for the full cell within this temperature range due to the graphite-electrolyte reactions and the associated formation of the secondary SEI layer[105].
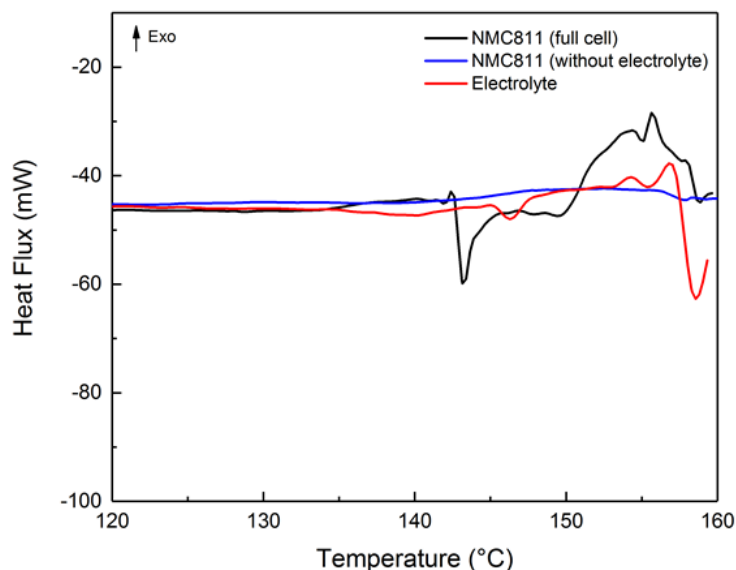
Figure 4.4 Heat flux signals obtained for the thermal decomposition of NMC811 full cell, full cell without electrolyte and electrolyte only. Electrolyte composition is 1 M LiPF6 in EC:DMC 3:7 v/v (Soulbrain MI), 60 µL. The thermal behaviour was measured by heating the samples at a constant rate of 1 °C min^{-1} up to 160 °C under adiabatic conditions in a coin cell calorimeter (MMC 274 Nexus, Netzsch Geratebau GmbH, Germany).

Whilst experimentally investigating the heat effects of various reactions is complex due to their overlapping nature, these results show that this method of adjusting sample and reference components in the coin-cell DSC is viable while still being close to the working cell environment, such as that shown in Figure 4.4 for the electrolyte contribution. It is evident that the electrolyte and its behaviour with other cell components (such as the anode), has one of the greatest effects on the overall heat generation during thermal failure and is a critical area for battery safety analysis.

4.3.2. Thermal behaviour under normal cycle conditions

The response of the heat generated during cell cycling under normal operating conditions was evaluated by independently studying the following variables: anode material and C-rate.

Table 4.3 Summary of coin cell samples with NMC111 cathode intended for the investigation of heat generation under normal conditions.

Sample / Coin cell number	8	9	10
Positive electrode	96 wt % Li(Ni$_{0.33}$Mn$_{0.33}$Co$_{0.33}$)O$_2$ (NMC111, Targray Technology International), 10 mm, 13.95 mg/cm^2		90 wt % Li(Ni$_{0.33}$Mn$_{0.33}$Co$_{0.33}$)O$_2$ (NMC111, NEI), 15mm, 12.55 mg/cm^2
Negative electrode	Lithium, 18 mm	92 wt % Graphite (WMG), 11 mm / 16 mm, 7.15 mg/cm^2	
Separator	Polypropylene–polyethylene–polypropylene (Celgard 2325, Celgard, LLC.), 18mm		
Electrolyte	1 M LiPF$_6$ in EC:DEC 1:1 v/v (Soulbrain MI), 60 µL		
Measured capacity (mAh)	1.2	3.0	2.75
Testing mode and temperature	Isothermal, 25 °C		
Operating voltage	3.0 – 4.2 V		
Cycling protocol (C-rate)	0.2, 0.5 & 1 C		0.5, 1.0, 5.0 & 10 C

4.3.2.1. Anode material: Graphite vs. Lithium metal

Preliminary coin cell DSC experiments were conducted to investigate the viability of the tests. Figure 4.5 (a) shows the heat flux signals, current and voltage profiles for two cells; one full-cell NMC111-Graphite and one half-cell NMC111-Lithium. A large exothermic peak is observed at the end of discharge and beginning of charge for both cells similar to that observed by Giel et al[207]. An endothermic peak appears during the beginning of the charge for the full cell which is not observed for the half cell, this cooling effect is consistent with the thermal behaviour reported initially by Hong et al[210], and others[97][211]. Figure 4.5 (b) shows the differential capacity profiles of the NMC111-Graphite and NMC111-Li. Characteristic peaks were observed during the charging and discharging of both cells. The peak occurring at ~ 3.61

V in the NMC111-Graphite cell during charge may be attributed to lithium intercalation into graphite, $C_6 \rightarrow LiC_x$[212] and the phase change from hexagonal-I to hexagonal-II (H1 $\rightarrow$ H2)[87]. During discharge, peaks at 3.45 V, 3.6 V and 4.0 V are visible, these are attributed to the phase changes from H2 $\rightarrow$ H1, H1 $\rightarrow$ monoclinic and lithium de-intercalation from the graphite. In the NMC111-Li cell, the peak occurring at 3.8 V is attributed to the structural change from H1 $\rightarrow$ H2 and the peak at 3.7 V during discharge for the reverse[213]. The thermal behaviour and phase transitions are as expected from various literature sources. Since full cell data more accurately represents the make-up of commercial LIBs, the following thermal analyses are conducted with graphite anodes.
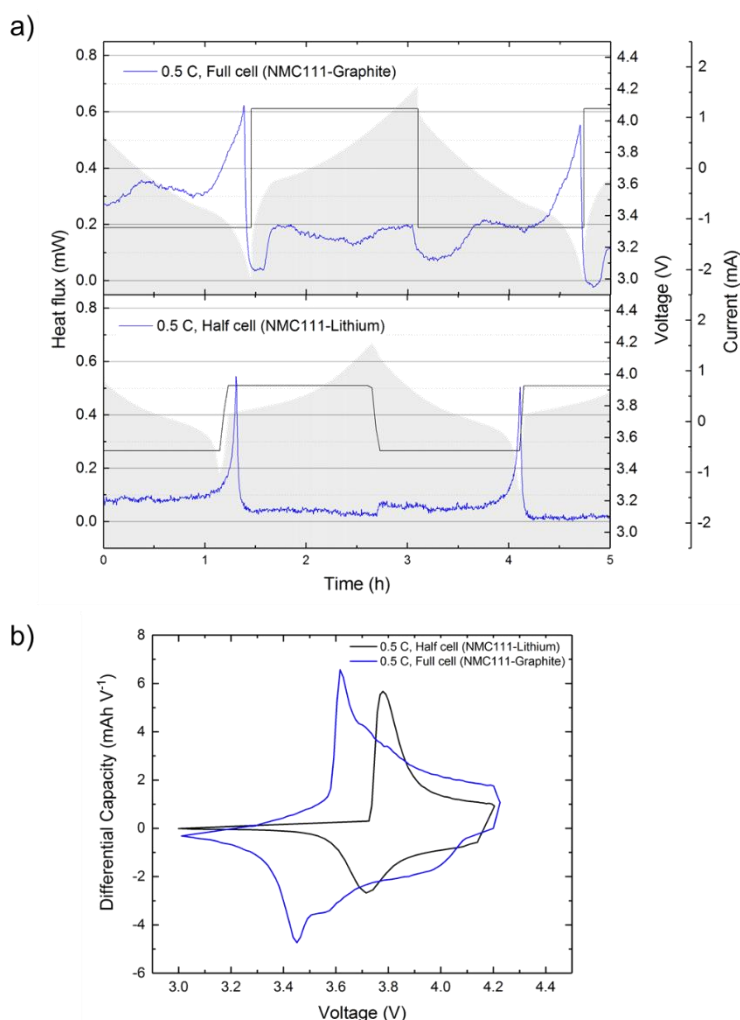
Figure 4.5 (a) Combination heat flux and cycling profiles and (b) differential capacity plot at 0.5 C-rate for an NMC111 vs Graphite and NMC111 vs Lithium cell during the 5th cycle. Data corresponds with Samples 8 and 9 in Table 4.3.

4.3.2.2. Heat generation and phase transition at different C-rates

An NMC111-graphite cell was charged with a C-rate of 0.5 C and 1 C, the results are shown in Figure 4.6 (a). Both cells exhibit the characteristic exothermic and endothermic peaks expected during charging and discharging. The trends of the different curves are similar; however, they differ with the varying current. For both cases, maximum heat is generated at the end of the discharge cycle, where the internal resistances are expected to increase. At 1 C the maximum heat flux is approximately 1.1 mW, while at 0.5 C it is approximately 0.6 mW, almost half. It also appears that the maximum heat flow rates for 1 C and 0.5 C are higher during discharge than during charge. The endothermic peak at the beginning of the charge cycle is a result of the entropy change during the de-intercalation of lithium from the cathode and the following intercalation of the lithium into the graphite. The height of the peak attributed to this phenomenon appears to remain the same as the C-rate varies.

The differential capacity from the two cycling capacities is shown in Figure 4.6 (b). As seen previously in Figure 4.5 (b), the peak at ~ 3.6 V is attributed to lithium intercalation into graphite, $C_6 \rightarrow LiC_x$ and the phase change from hexagonal-I to hexagonal-II (H1 → H2). Upon reducing the C-rate to 0.5 C from 1 C, the peak height decrease and shift towards a higher voltage during charge and a lower voltage during discharge. The shift of the peaks represents the increase in internal resistance at higher C-rates and the depression of the peaks represents the reduction of lithium inventory from the anode and the cathode at higher C-rates. In general, the cells behaved as expected for variations in C-rate. The overall shape and occurrence of the exothermic and endothermic peaks are similar for both C-rates, however, the maximum heat flux for 1 C (at 1.1 mW) is greater than that of the cell at 0.5 C (0.6 mW). There is no direct relation between the phase transition peak and heat generation, thus conclusions regarding the heat effects of phase transitions from these results are based on theoretical assumptions. Since the thermal behaviour is the main focus of this chapter section, the following cells are cycled using 1 C as the reference C-rate as it reduces the time required for large data collection while increasing the overall experimental feasibility.
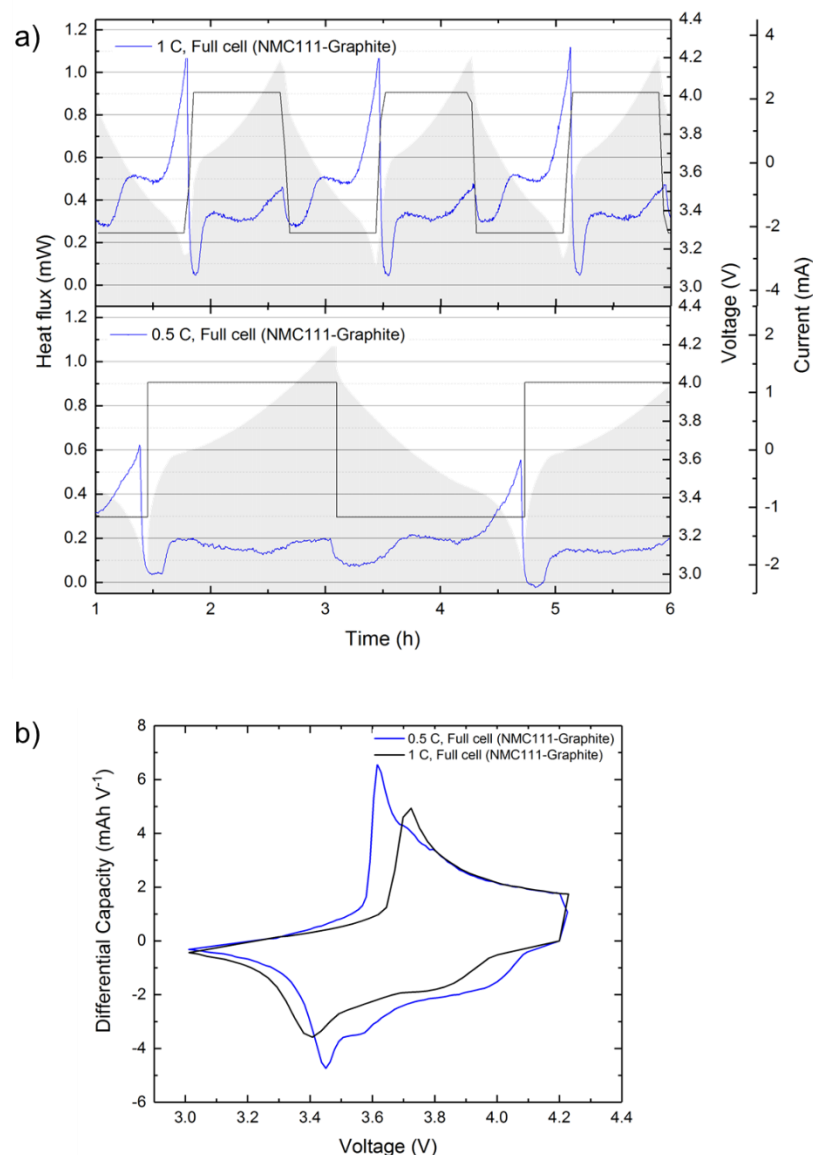
Figure 4.6 (a) Combination heat flux and cycling profiles and (b) differential capacity plot at 0.5 and 1 C-rate for an NMC111 vs Graphite cell. Data corresponds with Sample 9 in Table 4.3.

4.3.3. Thermal behaviour under aggressive cycle conditions

In this section, the effects on the total heat generated when cell operating conditions are varied are investigated using DSC. The materials and methodology used for preparing various coin cell samples are summarised in Table 4.4.

Table 4.4 Summary of coin cell samples with NMC811 cathode intended for the investigation of heat generation under more aggressive testing conditions, whereby variables such as the temperature, C-rates and voltage cut-off windows are adjusted.

Sample / Coin cell number	11 - 19
Positive electrode	90 wt % Li(Ni$_{0.8}$Mn$_{0.1}$Co$_{0.1}$)O$_2$ (NMC811, NEI), 15mm, 9.77 mg/cm^2
Negative electrode	92 wt % Graphite (NEI), 16 mm, 6.75 mg/cm^2
Separator	Polypropylene–polyethylene–polypropylene (Celgard 2325, Celgard, LLC.), 18mm
Electrolyte	1 M LiPF$_6$ in EC:DEC 1:1 v/v (Soulbrain MI), 60 µL
Measured capacity (mAh)	~ 3.5 mAh
Testing mode and temperature	Isothermal, 30 - 60 °C*
Operating voltage	3.0 – 4.3 V*
Cycling protocol	Formation: 2 cycles at C/20, followed by 10 cycles at 0.1 C*

*Varied for different tests

The heat generation during cell cycling under aggressive test conditions was evaluated by independently studying the following variables: temperature, cycling current and upper voltage cut-off. The three variables were studied independently as summarised in Table 4.5. The cells consisted of an NMC811 cathode (NEI Corporation) and a Graphite anode (NEI Corporation). The operating potential window was between 3.0 – 4 .3 V.

Table 4.5 Summary of the tests in this present section (heat generation during cycling).

Variable	Temperature / °C	C-rate / h^{-1}	Voltage upper limit / V
Temperature	30 40 50 60	1 C	4.3
C-rate	30	0.2 C 0.5 C 1 C	4.3
Voltage upper limit	30	1 C	4.1 4.2 4.3 4.4 4.5

4.3.3.1. Correlation between heat flux and various temperatures

The heat flux rates measured in the DSC during cycling at different temperatures (30, 40, 50, and 60 °C) are shown in Figure 4.7. At the beginning of charging, observed for all four temperatures, a small endotherm is visible. This endotherm has been previously reported in earlier studies[210] and can be described by the entropy change during the early stages of the de-intercalation of lithium from the cathode and to the intercalation of lithium in the anode. The rest of the charge and discharge periods, respectively, are as expected showing characteristic exothermic and endothermic peaks. Changes in the heat flux rate sign are a consequence of changes to the value of entropy during charge and discharge. The tests were repeated for further two identical samples.
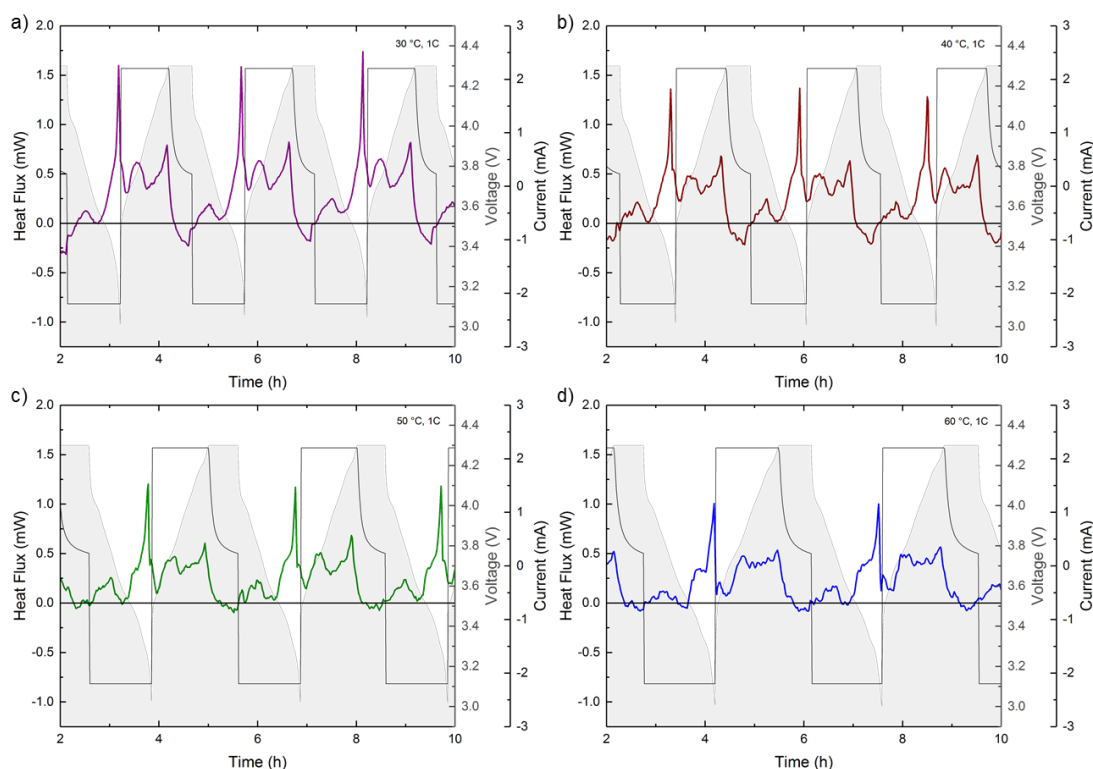
Figure 4.7 Combination heat flux and cycling (current and voltage) profiles for NMC811 vs Graphite cell, from a - d: at 30, 40, 50, and 60 °C. Data corresponds with Sample 11 in Table 4.4.

The total average heat flux rate taken for three samples tested identically and their uncertainties are shown in Figure 4.8. While the effects of SOC on the heat flux rate during charging are small, the greatest values in heat flux appear for discharge rates greater than 85 %. The maximum values

of the heat flux rates measured and calculated from three identical samples and tests for all SOCs and depths of discharge (DODs) are listed in Table 4.6.
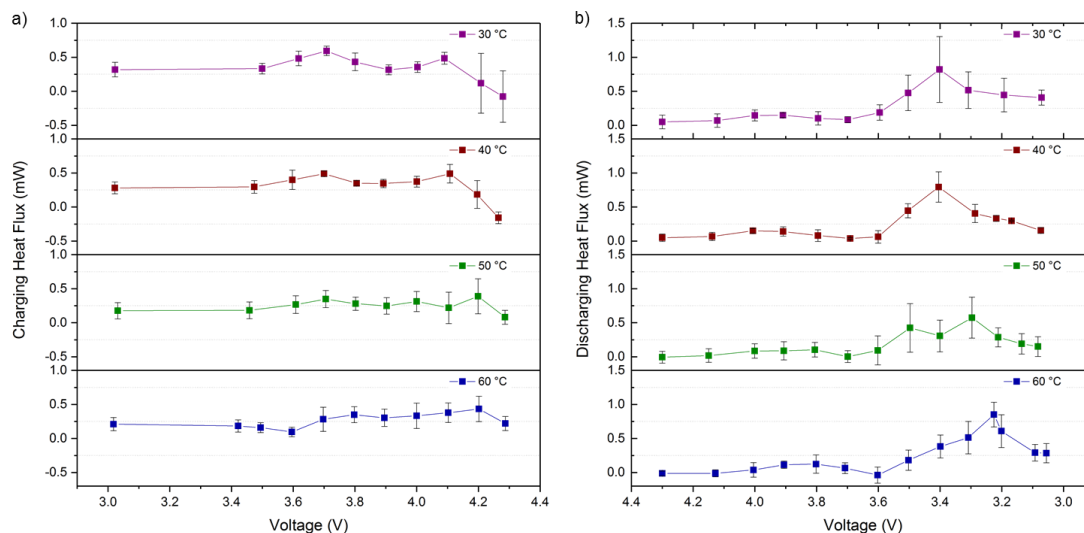
Figure 4.8 The total irreversible heat flow rates during (a) charge and (b) discharge with various temperatures versus voltage. Data is averaged for three identical cells which correspond to Samples 11 - 13 in Table 4.4.

Table 4.6 The maximum heat flux rate (mW) for charge and discharge at different temperatures.

	Temperature / °C			
	30	40	50	60
Maximum heat flux during charge (mW)	0.59 ± 0.1	0.49 ± 0.1	0.39 ± 0.3	0.43 ± 0.2
Maximum heat flux during discharge (mW)	0.82 ± 0.5	0.79 ± 0.2	0.57 ± 0.3	0.85 ± 0.2

The discharge behaviour of the coin cells for the four temperatures is shown in Figure 4.9 (a). The nominal capacity is 3.88 mAh, and the discharge capacity for 30, 40, 50, and 60 °C is increased to 3.89, 4.09, 4.62 and 5.11 mAh, respectively. To see the effects of temperature on the stability of the material, a differential capacity plot for the lithiation and de-lithiation of the NMC811-graphite coin cell in the 5th cycle is shown in Figure 4.9 (b). Four peaks are occurring during charge at 3.4, 3.8, ~ 3.95 and ~ 4.15 V, as expected for the lithium interaction into graphite, the second for the phase transition from a hexagonal to a monoclinic lattice (H1 → M) of the NMC, the third for the M → H2 phase transition and the last for H2 → H3. As the temperature increases, the peaks appear at the same voltages, however, become more pronounced.

The peak height at ~ 3.25 V during discharge increased with increasing temperature from 30 to 60 °C, indicating a kinetic hindrance to lithium diffusion[214]. The peaks at ~ 3.25 V and 4.2 V show the strongest dependence on temperature (becoming more pronounced at higher temperatures). This may suggest that the diffusion of lithium is slow at these states of charge. It is expected that the intercalation of lithium into the NMC cathode is limited by the number of available divacancies as per Van de Ven's divacancy model[215]. The peak is attributed to the phase change from H2 to H1[213], it is expected that the H1 phase is one whereby the state of vacancies is less ordered, and therefore exhibits a greater degree of a kinetic hindrance. The discharge process exhibited a larger maximum value for the total heat generated as shown in Table 4.6. Furthermore, the greatest heat flux values measured during discharge in Figure 4.8 (b) occur within the 3.2 – 3.4 V range. An increase in the differential capacity peak height is expected to represent a decrease in internal resistances and a drop in cell capacity[216]. However, while the peak heights increase with temperature, the cell discharge capacity increases. The impedance spectra in Figure 4.9 (c) show that the Ohmic resistance (defined by the intersection of the curve with the real Z'-axis at Z'' = 0 Ohm, or 'A' in Figure 4.9 (d)) also did not follow a clear trend. It increased from 15.00 to 19.22 Ohm for 30 to 40 °C, respectively, but reduced to 11.00 Ohm for temperatures 50 and 60 °C. The variation corresponds to a fairly large change of 75 %, which can largely be attributed to the system set-up: the contact resistance between the holder and the coin cell and/or the resistances in the Cu wire connections between the cycler and the calorimeter, which are backed by the series resistance increasing at higher temperatures. At temperatures greater than 50 °, a mild decomposition of the SEI layer may have begun. The material composition for the tests conducted at 60 °C may have been different to those at lower temperatures. This would also have an impact on the impedance behaviour.

The data was fitted using the equivalent circuit model described in Figure 4.1, the results of which are shown in Figure 4.9 (d), where 'B' and 'C' represent the charge transfer resistance occurring at the interface and active materials, respectively. The low-frequency tail is defined by 'C' and represents

the diffusion resistance. As expected, for the increase in temperature from 30 to 60 °C, the second arc in the impedance spectra became smaller. Higher temperatures are expected to limit the rate of migration of lithium through the bulk of the active electrode material[216]. The higher charge transfer resistances seem to have no direct correlation with the measured maximum irreversible heat generation values in Table 4.6. However, the higher peaks at ~ 3.25 V in the differential capacity diagram suggest there may have been decreases in the diffusion resistance. This correlates with Figure 4.9 (d), where the diffusion resistance decreases as the temperature increases. Furthermore, the peaks may be correlated with the maximum heat flux values measured during discharge in Figure 4.8 (b) which occurred in the 3.2 to 3.4 V range. The offset in the voltage region may suggest there is a delay in the propagation of the heat generation and the presence of a measurable difference.
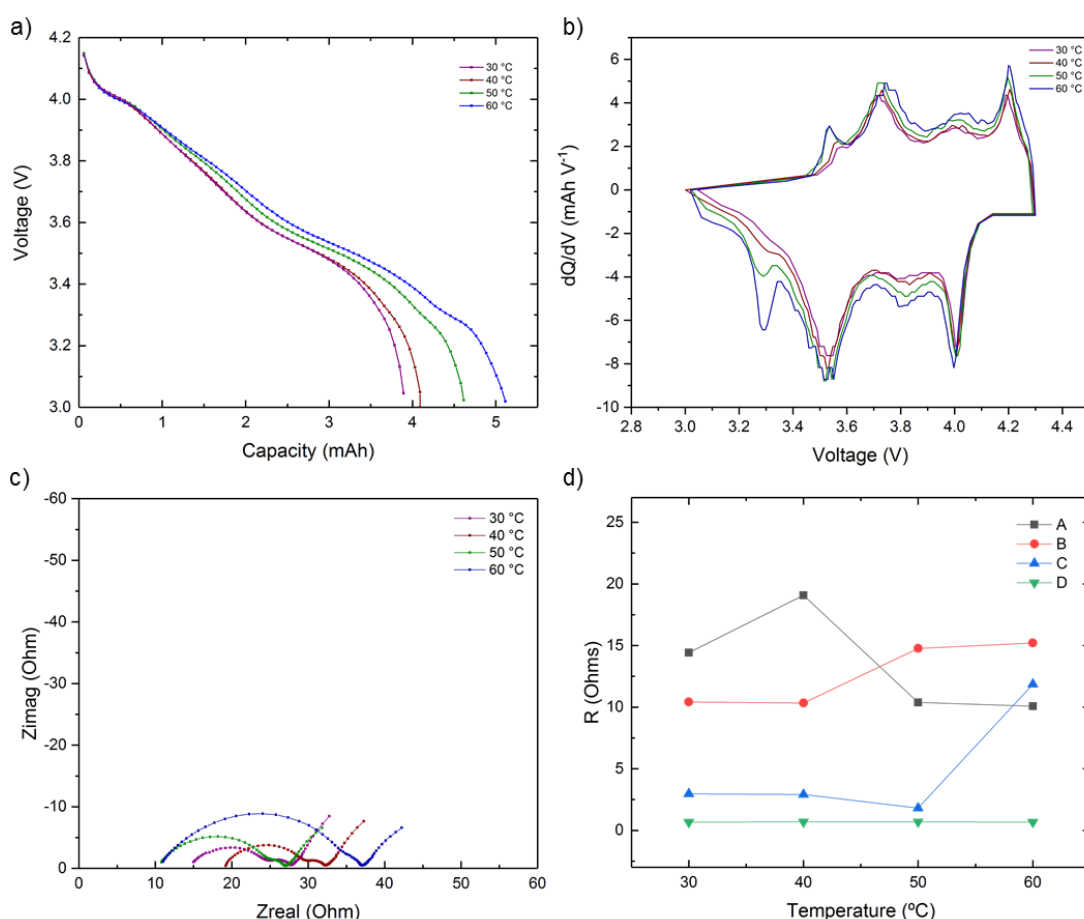
Figure 4.9 (a) Voltage as a function of the discharge capacity, (b) differential capacity for the 5th cycle, (c) impedance spectra with 1 C rate, and (d) ohmic (A), charge transfer at the interface (B) & active material (C), and diffusion (D) impedances for

four temperatures: 30, 40, 50, and 60 °C. Data corresponds with Sample 11 in Table 4.4.

4.3.3.2.   Correlation between heat flux and various C-rates

Similar to the correlation between heat flux and various temperatures in the previous section, the heat flux rates measured in the DSC during cycling at different C-rates (0.5, 1 and 2 C) are shown in Figure 4.10. In all cases, at the beginning of the charge, a small endothermic effect is visible followed by a larger exothermic event towards the end of discharge. Changes in the heat flux rate sign are a consequence of changes to the value of entropy during charge and discharge. The tests were repeated for two further samples.
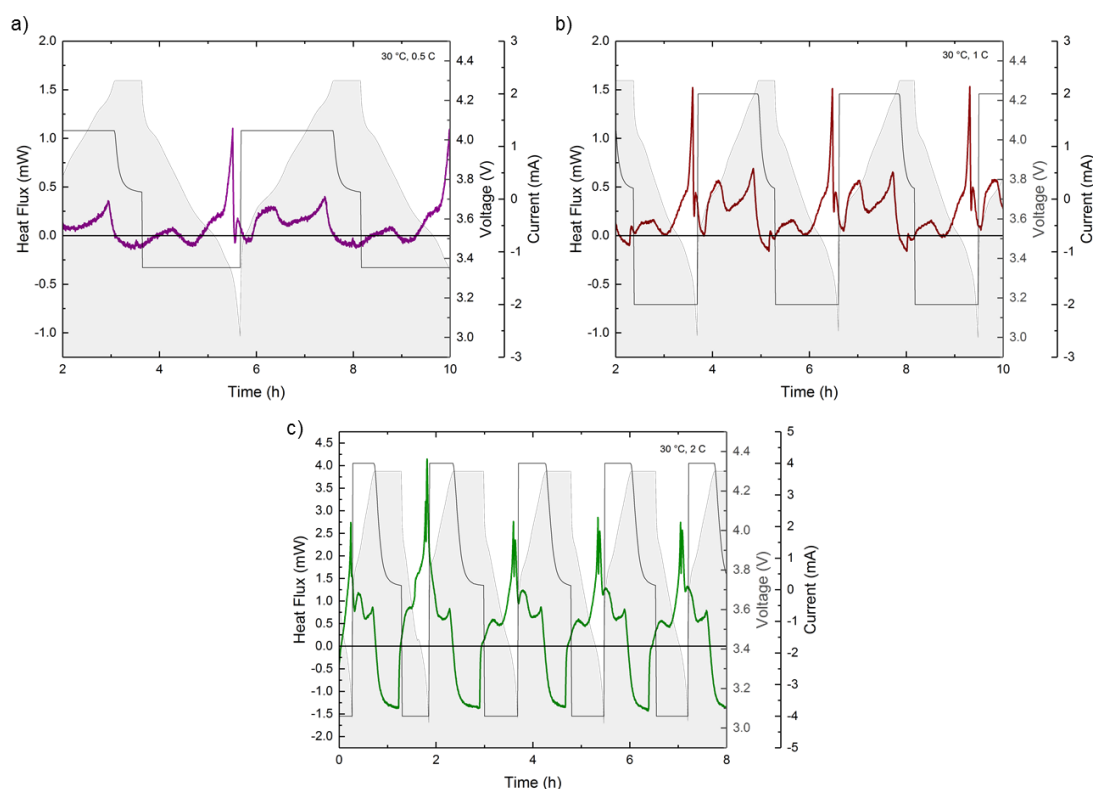
Figure 4.10 Combination heat flux and cycling (current and voltage) profiles for NMC811 vs Graphite cell, from left to right at: 0.5, 1 and 2 C. Data corresponds with Sample 14 in Table 4.4.

The total average heat flux rate during charge and discharge for three samples tested identically and their uncertainties are shown in Figure 4.11. The maximum values of the measured heat flux rates calculated from three identical samples and tests for all SOCs and DODs are listed in Table 4.7. The measured values of the generated heat flux increase at higher current

densities (in a non-linear way). The heat flux rate at 2 C is significantly larger than at C-rates 0.5 and 1 C, respectively.
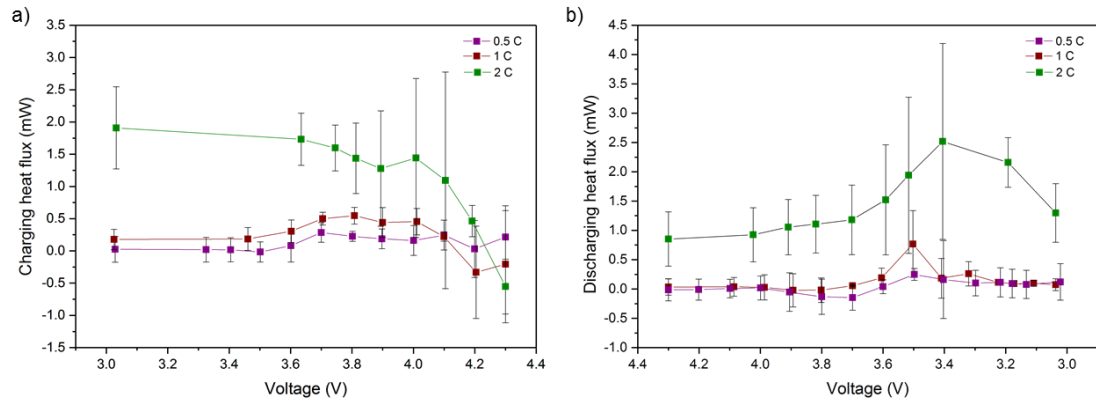
Figure 4.11 The total irreversible heat flow rates during (a) charge and (b) discharge with various C-rates versus voltage. Data is averaged for three identical cells which correspond to samples 14 - 16 in Table 4.4.

Table 4.7 The measured maximum heat flow rate, total heat generation and calculated impedance during cycling with various C-rates.

	C-rate		
	0.5 C	1 C	2 C
Maximum heat flux during charge (mW)	0.28 ± 0.2	0.54 ± 0.1	1.91 ± 0.6
Maximum heat flux during discharge (mW)	0.25 ± 0.1	0.77 ± 0.6	2.52 ± 1.7

The heat generation values are different for charging and discharging. The values for 0.5 and 1 C follow a similar trend, for example in Figure 4.11, there is a local maximum at approximately 3.7 V and a local minimum of 4.2 V during charging, and for discharging, there is a local maximum of 3.5 V. The values for 2 C although quite similar in trend, suggest that there may be a delay in the heat generation. For example during a charge, the minimum value occurs at 4.3 V (at the end of charge), and during discharge, the maximum value is recorded at a greater DOD, at 3.4 V (as opposed to 3.5 V, for 0.5 and 1 C, respectively). Furthermore, at C-rates 1 and 2 C, the maximum measured heat generation during discharge is greater in value (Table 4.7). Overall, the trends observed are similar to those reported in the literature whereby the highest heat generation during charge is expected at 50 % SOC and between 60 – 70 % DOD during discharge[211]. The complex dependence of charge

transfer and diffusion resistances on the SOC of the cell and the C-rate, respectively, may be correlated to the trends observed in the heat flux measurements.
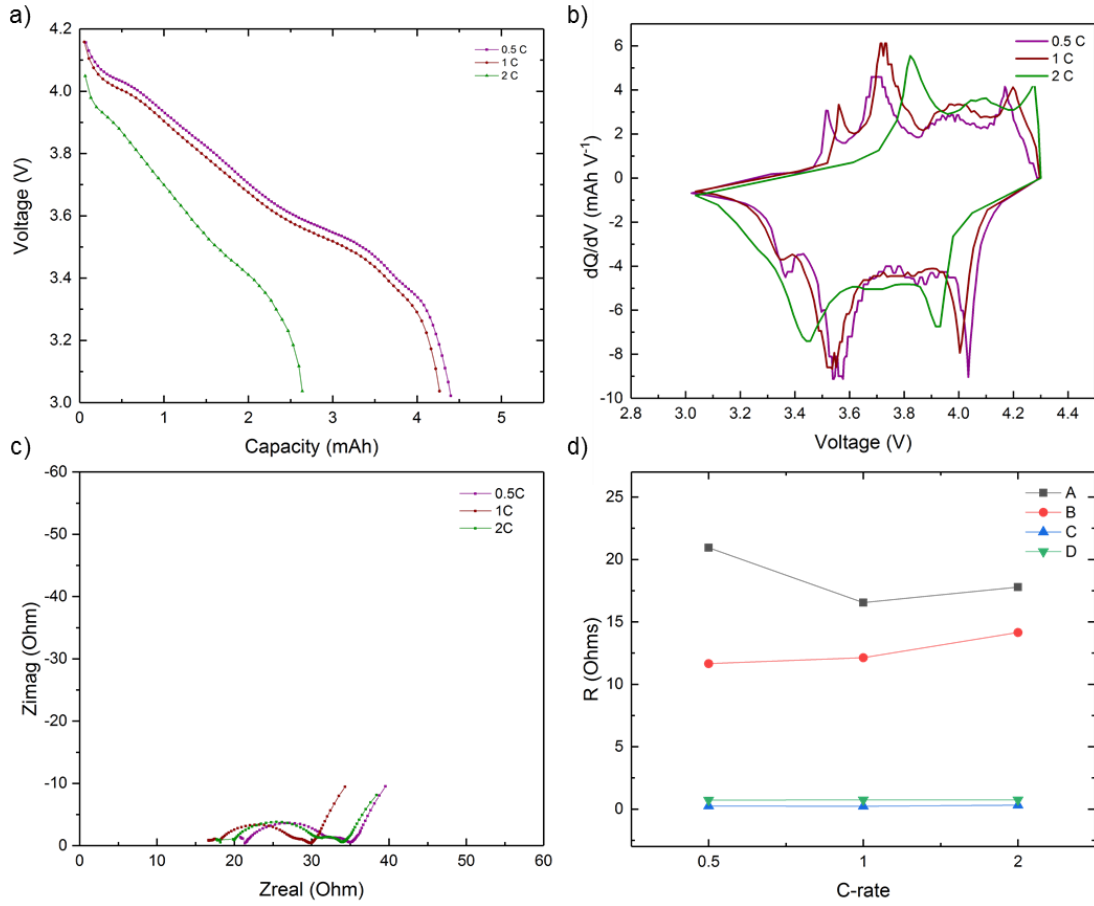
Figure 4.12 (a) Voltage as a function of the discharge capacity, (b) differential capacity for the 5th cycle, (c) impedance spectra with 1 C rate, and (d) ohmic, charge transfer, and diffusion impedances for three C-rates: 0.5, 1 and 2 C. Data corresponds with Sample 14 in Table 4.4.

The discharge behaviour of the cell for the three discharge rates shown in Figure 4.12 (a) shows that the nominal capacity was 4.16 mAh for 0.5, reduced to 4.05 mAh for 1 C and even further to 2.64 mAh for 2 C. The differential capacity in Figure 4.12 (b) features for 0.5 and 1 C were comparable (like the observation in their heat generation values), however a shift in the voltage range within which the peaks occur is present, and the peak height is significantly lower for the discharge at 2 C. For example, the initial peak during the charge for the lithium interaction into graphite occurs at 3.52 V for 0.5 C and 3.58 V for 1 C. However, the peak attributed to the same event occurs at 3.82 V for 2 C. The impedance spectra in Figure 4.12 (c) for the three

C-rates don't show an obvious trend regarding the pure Ohmic resistance (defined by the intersection of the experimental curve with the real Z axis), however, they all have similar patterns. After fitting the curves, the resistances from charge transfer and diffusion are separated and shown in Figure 4.12 (d). The charge transfer resistance, 'B', increases with higher current densities, similarly, the diffusion resistance, 'C', exhibits the same trend but at a lower degree. Zhao et al. report that at higher C-rates, the heat effects from charge transfer resistance tend to dominate (as opposed to diffusion resistances which dominate at lower C-rates)[211]. The values measured for heat generation correlate with the trends observed in the impedance spectra; values for heat generation increase with higher current densities due to greater charge transfer and diffusion impedance.

4.3.3.3. Correlation between heat flux and various upper cut-off voltages

The correlation between heat generation and various cut-off voltages is analysed by measuring the heat flux rates in the DSC during cycling up to cut-off voltages, 4.1, 4.2, 4.3, 4.4 and 4.5 V. The results of which are shown in Figure 4.13, for one sample. At the beginning of the charge, a small endothermic effect is visible followed by a larger exothermic event towards the end of discharge. Changes in the heat flux rate sign are a consequence of changes to the value of entropy during charge and discharge. The tests were repeated for two further samples. The maximum peak height at the end of discharge stays relatively similar as the voltage cut-off increases from 4.1 V to 4.5 V, similar to the minimum value for the endotherm that appears shortly after the current increases at the start of charge. At the end of charge, a large exothermic peak occurs, followed by an endotherm during the constant current step of the cycling protocol. The maximum point of the exothermic peak during the end of charge and the minimum point of the endothermic peak during the rest step increase and decrease, respectively, as the voltage cut-off increases from 4.1 V to 4.5 V.
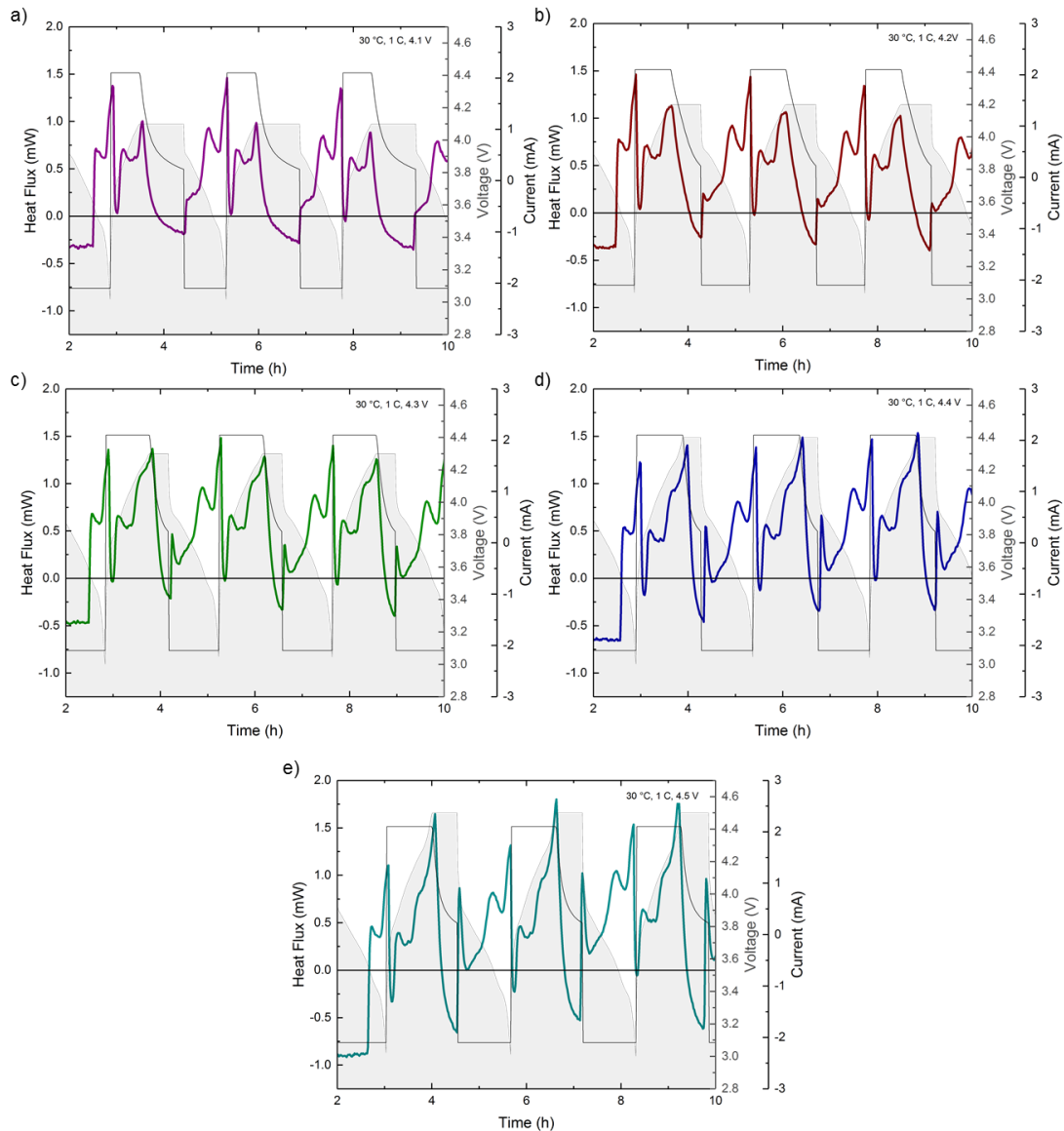
Figure 4.13 Combination heat flux and cycling (current and voltage) profiles for NMC811 vs Graphite cell, from left to right at: 4.1, 4.2, 4.3, 4.4, and, 4.5 V. Data corresponds with Sample 17 in Table 4.4.

The total average heat flux rate during charge and discharge for three samples tested identically and their uncertainties are shown in Figure 4.14. The maximum values of the measured heat flux rates calculated from three identical samples and tests for all SOCs and DODs are listed in Table 4.8. Generally, the measured values of the maximum generated heat flux increase as the cut-off voltage increases, apart from 4.4 V during charge and 4.1 V during discharge. During charge, there is a 50 % increase in the maximum value measured for the heat generated from 4.1 to 4.5 V. Similarly, during discharging, this value increases by 51 % from 4.1 to 4.5 V.
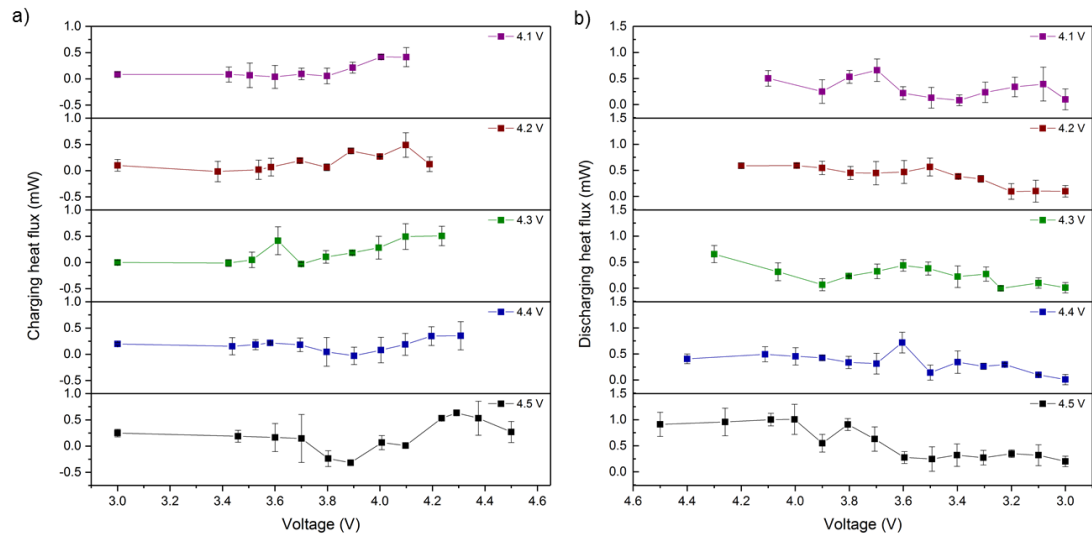
Figure 4.14 The total irreversible heat flow rates during (a) charge and (b) discharge with various cut-off voltages versus voltage. Data is averaged for three identical cells which correspond to Samples 17 - 19 in Table 4.4.

Table 4.8 The measured maximum heat flow rate, total heat generation and calculated impedance during cycling with various cut-off voltages.

	Cut-off voltage (V)				
	4.1	4.2	4.3	4.4	4.5
Maximum heat flux during charge (mW)	0.42 ± 0.1	0.48 ± 0.2	0.51 ± 0.2	0.35 ± 0.3	0.63 ± 0.1
Maximum heat flux during discharge (mW)	0.66 ± 0.2	0.59 ± 0.1	0.65 ± 0.2	0.72 ± 0.2	1.00 ± 0.3

The heat generation values for charging in Figure 4.13 across the five voltage cut-off values range all trend towards an increase in value and show a local maximum towards the end of charge. The trend for discharge, on the other hand, is the opposite as the heat generation values decrease towards the end of discharge. While the heat generation towards the end of discharge in Figure 4.14 (b) shows the lowest value across the whole voltage range, the local maximum appears to vary for each voltage cut-off. For example, in the 4.1 V cut-off range, the maximum appears at 3.7 V (9.5 % DOD), at 3.5 V (16.7 % DOD) in the 4.2 V cut-off range, at 3.8 V (11.6 % DOD) in the 4.3 V cut-off range, at 3.8 V (13.6 % DOD) in the 4.4 V cut-off range, and at 4.0 V (11.1 % DOD) in the 4.5 V cut-off range, respectively. There is no observable trend regarding the maximum heat flux value and the DOD of the cell from Figure

4.14 (b). However, during charge, the maximum heat flux value increases as the voltage cut-off value increases as seen in Figure 4.13. Furthermore, this maximum value appears during the end of charge, at higher SOC, as observed in Figure 4.14 (a).
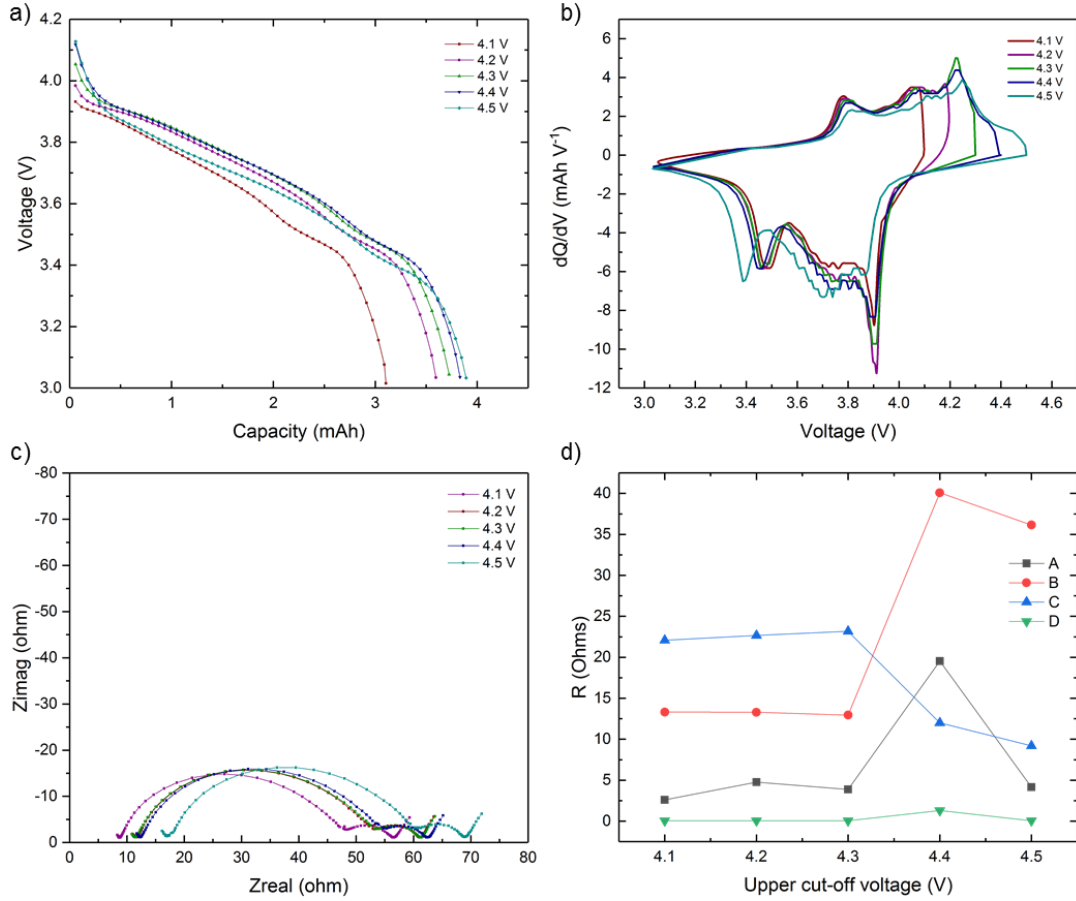
Figure 4.15 (a) Voltage as a function of the discharge capacity, (b) differential capacity for the 5th cycle, (c) impedance spectra with 1 C rate, and (d) ohmic, charge transfer, and diffusion impedances for five cut-off voltages: 4.1, 4.2, 4.3, 4.4, and 4.5 V. Data corresponds with Sample 17 in Table 4.4.

The discharge behaviour of the cells for increasing upper cut-off voltages is shown in Figure 4.15 (a). The nominal capacity decreased with a lower upper cut-off voltage. For 4.5 V, the discharge capacity was 3.89 mAh, this was reduced by 20 % to 3.11 mAh for a smaller cycling window with a cut-off voltage of 4.1 V. The differential capacity in Figure 4.15 (b) features for upper cut-off voltages 4.1 – 4.4 V were comparable in terms of the number and position of peaks observed between 3.0 V to 4.0 V. The discharge peak occurring at 3.9 V however, decreased in height as the cut-off voltage value increased. This is assumed to be due to the portion of lithium inventory that

remains trapped in the cathode at higher voltages[53][214]. The small exothermic peak at the beginning of discharge in Figure 4.13 shows that the peak height value increases as the upper cut-off voltage increases. The loss of active material that is occurring may be due to degradation by a number of mechanisms: structural disordering or the growth of the SEI layer as the voltage window reduces. Correlating the mechanisms to the heat flux suggest that these mechanisms influence heat generation. Furthermore, the discharge peaks for the upper cut-off voltage of 4.5 V have shifted to a lower voltage range, suggesting greater degradation, such as electrode decomposition or oxidation of the electrolyte. The impedance spectra (Figure 4.15 (c)) for the five upper cut-off voltages appear the same but with a gradual shift from lower to higher Ohmic resistance values (where the curve intersects with the real Z axis) as the voltage range increases. After fitting the curves, the resistances from charge transfer and diffusion are separated and shown in Figure 4.15 (d). For charge transfer resistance, 'B', the values for 4.4 V and 4.5 V increase by more than double of those between 4.1 – 4.3 V. The diffusion resistance on the other hand, decreases by almost a half for 4.4 V and 4.5 V compared to 4.1 – 4.3 V. This correlates with the differential capacity features and degradation mechanisms expected to occur at higher voltages.

4.3.3.4.   Total heat effect measured by DSC during cycling

The total amount of heat generated measured in the calorimeter was calculated for all three variables: temperature, cycling current and maximum cut-off voltage. The heat generation during the charge and discharge processes was calculated by the integration of the measured heat flux rate over time. Since the experiments were repeated thrice for each variable, the data was averaged and is presented in Figure 4.16 where the standard deviation is represented by error bars. The sample cells were prepared with good reproducibility - assembled with materials from the same manufactured batch, on the same day, left in storage and to dry under the same conditions, and cycled using the same equipment and protocols – giving similar capacities. However, some random errors produced from electrode alignment, cell contact resistance, and handling should be considered when assessing the validity of the presented results.
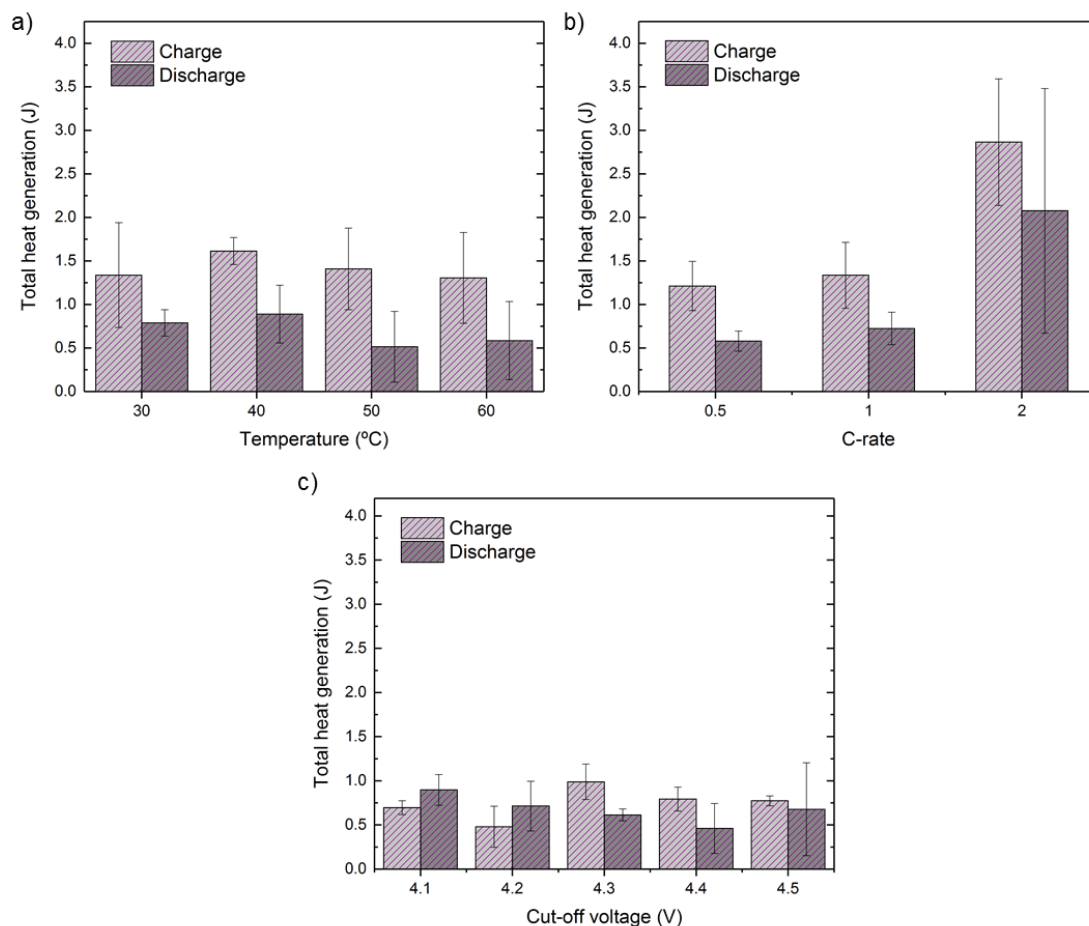
Figure 4.16 Measured total heat generation during charge and discharge for (a) temperatures: 30, 40, 50, and 60 °C, (b) C-rates: 0.5, 1 and 2 C, and (c) cut-off voltages: 4.1, 4.2, 4.3, 4.4, and 4.5 V. Data corresponds with Samples 11 - 19 in Table 4.4.

Figure 4.16 (a) shows the averaged total heat generation during the charge and discharge at each temperature, where the error bars represent the standard deviation. The heat generation of the cell varies at different temperatures for both charge and discharge. During charge, the heat generation at higher temperatures is higher and during discharge, this trend is the same. The main causes for these phenomena are attributed to the changes in internal resistance. As temperatures increase, overpotentials become smaller and less heat is generated. Table 4.9 summarises the total calculated average heat generation values as well as the values separately during charge and discharge. The total heat generated during charge and discharge at 60 °C was nearly 10 % less than that at 30 °C.

Table 4.9 Averaged total heat generation during cycling with various temperatures.

Temperature (°C)	30	40	50	60
Heat generation during charge, Q (J)	1.34 ± 0.5	1.61 ± 0.1	1.41 ± 0.4	1.30 ± 0.4
Heat generation during discharge, Q (J)	0.79 ± 0.1	0.89 ± 0.3	0.51 ± 0.3	0.58 ± 0.4
Total Q (J)	2.1 ± 0.5	2.5 ± 0.5	1.9 ± 0.9	1.9 ± 1.0

Similarly, Figure 4.16 (b) shows the averaged total heat generation at different C-rates. During both charge and discharge, the heat generation increases at greater C-rates. As the C-rate increases, the electrical energy entering and exiting the system as it charges and discharges decreases as a result of the increased overpotentials[217], conversely the irreversible heat increases causing the increase in overall heat generation. Hu et al. further suggest that some of the heat loss at higher C-rates is the proportion of electrical energy lost due to conversion to waste heat[217]. Table 4.10 summarises the total calculated average heat generation values as well as the values separately during charge and discharge. The total heat generated during charge and discharge at 2 C was nearly 175 % greater than that at 0.5 C.

Table 4.10 Averaged total heat generation during cycling with various C-rates.

C-rate:	0.5	1	2
Heat generation during charge, Q (J)	1.21 ± 0.3	1.33 ± 0.4	2.86 ± 0.7
Heat generation during discharge, Q (J)	0.57 ± 0.1	0.72 ± 0.2	2.07 ± 1.4
Total Q (J)	1.79 ± 0.3	2.06 ± 0.5	4.94 ± 1.7

The averaged total heat generation at different upper cut-off voltages for charge and discharge is shown in Figure 4.16 (c). The heat generation for cut-off voltages 4.1 V and 4.2 V during charging are greater than for those equal to or greater than 4.3 V, similarly, the heat generation during discharging is greater at cut-off voltages lower than 4.3 V. The increase in charge transfer resistance impedance with upper cut-off voltage is proportional to the increase in active material loss. Li et al. observed similar effects, where cells tested between 3.0 – 4.3 V showed the greatest loss of lithium inventory (compared

to 3.0 – 4.0 V, 3.0 – 4.1 V and 3.0 – 4.2 V) and suggested that a positive-negative electrode interaction becomes active above 4.2 V[214]. Table 4.11 summarises the total calculated average heat generation values as well as the values separately during charge and discharge. The total heat generated during charge and discharge between 3.0 – 4.5 V was nearly 190 % greater than that between 3.0 – 4.1 V.

Table 4.11 Averaged total heat generation during cycling with various upper cut-off voltages.

Upper cut-off voltage (V):	4.1	4.2	4.3	4.4	4.5
Heat generation during charge, Q (J)	0.66 ± 0.2	0.89 ± 0.5	1.49 ± 0.1	1.84 ± 0.2	2.40 ± 0.3
Heat generation during discharge, Q (J)	0.50 ± 0.4	0.67 ± 0.5	0.94 ± 0.3	1.07 ± 0.3	1.00 ± 0.8
Total Q (J)	1.17 ± 0.5	1.57 ± 1.1	2.43 ± 0.5	2.90 ± 0.4	3.40 ± 0.8

Overall, there is greater heat generation measured during charge than discharge, with the exception being cycling at smaller voltage ranges 3.0 – 4.1 V and 3.0 – 4.2 V which generate greater heat during discharge than charge. Values for a temperature of 30 °C, C-rate of 1 C and an upper cut-off voltage of 4.3 V across Figure 4.16 (a – c) all lie within the same range for the three datasets. It can be concluded that cycling at a lower temperature and higher C-rate will increase the amount of irreversible heat generation within a LIB, and that generally, a high C-rate and large upper cut-off voltage will have the greatest impact on heat generation during cycling.

4.4. Conclusions from Chapter 4

Multiple modes of degradation exist for lithium-ion battery components during thermal runaway. The most characteristic behaviour is the generation of heat and gas as it undergoes thermal failure. For example, the decomposition of the SEI layer at high temperatures can onset a series of exothermic reactions. In this chapter, preliminary thermal decomposition tests revealed the viability of coin-cell DSC to investigate the thermal decomposition of the cathode and electrolyte in working coin cells – more traditional DSC

systems while effective for thermal property measurements, measure materials (often powders) sealed inside a stainless-steel capsule, which are useful for new material characterisation, for example, but less useful for understanding how the material might behave in its operational environment. The results presented in this chapter provide a good, reproducible baseline for future tests of a similar manner, where variables such as changing the electrolyte composition or electrode chemistries can be tuned to measure their thermal effects.

Separately from thermal failure (operation above 80 °C), the LIB exhibits characteristic thermal behaviours during charge and discharge cycles. LIBs have inherent irreversible heat effects such as those arising from Ohmic, kinetic/activation and diffusion/mass transport resistances. Adding to the results above, the next set of tests established the capability of the novel-DSC coin cell calorimeter to directly measure the heat effects as cells were charged and discharged. Furthermore, since operating parameters such as temperature, capacity or voltage are intrinsically linked to heat generation, these parameters were tuned to produce more aggressive conditions such as high temperatures, to investigate their influence on total heat generation. In these findings, operating the cells at a lower temperature improved mass transport and reduced internal cell resistance, this was reflected in the EIS analyses as well as in the measured overall heat generation. As a result, an optimum cycling temperature can be established, one which improves cycle life and hinders material degradation mechanisms that are linked to temperature. This is extended to the further two variables investigated in this chapter (C-rate and maximum upper cut-off voltage).

Overall, this chapter has demonstrated the complexity of the thermal behaviour of LIBs. Both under normal, and aggressive operating conditions, understanding and measuring heat generation is crucial for complete battery safety assessment, owing to the LIBs' characteristic failure behaviour (thermal runaway). This chapter successfully established a method by which a novel coin-cell DSC can be used to test multiple samples, under various conditions, that are easily reproducible.

Chapter 5

5. Multi-scale Imaging

Sections of this work have been peer-reviewed and published in Johnson Matthey Technology Review (D. Patel, H. T. Reid, S. Ball, D. J. L. Brett, P. R. Shearing, *X-ray Computed Tomography for Failure Mechanism Characterisation within Layered Pouch Cells. (2022).*
doi:10.1595/205651322X16595441894422.

5.1. Introduction

The importance of assessing battery safety across multiple scales has been established[9]. Lab-based and synchrotron X-ray, 3D X-ray CT, SEM and FIB-SEM have all been demonstrated to be useful tools for characterising LIB batteries and their materials. This chapter begins to demonstrate the methods by which these techniques can be optimised firstly for imaging batteries of obscure dimensions (i.e. single layer pouch cells with a high aspect ratio and/or non-symmetrical cells), and for cathode material microstructures at resolutions high enough to elucidate primary and secondary particle morphologies. Lastly, a diagnostic method by which cells and their components can be imaged to understand failure mechanisms using two techniques: high-throughput non-invasive ROI scans and invasive (upon cell disassembly) electrode material scans is introduced and demonstrated. The benefits of each type of multi-scale imaging for LIB safety research and battery manufacturers alike are also discussed.

5.2. Single-layer pouch cells

In-situ and operando experiments have been performed on commercial cells with different geometries such as the 18650 cell[130] and pouch cells[191], however, their large sizes often limit the achievable spatial resolution or reconstruction quality. Often internal tomography scans mean only a small part of the cell is measured, reducing the overall

representativeness of the data[164]. Thus, investigations of LIB material microstructures often require controlled, and often significantly limited geometries to achieve the desired resolutions. In this section, X-ray CT imaging of single-layer pouch cell geometries (thin and wide) is analysed using the high aspect ratio (HART) capability of lab-based X-ray micro-CT equipment. Unlike normal tomography, which uses evenly distributed projections along the rotation angles, HART enables higher angular density projections for long views, while preserving the total number of projections taken. Any features that may be obscured due to the low signal-to-noise ratio and streak artefacts with normal tomography are subsequently reduced.

5.2.1. Samples and materials

For this analysis, three single-layer pouch cells of different sizes are imaged using the Zeiss Xradia 620 Versa X-ray micro-CT instrument (Carl Zeiss XRM, Pleasanton, CA, USA). Each sample consists of two single-sided electrodes: cathode and anode. The cathode material varies for each, however, the anode material (graphite) is the same but from different manufacturers with varying thicknesses. Table 5.1 summarises the key details of each sample.

Table 5.1 A summary of the manufacturers, materials, sizes, and capacities for the three single-layer pouch cell samples.

Sample	Manufacturer	Cathode material	Cathode tape thickness (μm)	Sample size, l x h (mm)	Capacity (mAh)
1	NEI	NMC111	75	55 x 100	26.5
2	Targray/QinetiQ	NMC811	80	57 x 110	90
3 a				65 x 95	
3 b	Johnson Matthey/Targray	$LiNi_wCo_xAl_yO_z$ (NCA)	30	Diameter: ~ 400 μm	N/A
3 c				Diameter: ~ 45 μm	

5.2.2. Single-layer pouch cell size and image optimisation

Given the trade-off that exists between sample size, field-of-view and achievable spatial resolution, and the numerous possible configurations of the X-ray CT technique, it is particularly important to optimise the sample size and its alignment. In general, for fixed-energy lab-based X-ray CT, the transmission required for high contrast and low noise images is challenging to obtain for battery materials that exhibit combinations of low- and highly attenuating materials[218]. Reiter et al. calculated the theoretical maximum transmission to be approximately 14 %, based on the Beer-Lambert Law rearranged and given in Equation 5.1; where I_0 is the initial radiation intensity, and I_p is the primary intensity after an absorption (defined by a linear attenuation coefficient, μ and penetration distance, d). A high contrast and low noise image, or a high contrast to noise ratio (CNR) for an ideal CCD detector, where the photon noise, σ is equal to square root of I_p, reaches its theoretical maximum when the first derivative of the CNR with respect to μ is zero.

$$\frac{I_p}{I_0} = e^{-\mu(E) \cdot d} = e^{-2} \approx 0.14$$

Equation 5.1

Since the penetration distance is the length at which the intensity of the beam after absorption falls to 1/e of the incident beam, the optimum sample thickness at which the ideal transmission is ~ 14 % can be determined for various battery materials and photon energies (of X-ray imaging instrument). This is, however, assuming that the materials are solid and uniform in shape which is rarely the case for whole cells and/or electrode materials which are often porous in nature. Furthermore, how interior tomography artefacts, the sample being larger than the field-of-view, insufficient angular projections, and/or exposure times that may affect the pixel intensity affect the overall CNR should also be considered when attempting to image batteries.

For high aspect ratio samples (non-cylindrical geometry), such as a single layer pouch cell, the transmission will vary as the samples rotate 360 °, and/or between the long (cell is parallel to the beam) and short view (cell is perpendicular to the beam) as illustrated in Figure 5.1. In the short view, the

transmission will be greater than the transmission in the long view. As a result, the sample, in this case, a single-layer pouch cell, should be shorter in length and longer in height to keep the average transmission (taken at 45 °) as close to the theoretical ideal transmission of 14 %. The HART feature of the Zeiss Xradia 620 Versa X-ray micro-CT instrument modifies the angular speed of the sample stage to achieve variable angle scans. In the long view, the angular density increases to the full strength; where the strength is calculated by dividing the transmission of the short view by the long view.
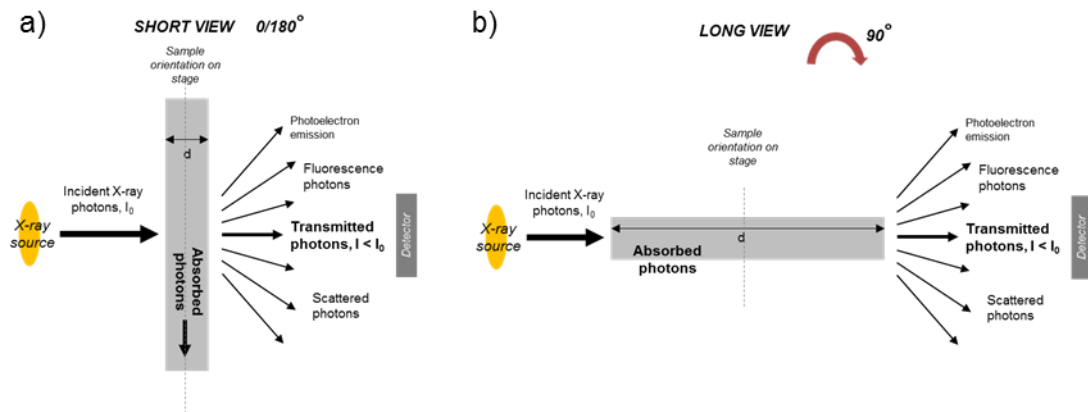
Figure 5.1 Incident beam through a high-aspect ratio sample, for example, single layer pouch cell (thin and wide). As the cell sample rotates it will be (a) perpendicular to the beam, i.e. in the short view, and (b) parallel to the beam, i.e. in the long view during X-ray CT image acquisition.

For all three samples, the most important variable investigated was the length of the cell. The shorter the length of the cell, the smaller the maximum source-sample and sample-detector distance. As a result, the pixel intensity can remain sufficiently high as the exposure time is reduced. In the short view, it is important to find a sufficiently low exposure time, as the number of counts through the width of the single-layer cell would be higher when perpendicular to the beam, resulting in a reduced signal-to-noise ratio. Additionally, as the sample will be larger than the field-of-view (e.g. for a 4 X objective lens with an approximate 3 - 4 mm field-of-view) when in the short view compared to when in the long view, which may reduce the signal-to-noise ratio and increase the likelihood of artefacts.

Table 5.2 summarises the scanning parameters used for the three single-layer pouch cell samples and the spatial resolutions achieved for each. The number of projections and camera binning was kept the same for all

samples, however, the exposure times were adjusted for the variations in sample length. The spatial resolutions achieved for each sample ranged between 1.72 – 1.86 µm for varying exposure times. In this instance, the shorter the sample length, for example for sample 1, at 55 mm, the shorter the source-to-sample and sample-to-distance lengths, and consequently, the shorter the exposure time required for an adequate transmission and therefore, better spatial resolution (1.72 µm).

Table 5.2 The scanning parameters used and achieved voxel sizes for each single layer pouch cell sample investigated.

Sample	Beam energy (kV)	Exposure time (s)	No. of projections	Camera binning	Voxel size (µm)
1	110	10	2801	1	1.8
2	110	15	2801	1	1.86
3	110	18	1601	1	1.72

A volume rendering of sample 1 and orthoslices and volume renderings of sample 3 is shown in Figure 5.2. Images of sample 2 can be found in Figure 10.1 in Chapter 10 . For a thin and wide, non-cylindrical LIB sample, this interior tomography successfully captures useful battery material characteristics: electrode thickness, manufacturing defects, irregular voids between particles and micro-cracks in primary cathode particles without actively dismantling the cell, i.e. in its original environment. The average active area of the cathode material is 1,500 mm^2 for the three samples, in this case, meaning a single scan using the 4 X magnification, captures 16 mm^2. As a result, the region of interest represents ~ 1.07 % of the active area of the single-layer pouch cell. There is a possibility of creating a recipe that allows for multiple regions of the cell to be imaged and later stitched together to increase the overall representability of the data. Furthermore, there is potential to locate particular defects of interest and track changes during cycling and/or aggressive degradation of the cell.

Figure 5.2 (d) shows the ability to segment the active particle phase to extract parameters such as material porosity or particle size distributions. These values are extracted for a sub-volume of this dataset and compared

with two ex-situ cathode samples at higher spatial resolutions in the following section.
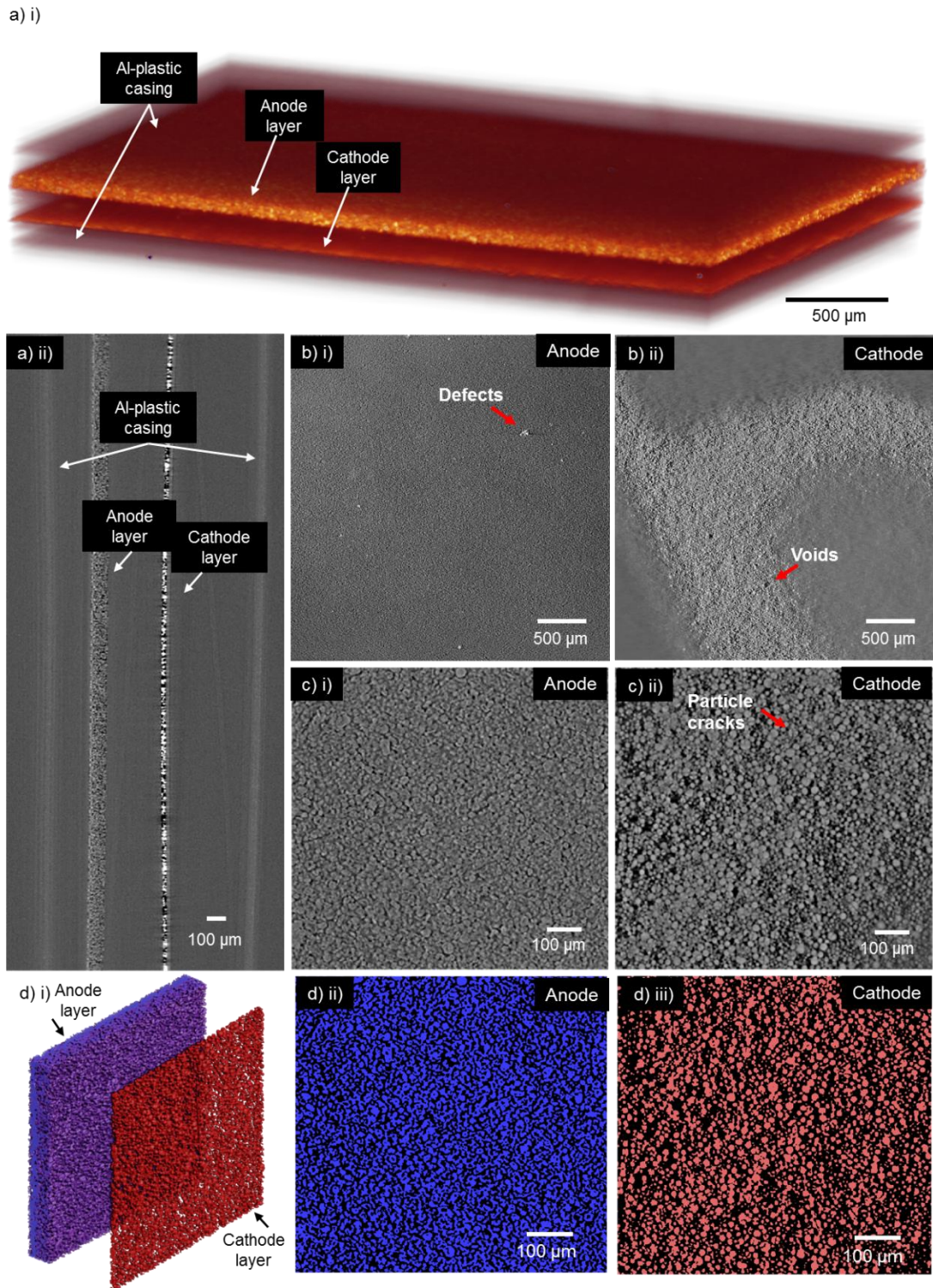
Figure 5.2 (a)(i) Volume rendering of a single-layer pouch cell (Sample 1) highlighting the anode and cathode layers. Orthoslices in the XY plane of the (b-c)(i) anode and (b-c)(ii) cathode from Sample 3. A (d)(i) volume rendering, and orthoslices of the (d)(ii) anode and (d)iii) the cathode of the segmented sub-volume of data is also shown.

5.2.3. Comparison of parameter extraction between interior tomography and ex-situ samples of the single-layer pouch cell

Battery materials imaged within the single-layer pouch cell using the HART technique result in a tomogram showing particles in the XY plane of the orthogonal slice shown in Figure 5.3 (a). For comparison, two ex-situ samples of the cathode material were imaged using micro- and nano X-ray CT methods. Parameters such as the porosity of the active material (NCA) and the mean particle size were extracted after applying the same image processing techniques to all three datasets and compared. The micro-CT datasets provide a direct comparison of the bulk electrode layer properties, while the nano-CT dataset allows for a direct comparison of the particle morphology. Furthermore, the representativeness of the data extracted from the single layer pouch cell interior tomography is discussed.

For each dataset, a similar image analysis workflow was applied (as discussed in more detail in Chapter 3, Section 3.5.6.). Each sample was prepared to best suit the X-ray CT equipment requirement and configuration; i.e. for the ex-situ samples, the micro-CT sample was cut to 400 µm to fit the field-of-view, whereas the sample for nano-CT was prepared into an electrode pillar (with an approximate diameter of 45 µm) using a laser milling technique[202]. As a result, the number of particles captured by X-ray CT is significantly reduced across the three datasets as the sample size reduces from the whole-cell (interior micro-CT) to 400 µm (micro-CT), and 45 µm (nano-CT).
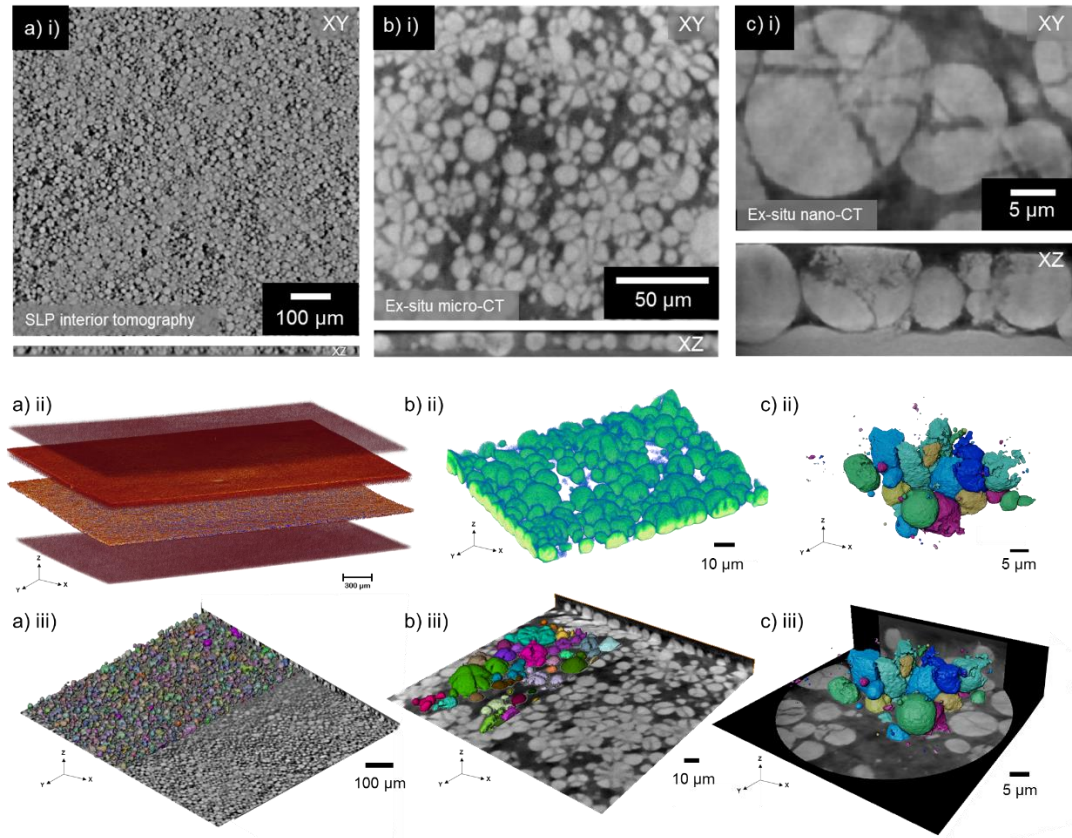
Figure 5.3 Top row shows the (i) orthogonal slices of the NCA electrode in the XY and XZ plane, the middle row shows the (ii) volume renderings and, the bottom row shows the (ii) orthogonal slices of the data after applying filters, segmenting and separating individual particles, for (a) the interior tomography of the single layer pouch cell, (b) ex-situ micro-CT and (c) ex-situ nano-CT samples.

Table 5.3 The X-ray CT image scanning parameters and the corresponding microstructural parameters of the $LiNi_wCo_xAl_yO_z$ cathode extracted from three different samples.

Parameters	Micro-CT		Nano-CT
	Interior tomography (HART)	Ex-situ	Ex-situ
Sample type/size	Whole-cell (65 x 95 mm)	Laser-milled pillar (~ 400 μm diameter)	Laser-milled pillar (~ 45 μm diameter)
Voxel size (μm)	1.72	0.21	0.13
Porosity	0.42	0.66	0.45
Sub-volume size (μm^3)	72.3 E+05	5.76 E+05	0.55 E+05
Cathode particle volume (μm^3)	42.0 E+05	1.81 E+05	0.30 E+05
Mean particle size (μm)	4.8	4.4	4.7
Standard Deviation	2.13	3.21	4.76

Microstructural parameters for the three datasets were extracted using a sub-volume of 723,000 µm^3 for the single layer pouch cell interior tomography data, 576,000 µm^3 for the micro-CT data and 55,000 µm^3 for the nano-CT data. Owing to the additional FOV offered by the pouch cell interior tomography, the volume of data extracted for HART scans compared to traditional micro-CT scans is much greater. In Table 5.3, the overall porosity from the three datasets varies, where the porosity for the ex-situ micro-CT dataset is 0.66 compared to 0.42, and 0.45, for the interior tomography and nano-CT datasets. This may be a factor of various reasons; the sample may have been from a section of the electrode where there were inconsistencies in the electrode manufacturing (e.g. tape application, or calendaring). Another possible reason could be from the user-chosen scanning parameters which may affect the image signal-to-noise ratio impacting the overall scan quality. Often, a better scan quality offers improved phase boundary distinguishability, revealing details such as surface roughness and micro-cracks[155][166]. Furthermore, the segmentation (data processing) depends on user-chosen filter settings which may be a cause for inconsistencies. It is recommended to carry out repeated tests and analyses on multiple samples to improve the overall reliability of the extracted parameters.

While the particle size may be used to distinguish or compare the thermal stability of the material, the cracks that are visible in the cathode can also reveal a great deal in terms of the performance and failure behaviour of the cell. For example, a greater number of cracks in particles can contribute to a higher rate of heat generation. Overall, the parameters extracted from the three types of samples show that an in-situ scan of the single-layer pouch cell offers a comparable resolution to extract parameters such as particle size and features (such as particle cracks). The most important benefit of the single-layer pouch cell scan is that the materials are imaged in as close to their operating environment i.e. active and soaked in electrolyte. The possibility of sample damage during preparation (such as in the ex-situ material scans) is significantly reduced or removed. There are still benefits to ex-situ micro- and nanoscale CT scans, to gain deeper understanding of the particle morphology,

transport phenomena across the microstructure or the characteristics of the carbon binder phase[181], for example.

5.3. Nano-scale cathode material characterisation

In this section, an investigation of the utility of parameters extracted from positive electrode materials using X-ray nano-CT is carried out to understand how they can be correlated with battery performance. In this case, ex-situ samples are prepared and imaged to understand their morphology and the results are compared to the thermal behaviour of the material under operation in coin cells (using differential scanning calorimetry). Three lithium nickel cobalt aluminium oxide, $LiNi_aCo_bAl_cO_d$, (NCA, Johnson Matthey) positive electrode materials each of varying compositions were used in this study. Their preparation techniques; as X-ray CT samples for imaging and assembled into coin cells for thermal analysis are described in the following section.

5.3.1. Materials and preparation techniques

The cathode materials were imaged using the Zeiss Xradia Ultra 810 with a fixed energy 5.4 keV, quasi-monochromatic beam. Samples in their fresh state (uncycled) were prepared using a micro-machining laser preparation method to obtain sample sizes that matched the FOV[202]. An A-Series/Compact Laser Micromachining System (Oxford Lasers, Oxford, UK) with an embedded Class 4, 532-nm-wavelength laser was used for all laser preparation of samples. All samples were imaged in the LFOV absorption mode with a 65 μm FOV. An objective lens with an optical magnification of 20 was used with binning 2 x 2 and an effective pixel size of 0.1262 μm. Reconstructions consisted of several projections and exposure times which varied for each material, these are summarised in Table 5.4.

Table 5.4 Dimensions of each sample after laser preparation and parameters used for X-ray nano-CT.

Sample	Active material thickness / μm	Sample size (diameter) / μm	Exposure time / s	Number of projections
JM1	36	63	40	1801
JM2	27	99	40	1801
JM3	30	86	30	2001

Samples intended for thermal analysis were assembled into coin cells as follows. All electrode discs were dried for 12 h under vacuum at 120 °C in a glass drying oven (B-585, BUCHI Ltd.) before being assembled into coin cells (CR2032, Hohsen Corp.). A full-cell electrode arrangement was used with $LiNi_aCo_bAl_cO_d$ (NCA, Johnson Matthey) as the working electrode and Graphite (WMG) as the counter electrode. A tri-layer polyolefin membrane was used as a separator (Celgard 2325, Celgard, LLC.) and the electrolyte used was 1.0 M lithium hexafluorophosphate in ethylene carbonate and diethyl carbonate (1.0 M $LiPF_6$ in EC:DEC (1:1 v/v), Soulbrain MI). All cells were assembled in a glove box with an argon atmosphere (O_2 and H_2O < 0.5 ppm, MBraun, Germany).

The theoretical capacities of the CR2032 cells were calculated to be ca. 4.6, 3.8 and 4.0 mAh, for each of the materials based on their mass loadings and electrode areas (14 mm diameter) and a specific capacity of 200 mAh g^{-1}. The cells underwent two initial formation cycles using a CCCV charge and CC discharge protocol. The current used during the constant current steps were equivalent to a C/20 rate with a cut-off condition of 4.2 V for charge and 3.0 V for discharge. For the constant-voltage charge step, the cells were held at 4.2 V until the current dropped to C/50. Formation cycles were performed on a multi-channel battery cycler (Novonix).

The coin cells were later placed in a coin cell calorimeter (MMC 274 Nexus, Netzsch Geratebau GmbH, Germany) and connected to the potentiostat (Interface 1000E, Gamry Instruments, USA). Two cells were placed symmetrically on either side of a carrier, the coin cell sample, and a reference cell. The heat flow between the two can be detected from room temperature up to 250 °C. An empty CR2032 cell sealed with a polypropylene

gasket inside an argon-filled glovebox (O_2 and H_2O < 0.5 ppm, MBraun, Germany) was used as a reference. Thermal measurements were carried out using the isothermal mode. As the temperature of the module reached a predefined temperature of 25 °C, time was given to the cell to reach thermal and chemical equilibrium before the cycling protocol started. The cells were also held at OCV for 1 h.

The cells followed a CCCV charge and CC discharge protocol as defined above. The current used during the constant current steps were equivalent to a C/2 rate with a cut-off condition of 4.2 V for charge and 3.0 V for discharge. The cells underwent 10 cycles while their heat flux signals were recorded by the calorimeter software.

5.3.2. Image processing and parameter extraction

Images obtained from tomographic reconstructions are enhanced by adjusting the greyscale levels and applying filters using Avizo image processing software (FEI VSG, France). Image brightness and contrast were adjusted for each dataset. The images were also cropped to remove pillar edges that may have been damaged during the laser-milling sample preparation technique. Background noise and unwanted artefacts were removed from datasets by applying digital image filters to the greyscale image stacks. A non-local means image filter[204] was applied to each of the material datasets, to enhance features of interest i.e. particle vs. pore. The greyscale images are segmented to identify homogeneous, non-intersecting regions by assigning a label to each pixel that shares a similar grayscale intensity. For example, the nickel-cobalt oxide particles (lighter regions) are separated from the pore space (darker regions). Figure 5.4 shows filtered images and their respective volume renderings upon segmentation.
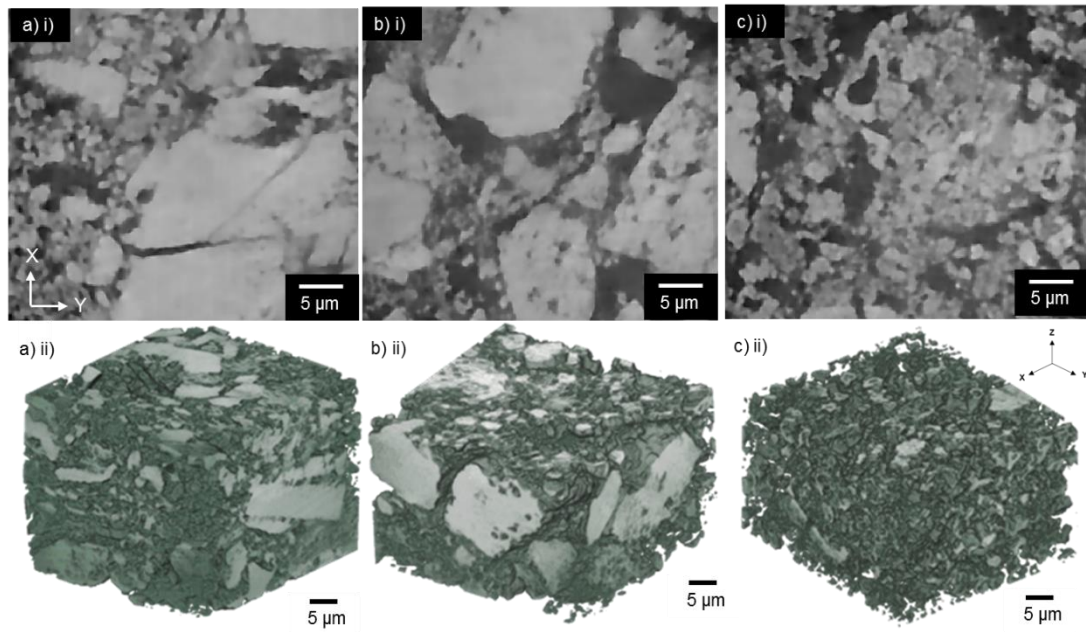
Figure 5.4 Orthoslice of the filtered images in the XY planes, and volume renderings obtained for each of the positive electrode materials: (a) JM1, (b) JM2, and (c) JM3.

Geometric parameters including volume fraction, volume-specific surface area, geometric tortuosity and PSDs were calculated using a stereological approach. 3D microstructural parameters were predicted based on 2D image slice stacks. A sub-volume of each material was selected for analysis, as listed in Table 5.5. Based on the nano-CT pixel resolution obtained, each voxel is 126 x 126 x 126 nm in size, therefore JM1 for example with dimensions 316 x 359 x 263 voxels represents a volume of 39.8 x 45.2 x 33.1 µm. An evaluation of whether the considered sample volume fully encompasses all heterogeneities and phases in the material was carried out. An RVE analysis defined the minimum volume which is statistically representative of the material as a whole (see Figure 5.5). A comparison of the ratio of the volume of each particle to its surface area shows that the volume-specific surface area of JM2 is the smallest when compared to JM1 and JM3.

Table 5.5 Parameters obtained from the binarised datasets for each sample material.

Sample	Porosity	Total Voxels	Volume Specific Surface Area / μm^{-1}	Directional Tortuosities			Characteristic Tortuosity, τ_c
				τ_x	τ_y	τ_z	
JM1	0.243	316 x 359 x 263	0.956	3.88	4.57	9.20	5.13
JM2	0.249	315 x 341 x 218	0.746	3.85	5.11	4.82	4.53
JM3	0.325	317 x 352 x 212	1.110	4.01	6.60	3.22	4.22

The influence of the electrode morphology on lithium-ion transport with electrolyte was characterised by determining the tortuosity of the pore phase within each cathode material. A finite element simulation of a scalar diffusion parameter[156] was used to determine the tortuosity factor of each sample using the MATLAB plugin TauFactor[205]. The tortuosity factors extracted from the subvolumes are presented in Table 5.5. To compare the calculated directional tortuosities, the characteristic tortuosity[156] was calculated using Equation 5.2.

$$\tau_c = 3\left[\tau_x^{-1} + \tau_y^{-1} + \tau_z^{-1}\right]^{-1}$$

Equation 5.2

As shown in Table 5.5, JM1 has the highest tortuosity factor, followed by JM2 and JM3. This corresponds with a visual comparison of the samples in Figure 5.4, where JM1 particles look more compact when compared to JM2 and JM3. While these values accurately define specific properties of the analysed samples, it is important to consider whether the chosen volume is representative of the bulk material. Highly heterogeneous materials such as battery electrodes can vary largely depending on the sample sub-volume size. An RVE analysis (Figure 5.5) of the tortuosity factor shows that the volume used to determine the tortuosity factor for each of the cathode materials did

not change significantly with the sample size, and therefore can be considered representative of the bulk material[159].
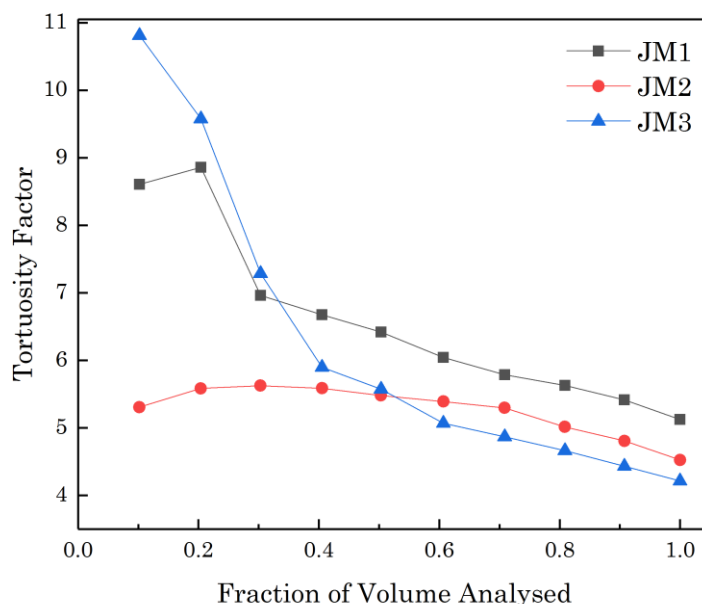
Figure 5.5 RVE analysis for each of the electrode materials showing that the full volumes of JM1, JM2 and JM3 provide representative tortuosity values of the bulk materials.

These measurements however do not provide sufficient information to determine the contribution of each phase in ionic transport across the cathode material. The porous network of carbon and binder which forms around the active material particles plays a significant role in ionic conduction across the electrode material as a whole. The nano-CT datasets in this study are treated only as two phases i.e. active particles and pores. However, Daemi et al. compared the tortuosity factor of a cathode material considering the CBD, in addition to the active particles and pore[181] and found a large increase in value when treated as three phases. Furthermore, the arrangement of the connective porous networks of each phase is a complex combination of macro- and nanoscale pore sizes. Thus, this data should be considered a macro study of transport phenomena. Carrying out a higher-resolution scan to resolve smaller pore sizes in the CBD may provide an improved study of the intricate transport properties within the electrode materials.

A PSD was performed on the extracted sub-volumes using Avizo software (FEI VSG, France). The results of which are shown in Figure 10.2 in Chapter 10. It should be noted that a large number of the particles intersected the outer interface of the sub-volume bounding box, consequently skewing the particle size measurements. The spread of data in the PSD for JM1 and JM2 are relatively similar, except for a difference in mean diameter, where the diameter extracted from the JM2 sample is almost half the size of that in JM1. A visual comparison of the two samples suggests the peaks may represent smaller particle fragments from fractured larger particles.

The PSD of JM3 shows a peak slightly below 0.5 μm which correlates with its high volume-specific surface area. While JM3 has the highest porosity, the relatively even spread of particle sizes may further describe its lower tortuosity[167][174]. The increased spread of smaller particles in JM3 compared to JM1 and JM2 would significantly affect the rate of decomposition of the electrode at elevated temperatures. Additional surface area would be exposed to the electrolyte, contributing to a lower onset temperature should it be incorporated into a cell undergoing failure. It is well understood that particle shape and size significantly affect the rate of heat generation during failure, however how these microstructures (including particle fractures) evolve would give greater insights into electrode behaviour under stress.

Each sample still has the potential to be milled further to sufficiently match the FOV of the nano-CT system (see sample size in Table 5.4). Adjusting the parameters used when applying filters to the original grayscale datasets may also improve phase boundary identification and consequently improve segmentation quality. With improved scan and segmentation quality, it is possible to identify the CBD, in addition to the active material particles and pore phases. A three-phase segmentation will provide a more accurate characterisation of the cathode materials, particularly regarding the transport phenomena.

5.3.3. Microstructure and thermal behaviour correlation

An electrode is made up of active particles and a binder all of which vary in terms of size, shape, the orientation of particles and material properties (e.g. thermal stability, conductivity etc.). These characteristics will influence the degradation, internal resistances, diffusion and thermal behaviour of a cell. A high surface area of the electrod ematerial can significantly reduce the thermal stability, however it may improve energy density, therefore a number of trade-offs between cell performance and safety exist. To analyse the relationship between the microstructure of the cathode materials, in terms of their particle morphologies, and their thermal behaviour, the positive electrode materials were assembled into full coin cells using graphite counter electrodes. The cells were cycled between 3.0 V and 4.2 V at 0.5 C for 10 cycles. The partial substitution of Ni by Co and Al has been reported to improve the thermal and structural stability of the traditional $LiNiO_2$ positive electrode material[219]. $LiNiO_2$ undergoes a phase transition from hexagonal H1, monoclinic M, and hexagonal H2 to hexagonal H3 during intercalation and de-intercalation of Li[220]. For Ni-contents < 80 %, the M → H2 and H2 → H3 phase transition has not been observed[214][87][221]. A differential capacity plot of the delithiation and lithiation of the three NCA-graphite cells (5th cycle) is shown in Figure 5.6 (a). The voltage region in which peaks appear is very similar for all three NCA compositions up to the cut-off voltage, with three distinct anodic peaks between 3.6 V and 4.2 V. The first belonging to the phase transition from a hexagonal to a monoclinic (H1 → M) lattice of the NCA and the second and third belonging to the M → H2 and H2 → H3 phase transitions. The presence of the last two transitions suggests that the positive electrode materials have Ni-contents > 80 %. The dq/dV curves for JM1 and JM3 deviate slightly from the JM2 cell, showing a fourth peak in the region between 3.5 V and 3.6 V. This is assumed to originate from the Li^+ intercalation into the graphite electrode[87].

Furthermore, Figure 5.6 (b) – (d) shows three charge-discharge curves for each material (grey) and the corresponding heat flux signal. Discharging of the cell is related to a large exothermic peak, whereas charging is an initial endothermic heat signal followed by an exothermic peak. In general,

irreversible effects exhibit exothermic signals, and reversible effects, such as reaction heat, lead to both exothermic and endothermic signals[219][207]. The reaction heat or entropy can change its sign as a function of SOC, hence its progression with SOC is a function of the microstructure of the material.

The microstructure of the cathode influences the thermal behaviour (i.e. Joule heating and reaction heat) during discharge. It is also evident from these results and widely observed in various literature[222], that the total rate of heat generation is mostly observed at the cathode-separator interface and the end of discharge[207]. In Figure 5.6 (b – d), at the end of discharge, the peak height of the heat flux signal is different for each sample; there is an observable trend whereby the maximum heat flux value for JM1>JM2>JM3. From Table 5.5, we observed that the porosity from JM1 to JM3 increases, and the tortuosity decreases. Increasing the porosity, or decreasing the fraction of active material, lowers the Li^+ concentration gradient. This contributes to a lower internal resistance which decreases the overall Joule heating rate within the cell. To obtain an optimum microstructure for LIB cathode materials, without affecting the capacity, it is important to consider the porosity and tortuosity. During cell discharge, the maximum heat released from the cell can be reduced by increasing the porosity of the cathode, low enough to maintain the required percentage of active material and/or overall capacity.

While the current study presented here is limited in terms of variables and repeatability, it is readily expandable to different chemistries and electrode microstructures which was demonstrated in Chapter 4. Variations in terms of manufacturing the electrodes can lie in the use of different particle morphologies and sizes. Overall, elucidating the thermal behaviour that is dependent on the microstructure provides a valuable direction in the aims to improve LIB safety assessment.
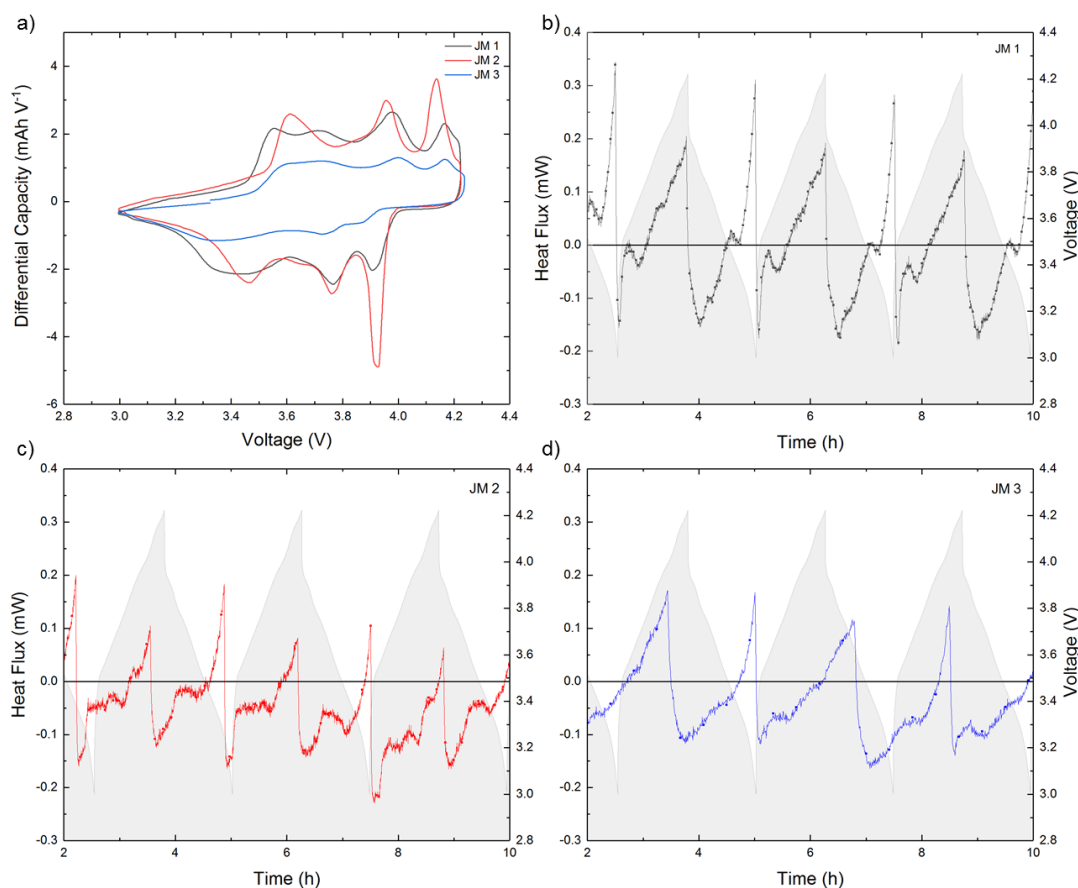
Figure 5.6 (a) Differential capacity vs. cell voltage of NCA-graphite cells recorded at 0.5 C (5th cycle) at 25 °C. The peaks are assigned to their corresponding phase transitions with H1, H2 and H3 representing the three hexagonal phases and M the monoclinic one, $C_6 \rightarrow LiC_x$ indicates the lithiation of graphite. Heat flux signals for charge and discharge profiles of the NCA-graphite coin cell samples are shown for (b) JM1, (c) JM2, and, (d) JM3, measured at a 0.5 C-rate and 25 °C.

5.4. Failure and post-mortem analysis

Manufacturers, organisations, and battery researchers investigate and characterise the various mechanisms related to LIB safety by deliberately creating scenarios that may trigger thermal runaway. A test set-up can involve overcharge/discharge, heating, short circuit, internal short circuit, nail penetration, or crushing. However, despite standardisation efforts across these, current LIB safety testing standards have different guidelines for each. Table 5.6 summarises two methods (heating and nail penetration) used to trigger battery failure in five selected safety testing standards adapted from Chen et al[133]. Heating tests are used to analyse the LIBs' thermal stability and heat distribution. For example, a safety requirement, or testing standard

for electric vehicle batteries (GB/T31485-2015[223]), deems a battery as 'safe' if it does not leak or combust after it is placed in a hot box and heated to 130 °C at 5 °C min^{-1} and kept at this temperature for 30 min. Nail penetration tests are designed to simulate an internal short circuit (ISC) that may occur when the internal components are penetrated with impurities. An ISC event generates large quantities of local heat which may lead to thermal runaway.

Table 5.6 Summary of heating and nail penetration testing guidelines from five selected safety testing standards adapted from Chen et al.[133]

Trigger mechanism for battery failure	Safety testing standard				
	GB/T31485-2015	IEC62133	SAE J2464	VW PV8450	USABC-GM
Heating	Heating at 5 °C min^{-1} from 25 °C to 130 °C, hold for 30 min	130 °C, 10 min	Max. stable temperature	2 °C min^{-1} to 130 °C or 200 °C hold for 30 min	0.5 °C min, 50-150 °C, hold for 30 min
Nail penetration	Penetration rate: 25 mm/s, diameter: 5 - 8mm, 100% depth	N/A	80 mm/s, diameter: 3 mm, 100% depth	0.1 mm/s, diameter: 1mm stainless steel, 2 mm depth	80 mm/s, diameter: 3 mm, 100% depth

As discussed in Chapter 2, Section 2.5 when attempting to understand the evolution of a particular failure mechanism within a LIB, it is important to consider the method by which the failed batteries are examined. X-ray CT for post-failure analysis is predominantly used to see where failure causing defects are located[48] and/or to assess where samples should be extracted from upon cell opening for further analysis[183]. This section investigates a method by which X-ray CT can be used to visualise and measure the effects of different failure triggers and compares results from non-invasive and invasive sample preparation. The results are analysed from the perspective of preventing ignition, i.e. finding the mechanisms by which Joule heating and decomposition of materials occur and how they can be mitigated: by controlling

heat generation and enhancing heat dissipation within a pouch cell. A multi-length scale imaging approach is applied using X-ray CT to investigate the cell architectures and electrode deformations within a thermally failed and nail-penetrated cell. A post-failure diagnostic method (cell-opening and sample extraction) is discussed and considered in the context of the failure mechanisms across the whole cell. This investigation proposes a technique for investigating the causes and mechanisms of LIB failure to aid the design, manufacture and use of LIBs in ways that can mitigate known safety hazards.

5.4.1. Methodology

Three 1 Ah layered lithium-ion batteries with a pouch cell format were tested for their response to two battery failure trigger modes. One cell was assigned as the control (Cell 1), and the remaining cells were investigated under external heating (Cell 2) and nail penetration (Cell 3), respectively. All cell samples consisted of twenty-one double-sided electrode layers, with ten positive electrodes, denoted as the cathode, and eleven negative electrodes (graphite) denoted as the anode. The cathode material, lithium nickel manganese cobalt oxide (NMC811), was sourced from Targray, Canada.

Tomographic reconstructions of multiple samples were produced using three lab-based X-ray CT systems: Nikon XT 225 (Nikon, Tring, UK), ZEISS Xradia 520 Versa and, ZEISS Xradia Ultra (Carl Zeiss XRM, Pleasanton, CA, USA). Whole battery scans, (i.e. without cell disassembly) are defined as 'non-invasive' and battery component scans, for imaging bulk electrode layers and particles, are defined as 'invasive'. For the latter, the battery was carefully dismantled and photographed during each stage of disassembly for sample collection. The features of interest, spatial resolution and imaging instrument used are categorised by the sample preparation method (invasive or non-invasive) and shown in Figure 5.7.
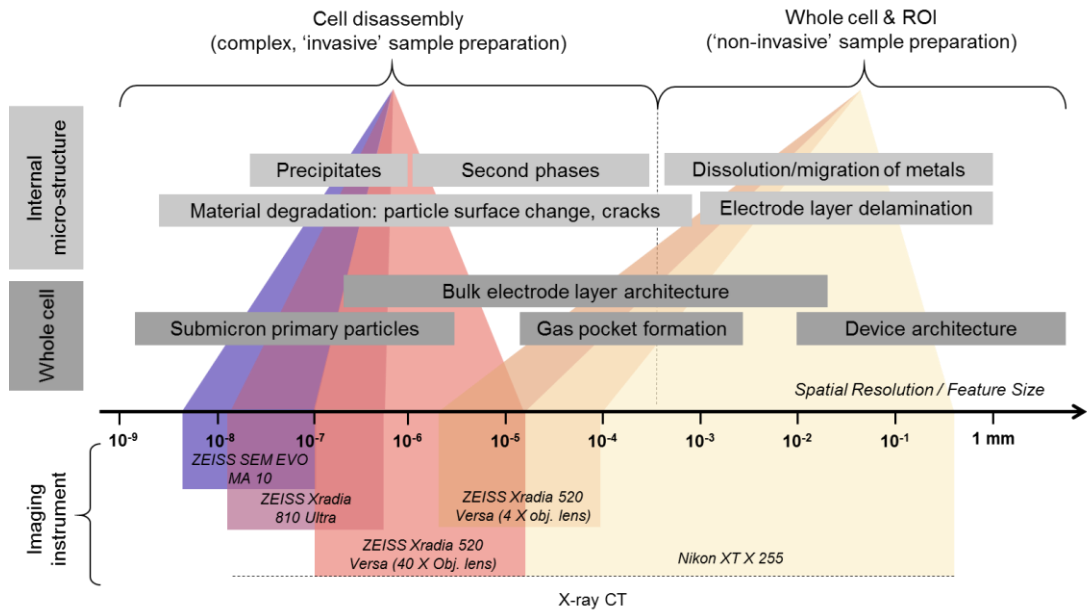
Figure 5.7 Imaging instruments (Scanning electron microscopy, SEM and X-ray Computed Tomography, X-ray CT) grouped for the type of sample preparation (invasive and non-invasive) required for the feature of interest/spatial resolution (adapted from Salvo et al.[23]).

For whole cell and ROI non-invasive scans, images were obtained using the Nikon XT 225 (Nikon) and the ZEISS Xradia 520 Versa (Versa) with a 4 X objective lens, respectively. For the Nikon, an accelerating voltage of 210 kV was used with a tungsten target to generate 3176 projections for each of the datasets acquired. The datasets were subsequently reconstructed using CT Pro 3D software with a built-in FBP algorithm. The acquired datasets had voxel sizes ranging between 27.8 – 33.6 µm. For the ROI datasets, a pixel binning of 1 was used and the voltage, exposure times, and number of projections were all varied for the sample type. The acquired pixel sizes are summarised in Table 10.2 in Chapter 10.

5.4.1.1.   Post-mortem sample preparation

Two methods were used to prepare the samples for the battery component (bulk electrode layer and particle morphology) analysis. Cells were left overnight in their respective instruments after failure for gases to safely evaporate. Once the cells had cooled to room temperature, they were imaged first via X-ray CT for the whole cell and ROI analysis. The cells were stored in the air and later taken apart inside a fume hood. For both cells, a scalpel was used to create an incision lengthwise at the side of the cell where the pouch

had been vacuum sealed. The outer casing of the pouch was peeled away carefully without disrupting the electrode layers as shown in Figure 5.8 (a)(i) and (b)(i). The electrode layer stack was removed first from within the cell casing by cutting the anode and cathode tabs. For the thermally failed cell (Cell 2), the central anode and cathode layer was removed and a 1 cm x 1 cm square from the centre of the electrodes was removed for further preparation (as shown in Figure 5.8 (a)(ii-iii) and (b)(ii-iii)). For the nail-penetrated cell (Cell 3), the central anode and cathode layers were removed and the separator was carefully peeled off their surfaces. 1 cm x 1 cm squares were cut from the centre of both electrodes of this cell and subsequently used for 2D imaging via SEM. For 3D imaging via X-ray CT, the samples were processed further using a high-precision laser, details of which follow.
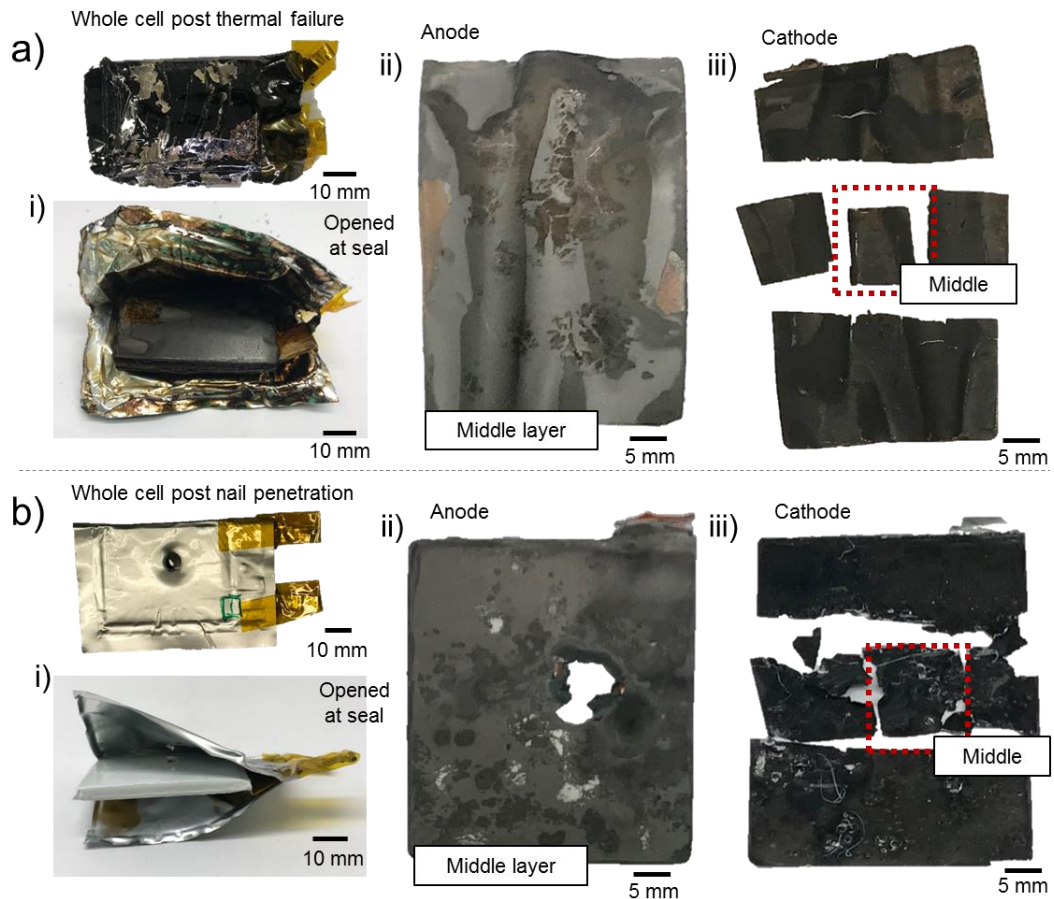
Figure 5.8 Photographs showing the disassembly of (a) the thermally failed cell (Cell 2) and (b) the nail-penetrated cell (Cell 3). The aluminium-plastic composite casing was carefully cut at the vacuum-sealed edge and peeled away in (a-b)(i). The central anode layer is shown in (a-b)(ii) and the central cathode layer is shown in (a-b)(iii) as well as where the samples for SEM and X-ray CT were extracted from.

After opening the failed cells, samples were prepared according to the feature of interest. Samples intended for 3D images of the bulk electrode were prepared by cutting 0.4 mm by 0.4 mm squares which were mounted onto a 3D printed stacker using Kapton tape. The samples fitted within the field-of-view (FOV) of the 40 X objective lens, ca. 400 µm, in the X-ray micro-CT instrument (Zeiss Xradia 520 Versa, Carl Zeiss XRM, Pleasanton, CA, USA) and were held upright in a 3D printed stacker (Figure 5.9) to reduce the overall signal-to-noise ratio and scan time. This method produced 3D images with a 0.387 µm voxel size of the four bulk electrode layers (anode and cathode each after thermal failure and nail penetration). The bulk electrode layer datasets were obtained using the ZEISS Xradia 520 Versa with a 40 X objective lens. Datasets for the thermally failed (Cell 2) and nail penetrated (Cell 3) cathode samples were obtained using a pixel binning of 2, a voltage of 80 kV, and an exposure time of 5 s, while the anode datasets were obtained using a lower voltage at 60 kV while all other parameters remained the same. The acquired pixel sizes are summarised in Table 10.2.
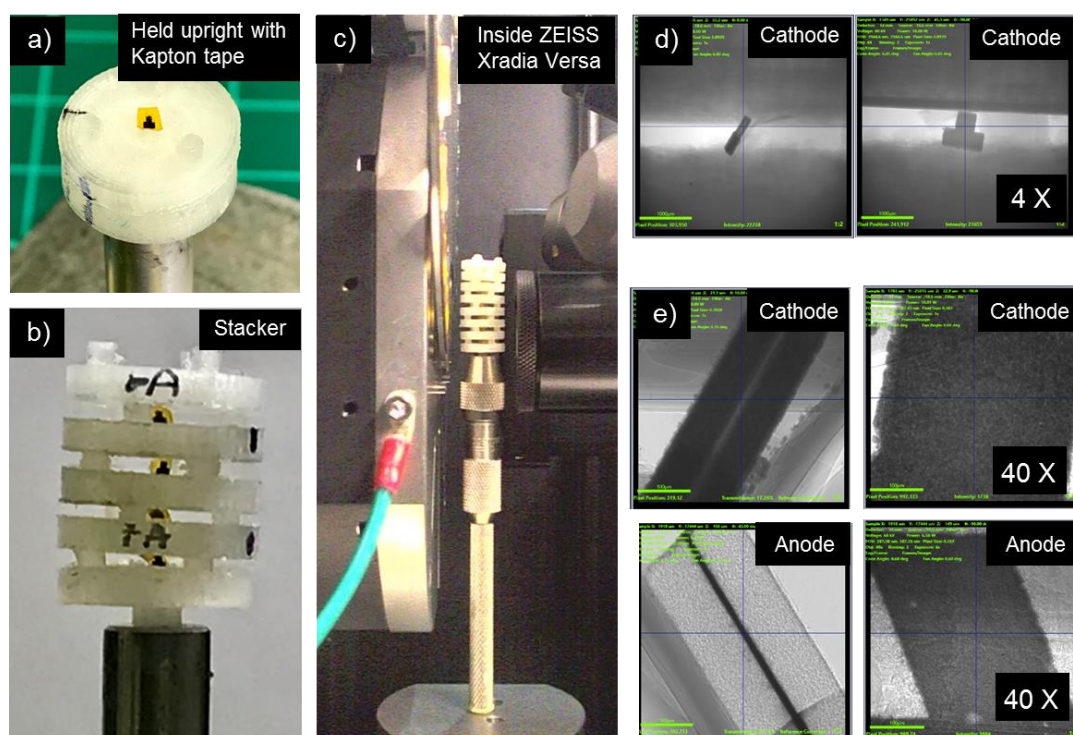
Figure 5.9 Photographs of (a) 0.4 x 0.4 mm sample placed upright in 3D printed holder, secured with Kapton tape, (b) samples stacked, and (c) placed inside the ZEISS Xradia Versa 520. Radiographs in (d) show the sample within the FOV with the 4X objective lens and (e) shows the cathode and anode in the FOV with the 40 X objective lens.

Samples intended for imaging at nano-scale resolutions to resolve individual particles (using the Zeiss Xradia Ultra 810) were prepared using a laser lathing micro-machining technique (A Series/Compact Class 4 532 nm Laser Micromachining System, Oxford Lasers, Oxford, UK) as described by Bailey et al. [202]. Small disks of 1 mm diameter were cut from the bulk electrode layers, glued to a pin and milled down to a diameter < 65 μm. All samples were imaged in the LFOV absorption mode with a 65 μm FOV. High-resolution images were obtained using the ZEISS Xradia Ultra 810 with a fixed energy 5.4 keV, quasi-monochromatic beam. A voxel size of 0.0631 μm was achieved for the pristine cathode and 0.126 μm for the post-failure cathode samples.

All SEM micrographs were obtained using the Zeiss EVO 10 SEM instrument. An SE1 signal was used at a 15 kV accelerating voltage and approximate magnifications ranging from 3,300 – 8,500, yielding a pixel size between 35 – 90 nm for all images.

5.4.1.2. Image processing

Reconstructed X-ray CT data was visualised using Avizo Fire 9.5 (FEI Company, Hillsboro, OR, USA). For all datasets, a non-local means filter was applied to reduce noise and preserve phase boundaries. This procedure was performed to prepare the datasets for threshold-based binarization. Phases were separated based on their grey scale values where weakly attenuating materials are displayed in shades of grey (such as the separator, graphite anode and aluminium current collector) and highly attenuating materials (such as the cathode active material and copper current collector) in white. Voxels in the bulk electrode layer and particle scans were assigned to a particle or pore phase based on the measured grayscale value. The resulting binary images were used for measurements of porosity and PSD using the Avizo Fire 9.5 label analysis tool. Tortuosity factors and representative volume analyses were extracted using TauFactor, an open-source MATLAB plugin, details of which are described in ref[205].

5.4.2. Whole-cell investigation

The whole cell analyses were carried out using the 'non-invasive' sample preparation technique. The cells pre- and post-failure were examined at two spatial resolutions as shown in Figure 5.10. The first set, using the Nikon X-ray macro-CT instrument achieved voxel sizes of 31.7 μm, 33.6 μm, and 27.8 μm for the pristine cell (Cell 1), thermally failed (Cell 2) and the nail penetrated (Cell 3), respectively. The second set, using the Zeiss Xradia Versa X-ray micro-CT instrument with a 4 X objective lens (ROI scan with ca. 3 – 4 mm field of view), achieved voxel sizes of 1.83 μm, 2 μm, and 1.7 μm for Cell 1 – 3, respectively. For the larger voxel size scans, the architecture of the whole cell, i.e. the outer casing of the pouch, the tabs, and the electrode layers (anode and cathode) are distinguishable based on their grayscale values. As a result, the behaviour of these features when subjected to different trigger mechanisms can be compared. For example, the outer casing and disorder in electrode layers in Cell 2 reveal that there was a greater pressure build-up and distribution within the thermally failed cell compared to that of the nail-penetrated cell (Cell 3). The microstructure of the electrode layers also reveals where cracks formed and how they differ between the two types of failure. For the nail-penetrated cell, the largest and most prominent cracks are all distributed directly above or below the nail, whereas cracks in the thermally failed cell are distributed across the whole cell architecture, but are concentrated in areas where kinks have occurred in the electrode layers due to large gas pockets. A more comprehensive analysis of the two failure types and comparisons with the pristine cell is reported in the following sections.
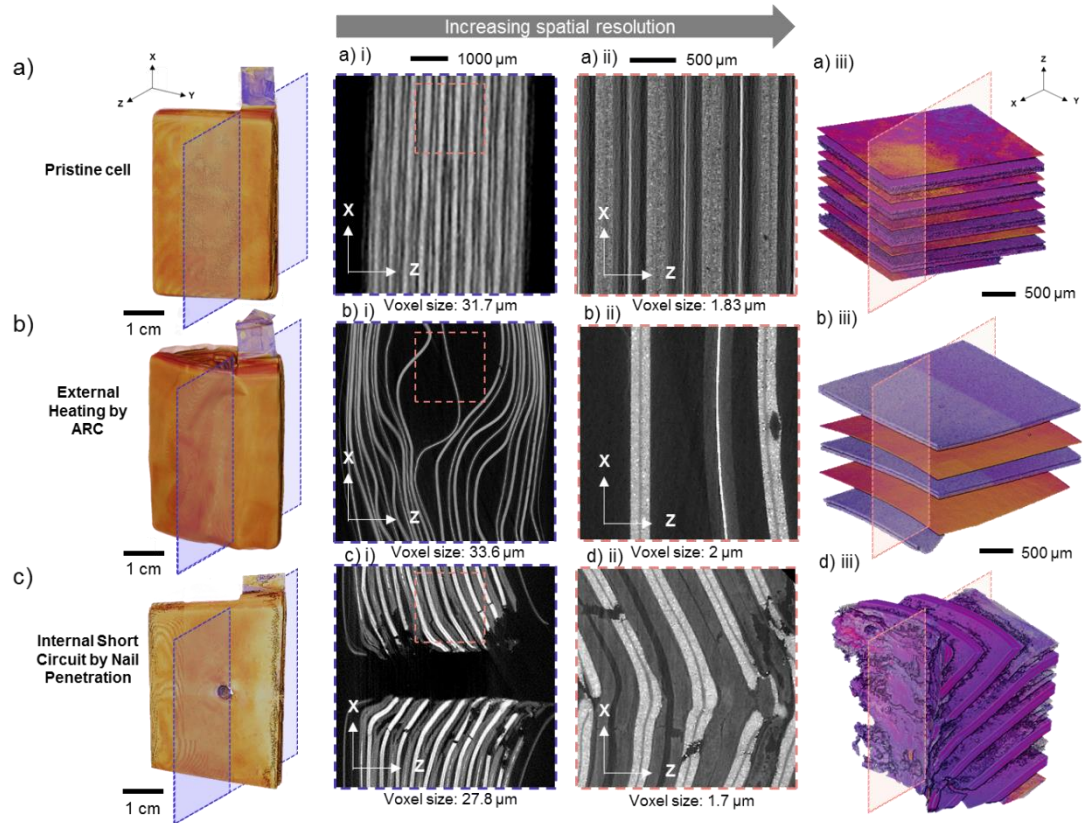
Figure 5.10 (a-c) shows volume renderings and orthogonal slices in the XZ planes for the pristine cell (Cell 1), the thermally failed cell (Cell 2), and the nail-penetrated cell (Cell 3), respectively. Corresponding scan numbers are 1 – 6 in Table 10.3 in Chapter 10.

5.4.3. Thermal failure: external heating by ARC

Increased reactivity due to external heating in lithium-ion batteries is often a consequence of SEI decomposition and exposure of the anode to the electrolyte causing self-heating reactions. When this heat is not well dissipated, the temperature of the cell continues to rise due to sustained exothermic reactions (often denoted the 'acceleration' stage). Further reactions involving electrolyte oxidation at the cathode surface eventually cause the cell to enter the 'thermal runaway' stage. During this stage, several high-rate electrode reactions will continue to generate heat, and the cell may eventually catch fire and disassemble. A typical self-heating rate used to characterise the thermal runaway of a lithium-ion cell is 10 °C min^{-1} or higher. Thermal runaway temperatures can vary between 130 °C to 200 °C or greater and are highly dependent on cell size, format, and materials. From Figure 5.11

(a), it appears that Cell 2 did not reach thermal runaway (i.e. a self-heating rate > 10 °C min^{-1}), however, visual inspection suggests significant thermal damage by fire (charring of outer case). The temperature profile in Figure 5.11Figure 5.11 (a) reveals that the self-heating rate between 60 °C and 130 °C remains below 1 °C min^{-1}. The decomposition of SEI is typically expected to begin at 60 °C, exposing the anode surface to the reactive electrolyte. Exothermic reactions between the two are expected to occur ca.100 °C. Heat generation from this promotes an elevation of the cell temperature. The inflection at ca. 125 °C may be a result of the separator melting since the self-heating rate shortly after this reaches the > 1 °C min^{-1} region. Shortly after the separator melts, short circuits between the Al and Cu current collectors may have caused a high local rate of Ohmic heat generation, as shown by the continuing rise in temperature in Figure 5.11 (a) and (b). After this point, the decomposition of the anode is expected to continue and as the temperature nears 200 °C, the decomposition of the electrolyte, binders and cathode materials may also occur. However, in this test, the self-heating rate drops below 1 °C min^{-1} at ca. 175 °C, this is suspected to be a result of the thermocouple detaching from the cell.
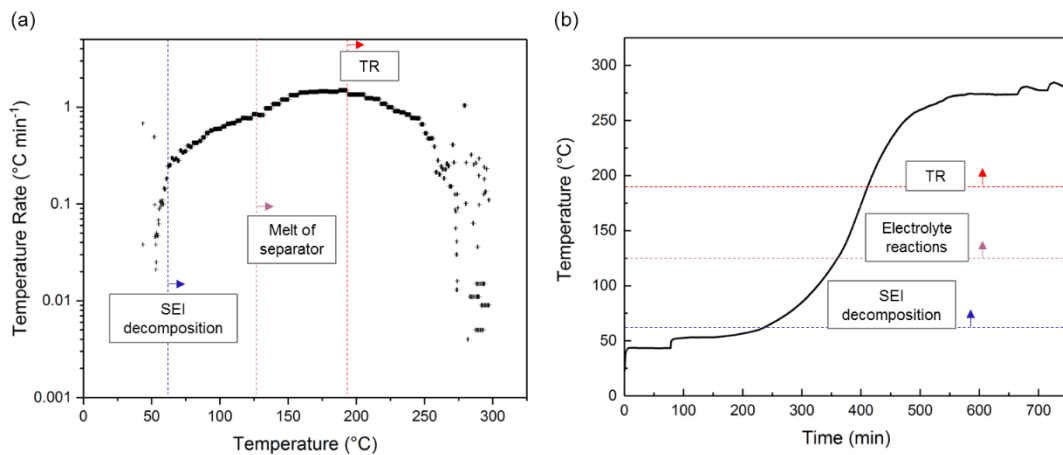
Figure 5.11 ARC self-heating rate profiles of a 1 Ah layered pouch cell. A start temperature of 50 °C was increased step-wise by 5 °C. (a) The inflection at ca. 125 °C shows the start of an increase in heat generation above 1 °C min^{-1} (b) this can be seen in the curve before the plateau in the self-heating profile. At this temperature, it can be assumed that this attributes to the breakdown of the SEI layer.

While the temperature profiles begin to provide a dynamic, thermo-mechanical understanding of the phenomena occurring within the pouch cell during thermal failure, there is limited understanding of the mechanical dynamics: such as how heat and gas generated from the SEI decomposition dissipate through the cell or areas where short circuits may have occurred. Figure 5.12 (b) shows a 3D image of the whole cell after thermal failure. The swelling of the outer pouch can be seen along with the dislocated electrode layers. The orthoslice views in the XZ and ZY planes offer an insight into the build-up of gas and the distribution of pressure within the cell. Orthoslice (position A) in the XZ plane (Figure 5.12 (a)) shows two distinct gaps where generated gas may have escaped through the vacuum seal vertically along the length of the cell. Orthoslice (position C) in the XZ plane reveals that there is a significantly larger space between the central (or 10th) layers vertically along the length of the cell; however, this is not the case in the perpendicular direction which has an uneven displacement across all the layers as shown in Figure 5.12 (c) in orthoslice (position G). It is evident that venting of the cell also occurs across the seals close to the tabs from orthoslice (position E) in the ZY plane, as expected since this is mechanically the weakest point of the cell architecture. As there were no internal temperature measurements taken, it is difficult to predict the temperature distribution across the cell. However, a comparable pouch cell that underwent thermal runaway in the literature suggests that the temperature distribution within a cell of this format is characteristically uneven and can result in a longer failure duration and more gradual mechanical expansion[224] when compared to a cylindrical cell for example[225]. The distribution of melted materials (e.g. Al or Cu) within a cell during failure often indicate internal cell temperatures; for example, Finegan et al. report that molten aluminium remnants enhanced the heat dissipation of local exothermic reactions. For Cell 2, however, there are no visible globules of Al in the obtained X-ray CT images, suggesting the internal cell temperatures did not exceed the melting point of aluminium (> 660 °C).

The 2D orthoslice at a higher spatial resolution in Figure 5.12 (d), although limited by the field of view (3 mm), reveals the undisturbed electrode layer architecture in greater detail. In the two cathodes and two anode layers

visible, there does not seem to be significant delamination of the active cathode or anode layer from their respective current collectors (aluminium and copper). Although the image is taken at the centremost part of the cell, it is difficult to deduce with confidence which layer number it is in reference to the whole stack (20 layers). The defect highlighted in the cathode active layer is suspected to be a due to a small defect from the cathode fabrication rather than as a result of the thermal failure. As expected, the separator layer is not visible as it had melted.
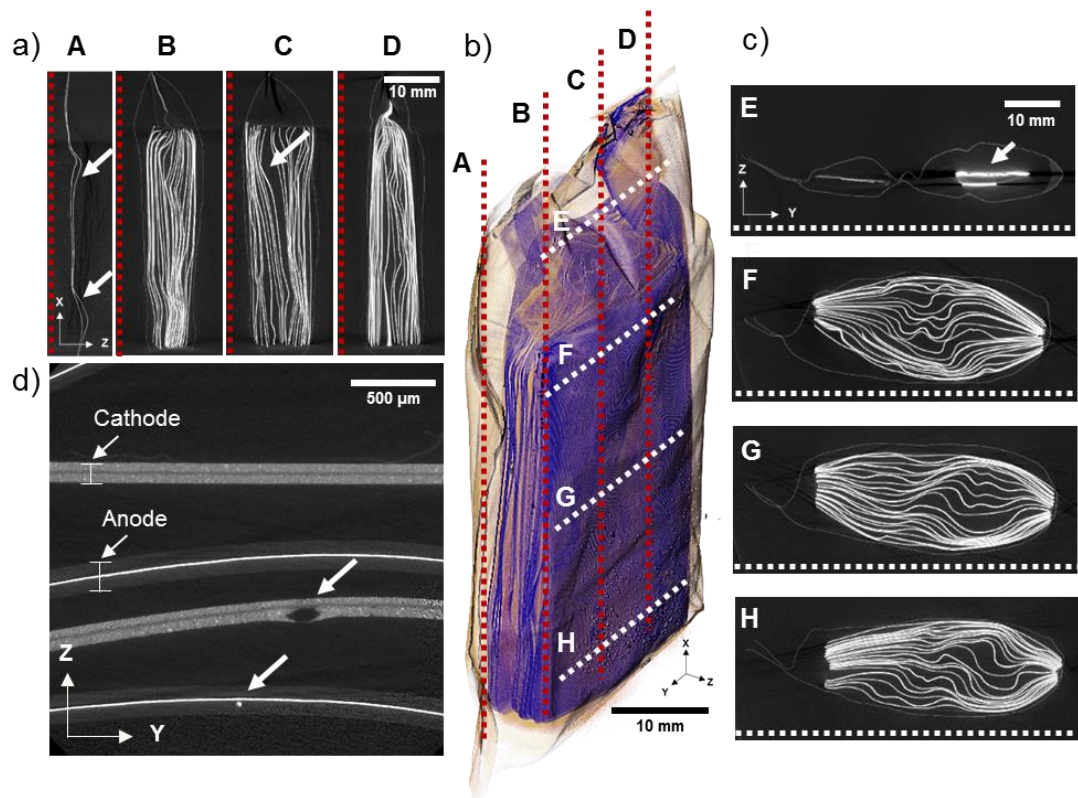
Figure 5.12 Images of pouch cell after thermal failure (Cell 2). Images from the whole cell X-ray CT scan in orthoslices along the (a) XZ planes and (c) ZY planes show the electrode architecture after deformation due to gas generation. Swelling of the outer casing is visible in (c) in the E, F, G and H positions (voxel size: 33.6 µm). The welded anode tab appears to be detached in (c) position E (where the bright white areas are the Cu current collector and Ni tab). A volume rendering in (b) shows the electrode layer architecture within the swollen outer casing, and (d) the orthoslice in the ZY plane with voxel size: 2 µm, shows defects in the cathode and anode layers. Corresponding scan numbers are 2 and 5 in Table 10.3 in Chapter 10.

5.4.4. Nail penetration: internal short circuit failure

Nail penetration can severely damage the internal components of the LIB. Metallic current collectors and separators with insufficient flexibility can fracture and cause direct contact between electrodes. As a result, heat is often generated after a localised short circuit and if the rate of heat dissipation is less than the rate of generation, thermal runaway may be initiated. The centre of Cell 3 was pierced by a nail during the test (100 % nail depth). It is believed that a large amount of heat may have been generated local to the nail tip and the electrolyte may have decomposed shortly after the short circuit: firstly, from the heat generated, and secondly, from reacting with the oxygen entering through the rupture. The gas generation is predicted to have only lasted a short amount of time, and no thermal runaway occurred. The cell did not catch fire and the photograph of the cell outer casing in Figure 5.8 (b) shows how the cell casing appears intact, aside from the point of nail ingress. A supplementary video (Chapter 5_Cell 3_Nail Penetration.mp4) shows the nail penetration and cell behaviour.

Figure 5.13 (b) shows X-ray CT images of the 1 Ah pouch cell after nail penetration and Figure 5.13 (a) shows the pristine, unfailed cell for comparison. From the orthoslice in the XZ plane of the whole cell scan in Figure 5.13 (b)(i), it is evident that all layers were affected by the nail penetration event as a result of the distribution of gas generation across the cell. A closer inspection in Figure 5.13 (b)(iv) reveals delamination of the cathode active material from the Al current collector across the whole cell, and at a greater degree concentrated near the point of nail ingress (positions A – E). The high specific heat and thermal conductivity of Al may have enhanced the dissipation of the heat generated from the electrolyte reactions. Fractures and cracks are also visible in the microstructure of the bulk electrode layers. When compared with the thermally failed cell (Cell 2), the estimated pressure (or disruption of electrode layers) within the nail-penetrated cell is significantly smaller.

A combination of multiple failure behaviours is visible in the ROI scans with voxel size 1.7 μm (Figure 5.13 (b)): the shear stress crossing multiple

layers, fracture and breaking of current collectors and dislodging of electrode particles. Under tension, the electrodes' mechanical response is dominated by the property of the current collector[226]. Furthermore, weak points caused by the intrusion of the active particles into the metal foil as a result of calendaring lower the tensile failure strain of the current collector[189]. In the orthoslice in the XZ plane in Figure 5.13 (b), and XY plane in Figure 5.135.13 (b)(ii), (i.e. looking through the rupture in the direction of the nail), delamination of the anode material (graphite) from the Cu current collector is visible. The Cu current collector also appears to have disintegrated near the rupture. In some areas, the heated Cu likely reacted with oxygen from the surrounding air entering the cell and produced CuO (as can be seen in the green areas highlighted in the photographs of the cell after failure in Figure 5.14). The greyscale value of a material is dependent on its X-ray absorption coefficient. Highly attenuating materials are brighter and/or whiter, such as Cu, and those with lower attenuation coefficients, such as Al, are darker. There is little contrast between the greyscale values of Cu and CuO owing to their similar densities (8.96 and 6.0 g cm^{-3}); as a result, it is difficult to distinguish this from the orthoslices in Figure 5.13 (b). Furthermore, Cu or CuO is only visible in small portions of the rupture. The heat response of a nail penetration induced short circuit event was not measured in this work, however, it is assumed that the temperature of the whole cell did not increase above 120 °C, the melting point of the polyethylene separator, as it was still intact after cell-opening.
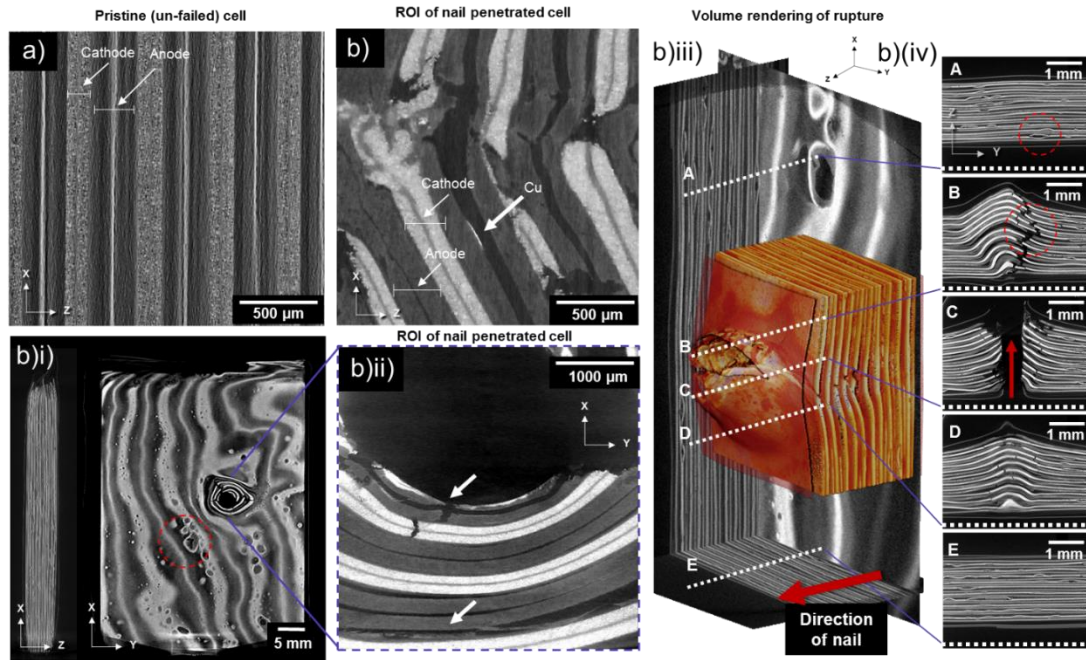
Figure 5.13 Orthoslice of the (a) pristine cell (Cell 1) in the XZ plane (voxel size: 1.83 µm) and orthoslice of the (b) nail penetrated cell (Cell 3) in various planes. The direction of the nail is highlighted in (b)(iii) where a volume rendering of the rupture is shown. Corresponding scan numbers are 3, 4, and, 6 in Table 10.3 in Chapter 10.

Cell after nail penetration
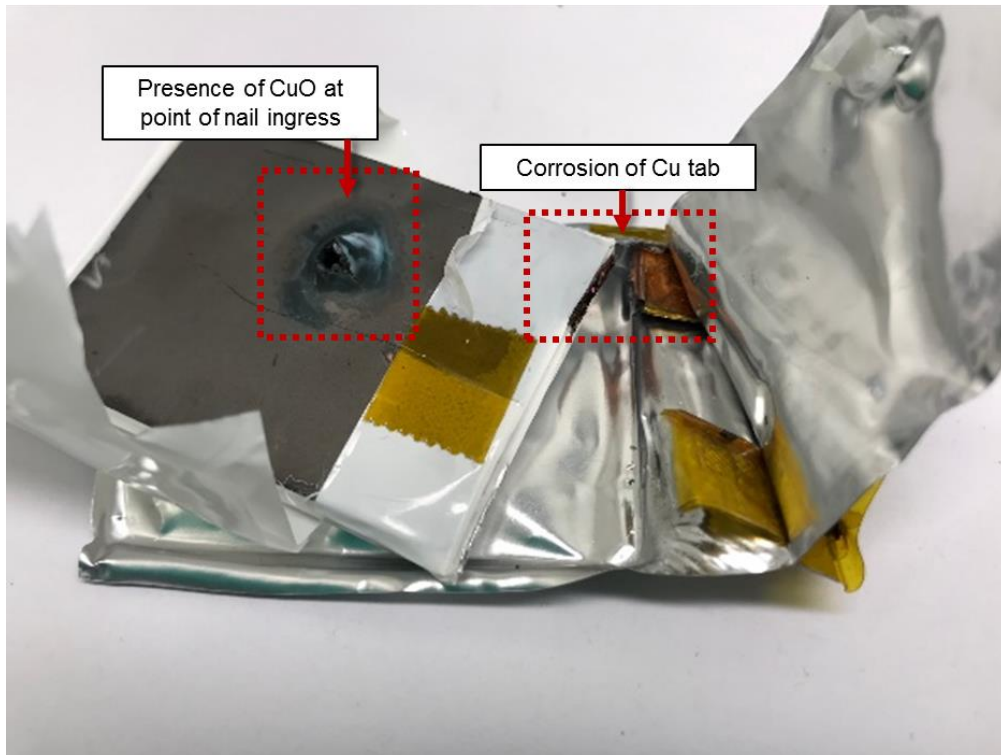
Figure 5.14 Photograph of the nail-penetrated cell upon opening. The presence of CuO (green) is highlighted near the point of nail ingress as well as the corroded Cu tab.

A volume rendering of the rupture and its corresponding orthoslices (in positions A – E) in Figure 5.13 (b)(iii) and (iv), respectively, show where breaks occurred. The rupture developed in both the transverse and nail direction, resembling the shape of a cross, as predicted by Sahraei et al. [189]. Directly above the nail (in position B), a transverse fracture, vertically along the length of the cell, and then across all the layers is visible. Areas, where the current collectors have folded, can also be seen (i.e. where multiple short circuits may have occurred). It is not well known how the evolving microstructural fractures, cracks and folds influence the heat distribution leading up to and/or during the thermal runaway process.

Electrode particles near the rupture centre are severely dislodged which may also have contributed to the short circuit failure. However, it is difficult to confidently conclude whether this was a result of the nail entering (during failure) or leaving the cell (after failure).

5.4.5. Cell opening: component investigation

5.4.5.1.　Bulk electrode layer

After opening the cells, the cathode, anode and separator were carefully separated (Figure 5.8). From the samples harvested from the thermally failed cell, both the anode and cathode displayed a non-homogeneous surface with some distinct deterioration as seen in Figure 5.8 (a)(ii – iii). Large, dark areas appear on the cathode surface primarily where the surface was still in contact with the anode surface. At temperatures greater than 120 °C, the SEI, binder materials and separator are expected to have melted[227]. This is likely to be the reason why the cathode active layer was easily detached from the aluminium current collector during handling. The anode material in Figure 3 (a)(ii), in some regions, is detached from the copper current collector. Some darker areas on the surface are primarily due to the detachment of the material from the cathode following its degradation under high temperatures. For the samples taken from the nail-penetrated cell (Figure 5.8 (b)(ii – iii)), there are some stark differences in the macroscopic appearance of the electrode surfaces: both surfaces have traces of the

separator which melted in some areas. The cathode surface has some distinct features: the surface is rough, and areas where gas pockets formed causing the active material from the Al current collector to delaminate are visible. Furthermore, the surface appears homogenous in colour, compared to the thermally failed cathode, and it was easier to handle (no flaking). The anode layer in comparison displayed a non-homogeneous surface with some silver-grey areas possibly indicating lithium plating is visible. In the areas close to the rupture (or hole left from the nail penetration), sections, where the Cu has oxidised, are visible in green. Darker regions are areas which are expected to be a result of some of the graphite layer being attached to the separator.

Figure 5.15 shows the SEM images of the pristine (a)(i – ii), thermally failed (b)(i) and, nail penetrated (c)(i) cathode materials as well as the thermally failed (b)(ii) and nail penetrated (c)(ii) anode materials. The cathode material of the pristine cell (Figure 5.15 (a)(i)) displays a uniform morphology with some dispersed binder, cracks and secondary particles. As seen in Figure 5.15 (a)(ii), the secondary particle is a spherical agglomerate constructed from primary particles. For the thermally failed cell, some microscopic features display areas where fragments from the melted separator and products from the electrolyte decomposition (i.e. $LiPF_6$, LiF, PF_5) have accumulated[141]. In comparison to the pristine cathode, there are fewer visible cracked particles. It is expected that temperatures above 175 °C would have resulted in the breakdown of the active cathode material[50], and the propagation of degradation may have occurred more due to the larger surface area than through particles with no visible micro-cracks[228]. The microscopic appearance of the cathode surface after nail penetration in Figure 5.15 (c)(i) on the other hand appears unchanged when compared to the pristine cathode. This is further explored (for the nail-penetrated cell) in Figure 5.16, where SEM images were taken from the top, middle and bottom samples of the central cathode layer to investigate the representativeness of the observed surface morphology. The appearance of the surface remains mostly uniform regardless of location, though the middle image (closest to the nail and rupture) appears to have a greater number of inter-particle voids, likely a result of gas expansion.

Figures 5.15 (b)(ii) and (c)(ii) show the morphology of the anode materials after thermal failure and nail penetration, respectively. After the breakdown of the SEI layer on the anode surface the exposed intercalated lithium reacts with the electrolyte solution. A thick deposited layer morphology and cracking of the layer is visible for the thermally failed anode; a single anode particle boundary cannot be distinguished through the layer which is predicted to be caused as a result of the decomposition reactions occurring at temperatures above 150 °C[229]. While images of the pristine anode were not collected in this work, comparisons with a pristine graphite anode surface in literature[139][193] demonstrate how the surface of the anode after nail penetration remains relatively intact with regard to the appearance of clear boundaries. However, the particle surface displays some evidence of degradation/exfoliation which could be explained by the breakdown of the SEI at high temperatures causing new graphitic edges and plane fragments to be exposed at the surface.

Overall, the SEM images reveal important microscopic and surface-level changes to the bulk electrode layers. While collecting the images is a relatively fast method and can cover a large area across the electrode surface, there are still several features, specifically delamination of the cathode and anode layers from their respective current collectors and microstructural parameters such as PSD that are difficult to quantify from 2D images alone. The following section reports the findings from a 3D analysis of the bulk electrode layers using X-ray micro-CT.
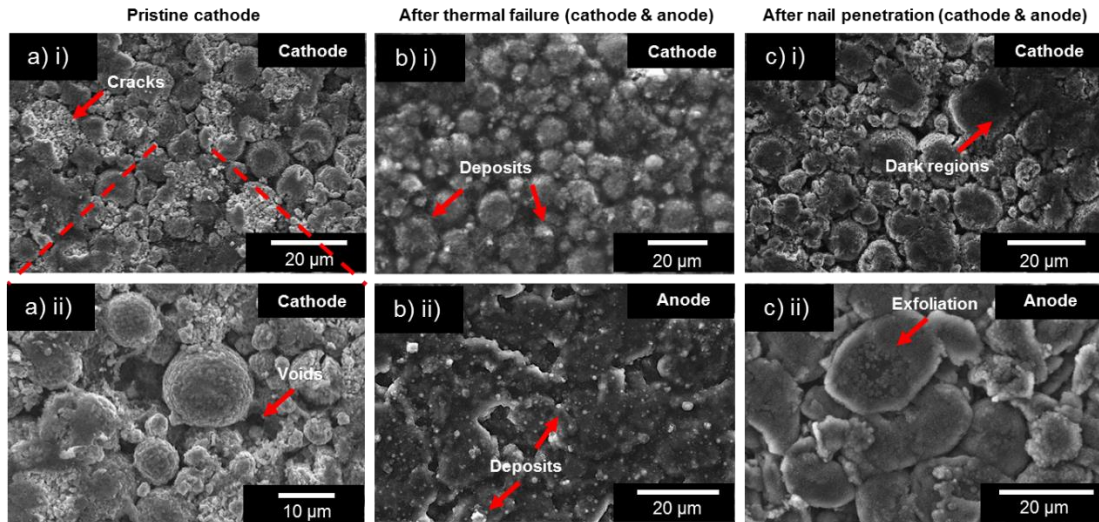
Figure 5.15 SEM micrographs of the (a)(i) pristine cathode at 3050 magnification (ii) and 4720 magnification, and the (b)(i) cathode, and (b)(ii) anode after thermal failure at approx. 3000 magnification. Similarly, the (c)(i) cathode, and (c)(ii) anode after nail penetration at approx. 3500 magnification.
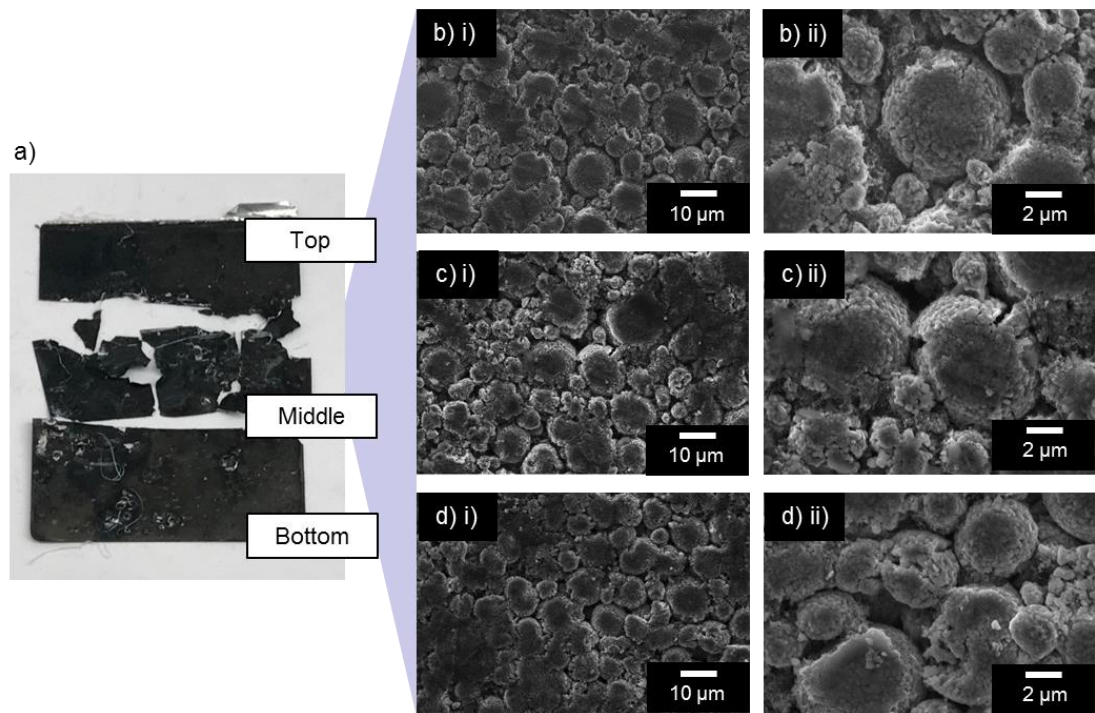
Figure 5.16 SEM micrographs taken at the (b)(i– ii) top, (c)(i– ii) middle, and, (d)(i– ii) bottom, at different magnifications across the cathode layer of the nail-penetrated cell.

The thermally failed and nail-penetrated cells, Cells 2 and 3 respectively, were opened and samples of the anode and cathode electrode layers (0.4 mm x 0.4 mm square) were extracted. Figure 5.17 shows orthoslices in the XY and XZ planes and their corresponding volume renderings from X-ray micro-CT scans. A visual comparison between the two

cathodes (thermally failed and nail penetrated) reveals that there is no significant change to the bulk electrode structure. Further comparison with the pristine cathode bulk layer in Figure 10.3 confirms there is little difference (at this resolution) from the fresh state to the failed. Anode samples from both cells follow the same trend.
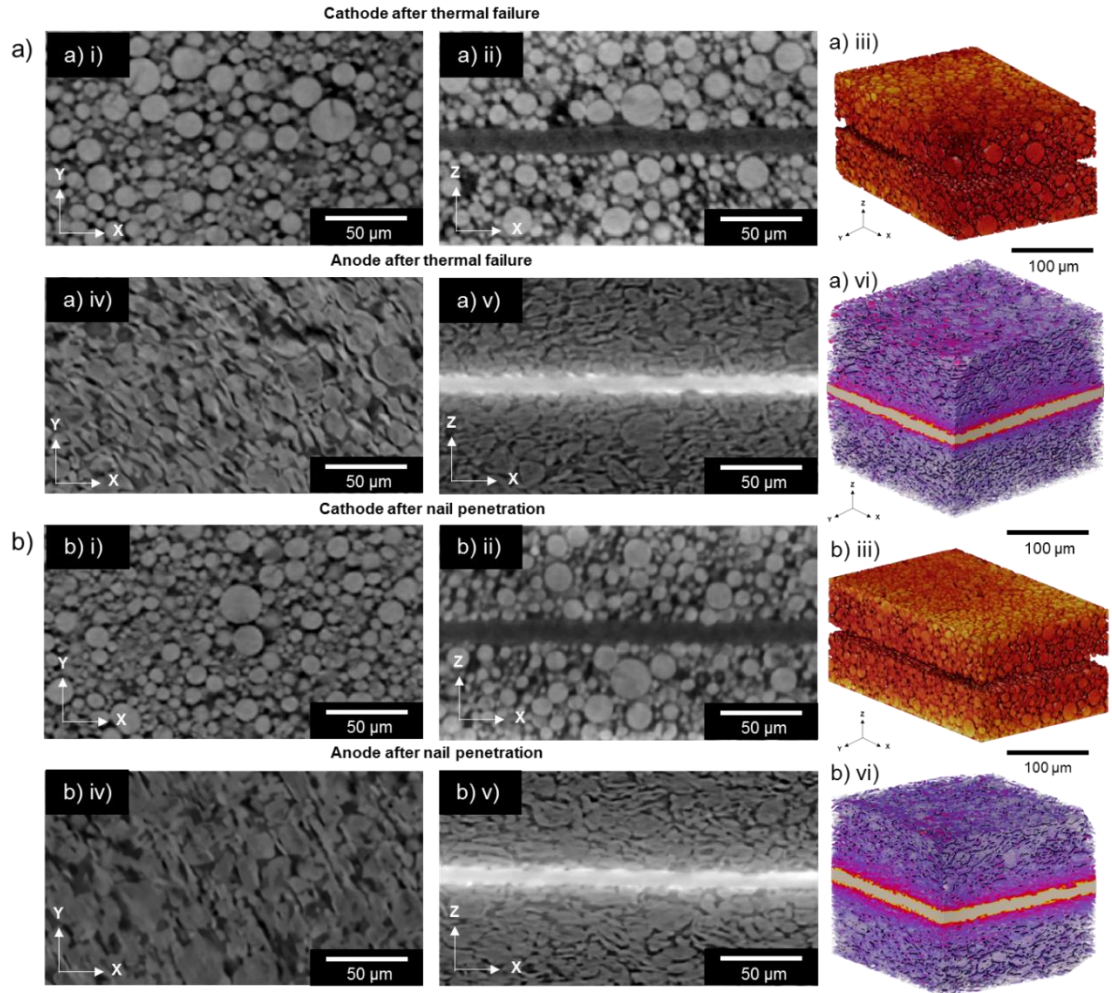
Figure 5.17 Orthoslices in the XY and XZ planes, and volume renderings, of the (a)(i – iii) cathode and (a)(iv – vi) anode after thermal failure and (b)(i – iii) cathode and (b)(iv – vi) anode after nail penetration. Corresponding scan numbers are 8 – 11 in Table 10.3 in Chapter 10.

The PSD of the pristine cathode sample is compared to that of the post-mortem samples: thermally failed (Cell 2) and nail penetrated (Cell 3). Table 10.3 (in Chapter 10) summarises the PSD findings, as well as the particle volume fraction, tortuosity factor and surface area per volume extracted from the datasets. The mean diameter extracted from the pristine bulk cathode layer is 5.39 µm, and the mean diameters for the samples extracted from Cells 2

and 3 were 4.76 µm and 6.10 µm, respectively. It is difficult to confidently conclude a trend from the mean particle diameters extracted from the bulk electrode layers due to the limited resolution of the X-ray technique and the small sample size. However, the spread of data in the PSD in Figure 5.18 (a – c) shows there is an additional peak below 2.5 µm for both the failed cathode layers when compared to the pristine cathode. This is predicted to be a result of debris, fractured surface particles and/or delamination of particles from the Al current collector. Figure 5.22 shows the percentage change of parameters extracted from the bulk cathode layers of Cell 2 (thermal failure) and Cell 3 (nail penetration) from the pristine bulk cathode layer.
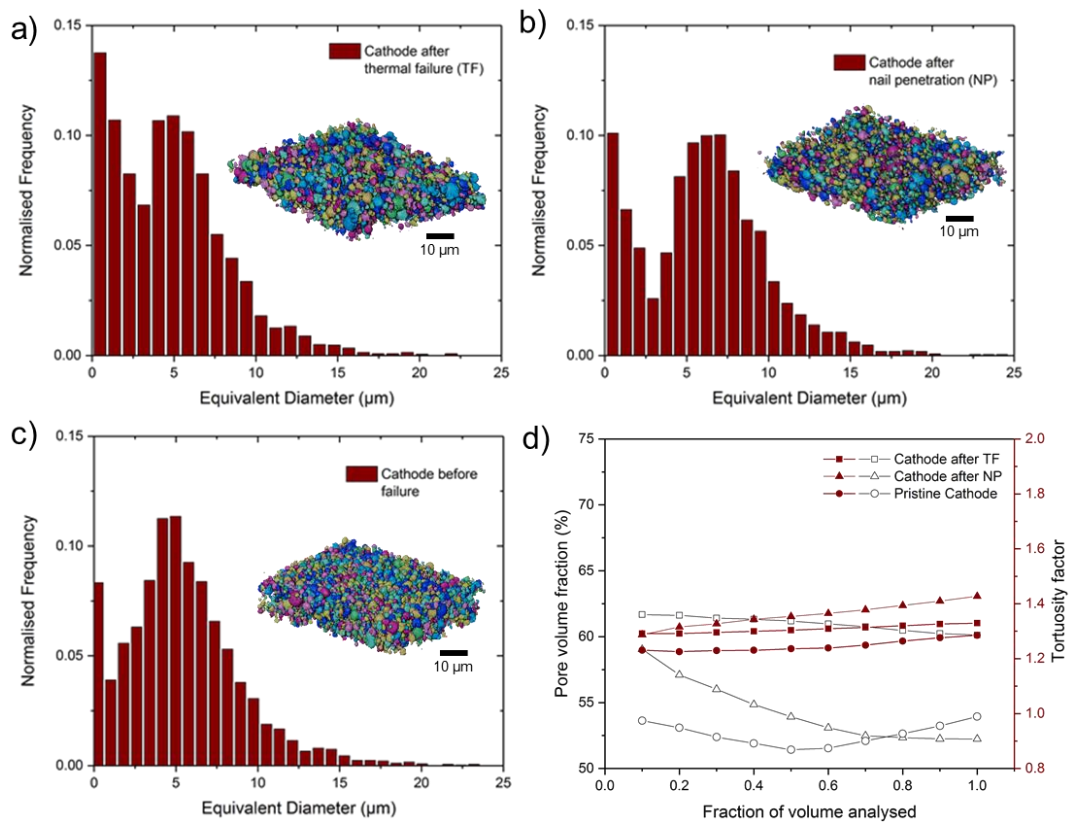
Figure 5.18 Particle size distributions for the (a) pristine, (b) thermally failed, and, (c) nail-penetrated bulk cathode layer samples. Representative volume analysis of the pore volume fraction and tortuosity factor as a function of the fraction of the volume analysed is shown in (d).

There are a greater number of particles with a diameter < 1 µm in the thermally failed cathode layer compared with the nail-penetrated sample. This is not reflected in the particle volume fractions and the surface area per volume for the three samples (Table 10.3), which are, in the same order, 0.46, 0.40 and 0.48, and 0.478, 0.408, 0.490. The particles that underwent thermal failure

(and reached temperatures > 250 °C) exhibit the lowest surface area per volume, which contradicts what is expected: the smaller the particle size, the lower the thermal stability of the material[168]. The temperature profile of the nail-penetrated cell (Cell 3) was not measured, however, from the literature[188][186], it is predicted that the nail tip for this cell type may have exceeded 120 °C and initiated localised heat generation: causing the electrolyte to boil and generate gas[227].

The bulk anode layer from Cell 2 has a greater mean particle diameter, 16.99 µm than the sample from Cell 3, 13.59 µm. However, the pore volume fraction (0.31 and 0.36), surface area per volume (0.654 and 0.660), and tortuosity factor (2.97 and 3.19), of the thermally failed and nail penetrated anodes are similar. The surfaces of the two anodes in Figure 5.15 (b)(ii) and (c)(ii) show the structure of the effects of heating to temperatures > 250 °C and the extent of decomposition and deposits on the surface of the thermally failed anode. However, the 3D analysis shows how the anode and its microstructural properties remained intact below the surface. This is reflected in the spread of data of the PSD in Figure 5.19 (a – b) where there are a greater number of particles with diameters > 25 µm for the thermally failed anode, which is expected to be those furthest away from the current collector and shown in the 2D surface images.
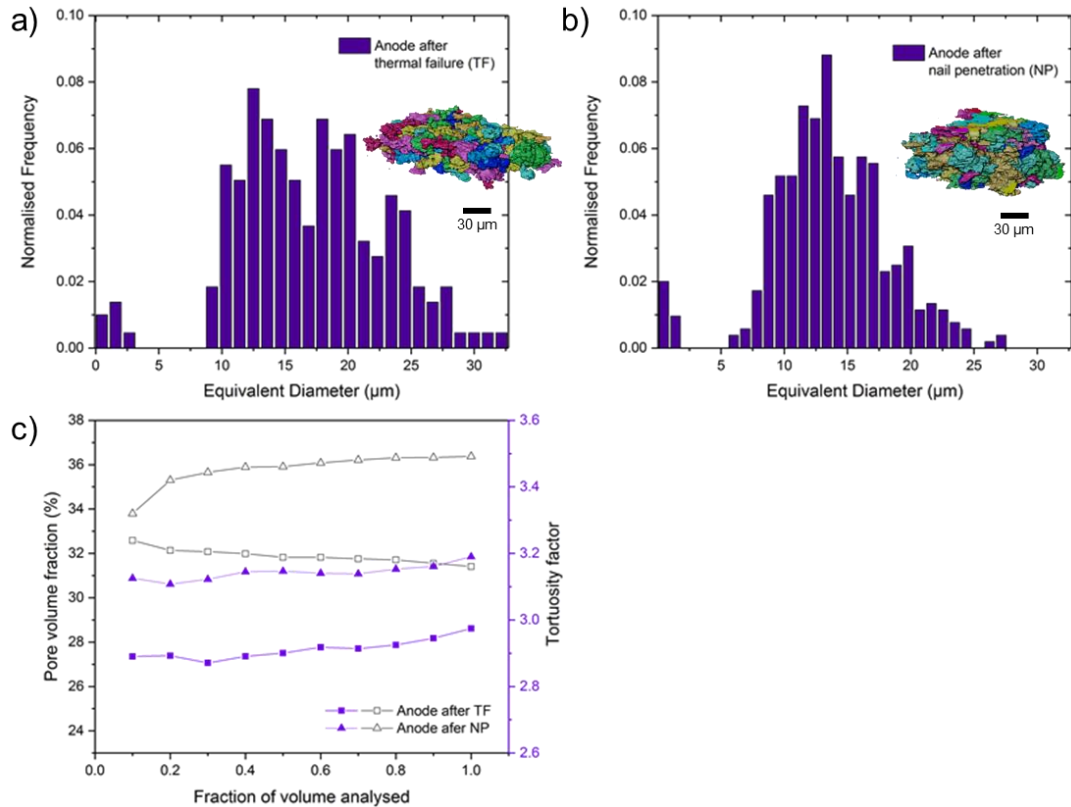
Figure 5.19 Particle size distributions for the (a) thermally failed, and, (b) nail penetrated bulk anode layer samples taken from the centre of the cell 2 and 3, respectively. Representative volume analysis of the pore volume fraction and tortuosity factor as a function of the fraction of the volume analysed is shown in (c).

From the whole cell scans, there were obvious areas where the cathode and anode layers had delaminated from their respective current collectors. However, due to the small sample size (0.4 mm x 0.4 mm) required for the bulk electrode layer scans, it is difficult to directly observe this phenomenon. Furthermore, despite using the whole cell scans to predict where to extract samples; it was still difficult to pinpoint an area where delamination had occurred. Bulk electrode layer scans are useful for determining key material characteristics such as PSDs and tortuosity. They are especially useful for understanding heat distribution across layers within a whole cell, however, they are limited by their sample size and may not give a full representation of the phenomena that occurred during failure.

5.4.5.2. Electrode particles

Figure 5.20 (a)(i) shows the cathode in its pristine state at a voxel resolution of 0.0631 µm, in the XZ plane. Similarly, Figures 5.20 (b)(i) and (c)(i) show the cathode extracted from the thermally failed and nail-penetrated cells,

at voxel resolutions of 0.126 µm. All three samples clearly show two phases: particle (light grey) and pore/carbon binder domain (dark grey). It is difficult to distinguish between the pore and CBD at this resolution[181]. The mean particle diameters are 2.93 µm (pristine), 4.43 µm (thermally failed) and 4.47 µm (nail penetrated). When compared to the Versa datasets, the pristine cathode has an unexpectedly small mean particle diameter in comparison to that extracted from the pristine bulk cathode layer (5.39 µm). This may have a direct correlation to the number of intra-particle cracks within the pristine sample. For example, the label analysis carried out during the PSD extraction may have assigned a single particle that was cracked in two as two separate particles with smaller diameters. As a result, the greater the number of particle cracks; the greater the number of smaller particle sizes in the PSD[230]. Figure 5.22 highlights the extent of variation of the parameters extracted from the bulk electrode layer (micro-) and particle morphology (nano-CT) 3D images. The surface area per volume of the post-failure cathode particles showed the greatest increase when compared to the surface area per volume of the pristine particles. This could be attributed to the changes in the particle morphology and/or orientation within the cathode layer as a result of the failure mechanisms[159][43]. Nevertheless, it is still important to consider the sample volume and its statistical significance here, while this resolution helps elucidate certain particle features, it is difficult to confidently compare the PSD trends obtained from the bulk electrode layers that have greater sample sizes/bounding box dimensions (see Table 10.3). Representative volume analysis of the particle scans shown in Figure 5.21 however illustrates the accuracy of the pore volume fraction and tortuosity factors across the sample sizes for Ultra scans (< 65 µm).
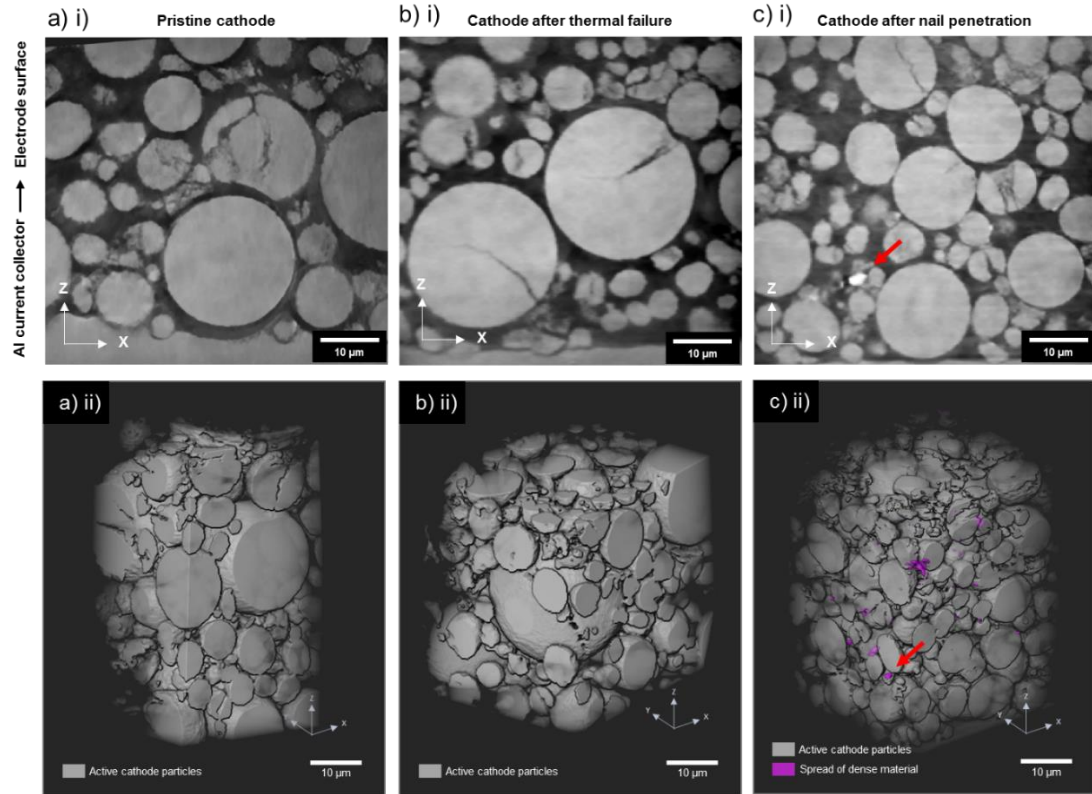
Figure 5.20 Orthoslices in the XZ plane of the cathode acquired using X-ray nano-CT for (a)(i) the pristine, (b)(i) after thermal failure (Cell 2), and (c)(i) after nail penetration (Cell 3) samples. The Al current collector is at the bottom (visible in (a)(i) and (b)(i)) and the electrode surface is at the top. A highly attenuating spot is highlighted in (c)(i). Volume renderings of the (a – c)(ii) pristine, Cell 2, and Cell 3, show the particles after segmentation. The denser material deposits are highlighted by the red arrow. Corresponding scan numbers are 12 – 14 in Table 10.3 in Chapter 10.
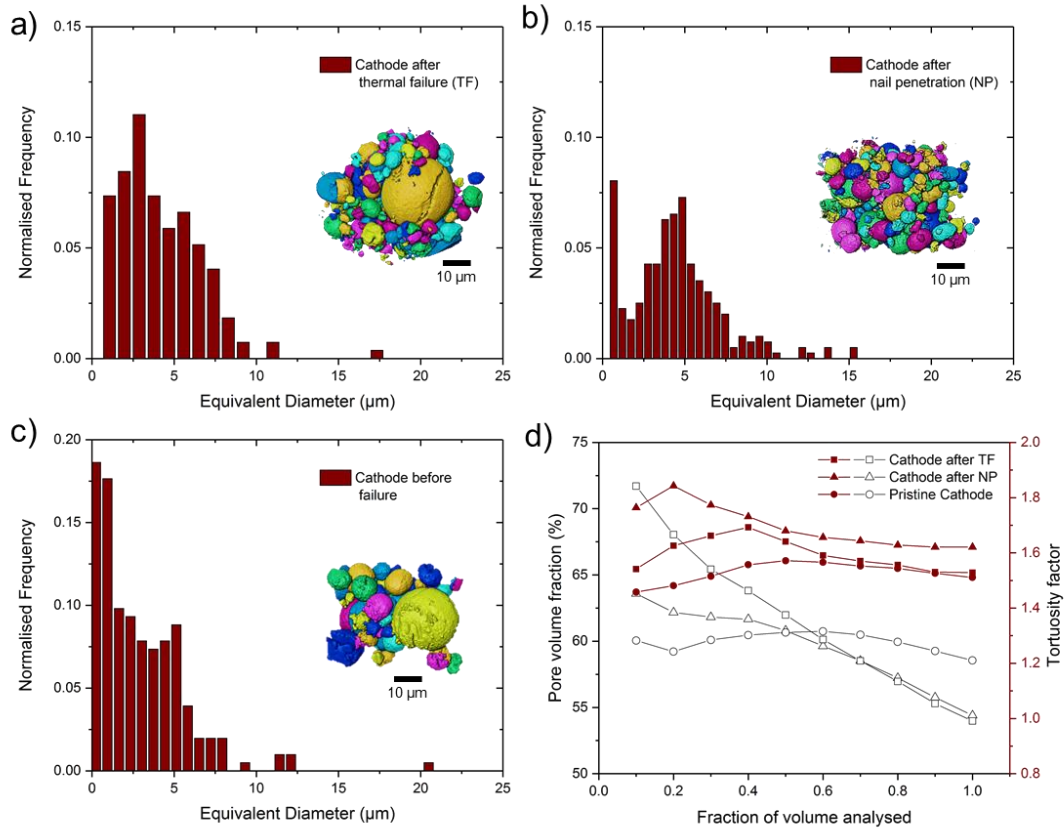
Figure 5.21 Particle size distributions for the (a) pristine, (b) thermally failed, and, (c) nail penetrated particles. Representative volume analysis of the pore volume fraction and tortuosity factor as a function of the fraction of the volume analysed is shown in (d).

The particles within the cathode layer after nail penetration display some bright regions, highlighted in the greyscale image in Figure 5.20 (c)(i). The brighter regions represent a highly attenuating/dense material, such as Co or Cu due to their high atomic masses. Figure 5.13 (b) displayed dislodging of electrode particles, however, it is difficult to predict the precise cause of the contamination in ex-situ. Typically, when a cell is forced to over-discharge, the cell voltage drops below the safe cut-off voltage. The nail penetration event is expected to have caused a localised internal short circuit and triggered similar mechanisms to that of an over-discharge[231]: rapid delithiation of the anode and lithiation of the cathode. As the anode potential increases it can overcome the overpotential required for Cu dissolution, as a result, Cu is oxidised. Cu^+/Cu^{2+} ions may penetrate the separator and become deposited on the cathode surface. A volume rendering in Figure 5.20 (c)(ii) shows the spread of the dense material within the cathode layer (acquired using X-ray nano-CT).

The volume fraction of the dense material is 0.00028, making it difficult to distinguish the SEM (Figure 5.15 (c)(i)) or micro-CT (Figure 5.17 (b)) images.

There are several micro-cracks, which don't span the entire particle diameter, and shattered particles, which present as small fragments across all three cathode samples (pristine, thermally failed and nail penetrated). It is predicted that the presence of these cracks is more likely to be a result of the manufacturing process (via calendaring)[228] than as a result of thermal and/or short circuit failure. Furthermore, Figure 5.20 (a – b)(i) shows areas where the active particles have intruded into the aluminium foil as a result of calendaring, suggesting that the local stress concentrations[170] were high enough to deform the current collector sheet, and subsequently high enough to induce micro-cracks and particle shattering.
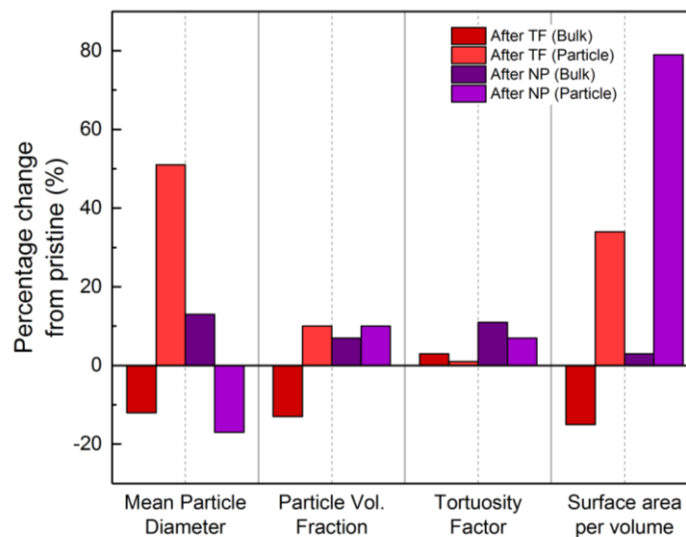
Figure 5.22 Percentage change for the mean particle diameter, particle volume fraction, tortuosity factor and, surface area per volume, of the micro-CT bulk electrode layer image (Bulk), and nano-CT image (Particle) of the thermally failed (TF) and nail penetrated (NP) cathode layers, from the pristine cathode layer and particle scans. A positive percentage represents an increase, and a negative represents a decrease. Corresponding scan numbers are 7, 9, 11 – 14 in Table 10.3 in Chapter 10.

Figure 5.22 shows how the mean particle diameter, particle volume fraction, tortuosity factor and surface area per volume changes after thermal failure and nail penetration (compared to those of the pristine sample). This is shown separately for the two types of analyses: bulk layer and particle. The mean particle diameter increased by 50 % for the analysis at higher magnification, while it reduced by approximately 10 % in the analysis at a bulk

electrode layer level. The dataset at a higher magnification involves using a smaller sample size, making the result less statistically significant. The results obtained for the surface area per volume at the nano-scale for both the thermal failure and nail penetration samples shows a very large increase compared to the pristine sample. Although the pristine sample and the failed sample are from the same material, they are not direct comparisons of the same particles i.e. the samples are collected from two different cells. Furthermore, at higher magnification, the smaller sample size makes the result less representative of the entire bulk material. Generally it is important to consider which method a parameter is collected by within the context of multi-scale X-ray CT imaging, as a higher resolution does not always translate to a more accurate characterisation of a material.

5.5. Conclusions from Chapter 5

Various methods and techniques for multi-scale imaging using X-ray CT were introduced and explored in this chapter. The variations in LIB materials in terms of size, shape, format, and internal structure, at various length scales ranging from particle morphology, and bulk electrode structures up to whole cell design were each addressed in the context of materials characterisation.

A methodology for interior tomography of high aspect ratio samples; i.e. single-layer pouch cells was introduced and compared with the resolutions achieved in literature for cathode materials. The non-destructive technique is useful for in-situ testing for single-layer pouch cells samples up to ~ 1 Ah, however, this can be further expanded up to cells with multiple layers and/or thicker electrode tapes, which was later shown for the failure and post-mortem analysis datasets.

The electrode microstructure can have a profound effect on LIB performance and safety. This chapter correlated microstructural data obtained from nanoscale X-ray CT of three cathode materials of the same chemistry but varying composition. Parameters such as their particle size, porosity and tortuosity were extracted and used to probe the role of microstructure in

thermal behaviour. Heat flux signals from differential scanning calorimetry showed that a decreased particle size, the presence of particle cracks or increased particle surface area contributes to a faster rate of heat generation, whereas a decreased porosity can reduce the overall heat generation within the cell.

The LIB can fail by multiple different failure mechanisms across their multi-layered structures and scales. While they're extensively investigated and tested at a whole and particle scale, there is limited standardisation across the methodologies for safety testing and post-mortem analyses. The use of X-ray CT to investigate failure mechanisms by invasive and non-invasive methods was also demonstrated in this chapter.

At present, whole-cell X-ray CT is used to investigate the architecture of a battery post-failure concerning its electrode deformation and/or safety features. Oftentimes it is used as a technique to determine specific areas of interest, for example, dendrite growth, electrode folds, tab placement etc. This chapter showcased the benefits of ROI scans at voxel resolutions between 1.7 - 2 µm in post-mortem cells. The whole cell X-ray CT in this work offered a method to investigate the volume change due to swelling, gas dispersion and bulk electrode behaviour from various stresses (heat and gas generation and puncture with a nail) within the cells without disturbing their delicate environments.

While invasive measurements yielded useful bulk electrode layer and particle parameters, they did not demonstrate a full representation of the failure phenomena. The post-mortem analysis by SEM is a relatively faster analysis method, however conclusions made solely from 2D images gave only a surface-level understanding and key features such as particle mixing and/or electrode delamination were difficult to identify. X-ray micro- and nano-CT of the bulk electrode layer and particle morphologies were more useful in understanding the particle behaviour as a whole, for example, PSDs and cracking and how they may have affected heat dissipation throughout the cell, however, they were also proven to be insufficiently representative and limited by sample size. Furthermore, the technique required complex sample

preparation techniques and can make it a relatively slow method for commercial post-mortem analyses.

Of the two failure mechanisms analysed in this chapter, the thermally failed cell appeared to undergo a more severe failure. It reached a higher maximum temperature and had significantly more damage across various length scales from its whole-cell architecture (swelling and distribution of gas), layers (melted separator) and electrode surfaces (deposits). The nail-penetrated cell, on the other hand, was relatively less severe: the majority of its outer shell casing remained intact and heat dissipated through the cell more uniformly.

It is important to note that due to the limited number of repeat tests presented here, conclusions with high confidence cannot be drawn from these results. Nevertheless, these results demonstrate the utility of both invasive and non-invasive X-ray CT at multiple length scales for evaluating the effects of microstructure on thermal behaviour, and battery failures (thermal and internal short circuit) of various formats and shapes. The workflows introduced in this chapter can be readily applied to parametric studies of battery performance, safety and failure.

Chapter 6

6. Combination of Thermal Analysis and Multi-scale Imaging

Sections of this work have been peer-reviewed and published in the Journal of The Electrochemical Society (D. Patel, J. Robinson, S. Ball, D. J. L. Brett, P. R. Shearing, *Thermal Runaway of a Li-Ion Battery Studied by Combined ARC and Multi-Length Scale X-ray CT. (2020). doi:10.1149/1945-7111/ab7fb6.*

6.1. Introduction

LIB failure occurs across multiple length scales. In this chapter, the properties of thermal failure and its effects on electrode materials were investigated in a cylindrical commercial battery (18650) using a combination of ARC and multi-length scale X-ray CT. ARC measured the heat dissipated from the cell during thermal runaway and enabled the identification of key thermal failure characteristics such as onset temperature and the rate of heat generation during the failure. Analysis before and after failure using SEM and X-ray CT were performed to reveal the effects of failure on the architecture of the whole cell and microstructure of the cathode material at two resolutions for bulk electrode and particle morphology analysis.

Mechanical deformations to the cell architecture were revealed due to gas generation at elevated temperatures (> 200 °C). The extreme conditions during thermal runaway caused the cathode particles to reduce in size by a factor of two. Electrode surface analysis revealed surface deposits on both the anode and cathode materials. The link between electrode microstructure and heat generation within a cell during a failure is analysed and compared to commercially available lithium-ion cells of varying cathode chemistries. The optimisation of electrode designs for safer battery materials is also discussed.

To decipher the sequence and severity of thermal runaway reactions, ARC measurements of high-power lithium batteries in a 18650 format have been widely reported. These studies quantify failure by determining the onset temperature (the critical temperature at which the thermal runway is initiated) and the rate of heat generation during failure. Experiments in literature are primarily conducted on commercial cells with cathode materials such as $LiCoO_2$ (LCO), $Li(Ni_xMn_xCo_x)O_2$ (NMC) and $LiFePO_4$ (LFP)[232][233][234] each showing varying onset temperatures of 150 °C, 170 °C and 195 °C, respectively[124]. Studies have also revealed that high SOCs aggravate exothermic reactions, where the self-heating rate increases exponentially with SOC[78]. For a $LiNi_{0.8}Co_{0.15}Al_{0.05}O_2$ (NCA), 1 Ah capacity cell, Abraham et al.[229] reported self-heating initiated at the anode at 84 °C and surface deposits on both the anode and cathode surfaces were found using X-ray photoelectron spectroscopy.

In addition to the thermodynamic stability of components and cell size, the composition and morphology of the electrode materials directly influence cell behaviour during failure[47][123][124][235]. Surface-dependent features such as specific surface area play a large role in determining the degree of heat generation during failure[128]. Smaller particles have been shown to release oxygen at a higher rate during decomposition, corresponding to an increase in heat generation, and greater loss of mass during failure. At high temperatures, the decomposition rate of the cathode increases linearly with great particle surface area[168]. Jiang and Dahn[129] have demonstrated a reduction in particle size of $LiCoO_2$ from 5 μm to 0.8 μm resulted in a lower onset temperature due to faster kinetics.

The fast kinetics of the exothermic reactions leading up to thermal runaway (within seconds) require high-speed techniques to record developments within a battery during failure. High-speed operando X-ray imaging has previously been used to track structural deformations leading up to and during thermal runway in 18650 format cells[185][131]. Additionally, X-ray CT with a multi-length scale approach has been used to analyse Li-ion battery materials[155] and demonstrated as an effective diagnostic tool for cells during[161][63] and after failure[131]

In this chapter, ARC in combination with (pre and post-mortem) lab-based multi-length scale X-ray CT imaging is used to understand the failure of a commercial LIB. The image-based analysis is used to quantify the changes in particle morphologies of the cathode, before and after failure, to investigate the effect of this design feature on battery safety.

6.2. Experimental

6.2.1. Thermal failure/runaway

A commercial 2.2 Ah 18650 battery LGDAS31865 P313K083A6 LG Chem, South Korea), consisting of a $Li(Ni_{0.6}Mn_{0.2}Co_{0.2})O_2$ cathode, polymer separator and graphite anode, was fully charged to the maximum rated voltage, 4.2 V at 1 C via a CCCV charging protocol. Before conducting the ARC experiments, the OCV was checked to ensure no capacity fade had occurred. The thermal abuse test was performed using ARC inside a calorimeter (Phitec Battery Test Calorimeter, HEL Group, Herts., UK) using the heat-wait-search method. Once the battery had reached a start temperature (25 °C) the following procedure was initiated: the calorimeter increased the temperature in discrete steps (5 °C), waited for any thermal transients to decay and subsequently monitored the battery temperature. If within this time, the temperature remained unchanged, up to a threshold value (0.02 °C min-1), the calorimeter continued to increase the temperature by 5 °C until self-heating was detected.

6.2.2. Pre- and post-mortem X-ray CT

Tomographic reconstructions of varying length scales and sample sizes were produced using three different lab-based X-ray CT systems; a Nikon XT 225 (Nikon Metrology, Tring, UK, a Zeiss Xradia Versa 510 and a Zeiss Xradia Ultra 810 (Carl Zeiss XRM, Pleasanton, CA, USA). Pre- and post-failure X-ray CT images of the whole battery were captured using a Nikon XT 225: the geometric configuration of the radiographic scans resulted in a pixel resolution of 38 μm and 35 μm, for the pre- and post-failure scans, respectively. An accelerating voltage of 210 kV with a tungsten target was used to generate

3176 projections. The acquired datasets were reconstructed using CT Pro 3D software with a built-in FBP algorithm with subsequent data was visualised using Avizo Fire 9.5.

Before the pre- and post-failure X-ray micro-CT scans and SEM, the cylindrical cell casing was removed using a pipe cutter inside an argon glovebox as described in Section 3.3.3. The spiral wound layers were carefully unrolled and the separator, positive and negative electrodes were isolated from one another. The electrodes were washed with dimethyl carbonate to remove any electrolyte and left for two days to dry. The fresh cell was discharged to 0 V before being dismantled. Electrode samples were taken from the centre of the unrolled cell. SEM samples were prepared by cutting a ~5 mm electrode square while micro-CT samples were prepared by cutting a ~3 mm triangle from the corner of an electrode and attaching (5-minute epoxy, ITW Devcon, USA) it to the end of a pin attached to the sample holder. Details of the parameters used to capture the microscale images and the pixel resolutions achieved are summarised in Table 6.1.

Nanoscale post-failure analysis of the positive electrode was imaged using an X-ray nano-CT system (Zeiss Xradia Ultra 810). Electrode samples for nanoscale characterisation were prepared using a laser micro-machining procedure to achieve the desired sample size[202]. A resolution of 63.1 nm was achieved using a Cr target with an accelerating voltage of 35 kV and a tube current of 25 mA. Further details of the image scanning parameters are summarised in Table 6.1. For both micro- and nano-scale CT, tomographic reconstruction was achieved using the XM Reconstructor software suite (Zeiss, Pleasanton, CA, USA).

Table 6.1 Summary of the multi-scale X-ray CT scanning parameters used in this work.

Parameter	Macroscale		Microscale		Nanoscale
	Pre-failure	Post failure	Pre-failure	Post failure	Post failure
Voltage (kV)	210		80	100	35
Projections	3176		1601	1301	1601
Exposure time (s)	1		38	35	
Pixel size (µm)	38	35	0.48	0.37	0.0631

Reconstructed data was processed using Avizo Fire 9.5 software (FEI VSG, France). After reconstruction, a non-local means filter was applied to the images to reduce noise and preserve phase boundaries. Phases were separated based on their grey scale values, where weakly attenuating materials are displayed in shades of grey and highly attenuating materials in white. Binary images and volume renderings are subsequently used for measurements of porosity and PSD using Avizo Fire 9.5's label analysis tool. Image processing in the context of LIB materials requires pre-processing to enhance particular features by using a set of filters. This procedure is often performed to prepare data for threshold-based binarisation. The second step is to distinguish phases by assigning each voxel to a particle or pore phase based on the measured grayscale value. This is often sensitive to variations such as enhanced edge contrast and so the choice of thresholding approach becomes important for particular data sets and their features. Detailed descriptions of various image analysis techniques are provided specifically for lithium-ion battery electrodes in the following reviews[236][164].

All SEM micrographs are obtained from a Zeiss EVO 10 SEM, using the SE1 signal at 12 kV accelerating voltage with a magnification of approximately 5,000 yielding pixel sizes ranging between 57 – 69 nm for all images.

6.3. Results

6.3.1. Thermal runaway

ARC was performed to initiate thermal runway in a commercial 18650 cell. The temperature profiles obtained for the cell are shown in Figure 6.1. The initial exothermic event observed in Figure 6.1 (a) between 30 – 50 °C is a result of the breakdown and reformation of the SEI layer[76], while the second visible exotherm at 175 °C indicates the onset of thermal runaway. It is possible that the discontinuity between the two exotherms is a result of the cell rupturing during failure, initiating the Joule-Thompson effect, as previously reported in literature[235]. Further evaluation of the thermal failure process reveals the reaction rate of initial degradation and self-heating rate of thermal runway to be 7.82×10^{-3} min^{-1} and 8.5×10^{-2} min^{-1}, respectively. The plateau after the initial SEI layer exotherm observed in Figure 6.1 (b), may be attributed to the shutdown separator incorporated into the cell design. The tri-layer composite nature of the polypropylene (PP) melting at approximately 135 °C and polyethylene (PE) at 165 °C, arranged as PP|PE|PP, is shown to have delayed the onset of thermal runway by approximately 1,750 minutes. This is outlined further in Figure 6.1 (a), at 165 °C, where the separator melts and possible rupture of the cell may have occurred. It is considered that the thermal runaway is only delayed, in this case, due to the ARC operating in the heat-wait-search mode[96]. No venting or material rejection was observed.
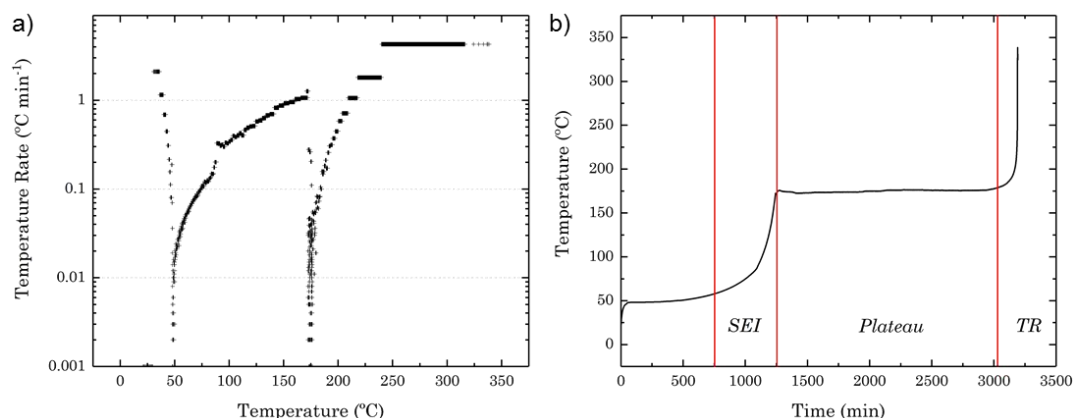
Figure 6.1 ARC self-heating rate profiles of a commercial 18650 cell. (a) The start temperature of 50 °C was increased step-wise by 5 °C. An onset temperature of 175 °C is shown. (b) Plateau in self-heating rate can be attributed to the shutdown separator.

While the self-heating rate determined from this study reveals important information regarding heat dissipation within the cell, further studies are required to compare the influence of different cell chemistries and designs. A cylindrical cell with tightly wound layers (like a 18650 format) will have a different heat dissipation time constant when compared to a pouch cell of equivalent capacity. Robinson et al. have previously reported a thermal runaway rate of 0.213 min^{-1} using ARC with similar parameters for a 2.5 Ah pouch cell[96].

NMC is amongst the most widely used contemporary cathode materials, and its demand is projected to plateau until 2025[237]. Results from this work correlate well with literature values for commercial 18650 cells with similar cathode chemistries and capacities. While these comparisons offer valuable insights into the thermal runaway process regarding the onset temperature, and rate of heat generation, the specific effects of whole cell structure and electrode morphology on this behaviour are not well understood. Understanding heat dissipation at the whole cell level, as well as a component level, is essential for accurately comparing the thermal runaway mechanism in commercial LIBs.

Macroscale X-ray CT results of the fully charged cell pre- and post-failure are shown in Figure 6.2. The non-destructive nature of the technique enables the visualisation of the architectural changes within the structure of the cell after failure and can be compared to the same cell before failure. A 3D reconstruction of the cell before failure is presented in Figure 6.2 (a); where orthogonal slices in the (X, Z) and (Y, Z) planes are also shown, similarly orthogonal slices of the failed cell are shown in Figure 6.2 (b) for comparison. Figure 6.2 (b) shows the propagation of gas formation due to the decomposition of the SEI layer during failure. For example, Arrow 1, highlights the possible delamination of an electrode layer where a gas pocket has formed[191]. Arrows 2 and 3 show changes both to the outer casing of the cell as well as the arrangement of electrode layers. As the internal cell pressure increased, the ridge depicted by arrow 2, has expanded and changes to the tightly wound electrode layers are visible.

At temperatures above 200 °C thermal decompositions of the cathode occurs, where changes to the crystal structure begin and heat, in addition to CO_2 and H_2O are released[238]. The effects of this phenomenon can be visualised in Figure 6.2 (b) where the active cathode material may have delaminated from the aluminium current collector. Furthermore, changes to the outer casing, particularly at the positive terminal are shown, although there is expansion, there were no visible ruptures to the cell during post-failure analysis. Similarly, Finegan et al. reported that the cell casing and positive cap of a $Li(Ni_{0.33}Mn_{0.33}Co_{0.33})O_2$ 2.6 Ah 18650 cell at 100% SOC remained intact as it experienced thermal runaway[185]. Although gas formation within the cell increases the internal pressure, it does not necessarily lead to cell rupture. In this case, the internal cell structure collapsed on itself as observed in Figure 6.2 (b). A cylindrical mandrel at the centre of the electrode layers has been reported to play an important role in the mechanical failure of the cell; providing both mechanical strength and a route for gasses to reach the vent during failure[16].
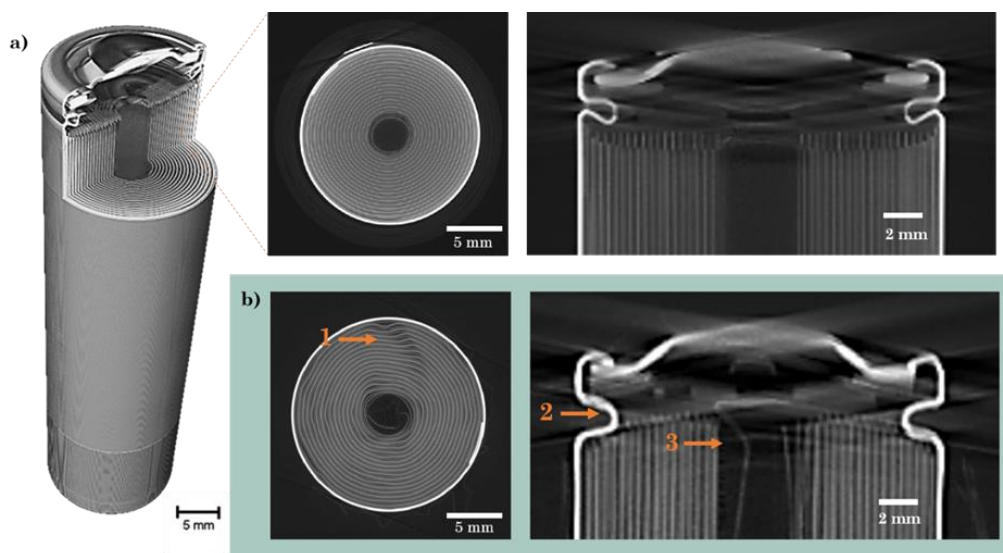
Figure 6.2   X-ray macro-CT results of a commercial 18650 cell (a) showing a 3D reconstruction of the whole cell and orthogonal slices in the XY and YZ planes before thermal runaway and (b) showing orthogonal slices in the XY and YZ planes after thermal runaway using ARC. Arrows depict areas of deformation within cell architecture.

6.3.2. Correlative analysis

For micro-scale, pre- and post-failure analysis, the cells were disassembled and samples of the electrode layers were extracted as close to the centre of the cell as possible. The cathode of the failed cell was noted to be brittle with weak adhesion to the aluminium current collector, in contrast to the fresh cathode, but similar to that reported by both Finegan et al. and Robinson et al.[131][96]. The fresh and failed anodes, on the other hand, were both relatively intact macroscopically. Figure 6.3 shows the SEM images obtained of the anode (a, b) and cathode (c, d) before and after failure. Changes to the anode surface are evident. Continuous exothermic decomposition and reformation of the SEI layer[239] are believed to occur up to approximately 220 °C[96]. Reaction products such as lithium-alkyl carbonates and lithium carbonate species make up the small precipitates of a surface film that are visible on the carbon particles. Exfoliation of the graphitic phase can also be seen. Although the particle size seems to have remained the same after failure, the porosity is observed to have reduced, in contrast to the observations by Robinson et al. in hard carbon electrodes in Na-ion batteries[96]. SEM images of the cathode after failure show a rougher surface than compared to the fresh electrode; this could be attributed to the delamination and agglomeration of cobalt containing species as suggested by Finegan et al.[131]. Furthermore, it suggests that the temperature at the centre of the cell reached > 350 °C. This is not visible in the ARC profile since the temperature is recorded by thermocouples attached to the outer casing of the cell only. Upon disassembly, the bulk cathode was scanned and the individual cathode particles were segmented and separated (as shown in Figure 6.4) for analysis such as PSD. While the electrode thickness remained the same after failure, particle sizes are visibly reduced in the volume reconstructions and PSD suggesting an increase in specific surface area and consequently a higher rate of heat generation[168].
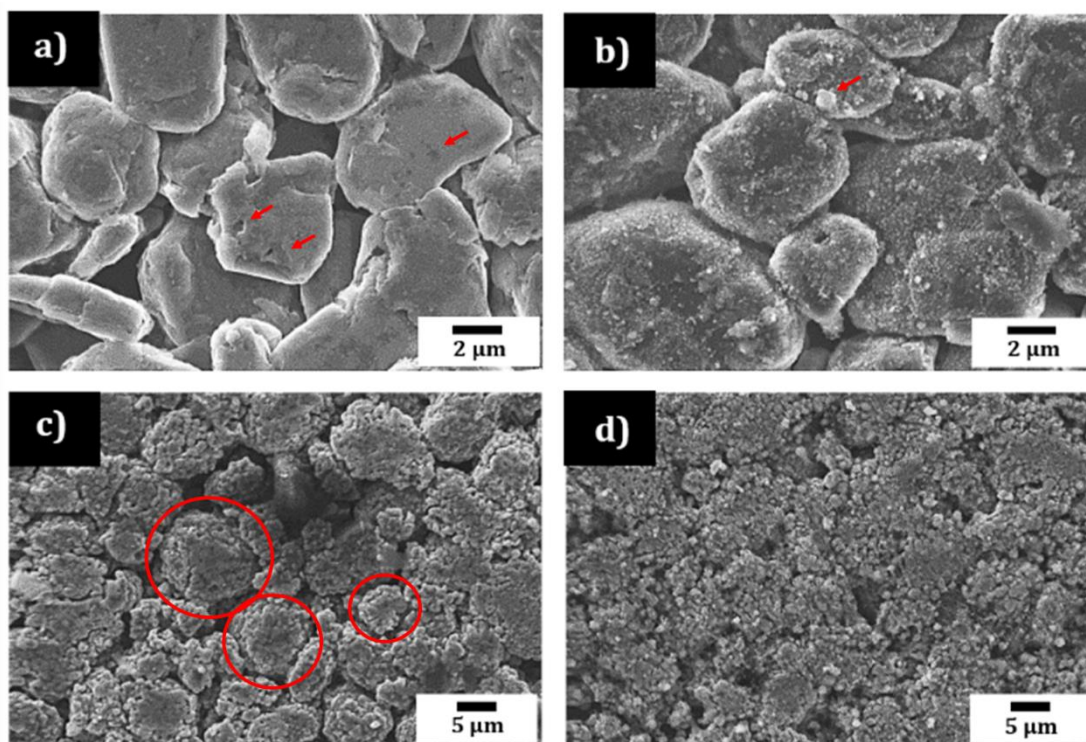
Figure 6.3 SEM images of (a) fresh, and (b) failed negative electrode (anode) from the commercial 18650 cells, (c) fresh, and (d) failed positive electrode (cathode) after thermal runaway using ARC.
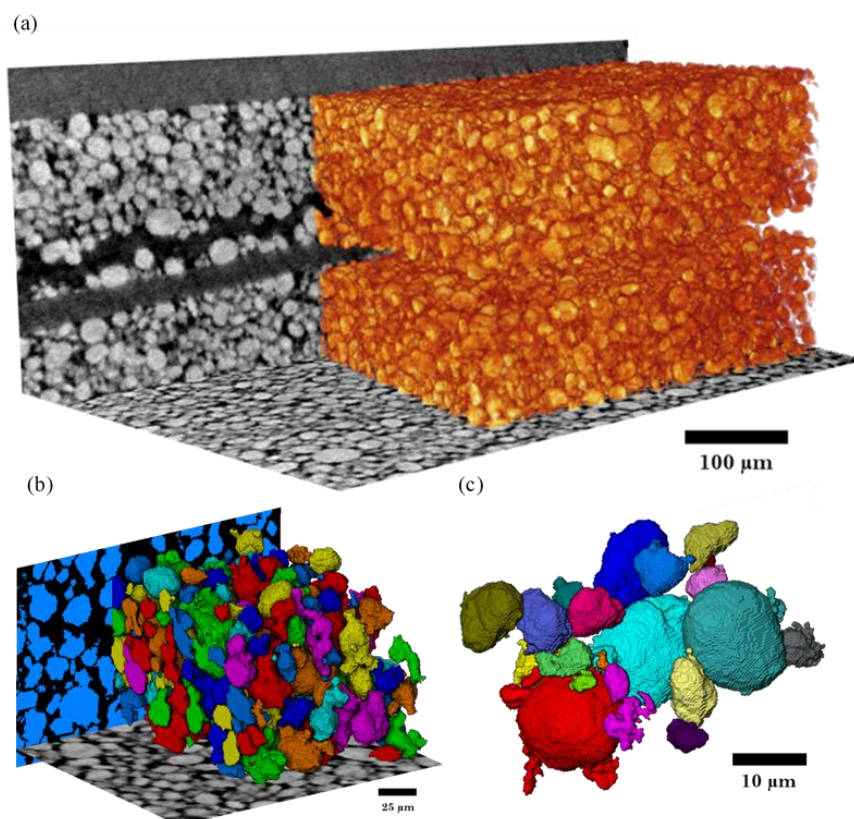
Figure 6.4 Volume renderings of (a) bulk cathode structure, (b) segmented bulk cathode structure, and (c) individual cathode particles after label analysis.

A PSD shown in Figure 6.5, comparing tomography data of the fresh and failed cathode reveals there is a significant reduction in the mean diameter of the post-failure particles, approximately half their original size (from 9.6 to 6.5 μm). The sub-volumes used for the PSD of each sample were 86,132 μm^3 and 41,612 μm^3 for the fresh and failed samples, respectively. The volumes differ due to the quality of the dataset (i.e. for the latter, the sample appeared to have moved during the scan duration, so the dataset was cropped to a smaller sub-volume). The spread of data for the post-failure particles differs greatly from the fresh sample. For example, there is a significant shift in the peak diameter from approximately 10 μm to 5 μm. Furthermore, the porosity of the failed sample was almost half of the fresh sample; i.e. 0.24 and 0.44, suggesting particle cracking and mass loss may have occurred. An evaluation of whether the considered sample volume fully encompasses all heterogeneities in the material is necessary[17]. In this work, only a sample taken from the centremost point of the cell is analysed. Since it cannot be assumed that the cell reacts in a uniform way[185], comparing pre- and post-failure samples from separate points in the cell may give a more accurate understanding of electrode morphology changes. Furthermore, an RVE analysis may be performed on the extracted sub-volumes to define the minimum volume which statistically represents the cathode material[156][159].

The links between cathode microstructure and thermal failure behaviour can be analysed further at finer lengths to accurately identify features which may not be visible at lower resolutions. In this study, X-ray nanoscale CT provided a pixel resolution of 63.1 nm, which enabled fine structural features to be seen. Micro-cracks and fractures within the failed cathode particles are shown in Figure 6.6. Cracks in the particles increase the surface area available for reactions with the electrolyte during failure. The presence of smaller cracked particles may result in an accelerated thermal runaway rate.
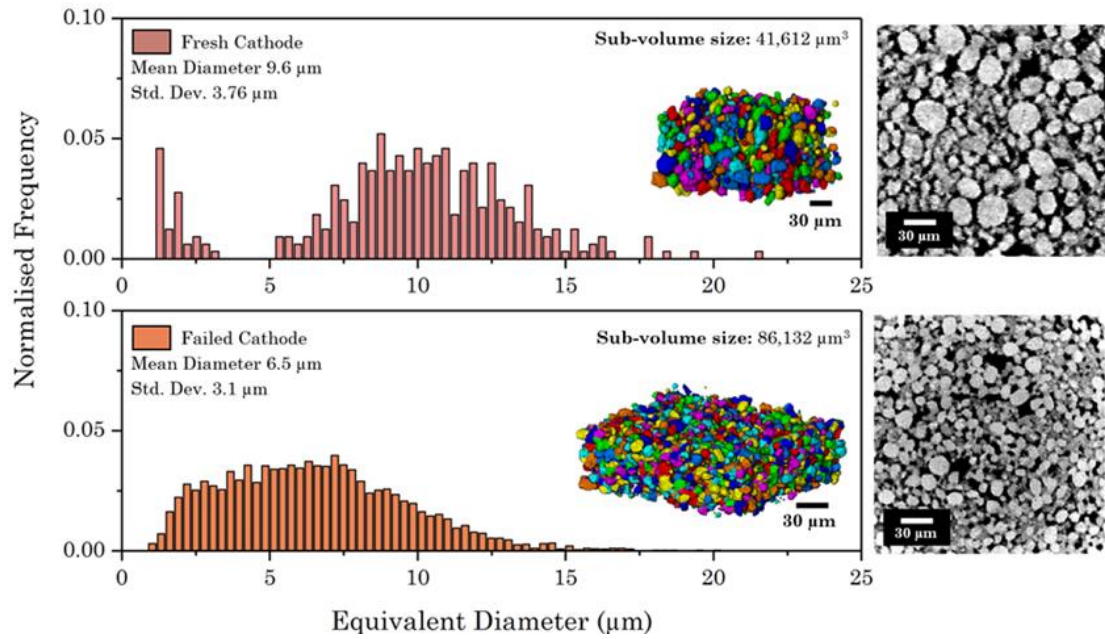
Figure 6.5 Particle size distribution for particles from the fresh (top) and failed cell (bottom) with complementing XZ orthogonal slices obtained from X-ray micro-CT. For the PSD analysis a sub-volume was extracted from each electrode sample.
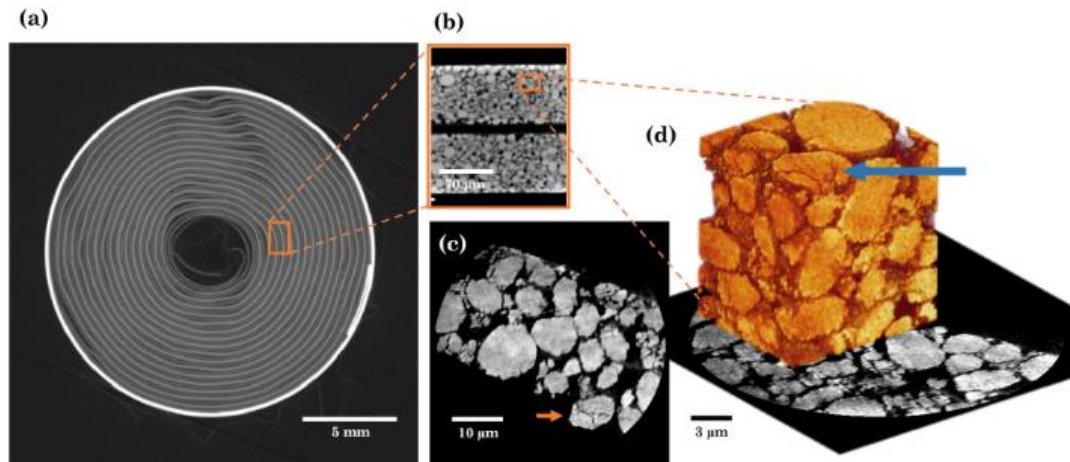
Figure 6.6 Multi-scale X-ray CT results of a commercial 18650 cell after thermal failure induced by ARC showing (a) an orthogonal slice in the XY plane where gas generation and delamination of the electrode layers is visible, (b) a microscale orthogonal slice of the failed cathode in the XZ plane, and (c) showing an orthoslice of the failed cathode highlighting cracked particles with (d) showing a 3D reconstructed sub-volume.

6.4. Conclusions from Chapter 6

The thermal failure of a commercial LIB with a 18650 format was analysed across multiple length scales. ARC was used to induce thermal runaway and the temperature at which the SEI layer breakdown occurs (30–50 °C) and the onset temperature (175 °C) was revealed. It was found that the melting of the shutdown separator significantly delayed the time taken to reach the onset temperature.

Pre- and post-failure examination of the cell using lab-based X-ray CT imaging revealed severe deformation of the electrode layers. Image analysis techniques applied to the bulk cathode both pre- and post-failure demonstrated that both the porosity of and PSD within the cathode nearly halved after failure. Nanoscale X-ray CT was more representative of the material showing evidence of particle cracking which is difficult to visualise in the SEM images of the cathode surface. Changes to the anode surface were also observed, suggesting its interaction with decomposed electrolyte may play a role in the thermal runaway process. In this work, electrode morphology has been considered when analysing battery failure behaviour. While it is suggested that larger particle sizes may increase thermal stability, they can drastically reduce the overall power density of a battery[105]. A critical balance between performance and safety exits, and future work considering electrochemical characteristics of a material alongside its contribution towards battery failure is imperative.

This chapter demonstrates how multi-length scale X-ray CT imaging in combination with ARC can be used as a diagnostic tool to decipher the series of events that a LIB undergoes during thermal failure. The investigation of various microstructural parameters of the cathode material and their possible influence on battery failure severity have been discussed and the 'safety' and of a commercial LIB has been characterised by determining the onset temperature and the rate of heat generation. In addition, X-ray CT imaging at a nanoscale has revealed features such as particle cracks that could be useful for optimising electrode manufacturing processes for safer batteries with lower onset temperatures and heat generation rates.

Chapter 7

7. In-Situ Operando Technique Development for Thermal Failure

7.1. Introduction

High-speed imaging with in-situ/operando X-ray CT has been used extensively to study various LIB safety features and failure mechanisms[131][185], including thermal failure[224]. However, to date, these have principally used synchrotron X-ray sources, which are limited in terms of both access and data recording capabilities. Generally, lengthy application processes and available resources can often limit access to synchrotron sources. Furthermore, in the case of battery failure experiments, although cell rupture/ejection can occur within seconds, the events leading up to failure or a main event can take anywhere between a few hundred seconds to minutes. The high frame rates in high-speed synchrotron imaging require the data collection window to be restricted to a few seconds depending on data storage capacity which is typically limited to < 10 seconds. In this chapter, the development of an instrument that simulates thermal failure for lab-based radiography at slower imaging speeds and longer recording lengths is presented. The method introduced allows for the slower, incremental mechanisms leading up to thermal runaway to be investigated, with the added capability for it to be utilised with high-speed imaging and/or with different cell formats.

7.2. Experimental

7.2.1. Cell chamber design

A custom cell chamber was developed using CAD software. It is designed to operate like an accelerated rate calorimeter where the self-heating rate of thermally failed pouch cells can be monitored. The chamber is comprised of three parts: a base, a battery enclosure and a cylindrical lid. The base is designed to fix the chamber to the rotating stage of the Nikon XT X 255 X-ray CT machine. The design keeps the chamber stable and provides a mechanism by which to dissipate excess heat. Four holes are provided to secure the battery enclosure of the chamber to the base. The battery enclosure (Figure 7.1 (b)(ii)) is designed with a compartment for the pouch cell. Two aluminium spacers are used on either side of the pouch cell to reduce the air gap and improve the conduction of heat from the surrounding heating cartridges (Omega HDC00014 321, Stainless Steel Cartridge Heater, 0.25" OD, 1 - 13" long). Two heating cartridge holders are placed adjacent to the pouch cell (not in direct contact with the cell samples). The cartridges are coated with a thermally conductive grease (silicon) to improve the contact between the holder and the cartridge. The Al spacers are attached to the battery and an internal thermocouple using Al tape. The battery enclosure is also made from aluminium for X-ray transparency. A high-temperature, chemically resistant gasket (Flexitallic, Thermiculite 815 UK), is used between the battery enclosure and the cylindrical lid. Upon thermal failure, the cells are expected to rupture and vent gas. The cylindrical lid is made from stainless steel and designed to capture the maximum expected gas ejection. It is sealed using the gasket and 12 bolts. The lid was pressure tested to 1.3 bar (which was based on a calculation of the volume of solvent for the 210 mAh cell and the volume of the lid).

The chamber has three thermocouples, one on the sample cell, and a further two near each of the heating cartridges. The latter two are implemented to control the heat output of the cartridges via a temperature controller (running under PID control), which is managed by a custom LABview programme.
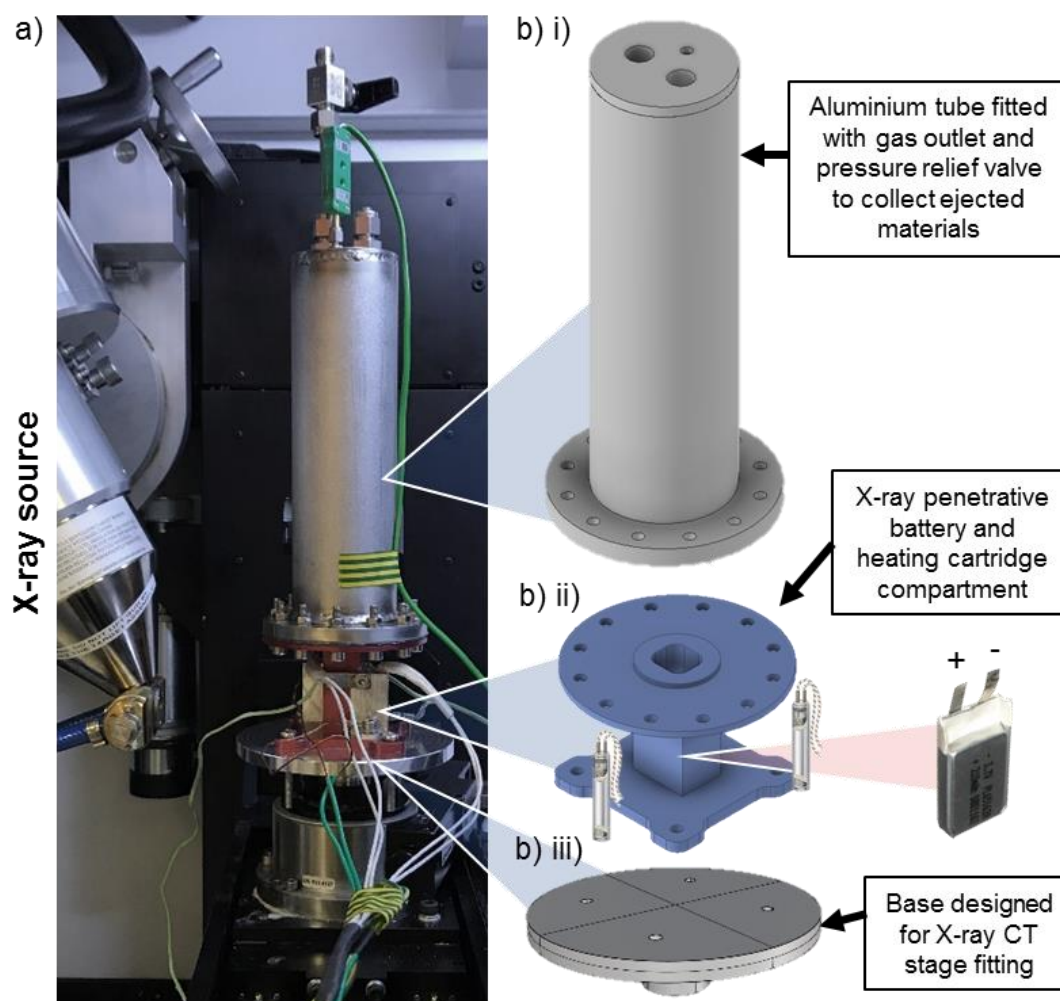
Figure 7.1 Experimental set-up of the chamber shown (a) inside the X-ray CT Nikon XT 255 and an illustration of the bespoke design from the top (b)(i) stainless steel cylindrical lid, (b)(ii) battery module fitted with two heating cartridges and the sample, and (b)(iii) the base designed to hold the chamber to the rotating stage of the X-ray CT machine.

7.2.2. Materials, equipment and procedure

The failure mechanisms within three fully charged (100 % SOC, 4.2 V) commercially available $LiCoO_2$ cathode and graphite anode pouch cells (651628-2C, AA Portable Power Corp) rated at 210 mAh are investigated using lab-based X-ray radiography that offers a frame rate up to 3.75 fps and pixel resolution down to 3 μm. For comparison, an additional three samples are studied using synchrotron X-ray sources at 20,000 fps with a 13.3 μm pixel resolution. A summary of each sample and its corresponding experiment can be found in Table 7.1. The experimental details such as imaging parameters can be found in the next section.

Table 7.1 Summary of the experimental system used and the number of samples and their assigned labels.

Experiment equipment	Sample numbers
Lab-based X-ray system (UCL)	1, 2 and 3
Synchrotron radiation (ESRF)	4, 5 and 6

The cells are all charged to 100 % SOC up to the maximum rated voltage of 4.2 V. A pouch cell is then placed inside the battery compartment surrounded by aluminium spacers, heating cartridges and a thermocouple. A heat-wait-search-like protocol begins once the external cell temperature reaches 80 °C. The programme ramps the temperature up by 2 °C every 5 minutes. If in the time it waits, a self-heating rate greater than 15 °C s^{-1} is detected, then the cell is deemed to have reached thermal runaway. The onset temperature (the temperature at which self-heating is detected) is defined as T_0, the temperature at which a significant failure event occurs is defined as T_i. The maximum temperature that the battery (external) reaches is also recorded. The recording software, control box, thermocouple and heating chamber set-up are shown in Figure 7.2.
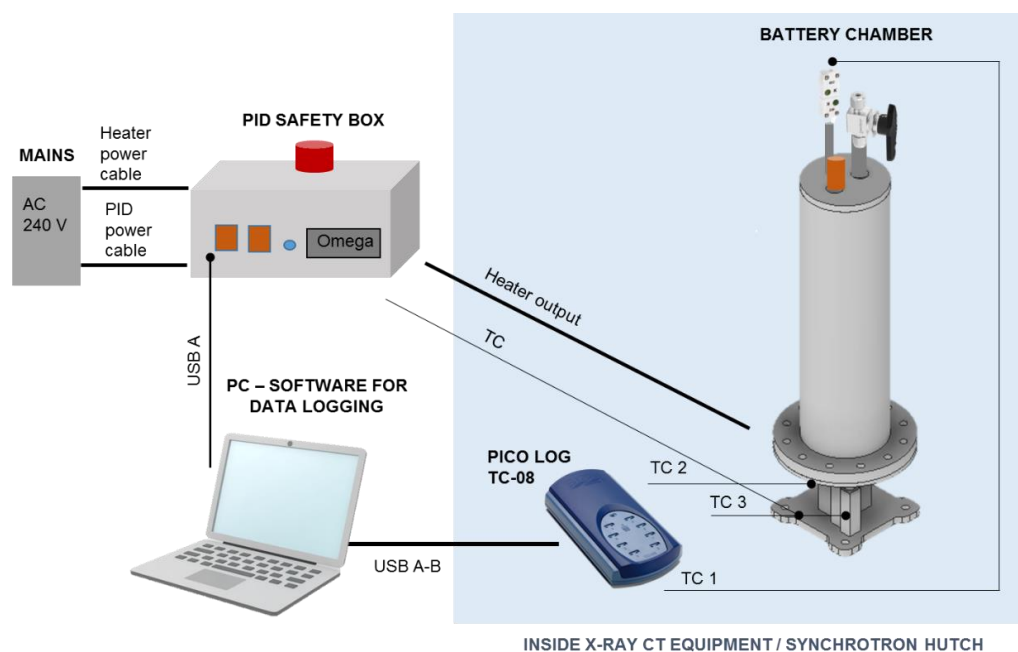
Figure 7.2 The heating chamber is placed inside the X-ray imaging equipment while the control box for heat-wait-search like testing and corresponding software are placed outside.

7.2.3. X-ray radiography and CT measurements

X-ray imaging at 3.75 frames per second was performed using the Nikon XT X 255 to capture the architectural changes within the pouch cells in real-time as they underwent thermal failure. The cells were imaged with a pixel size of 16.1 µm and a FOV of 2000 by 2000 pixels acquired using a 16-bit flat panel detector (PerkinElmer 1620, Waltham, MA, USA). Laboratory-based X-ray CT was conducted before and after the thermal failure (and while the cell remained inside the chamber) using a Tungsten target and accelerating voltage and power of 220 kV and 16 W, respectively. A 1 mm copper filter was used to reduce the attenuation of the samples and improve the contrast of the electrode layers. Radiographs were reconstructed using the CT Pro 3D software package. The acquired 3D volumetric for all samples had a voxel size of 24 µm and took approximately 22 minutes to collect with a 0.5 s exposure time and 2643 projections. The reconstructed 3D data was processed using Avizo Fire 9.5 software.

Higher-speed X-ray imaging at 20,000 fps was performed at beamline ID19 at ESRF to capture the same internal architectural changes. The collimated and coherent beam allows for higher spatial and temporal resolutions to be achieved. Radiographic data was recorded using a 1024 x 1024 pixels CMOS model SA-Z detector (Photron, Japan) in combination with a x 1.5 magnifying lens, giving a 13.3 µm pixel size.

7.2.4. Image quantification

Characteristic failure events such as cell rupture, venting, crack formation and propagation are often difficult to visualise in radiographic data alone. Additionally, some of these events occur within milliseconds. Radiographic data obtained here were processed using an analytical toolbox developed in Python by Radhakrishnan et al., details of which can be found in the referenced paper[182]. The radiographic data captured the whole cell and consisted of a series of radiographs taken for the duration of the failure event at 3.75 fps (or 20,000 fps for the datasets obtained using the synchrotron

facilities). The toolbox application allows for the effects of cell failure on the architectural changes, such as electrode displacement within the cell to be quantified.

The textures in the radiograph images are classified using Gabor filters. A region of interest from the cell interior is selected and the Gabor filter is applied across the selected frames. The filter direction and frequency are optimised when applied to the dataset to give the best match that represents the spacing and orientation of the electrode layers. Generally, when the filter is applied parallel to the electrode layers, the output signal, if positive represents the current collector layers (higher attenuation), and if negative, the graphite (lower attenuation). Values of 0 represent the separator and positive electrode active layer. Temporal cross-correlation of the Gabor signal allows for the changes in the cell's internal structure to be tracked and quantified over time (that is, the duration of the failure event of interest). Furthermore, plotting the cross-correlation at every position in the axial direction, at every X cross-section as a surface plot produces a spatiotemporal map. The map allows the propagation of the failure event across the selected region of interest to be visualised.

7.3. Results

7.3.1. Longer acquisition times (laboratory studies)

The first three heating experiments resulted in cell failures that took approximately 18 – 23 minutes to reach failure from start (room temperature) to end (cooling after thermal runaway). During this time, three distinct events occurred: (A) cell expansion from electrolyte/anode reactions, (B) melting of the separator, and (C) a wave-like propagation as shown in Figure 7.3. Although the test was repeated for three identical samples (named Sample 1, 2 and 3, respectively) following the same procedure, there were some variations in the recorded onset temperature and maximum temperature reached. The onset temperature may have varied as a result of the cell make-up, although the voltage recorded at the start of the experiments was 4.2 V, there is a risk that after being placed inside the chamber, they may have dropped to a lower voltage. The dependence of the onset temperature during thermal runaway on the cell SOC has been widely researched in the wider literature. The higher the SOC, the lower the onset temperature. Furthermore, variations in the measured maximum temperature that was reached by each sample may have been caused by variations in the placement of the thermocouple on the sample. Upon examination of the post-failure cell, it was apparent that in some cases the adhesive on the aluminium tape had weakened at high temperatures and caused the thermocouple to have marginally detached from the sample. Figure 7.3. shows the features visible in the field of view. The sample is visible, where the outer edges and inner electrode layers are distinguishable. Furthermore, the contact between the thermocouple and the sample is also visible. The full video of the radiography experiment (Chapter 7_Sample 1_Thermal Failure.mp4) is provided to compliment Figure 7.3 and Figure 7.5.
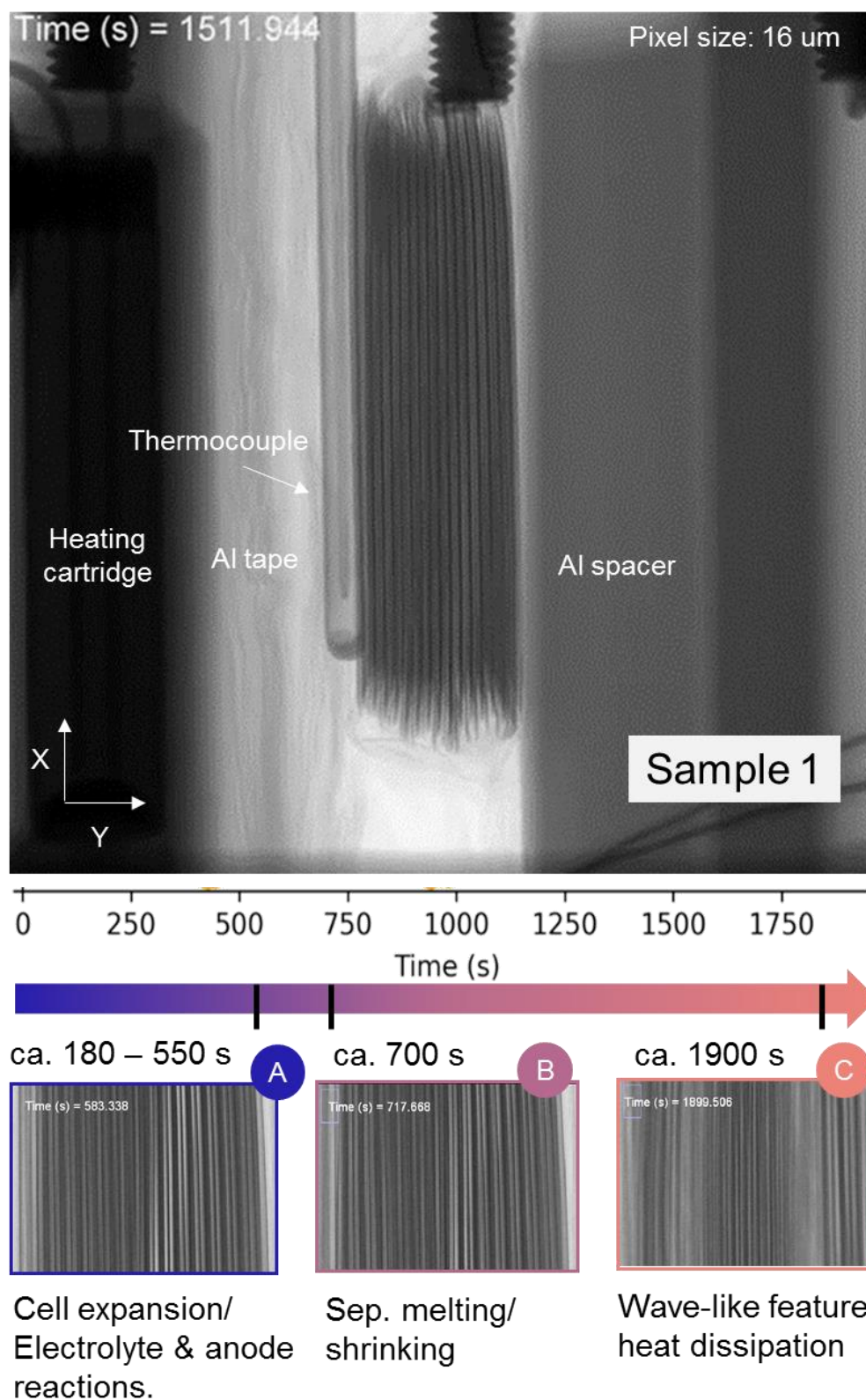
Figure 7.3 Image of the field of view showing the inside of the chamber module where the sample, thermocouple, aluminium spacer/tape and heating cartridges are visible. The acquired pixel size was 16 µm using the Nikon XT 225 with a frame rate of 3.75 fps. Three distinct events A – C are highlighted.

The first two distinct features; electrolyte/anode reactions and the melting of the separator, or A and B, respectively, appear to occur approximately within the same temperature and time, whereas the final wave propagation feature occurs at a different point in time for all three samples as shown in Figure 7.4. The wave-like feature is observed for all three samples and lasts under one second.
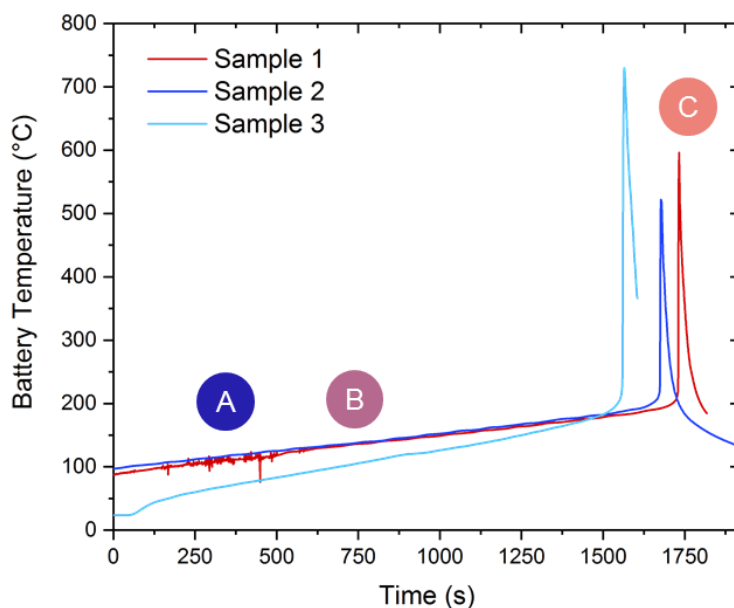
Figure 7.4 Temperature profiles of three samples all heated by ramping temperature until self-heating is detected (> 15 °C s^{-1}). Three distinct events A – C are highlighted. This dataset correlates with images captured using lab-based X-ray instruments.

A detailed frame-by-frame depiction of the three events is shown in Figure 7.5. For event A, the expansion caused due to the electrolyte and anode reactions is visible. At 0 s, the cell is 6.02 mm in width, however by 583 s, the cell expands to approximately 6.35 mm. Therefore, within the first 10 minutes of heating from temperature 100 – 125 °C, the cell expands by approximately 5.5 %. The second feature is the melt of the separator. It does not appear to affect the cell width; however, some electrode displacement is visible as highlighted in Figure 7.5 (b). The event occurs far more rapidly than the electrolyte and anode reactions. For example, event A is gradual over 10 minutes, whereas the separator melting initiated at 707.826 s (or ~ 11.8 minutes) occurs within 10 s. The effects of the separator melting on the electrode displacement are difficult to quantify at this stage, however, this is explored in later sections. Event C the wave-

like propagation feature, begins at 1899.506 s (~ 31.7 minutes). It occurs within 1.5 seconds from beginning to end where in Figure 7.5 (c), it can be seen that the electrode displacement begins at the centre of the cell and moves outwards towards the cell edges. This is believed to be a result of gas displacement from high temperatures to lower temperatures as a means of heat dissipation. The thickness of the expansion at the edges of the wave-like feature remains relatively equal further suggesting it is caused by the movement of gas rather than the generation of gas. Not pictured is the rapid contraction of the electrode layers at the end stage of the wave-like feature. This event occurs shortly after the highest temperature of the outer cell is measured as seen in Figure 7.4 where the rapid decline in temperature is also shown. In the last frame, the damage to the electrodes is visible, it is expected that some delamination would have occurred, however, this is not quantifiable at this stage, but is discussed in later sections using X-ray CT.
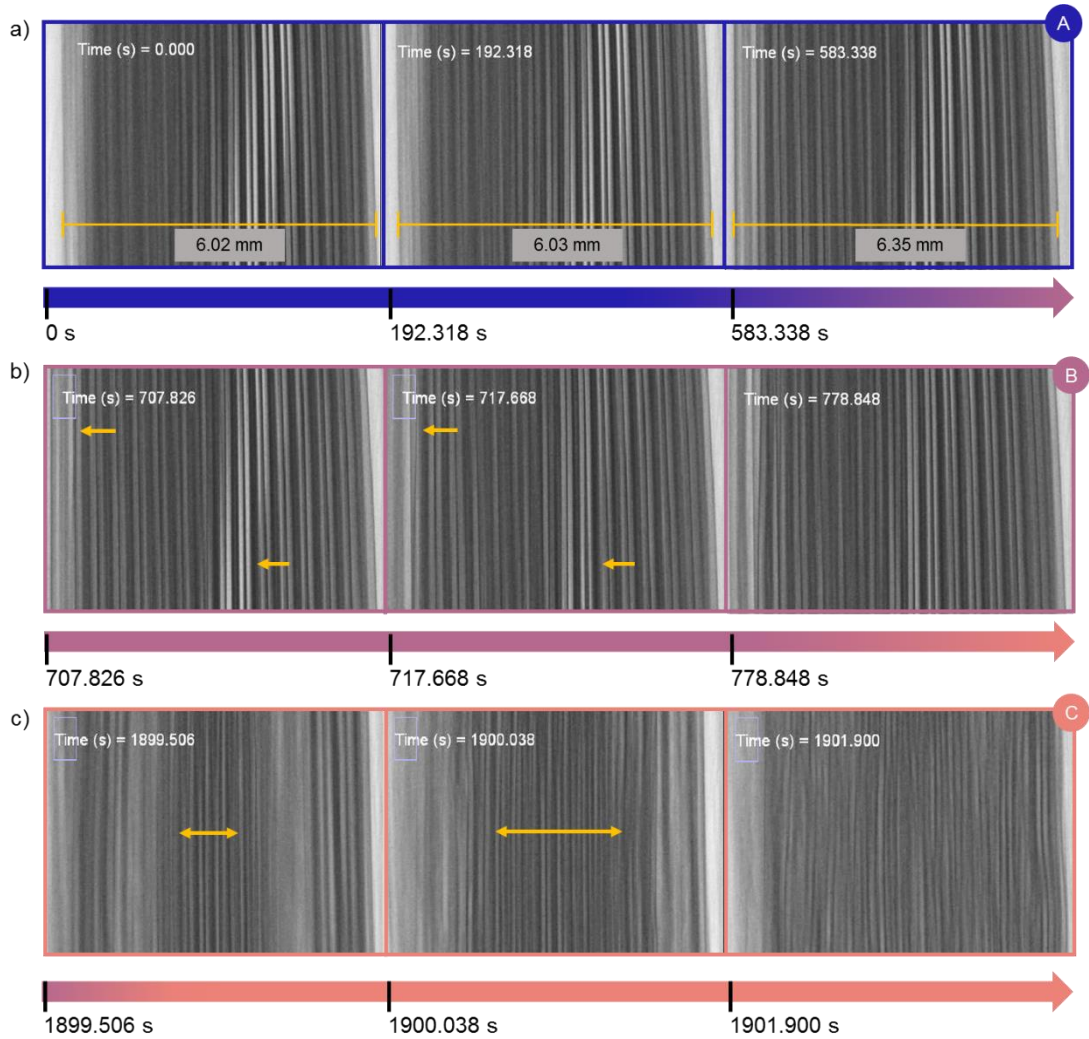
Figure 7.5 Frame-by-frame images of the three distinct events, where (a) shows event A, the cell expansion from electrolyte/anode reactions between 0 – 583 s, (b) shows event B, the melting of the separator, and (c) shows event C, a wave-like propagation as heat is dissipated.

7.3.2. Electrode displacement during the wave-like feature

By temporal cross-correlation of the Gabor signal, the electrode displacement during the wave propagation within the cell is tracked. Approximately 31 electrode layers are identified at T_0 after optimising the angle and frequency of the filter. Figure 7.6 shows how the wave-like feature propagates across the electrode layers and the quantity by which they are displaced over time. The signal at T_0 is compared to the signal at T_i for each frame; when the correlation magnitude is positive, it indicates that the signals

from both times are similar. On the other hand, when the correlation magnitude is negative, the electrodes have shifted. At 0, there is either a misalignment in the electrode layers or no Gabor signal (indicating the absence of electrode texture from the radiograph). Note here that the dataset was cropped along the time scale to begin at 1895.5 s (which is approximately 5 seconds before the wave-like propagation begins) before being processed using the Python toolbox. Therefore T_0 in this case, does not correlate to the beginning of the heating experiment or 0 s.

Figure 7.6 Temporal cross-correlation of the electrodes from the dataset of Sample 1 conducted using lab-based X-ray instrumentation with a frame rate of 3.75 fps. The top plot shows a 2D map of the temporal evolution of the normalised Gabor signal at a fixed X position. The bottom plot shows the corresponding normalised temporal cross-correlation, where the Gabor signal at time T_i is cross-correlated with that of the electrode structure before the wave-like feature begins, T_0 (which is close to 'pristine').

Around 6 s, the electrodes rapidly and linearly shift across the cell as the wave-like feature begins. From the temporal cross-correlation, this corresponds to the electrodes moving out of alignment and then realigning twice over. In the shifting signal, the total shift appears to be approximately 4.5 electrode layers. Furthermore, the second minimum point at ~ 8 s indicates that the electrodes get pushed together. The temporal cross-correlation indicates the position and time at which the wave-like feature began and how

far the electrodes shifted across the cell. It appears the space between the electrode layers expanded and contracted twice. During this phenomenon, the cell also reaches its maximum temperature (between 500 – 700 °C when considering all three samples in Figure 7.4). At these temperatures, the LiCoO$_2$ cathode, binder and electrolyte materials will decompose and generate large amounts of heat, together with other exothermic reactions between the deposits from the earlier anode reaction, electrolyte and melting of the separator which occurred between temperatures between 120 – 250 °C. From the radiograph alone, it is believed that the wave-like feature is initiated at the centre of the cell from top to bottom as can be seen in the top row of Figure 7.7 (a). It is assumed that the movement of generated gas from the decomposition reactions is what causes the wave-like feature to propagate. Although no internal temperature measurements were made, it is anticipated that the centre of the cell is the hottest as this has the poorest capability for heat rejection. This would explain why the gas moves from the centre to the outer edges of the cell – as a form of heat dissipation. The movement of gas is rapid and destroys the electrode architecture as the cell begins to cool.

A 2D spatiotemporal map further elucidates the wave-like feature in Figure 7.7 (b). The cross-correlation at every X-cross section reveals the behaviour of the electrodes as they develop over time along the x-axis. The colour red (or high positive values) shows areas where the electrode position is similar to the initial electrode position; darker blue regions (or values near 0) represent areas of either misalignment of the electrodes from their initial position or even disappearance of the electrode altogether. Purple (values that are large and negative) show areas where the Gabor signal is inverted which can represent localised delamination and/or structural failure of the electrodes.

Between 0 – 6 s, there is significant electrode misalignment between 6 – 14 mm in the X direction. The 0 mm point in this case represents the beginning of the region of interest box, and not the top of the cell, therefore 6 – 14 mm corresponds to approximately halfway down the height of the cell (which is 29 mm). When compared directly with the raw video frames in Figure 7.7 (a), between 4.67 – 6.26 s there are distinct areas where electrode misalignment can be seen (particularly towards the bottom centre of the cell).

After 6.26 s, the outer edges of the wave-like feature can be seen – lighter grey areas suggest larger spacing between electrode layers, i.e. expansion. As the 'grey' areas move outwards, the electrode layers appear to contract or move back to their initial position. However, when correlated with the 2D spatiotemporal map in Figure 7.7 (b), after 6 s it appears that electrodes across the whole height of the region of interest are affected (no red regions), meaning the electrodes are misaligned and not arranged back to their initial positions during contraction. This correlates with the observations made from the earlier temporal cross-correlation in Figure 7.6. A purple region between 6.5 – 7.8 s, which is approximately the top of the sample, represents an area where there may have been localised electrode delamination and/or structural failure. It is expected that the pressure from the generated gas at high temperatures would have escaped the sample from areas where any mechanical weakness was present. The seal around the tab (located at the top of the cell) is a common area for outer case seal failures and gas/electrolyte leaks.
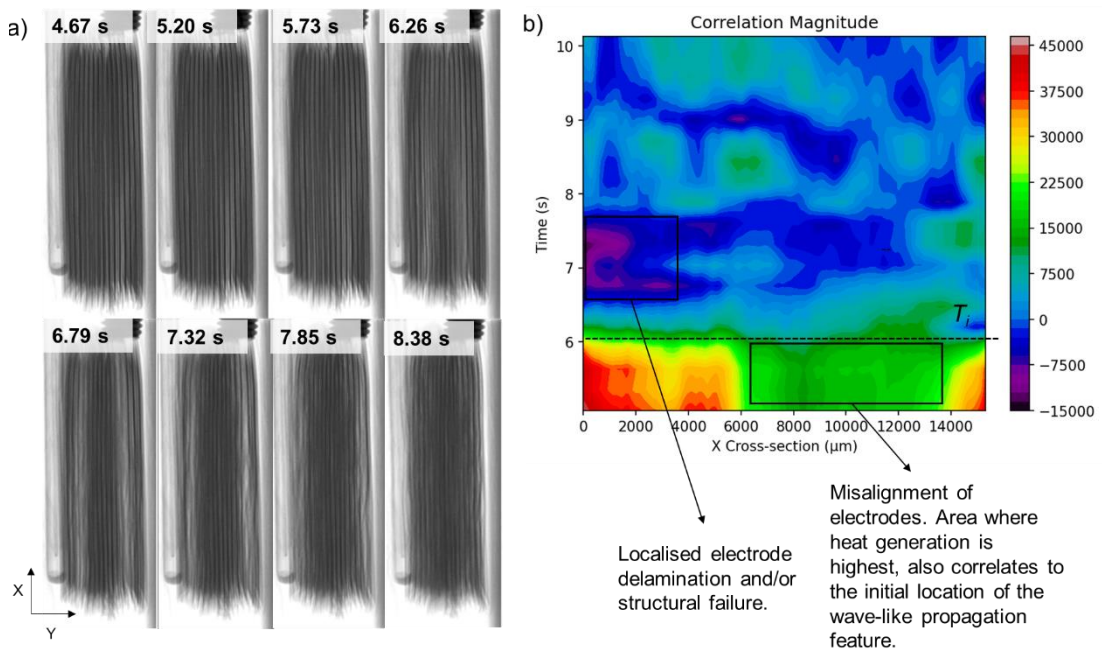
Figure 7.7 (a) Frames captured from the beginning of the wave-like feature to the end and, (b) 2D map spatiotemporal map produced by calculating the normalised cross-correlation values at every X position.

7.3.3. Events leading up to thermal runaway

The benefit of recording at a lower frame rate is that for any given data size, the ability to capture events over a longer length of time is made possible, albeit some shorter time-scale events may not be captured. For example, the thermal failure of a LIB includes several characteristic events from early 'low' temperature events such as the SEI decomposition (~ 60 °C), to events such as the combustion of the active cathode materials at higher temperatures (> 500 °C). The early decomposition reactions are often slow when compared to the reactions such as the melt of the separator. However, these 'slow' processes have been largely overlooked in X-ray investigations, which have focused on elucidating the workings of various failure mitigation mechanisms within LIBs or more catastrophic events such as cell rupture and mass ejection. However, since the various decomposition reactions generate gas, it is useful to understand if and/or how gas is dispersed and how events such as the separator melting may play a role in the movement of electrodes. The samples recorded using the lab-based system (Nikon XT 225) were recorded across the whole heating range from 0 s to an average of 1950 s. The whole dataset (without cropping along the time scale) was processed using the aforementioned toolbox in Python. For all three datasets (Samples 1, 2 and 3) the Gabor signal was temporally cross-correlated for the full-length video from when the cell reached the start temperature of 80 °C to shortly after the wave-like feature (maximum temperature). Figure 7.8 highlights the areas where the three distinct events occurred along the timescale: (A) electrolyte/anode reactions, (B) melting of the separator, and (C) wave propagation.
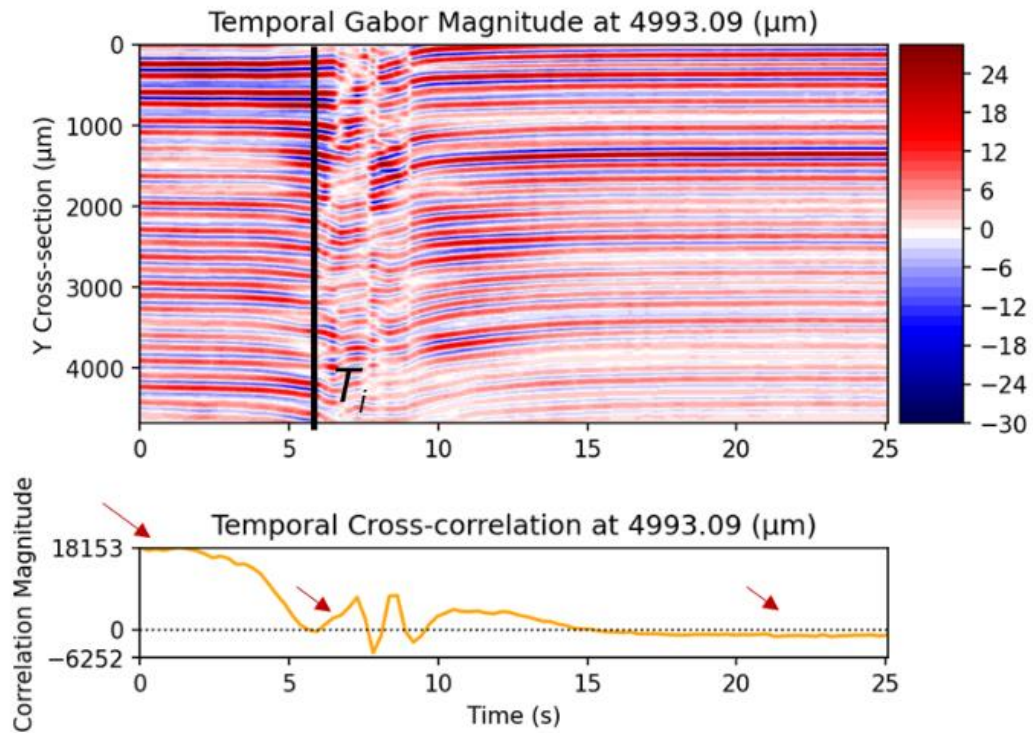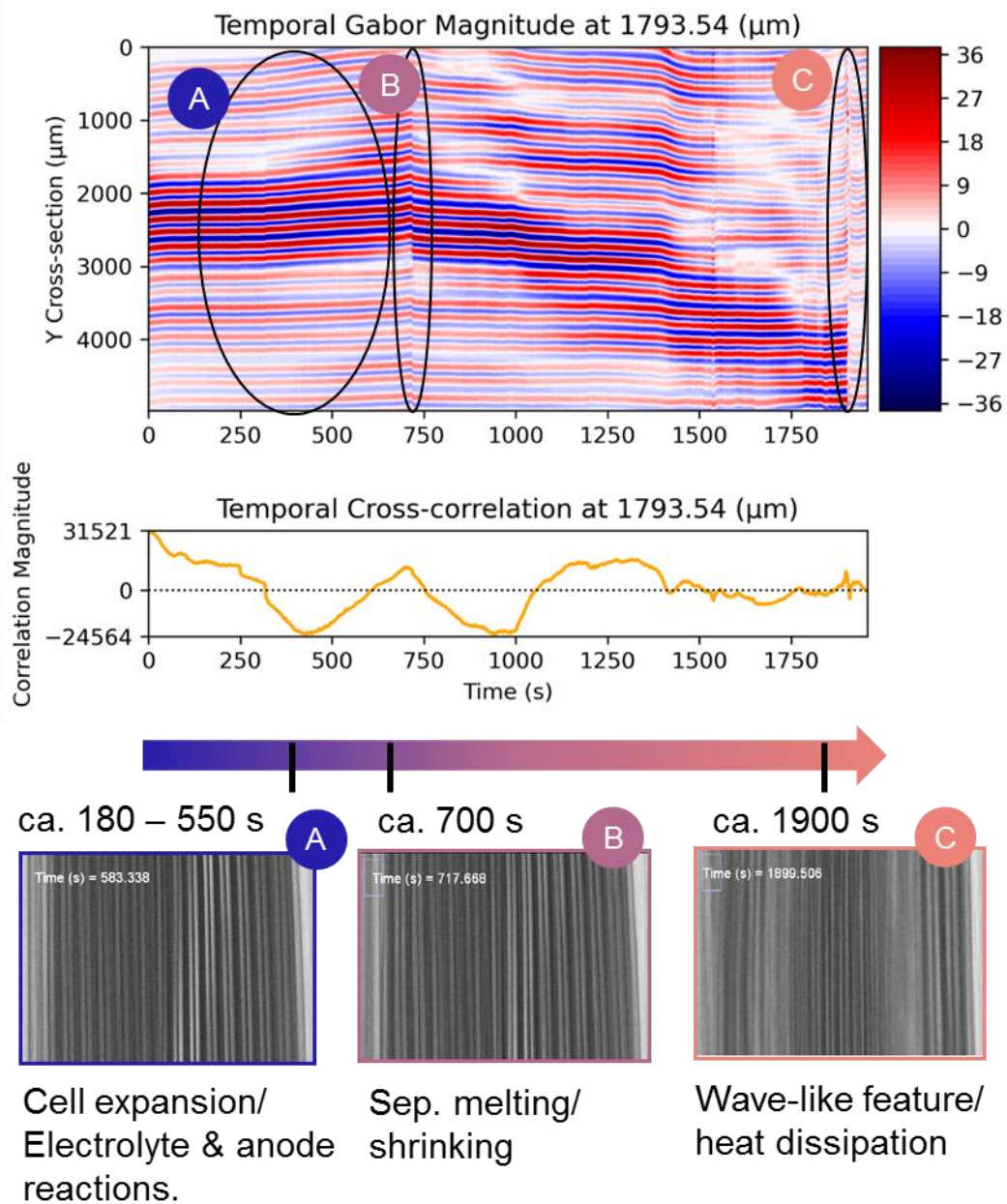
Figure 7.8 Temporal cross-correlation of the electrodes from the dataset of Sample 1 conducted using lab-based X-ray instrumentation with a frame rate of 3.75 fps across the whole experiment duration. The top plot shows a 2D map of the temporal evolution of the normalised Gabor signal at a fixed X position. The bottom plot shows the corresponding normalised temporal cross-correlation, where the Gabor signal at time T_i is cross-correlated with that of the electrode structure at the beginning of heating where the cell is approximately 100 °C. Three distinct events A – C are highlighted with respective frames taken near the time the events occur.

During the electrolyte and anode reactions, gases such as CH_4, CO_2, C_2F_6, H_2, and CO are formed[240]. The gas generation is gradual, and this is reflected in the temporal Gabor magnitude in Figure 7.8, where a gradual shift in the electrodes is shown between 0 to 750 s. The electrodes are shifting linearly and from the temporal cross-correlation, this corresponds to the

electrodes moving out of alignment as shown by the first minimum poin t in the signal. The generation of gas due to the electrolyte and anode reactions is predicted to cause a shift of approximately one electrode layer. The second characteristic feature is the melting of the separator. The polymer separator is expected to melt, shrink and collapse under high temperatures and lead to internal short circuits[241]. The separator material and structure of these cells are unknown, however, from deduction, it is predicted that they may be standard polypropylene layer or tri-layer consisting of polypropylene and polyethene. Zhou et al. conducted a series of ARC tests on single-layer pouch cells while monitoring the cell voltage[93]. During multiple tests conducted with a standard PP separator, exothermic peaks began anywhere between 142 °C to 152 °C, and a significant cell voltage drop to 0 V occurred between 153 °C to 177 °C. It is assumed that a significant ISC event occurs in this temperature range and a destructive physical analysis revealed that the separator material totally vaporised at the end of the tests that went up to 191 °C. Similarly, for the tri-layer separator, an exothermic phase was observed starting at 142 °C, and the cell voltage dropped to 0 V from 3.86 V between 150 °C and 171 °C. Between 135 °C and 155 °C, a micro-ISC event was observed suggesting the onset of the tri-layer separator shrinkage. Following a destructive physical analysis, the separator was observed to also have totally vaporised. Since the tests were conducted on single-layer pouch cells, these temperatures cannot be directly compared to the cells in this work. Although the SLPs were not designed to be consumer cells and will have considerable non-uniformity owing to their fabrication methods, they prove that separator failure is a significant feature in thermal abuse tests that has a considerable impact on failure propagation - and on electrode architecture as the results in this chapter elucidate.

A small but rapid shift in the electrodes is observed in Figure 7.8, labelled as event B which appears at approximately 750 s when the external battery temperature is 140 °C. The temperature profile shows a steady increase in temperature and a large exothermic peak does not occur until event 'C' at 1980 s. At 140 °C, it is predicted that the separator microstructure does not totally collapse and cause a rapid ISC event; instead, it is considered

that a micro-ISC event occurs where the cell voltage drops but keeps above 0 V. In this case, it is predicted that energy is partially released at a slow and irregular rate at this temperature. However, as time progresses and the temperature of the cell increases, the separator may become fully vaporised as the internal temperature of the cell surpasses the melting point (~ 165 °C).

7.3.4. Correlation with high-speed imaging

The wave-like feature was investigated at a higher imaging speed of 20,000 fps using synchrotron radiation. The event takes approximately 1.5 seconds and the data was recorded for 6 seconds. Similar to the slower-speed images, the electrode displacement during the wave-like feature is tracked by temporal cross-correlation of the Gabor signal. Figure 7.9 shows the temperature profiles recorded for three identical samples (Samples 4, 5 and 6) under the same experimental conditions (i.e. chamber set-up and protocol). These cells behaved more similarly to one another than the three at lower imaging speeds (Figure 7.4), suggesting perhaps that high-speed failures are more uniform while pre-cursor events are more random. Furthermore, the first set had been bought and stored under nominal voltages for 2.5 years before their first charge ahead of the experiments, so may have degraded/aged[53], affecting their failure response. Some differences existed between the experimental set-up in the lab-based experiments and the synchrotron experiments, shown in Figure 7.10. The whole chamber for the second set of experiments was placed on a stage inside the experimental hutch, which had a greater working area surrounding it than within the restrictions of the lab-based X-ray instrument. Additionally, the FOV was smaller and captured only a small area of the sample. However, these differences are not expected to have had any effect on the cell behaviour during thermal failure.
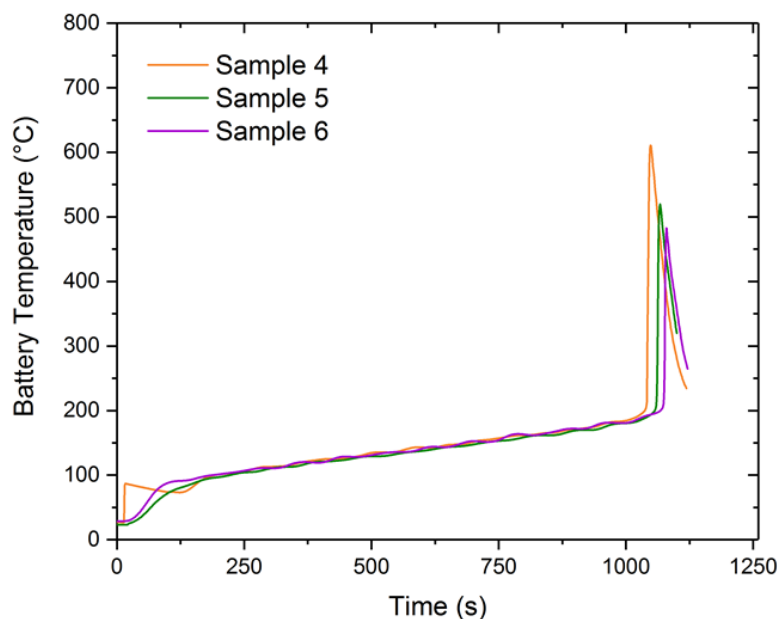
Figure 7.9 Temperature profiles for Samples 4 – 6, all heated by ramping temperature until self-heating is detected (> 15 °C s^{-1}). This dataset correlates with high-speed images captured using synchrotron radiation.
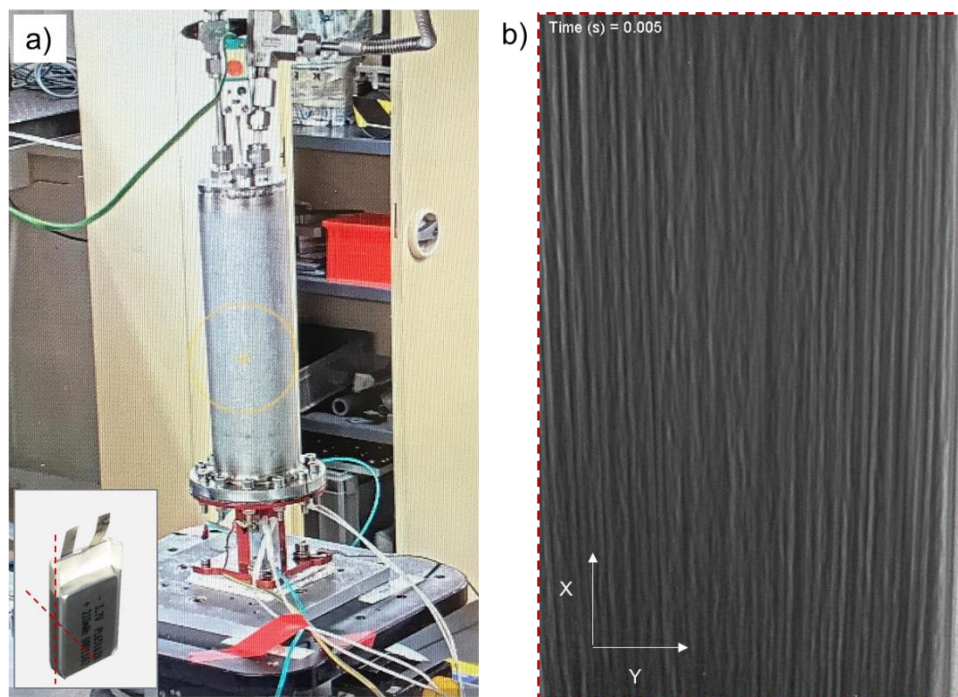
Figure 7.10 (a) Experimental set-up showing the heating chamber on the rotating stage inside the experimental hutch of beamline ID19 at ESRF, and (b) Preliminary image showing the electrode layers visible in the 1024 x 834 pixels FOV.

A frame-by-frame sequence of Sample 4 is shown in Figure 7.11 (a), starting from time 0 s, which is not the sample in its 'pristine' state but at a point in time before the wave-like feature propagates. The electrode layers already look non-uniform from pre-cursor events such as the separator melting

and electrolyte reactions. In the following frame, at 2 s, a small gap between the electrodes is highlighted, which is believed to be caused by a build-up of generated gas from reactions occurring at high temperatures. The movement of this gas can be followed from the centre of the cell to the outer edges from the images at 2 s to 3.455 s.

The datasets for all three samples (Sample 4, 5 and 6) were processed using the aforementioned toolbox in Python. The Gabor signal was temporally cross-correlated for the full 6 s of data collection and is shown in Figure 7.11 (b). Some vertical lines in the signal can be observed, this is because before analysis the datasets were reduced from 20,000 fps to 2,000 fps, (which was condensed to increase the processing time to an appropriate length for the scope of the analyses). Around 2 s, there is an abrupt change in the electrode architecture. They appear to shift in several directions and magnitudes, as can be seen in the distinct semi-circle shape that it has formed. It appears that the electrodes at the centre (of the region of interest selected), or at approximately 25000 µm in the Y cross-section, undergo a rapid misalignment earlier (around 2.4 s) than the electrodes towards the outer edges, at 0 or 5000 µm, which show a similar phenomenon much later around 3.5 s and 2.9 s, respectively. Overall, between 2.0 – 2.5 s, there is a gradual movement of electrodes which correlates with the subtle movement of electrodes shown in the corresponding time frames in Figure 7.11 (a). When further correlated with the 2D spatiotemporal map in Figure 7.11 (c), it appears that the centre of the cell is where the majority of electrode architecture is affected. Two areas are highlighted that show this, first between 0 and 1 s, where there are red regions towards the higher X cross-section (which represents the height of the cell top-down) values showing the extent of misalignment and second, between 1.75 and 2.5 s, where dark blue regions show areas of localised electrode delamination and/or total structural failure of the electrodes. While these findings are similar to those found in the slow-speed imaging results, there is a more in-depth understanding of the structural evolution of the wave-like feature at this higher time resolution (i.e. the duration and direction).
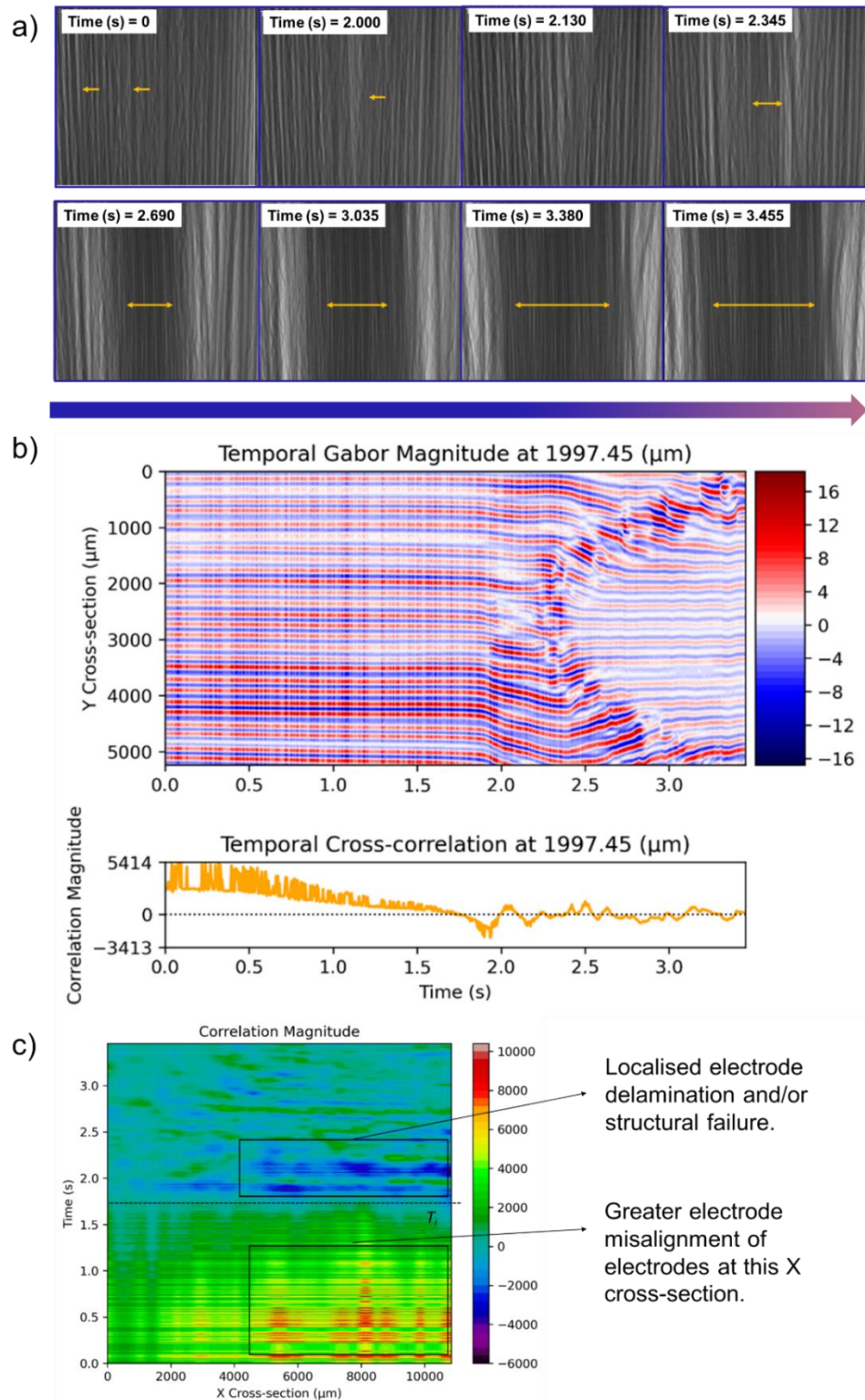
Figure 7.11 Radiographs and processed data for the analyses of Sample 4 using high-speed imaging using synchrotron radiation. (a) Frame-by-frame images are taken across the wave-like feature, where the movement of electrode layers is highlighted. (b) Temporal cross-correlation is conducted for the duration of the wave-like feature. The top plot shows a 2D map of the temporal evolution of the normalised Gabor signal at a fixed X position. The bottom plot shows the corresponding normalised temporal cross-correlation, where the Gabor signal at time T_i is cross-correlated with that of the electrode structure at the beginning of the recording.

7.3.5. Pre- and post-mortem X-ray CT

The uses of 3D X-ray CT in the analyses of battery failure have been explored extensively in earlier sections of this thesis. Building on the numerous benefits outlined by non-destructive image analyses, the chamber was specifically designed so that cell samples could be imaged while they were inside the chamber. The parameters used for the acquisition of these images are described in detail in the Section 7.3.2. Figure 7.12 shows volume renderings of Sample 1 before and after thermal failure (without interrupting the experimental setup between scans).
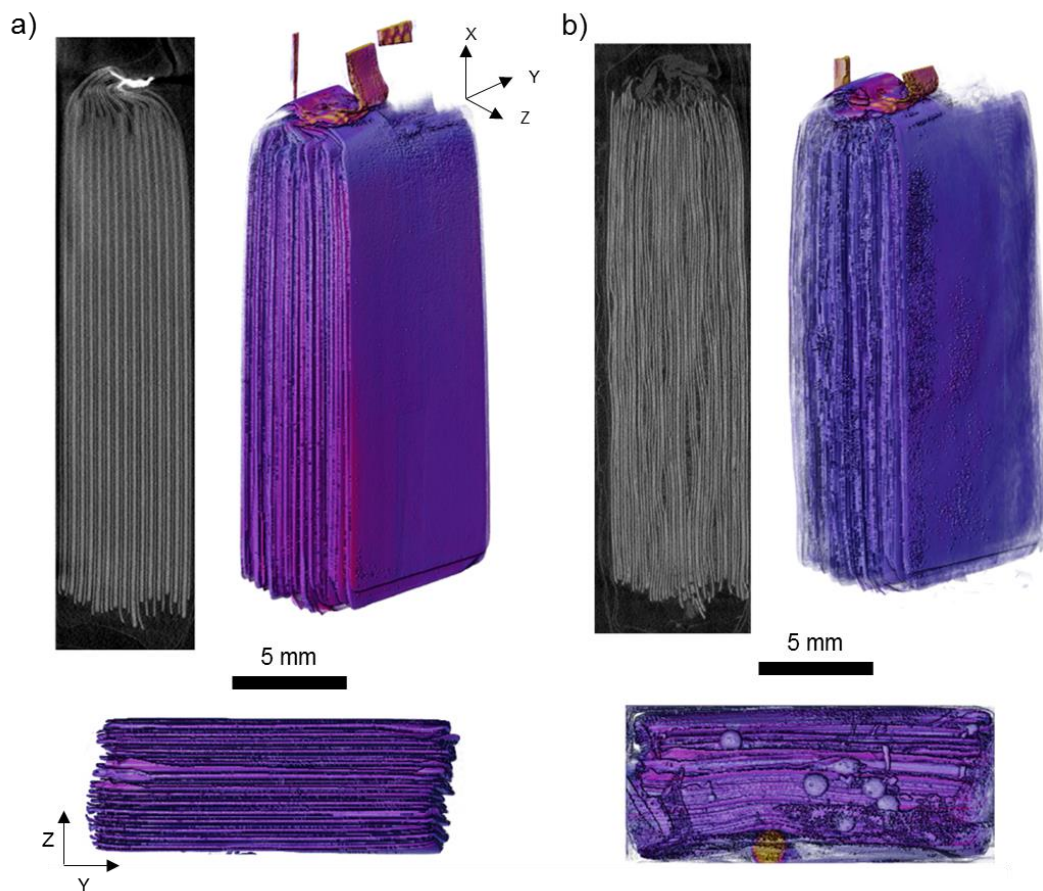
Figure 7.12 2D orthoslices in the XZ planes and the corresponding 3D volume rendering of the datasets in various planes of the 210 mAh Sample 1 (a) before, and (b) after thermal failure. Images were captured while the sample was still inside the experimental chamber.

A preliminary comparison of the 2D grayscale orthogonal slices for the cell sample before and after failure shows obvious signs of electrode delamination - in particular, where darker (grey and black) regions appear in the cell centre after failure, it is expected these are voids (or areas where large

expansion has accumulated). What is easier to assess using 3D volume renderings is where attenuating material has accumulated, such as those highlighted in Figure 7.12 (b). The globules are expected to be an amalgamation of various elements from the numerous components of the cell. It is predicted that aluminium forms the majority of these globules since the cell temperature was measured to exceed 660 °C (the melting point of aluminium), however, further analysis such as that by opening the cell and carrying out an EDX analysis can aid in understanding what elements are present in particular areas of the cell. While this detail/or focus was not in the scope of this chapter, it is acknowledged that the chamber experiments can be followed by a wide range of analyses.

7.4. Conclusions from Chapter 7

For the six samples investigated in this chapter, the total time taken from a start temperature of 80 °C to thermal runaway was approximately 20 minutes and the onset temperatures for thermal runaway were recorded within the range of 196 °C to 210 °C. The beginning of the thermal runaway event (defined as a sample temperature increase greater than 15 °C s^{-1}), where the effects on the electrode structure are the most catastrophic, lasted for approximately 1 s. *Operando* radiographic images during this event revealed that the structural displacement of electrode layers begins at the centre of the cell and propagates outwards in a wave-like motion, this was further corroborated by cross-correlating Gabor signals and spatiotemporal mapping[182] for the three lab-based datasets and the three correlating datasets obtained using synchrotron radiation alike. For the lab-based radiography, data was recorded from the start temperature to thermal runaway, and reactions such as the electrolyte decomposition, ca. 105 °C, and separator melting, ca.130 °C were correlated with the observations in frame-by-frame images and plots of cross-correlating Gabor signals. A gradual shift (approximately by one electrode layer) of the electrodes in the events leading up to thermal runaway correlated with the predicted 'slow' nature of gas generation during electrolyte and anode reactions. Furthermore, the shrinkage of the separator was captured and labelled as the next characteristic event,

event (B) in the lead-up to thermal runaway. It was revealed that the separator microstructure did not fully collapse and cause a rapid ISC event; instead, a micro-ISC event occurred where the cell voltage is predicted to have dropped but kept above zero. Lastly, the quantitative analysis revealed that a wave-like motion began at the centre of the cell and propagated outwards which suggests that the centre of the cell was the area that had the poorest capability for heat rejection.

By comparison with correlative synchrotron measurements, the instrument introduced in this chapter, which induces thermal failure for lab-based X-ray CT, is proven to be a viable and more accessible method to investigate thermal failure within a 210 mAh pouch cell. While synchrotron data has a higher-speed imaging advantage, it is limited to only recording characteristic events of short duration due to limits in data storage capacity. Whereas continuous imaging in lab-based radiography has the benefit of measuring the slower architectural changes taking place up to thermal runaway, albeit at a marginally lower spatial resolution. The findings in this chapter revealed that imaging speeds of 3.75 fps can be successful in revealing key architectural features during the thermal failure of pouch cells with an approximate capacity of 250 mAh. Cells of a higher capacity may degrade faster and should be the focus of future work (e.g. testing how the adjustment of various variables affects the ability of this methodology and imaging speed to capture events). Higher-speed imaging, at 20,000 fps, revealed marginally fewer insights for the pouch cell failures in this chapter, and their corresponding analyses when compared to the comparably limited capability of the lab-based sources. Slower recording times revealed greater detail owing to greater data storage capability (fewer images over more time) and higher FOV.

3D X-ray CT of the cell samples further showed the capabilities of the experimental design. The benefits of non-destructively imaging whole-cell samples, particularly those with high aspect ratios, such as pouch cells, have been discussed in detail in earlier sections of this thesis. This result sets the outer framework for ex-situ analyses where local shifts in the 3D volumes of the pristine cell (before thermal failure) to the failed cell can be computed by

digital volume correlation or multi-scale imaging can be carried out after dismantling the cell after failure. Furthermore, the impact of adjusting variables such as the sample format (cell dimensions), cell SOC, or rate of heating on electrode architecture are all ideas for future work.

Chapter 8

8. Conclusions

Battery technology has been growing in its application to the various energy storage systems that feature in our day-to-day lives; from mobile phones to homes. Alongside this, concerns regarding their safety have also grown. Several high-profile LIB failures have accelerated the need for research in this field. Stakeholders from the industry, regulatory bodies, and academia have all laid the foundations for current methods in battery safety assessment. The goal of this work was to establish the correlations between conventional assessment techniques and to advance or develop existing or new methodologies through the use of thermal and imaging analysis. Each results chapter in this thesis adds value to this goal and, the following conclusions can be made in this context.

Chapter 2 reviewed the multiple modes of degradation that exist for LIB components during thermal runaway. The most characteristic behaviour was the generation of heat and gas. Several methods exist for the measurement and analysis of heat generation in a LIB during operation under normal conditions and during failure. It was understood that DSC, a technique used to assess the thermal behaviours of battery materials, was limited in the sense that it could only measure the heat effects of battery materials if they were collected as electrode powders from raw materials or from dismantling cycled cells. Furthermore if analysing the heat effect of the electrolyte, it would need to be conducted outside of the normal cell operating environment. As a result, it was difficult to correlate the measured heat effects to real working cells. Several simulation models have been set out to predict these same component-level heat effects. The methodology established in Chapter 4, which utilised a novel-DSC coin cell calorimeter advanced upon the existing approaches to heat generation measurements using DSC in literature.

By establishing a robust baseline for heat generation measurements, the results in Chapter 4 demonstrated two methods in which a novel-DSC coin

cell calorimeter can be used. Firstly, to conduct thermal stability tests, like that of changing the electrolyte composition where its effects can be analysed and isolated from the other components (without physically isolating it from the working cell). Second, for analysing the heat effects as the cell undergoes charge and discharge (under various operating conditions). The novel correlation with electrochemical data provided new insights into heat effects arising from the various reactions, internal resistances and transport phenomena occurring within the LIB during operation. Furthermore, the results highlighted the replicability and scalability of the methodology for testing large numbers of cells and experimental variables. The calculated heat generation for charge and discharge from the measured heat flux found in this chapter can be used to validate existing simulation models of heat generation.

Battery safety can be assessed from various perspectives and across multiple scales. Chapter 5 utilised a well-established technique (X-ray CT) to show how it can be applied to the multiple variations of LIB materials in terms of size, shape, format, and internal structure, and at various length scales ranging from particle morphology, and bulk electrode structures up to whole-cell design. The need for high-resolution interior topographies of high aspect ratio samples; i.e. single-layer pouch cells was highlighted and a methodology was developed to address this. Parameters such as particle size and porosity are vital to understanding cell behaviour and performance. In this same chapter, this was taken a step further when such parameters were correlated to the heat flux signals for three cathode samples. This correlation of multi-scale imaging with thermal analyses continued in the development of a procedure for examining cells before and after thermal (and other) failures. The benefits of invasive and non-invasive imaging were discussed using a baseline made up of two cells that underwent two different failure types (thermal and mechanical). Overall, the findings in these chapters provide an extensive and exhaustive demonstration of how multi-scale imaging can be used in correlation with failure testing and thermal analyses. The methods introduced (scanning whole cells, cell disassembly and sample preparation can all be readily applied to assessments of battery performance, safety and failure.

Building on the post-mortem analysis and multi-scale imaging methodology established in Chapter 5, the next investigation used this to assess the failure of a popular commercially available cell with a cylindrical format (18650). The cell underwent thermal failure (via ARC) and was analysed in detail in Chapter 6. While the investigation lead to the understanding of how individual components behaved, it was limited to snapshots immediately before and after failure; i.e. ex-situ.

Chapter 6 highlighted a strong need for dynamic investigations when considering battery safety assessment, as it can reveal where gas generates, how the structure deforms, and how the integrated safety features behave. With this in mind, Chapter 7 introduced a custom-built chamber design that can be fitted to X-ray CT instruments to aid the failure and imaging of battery failures in real time. Building on existing literature for operando imaging of high-speed battery failures, this technique addressed the gap in knowledge of how the slower degradation mechanisms that lead up to the catastrophic thermal runaway event affect cell mechanics (particularly the internal electrode architecture). In addition, the assessment technique developed in this chapter highlighted ways in which safety testing can be more accessible, easily and quickly reproduced for testing large numbers of cells.

Overall, the findings in this thesis verify that X-ray CT and calorimetry remain promising methods for the safety evaluation of LIBs. In the context of DSC tests, it is possible to establish a cause-effect relationship between temperature, C-rate, maximum voltage cut-off and heat effects (and/or failure occurrence). In doing so, the DSC methodology can deliver a detailed insight into the progressive mechanisms of degradation, as well as the onset of thermal runaway through heat generation. Different cell components, design parameters as well as temperature and electrochemical operating conditions can therefore be critically evaluated in terms of safety. These results, in combination with those established using X-ray CT, are a valuable contribution to the overall goal of advancing battery safety assessment.

8.1. Future Work and Outlook

This thesis has presented a multitude of advanced characterisation techniques for battery safety assessment. Many of the techniques and methodologies established in this work have been demonstrated with preliminary investigations. Therefore, a clear initial path for future work exists in fine-tuning these methods. The following points should be addressed in future work.

<u>Detailed studies of heat generation, using the DSC analyses introduced in this work, to evaluate its full potential.</u>

The results presented in Chapter 4 provided a good baseline for future tests of a similar manner to be reproduced, where variables such as changing the electrolyte composition or electrode chemistries can be tuned to measure their thermal effects. Furthermore, isolating the heat effects from different components (the separator, cathode and anode) can help establish a databank for components tested in real working cells and correlated with existing simulation models. The methodology was proven to have good replicability and therefore could be used as a precursor study before scaled-up tests are conducted – the possibility of this should be assessed.

<u>Greater refinement of the methodology when imaging at multiple length scales and standardising the protocol for cell disassembly.</u>

The X-ray CT images of single-layer pouch cells in Chapter 5 outlined the possibility of extracting useful electrode material parameters without cell disassembly. This can still however be optimised for cells with larger cell dimensions, or cells in a module pack, such that methodology can be utilised by EV battery manufacturers, for example. Additionally, the findings in Chapter 5 highlighted the need for standardising methods of cell disassembly, especially for subsequent analyses like X-ray CT imaging. The standardisation would have multiple benefits for research advancements as researchers in academia and industry could easily share and compare findings.

Evaluate the use of the calorimetry chamber for an all-encompassing approach to real-time failure imaging.

The chamber design introduced in Chapter 7 highlighted ways to quickly and easily test the thermal failure of cells with a capacity below 250 mAh. The custom design however still has much room for additions, such as gas analyses and voltage measurements. Furthermore, the battery module and lid can be easily replaced to accommodate cells of varying capacities and formats (as long as they remain suitable for operation inside the size constraints of X-ray CT imaging equipment). Imaging at slower speeds hosts a range of advantages and is particularly useful for studies where gas evolution through a cell may be of interest.

Chapter 9

9. References

[1]   International Energy Agency, "World Energy Outlook 2021," 2021.

[2]   EIA, "Annual Energy Outlook 2017 with projections to 2050," *J. Phys. A Math. Theor.*, vol. 44, no. 8, pp. 1–64, 2017.

[3]   European Comission, "Batteries - modernising EU rules," 2020. [Online]. Available: https://ec.europa.eu/info/law/better-regulation/have-your-say/initiatives/12399-Batteries-modernising-EU-rules_en.

[4]   D. Harrison, "Electrifying Europe: EU 'Fit for 55' legislation will transform the automotive supply chain," *Automotive Logistics*, 2021. [Online]. Available: https://www.automotivelogistics.media/electric-vehicles/electrifying-europe-eu-fit-for-55-legislation-will-transform-the-automotive-supply-chain/42207.article.

[5]   UK Department of Transport, "Decarbonising Transport; A Better, Greener Britain," 2021.

[6]   S. Chu and A. Majumdar, "Opportunities and challenges for a sustainable energy future," 2012.

[7]   D. Howell, B. Cunningham, T. Duong, and P. Faguy, "VTO Battery R & D Funding," p. 24, 2016.

[8]   Office of Energy Efficiency & Renewable Energy, "Battery500: Progress Update," *Energy.gov*, 2020. [Online]. Available: https://www.energy.gov/eere/articles/battery500-progress-update.

[9]   D. H. Doughty and E. P. Roth, "A General Discussion of Li Ion Battery Safety," *Interface Mag.*, vol. 21, no. 2, pp. 37–44, 2012.

[10]   J. R. Dahn and E. W. Fuller, "Thermal-Stability of Lixcoo2, Lixnio2 and Lambda-Mno2 and Consequences for the Safety of Li-Ion Cells," *Solid State Ionics*, vol. 69, no. 3–4, pp. 265–270, 1994.

[11]   H. Noh, S. Youn, C. Seung, and Y. Sun, "Comparison of the structural and electrochemical properties cathode material for lithium-ion batteries," vol. 233, pp. 2–11, 2013.

[12]   J. Christman, "The Case of the Burning Laptops," *J. Case Stud.*, vol. 30, no. 1, pp. 88–97, 2012.

[13]   Reuters, "Note 7 Fiasco Could Burn a $17 Billion Hole Samsung Accounts," 2016. [Online]. Available: https://www.reuters.com/article/us-samsung-elec-smartphones-costs/note-7-fiasco-could-burn-a-17-billion-hole-in-samsung-accounts-idUSKCN12B0FX.

[14]   M. J. Loveridge *et al.*, "Looking deeper into the galaxy (Note 7)," *Batteries*, vol. 4, no. 1, pp. 1–11, 2018.

[15]   E. Darcy, "Screening Li-ion batteries for internal shorts," *J. Power Sources*, vol. 174, no. 2, pp. 575–578, 2007.

[16]   D. P. Finegan *et al.*, "Characterising thermal runaway within lithium-ion cells by inducing and monitoring internal short circuits," *Energy Environ. Sci.*, vol. 10, no. 6, pp. 1377–1388, 2017.

[17]   D. Kehrwald, P. R. Shearing, N. P. Brandon, P. K. Sinha, and S. J. Harris, "Local tortuosity inhomogeneities in a lithium battery composite electrode," *J. Electrochem. Soc.*, vol. 158, no. 12, p. A1393, 2011.

[18]   S. J. Harris, D. J. Harris, and C. Li, "Failure statistics for commercial lithium ion batteries: A study of 24 pouch cells," *J. Power Sources*, vol. 342, pp. 589–597, 2017.

[19]   Chartered Trading Standards Institute UK, "Take charge of battery safety, vapers urged by Office for Product Safety and Standards," 2020. [Online]. Available: https://www.tradingstandards.uk/news-policy/news-room/2020/take-charge-of-battery-safety-vapers-urged-by-office-for-product-safety-and-standards.

[20]   P. Biensan *et al.*, "On safety of lithium-ion cells," *J. Power Sources*, vol. 81–82, pp. 906–912, 1999.

[21]   L. Bravo Diaz *et al.*, "Review—Meta-Review of Fire Safety of Lithium-

Ion Batteries: Industry Challenges and Research Contributions," *J. Electrochem. Soc.*, vol. 167, no. 9, p. 090559, 2020.

[22] S. J. Harris and P. Lu, "Effects of inhomogeneities -Nanoscale to mesoscale -on the durability of Li-ion batteries," *J. Phys. Chem. C*, vol. 117, no. 13, pp. 6481–6492, 2013.

[23] L. Salvo, M. Suéry, A. Marmottant, N. Limodin, and D. Bernard, "3D imaging in material science: Application of X-ray tomography," *Comptes Rendus Phys.*, vol. 11, no. 9–10, pp. 641–649, 2010.

[24] A. J. Smith, J. C. Burns, S. Trussler, and J. R. Dahn, "Precision Measurements of the Coulombic Efficiency of Lithium-Ion Batteries and of Electrode Materials for Lithium-Ion Batteries," *J. Electrochem. Soc.*, vol. 157, no. 2, p. A196, 2010.

[25] T. Spila *et al.*, "Cycling Behavior of NCM523 / Graphite Lithium-Ion Cells in the 3 – 4 . 4 V Range : Diagnostic Studies of Full Cells and Harvested Electrodes," vol. 164, no. 1, pp. 6054–6065, 2017.

[26] M. S. Ziegler, J. Song, and J. E. Trancik, "Determinants of lithium-ion battery technology cost decline," *Energy Environ. Sci.*, vol. 14, no. 12, pp. 6074–6098, 2021.

[27] Volta Foundation & Intercalation, "The Battery Report 2021," *Report*, 2022. [Online]. Available: https://www.batterybrunch.org/battery-report%0Ahttps://medium.com/batterybits/the-battery-report-2021-442ed2a06324.

[28] S&P Global Platts, "Volkswagen's plan on LFP use shifts hydroxide dominance narrative in EV sector," 2021. [Online]. Available: https://www.spglobal.com/platts/en/market-insights/latest-news/metals/031721-volkswagens-plan-on-lfp-use-shifts-hydroxide-dominance-narrative-in-ev-sector.

[29] Electrive.com, "Daimler to use LFP cells from 2024," *Electrive*, 2021. [Online]. Available: https://www.electrive.com/2021/10/28/daimler-to-use-lfp-cells-from-2024/.

[30] CNBC, "Tesla will change the type of battery cells it uses in all its standard-range cars," *Climate*, 2020. [Online]. Available: https://www.cnbc.com/2021/10/20/tesla-switching-to-lfp-batteries-in-all-standard-range-cars.html.

[31] BloombergNEF, "Battery Pack Prices Fall to an Average of $132/kWh, But Rising Commodity Prices Start to Bite," *Annual Battery Price Survey*, 2021. [Online]. Available: https://about.bnef.com/blog/battery-pack-prices-fall-to-an-average-of-132-kwh-but-rising-commodity-prices-start-to-bite/.

[32] Amnesty International, "Exposed: Child labour behind smart phone and electric car batteries," 2016. [Online]. Available: https://www.amnesty.org/en/latest/news/2016/01/child-labour-behind-smart-phone-and-electric-car-batteries/.

[33] G. E. Blomgren, "The Development and Future of Lithium Ion Batteries," vol. 164, no. 1, pp. 5019–5025, 2017.

[34] P. G. Balakrishnan, R. Ramesh, and T. Prem Kumar, "Safety mechanisms in lithium-ion batteries," *J. Power Sources*, vol. 155, no. 2, pp. 401–414, 2006.

[35] M. Jacoby, "Assessing The Safety Of Lithium-Ion Batteries," *Chemical and Engineering News*, 2013. .

[36] Reuters, "Sony recalls PC batteries," 2008. [Online]. Available: https://www.reuters.com/article/us-sony-battery/sony-recalls-pc-batteries-idUSTRE49U1EZ20081031.

[37] E. Musk, "Model S Fire," *Tesla Blog*, 2013. [Online]. Available: https://www.tesla.com/en_GB/blog/model-s-fire.

[38] Reuters, "Tesla top-of-range car caught fire while owner was driving, lawyer says," *Autos & Transportation*, 2021. [Online]. Available: https://www.reuters.com/business/autos-transportation/tesla-top-of-range-car-caught-fire-while-owner-was-driving-lawyer-says-2021-07-02/.

[39] InsideEVs, "Jaguar I-Pace Catches Fire While Charging In Hungary," 2021. [Online]. Available: https://insideevs.com/news/544255/jaguar-ipace-charging-fire-hungary/.

[40] V. Srinivasan, "Batteries for vehicular applications," *AIP Conf. Proc.*, vol. 1044, pp. 283–296, 2008.

[41] A. M. Boyce *et al.*, "Design of Scalable, Next-Generation Thick Electrodes: Opportunities and Challenges," *ACS Nano*, vol. 15, no. 12, pp. 18624–18632, 2021.

[42] D. J. Noelle, M. Wang, and Y. Qiao, "Improved safety and mechanical characterizations of thick lithium-ion battery electrodes structured with porous metal current collectors," *J. Power Sources*, vol. 399, no. July, pp. 125–132, 2018.

[43] X. Lu *et al.*, "3D microstructure design of lithium-ion battery electrodes assisted by X-ray nano-computed tomography and modelling," *Nat. Commun.*, no. 2020, pp. 1–13.

[44] S. M. Bak *et al.*, "Structural changes and thermal stability of charged LiNixMnyCozO2 cathode materials studied by combined in situ time-resolved XRD and mass spectroscopy," *ACS Appl. Mater. Interfaces*, vol. 6, no. 24, pp. 22594–22601, 2014.

[45] J. R. Dahn, E. W. Fuller, M. Obrovac, and U. von Sacken, "Thermal stability of LixCoO2, LixNiO2and λ-MnO2and consequences for the safety of Li-ion cells," *Solid State Ionics*, vol. 69, no. 3–4, pp. 265–270, 1994.

[46] U. von Sacken, E. Nodwell, A. Sundher, and J. R. R. Dahn, "Comparative thermal stability of carbon intercalation anodes and lithium metal anodes for rechargeable lithium batteries," *J. Power Sources*, vol. 54, no. 2, pp. 240–245, Apr. 1995.

[47] Y. Baba, S. Okada, and J. ichi Yamaki, "Thermal stability of LixCoO2 cathode for lithium ion battery," *Solid State Ionics*, vol. 148, no. 3–4, pp. 311–316, 2002.

[48] X. Y. Yao and M. G. Pecht, "Tab design and failures in cylindrical li-ion batteries," *IEEE Access*, vol. 7, pp. 24082–24095, 2019.

[49] S. Tobishima and J. Yamaki, "A consideration of lithium cell safety," *J. Power Sources*, vol. 81–82, pp. 882–886, 1999.

[50] Q. Wang, B. Mao, S. I. Stoliarov, and J. Sun, "A review of lithium ion battery failure mechanisms and fire prevention strategies," *Prog. Energy Combust. Sci.*, vol. 73, pp. 95–131, 2019.

[51] N. Nitta, F. Wu, J. T. Lee, and G. Yushin, "Li-ion battery materials: Present and future," *Mater. Today*, vol. 18, no. 5, pp. 252–264, 2015.

[52] A. Du Pasquier, I. Plitz, S. Menocal, and G. Amatucci, "A comparative study of Li-ion battery, supercapacitor and nonaqueous asymmetric hybrid devices for automotive applications," *J. Power Sources*, vol. 115, no. 1, pp. 171–178, 2003.

[53] C. R. Birkl, M. R. Roberts, E. Mcturk, P. G. Bruce, and D. A. Howey, "Degradation diagnostics for lithium ion cells," *J. Power Sources*, vol. 341, pp. 373–386, 2017.

[54] S. Jin, J. Li, C. Daniel, D. Mohanty, S. Nagpure, and D. L. Wood, "The state of understanding of the lithium-ion-battery graphite solid electrolyte interphase (SEI) and its relationship to formation cycling *," *Carbon N. Y.*, vol. 105, pp. 52–76, 2016.

[55] J. P. Tu, X. B. Zhao, G. S. Cao, D. G. Zhuang, T. J. Zhu, and J. P. Tu, "Enhanced cycling stability of LiMn2O4by surface modification with melting impregnation method," *Electrochim. Acta*, vol. 51, no. 28, pp. 6456–6462, 2006.

[56] G. Ceder and S. K. Mishra, "The Stability of Orthorhombic and Monoclinic-Layered LiMnO[sub 2]," *Electrochem. Solid-State Lett.*, vol. 2, no. 11, p. 550, 1999.

[57] K. M. Shaju and P. G. Bruce, "Macroporous Li(Ni1/3Co1/3Mn1/3)O2: A High-Power and High-Energy Cathode for Rechargeable Lithium Batteries," *Adv. Mater.*, vol. 18, no. 17, pp. 2330–2334, 2006.

[58] Y. K. Sun, S. T. Myung, B. C. Park, J. Prakash, I. Belharouak, and K. Amine, "High-energy cathode material for long-life and safe lithium batteries," *Nat. Mater.*, vol. 8, no. 4, pp. 320–324, 2009.

[59] A. Yoshino, K. Sanechika, and T. Nakajima, "Secondary battery," 1986.

[60] R. Fong, "Studies of Lithium Intercalation into Carbons Using Nonaqueous Electrochemical Cells," *J. Electrochem. Soc.*, vol. 137, no. 7, p. 2009, 1990.

[61] K. Matsuki and K. Ozawa, "Lithium Ion Rechargeable Batteries: Materials, Technology, and New Applications," *Lithium Ion Recharg. Batter. Mater. Technol. New Appl.*, pp. 1–9, 2009.

[62] Y. Nishi, "Lithium ion secondary batteries; past 10 years and the future," *J. Power Sources*, vol. 100, no. 1–2, pp. 101–106, 2001.

[63] D. S. Eastwood *et al.*, "Lithiation-Induced Dilation Mapping in a Lithium-Ion Battery Electrode by 3D X-Ray Microscopy and Digital Volume Correlation," *Adv. Energy Mater.*, vol. 4, no. 4, pp. 1–7, 2014.

[64] D. Fouchard and L. Lechner, "Analysis of safety and reliability in secondary lithium batteries," *Electrochim. Acta*, vol. 38, no. 9, pp. 1193–1198, Jun. 1993.

[65] M. Winter, J. O. Besenhard, M. E. Spahr, and P. Novák, "Insertion Electrode Materials for Rechargeable Lithium Batteries," *Adv. Mater.*, vol. 10, no. 10, pp. 725–763, Jul. 1998.

[66] T. Placke, R. Kloepsch, S. Dühnen, and M. Winter, "Lithium ion, lithium metal, and alternative rechargeable battery technologies: the odyssey for high energy density."

[67] X. Xu *et al.*, "Bamboo-like amorphous carbon nanotubes clad in ultrathin nickel oxide nanosheets for lithium-ion battery electrodes with long cycle life," *Carbon N. Y.*, vol. 84, no. 1, pp. 491–499, 2015.

[68] J. B. Goodenough and P. Singh, "Review—Solid Electrolytes in Rechargeable Electrochemical Cells," *J. Electrochem. Soc.*, vol. 162, no. 14, pp. A2387–A2392, 2015.

[69] D. Aurbach *et al.*, "Design of electrolyte solutions for Li and Li-ion batteries: A review," *Electrochim. Acta*, vol. 50, no. 2-3 SPEC. ISS., pp. 247–254, 2004.

[70] H. Yang, G. V. Zhuang, and P. N. Ross, "Thermal stability of LiPF6 salt and Li-ion battery electrolytes containing LiPF6," *J. Power Sources*, vol. 161, no. 1, pp. 573–579, 2006.

[71] S. E. Sloop, J. K. Pugh, S. Wang, J. B. Kerr, and K. Kinoshita, "Chemical Reactivity of PF[sub 5] and LiPF[sub 6] in Ethylene Carbonate/Dimethyl Carbonate Solutions," *Electrochem. Solid-State Lett.*, vol. 4, no. 4, p. A42, 2001.

[72] E. P. Roth and C. J. Orendorff, "How Electrolytes Influence Battery Safety," *Interface*, vol. 21, no. 2, pp. 45–50, 2012.

[73] J. Y. Luo, W. J. Cui, P. He, and Y. Y. Xia, "Raising the cycling stability of aqueous lithium-ion batteries by eliminating oxygen in the electrolyte," *Nat. Chem.*, vol. 2, no. 9, pp. 760–765, 2010.

[74] S. S. Zhang, "A review on electrolyte additives for lithium-ion batteries," *J. Power Sources*, vol. 162, no. 2 SPEC. ISS., pp. 1379–1394, 2006.

[75] P. Verma, P. Maire, and P. Novák, "A review of the features and analyses of the solid electrolyte interphase in Li-ion batteries," *Electrochim. Acta*, vol. 55, no. 22, pp. 6332–6341, 2010.

[76] Z. Chen *et al.*, "Multi-scale study of thermal stability of lithiated graphite," *Energy Environ. Sci.*, vol. 4, no. 10, p. 4023, 2011.

[77] A. Jana, D. R. Ely, and R. E. García, "Dendrite-separator interactions in lithium-based batteries," *J. Power Sources*, vol. 275, pp. 912–921, 2015.

[78] T. Ohsaki *et al.*, "Overcharge reaction of lithium-ion batteries," *J. Power Sources*, vol. 146, no. 1–2, pp. 97–100, 2005.

[79] Addionics, "Pouch, Cylindrical or Prismatic: Which Battery Format Will Rule the Market?," 2021. [Online]. Available: https://www.addionics.com/post/pouch-cylindrical-or-prismatic-which-battery-format-will-rule-the-market.

[80] D. Bernardi, E. Pawlikowski, and J. Newman, "General Energy Balance for Battery Systems.," *Electrochem. Soc. Ext. Abstr.*, vol. 84–2, pp. 164–165, 1984.

[81] H. Maleki, G. Deng, A. Anani, and J. Howard, "Thermal Stability Studies of Li-Ion Cells and Components," *J. Electrochem. Soc.*, vol. 146, no. 9, pp. 3224–3229, 1999.

[82] S. C. Levy and P. Bro, *Battery Hazards and Accident Prevention*, 1st ed. Springer US, 1994.

[83] D. Doughty, "Li Ion Battery Safety and Abuse Tolerance Report," *Total Battery Consulting, Industry Report: Battery Safety*, 2019. [Online]. Available: https://totalbatteryconsulting.com/industry-reports/Battery-safety-report/overview.html.

[84] J. Jiang and J. R. Dahn, "ARC studies of the thermal stability of three different cathode materials: LiCoO2; Li[Ni0.1Co0.8Mn0.1]O 2; and LiFePO4, in LiPF6 and LiBoB EC/DEC electrolytes," *Electrochem. commun.*, vol. 6, no. 1, pp. 39–43, 2004.

[85] G. Zhong, J. Gong, C. Wang, K. Xu, and H. Chen, "Comparison of the Electrochemical Performance and Thermal Stability for Three Kinds of Charged Cathodes," vol. 6, no. October, pp. 1–7, 2018.

[86] W. Belharouak, IliasLu, D. Vissers, and K. Amine, "Safety characteristics of Li(Ni0.8Co0.15Al0.05)O2 and Li(Ni1/3Co1/3Mn1/3)O2," *Electrochem. commun.*, vol. 8, pp. 329–335, 2006.

[87] R. Jung, M. Metzger, F. Maglia, C. Stinner, and H. A. Gasteiger, "Oxygen Release and Its Effect on the Cycling Stability of LiNi $_x$ Mn $_y$ Co $_z$ O $_2$ (NMC) Cathode Materials for Li-Ion Batteries," *J. Electrochem. Soc.*, vol. 164, no. 7, pp. A1361–A1377, 2017.

[88] W. Li, E. M. Erickson, and A. Manthiram, "High-nickel layered oxide cathodes for lithium-based automotive batteries," *Nat. Energy*, vol. 5, no. 1, pp. 26–34, 2020.

[89] S. Lee *et al.*, "In-Depth Analysis of the Degradation Mechanisms of High-

Nickel, Low/No-Cobalt Layered Oxide Cathodes for Lithium-Ion Batteries," *Adv. Energy Mater.*, vol. 11, no. 31, pp. 1–14, 2021.

[90]   M. Yi, W. Li, and A. Manthiram, "Delineating the Roles of Mn, Al, and Co by Comparing Three Layered Oxide Cathodes with the Same Nickel Content of 70% for Lithium-Ion Batteries," *Chem. Mater.*, vol. 34, no. 2, pp. 629–642, 2022.

[91]   H. Li, M. Cormier, N. Zhang, J. Inglis, J. Li, and J. R. Dahn, "Is Cobalt Needed in Ni-Rich Positive Electrode Materials for Lithium Ion Batteries?," *J. Electrochem. Soc.*, vol. 166, no. 4, pp. A429–A439, 2019.

[92]   M. M. E. Cormier, N. Zhang, A. Liu, H. Li, J. Inglis, and J. R. Dahn, "Impact of Dopants (Al, Mg, Mn, Co) on the Reactivity of Li x NiO 2 with the Electrolyte of Li-Ion Batteries," *J. Electrochem. Soc.*, vol. 166, no. 13, pp. A2826–A2833, 2019.

[93]   H. Zhou *et al.*, "The Role of Separator Thermal Stability in Safety Characteristics of Lithium-ion Batteries," *J. Electrochem. Soc.*, vol. 169, p. 090521, 2022.

[94]   B. Ravdel, K. M. Abraham, R. Gitzendanner, J. DiCarlo, B. Lucht, and C. Campion, "Thermal stability of lithium-ion battery electrolytes," *J. Power Sources*, vol. 119–121, pp. 805–810, 2003.

[95]   L. Geng *et al.*, "Probing Thermal Stability of Li-Ion Battery Ni-Rich Layered Oxide Cathodes by means of Operando Gas Analysis and Neutron Diffraction," *ACS Appl. Energy Mater.*, vol. 3, no. 7, pp. 7058–7065, 2020.

[96]   J. Robinson *et al.*, "Microstructural Analysis of the Effects of Thermal Runaway on Li-Ion and Na-Ion Battery Electrodes," *J. Electrochem. Energy Convers. Storage*, vol. 15, no. November, pp. 1–9, 2017.

[97]   R. E. Williford, V. V. Viswanathan, and J. G. Zhang, "Effects of entropy changes in anodes and cathodes on the thermal behavior of lithium ion batteries," *J. Power Sources*, vol. 189, no. 1, pp. 101–107, 2009.

[98]   A. Kriston, I. Adanouj, V. Ruiz, and A. Pfrang, "Quantification and

simulation of thermal decomposition reactions of Li-ion battery materials by simultaneous thermal analysis coupled with gas analysis," *J. Power Sources*, vol. 435, no. July, p. 226774, 2019.

[99] S. Arora and A. Kapoor, "Experimental study of heat generation rate during discharge of lifePO4 pouch cells of different nominal capacities and thickness," *Batteries*, vol. 5, no. 4, 2019.

[100] A. Wang, S. Kadam, H. Li, S. Shi, and Y. Qi, "Review on modeling of the anode solid electrolyte interphase (SEI) for lithium-ion batteries," *npj Comput. Mater.*, vol. 4, no. 1, 2018.

[101] S. S. Zhang, K. Xu, and T. R. Jow, "Formation of solid electrolyte interface in lithium nickel mixed oxide electrodes during the first cycling," *Electrochem. Solid-State Lett.*, vol. 5, no. 5, pp. 92–95, 2002.

[102] T. Kawamura, A. Kimura, M. Egashira, S. Okada, and J. I. Yamaki, "Thermal stability of alkyl carbonate mixed-solvent electrolytes for lithium ion cells," *J. Power Sources*, vol. 104, no. 2, pp. 260–264, 2002.

[103] M. H. Ryou *et al.*, "Effects of lithium salts on thermal stabilities of lithium alkyl carbonates in SEI layer," *Electrochim. Acta*, vol. 83, pp. 259–263, 2012.

[104] G. G. Botte, R. E. White, and Z. Zhang, "Thermal stability of LiPF6-EC:EMC electrolyte for lithium ion batteries," *J. Power Sources*, vol. 97–98, pp. 570–575, 2001.

[105] Q. Wang, J. Sun, X. Yao, and C. Chen, "Thermal Behavior of Lithiated Graphite with Electrolyte in Lithium-Ion Batteries," *J. Electrochem. Soc.*, vol. 153, no. 2, p. A329, 2006.

[106] H. Park, T. Yoon, J. Mun, J. H. Ryu, J. J. Kim, and S. M. Oh, "A Comparative Study on Thermal Stability of Two Solid Electrolyte Interphase (SEI) Films on Graphite Negative Electrode," *J. Electrochem. Soc.*, vol. 160, no. 9, pp. A1539–A1543, 2013.

[107] T. Yoon, M. S. Milien, B. S. Parimalam, and B. L. Lucht, "Thermal Decomposition of the Solid Electrolyte Interphase (SEI) on Silicon

Electrodes for Lithium Ion Batteries," *Chem. Mater.*, vol. 29, no. 7, pp. 3237–3245, 2017.

[108] Z. Lu, L. Yang, and Y. Guo, "Thermal behavior and decomposition kinetics of six electrolyte salts by thermal analysis," *J. Power Sources*, vol. 156, no. 2, pp. 555–559, 2006.

[109] K. Edström, A. M. Andersson, A. Bishop, L. Fransson, J. Lindgren, and A. Hussénius, "Carbon electrode morphology and thermal stability of the passivation layer," *J. Power Sources*, vol. 97–98, pp. 87–91, 2001.

[110] Z. Zhang, D. Fouchard, J. R. Rea, and R. Corporation, "Differential scanning calorimetry material studies: implications for the safety of lithium-ion cells," vol. 70, pp. 16–20, 1998.

[111] M. N. Richard and J. R. Dahn, "Accelerating Rate Calorimetry Study on the Thermal Stability of Lithium Intercalated Graphite in Electrolyte," vol. 146, no. 6, pp. 2068–2077, 1999.

[112] J. ichi Yamaki, H. Takatsuji, T. Kawamura, and M. Egashira, "Thermal stability of graphite anode with electrolyte in lithium-ion cells," *Solid State Ionics*, vol. 148, no. 3–4, pp. 241–245, 2002.

[113] R. C. Shurtz, J. D. Engerer, and J. C. Hewson, "Predicting High-Temperature Decomposition of Lithiated Graphite : Part I . Review of Phenomena and a Comprehensive Model," vol. 165, no. 16, pp. 35–40, 2018.

[114] R. Spotnitz and J. Franklin, "Abuse behavior of high-power, lithium-ion cells," *J. Power Sources*, vol. 113, no. 1, pp. 81–100, 2003.

[115] G. H. Kim, A. Pesaran, and R. Spotnitz, "A three-dimensional thermal abuse model for lithium-ion cells," *J. Power Sources*, vol. 170, no. 2, pp. 476–489, 2007.

[116] T. D. Hatchard, D. D. Macneil, A. Basu, and J. R. Dahn, "Thermal Model of Cylindrical and Prismatic Lithium-Ion Cells," *J. Electrochem. Soc.*, vol. 148, no. 7, pp. A755–A761, 2001.

[117] D. Ren *et al.*, "Model-based thermal runaway prediction of lithium-ion

batteries from kinetics analysis of cell components," *Appl. Energy*, vol. 228, no. July, pp. 633–644, 2018.

[118] S. Santhanagopalan, P. Ramadass, and J. (Zhengming) Zhang, "Analysis of internal short-circuit in a lithium ion cell," *J. Power Sources*, vol. 194, no. 1, pp. 550–557, 2009.

[119] A. S. Gozdz *et al.*, "Differential Scanning Calorimetry Study of the Reactivity of Carbon Anodes in Plastic Li-Ion Batteries," vol. 145, no. 2, pp. 472–477, 1998.

[120] G. Gachot *et al.*, "Thermal behaviour of the lithiated-graphite/electrolyte interface through GC/MS analysis," *Electrochim. Acta*, vol. 83, pp. 402–409, 2012.

[121] H. Lee, Y. Wang, C. Wan, M. Yang, and D. Shieh, "The function of vinylene carbonate as a thermal additive to electrolyte in lithium batteries," pp. 615–623, 2005.

[122] H. F. Xiang *et al.*, "Thermal stability of LiPF6-based electrolyte and effect of contact with various delithiated cathodes of Li-ion batteries," *J. Power Sources*, vol. 191, no. 2, pp. 575–581, 2009.

[123] S. P. Ong, A. Jain, G. Hautier, B. Kang, and G. Ceder, "Thermal stabilities of delithiated olivine MPO4(M = Fe, Mn) cathodes investigated using first principles calculations," *Electrochem. commun.*, vol. 12, no. 3, pp. 427–430, 2010.

[124] A. W. Golubkov *et al.*, "Thermal-runaway experiments on consumer Li-ion batteries with metal-oxide and olivin-type cathodes," *RSC Adv.*, vol. 4, no. 7, pp. 3633–3642, 2014.

[125] H. Arai, M. Tsuda, K. Saito, M. Hayashi, and Y. Sakurai, "Thermal Reactions Between Delithiated Lithium Nickelate and Electrolyte Solutions," *J. Electrochem. Soc.*, vol. 149, no. 4, p. A401, 2002.

[126] P. Ribière, S. Grugeon, M. Morcrette, S. Boyanov, S. Laruelle, and G. Marlair, "Investigation on the fire-induced hazards of Li-ion battery cells by fire calorimetry," *Energy Environ. Sci.*, vol. 5, no. 1, pp. 5271–5280,

2012.

[127] P. Huang, Q. Wang, K. Li, P. Ping, and J. Sun, "The combustion behavior of large scale lithium titanate battery," *Sci. Rep.*, vol. 5, pp. 1–12, 2015.

[128] D. D. MacNeil, "Comparison of the Reactivity of Various Carbon Electrode Materials with Electrolyte at Elevated Temperature," *J. Electrochem. Soc.*, vol. 146, no. 10, p. 3596, 1999.

[129] J. Jiang and J. R. Dahn, "Effects of particle size and electrolyte salt on the thermal stability of Li0.5CoO2," *Electrochim. Acta*, vol. 49, no. 16, pp. 2661–2666, 2004.

[130] J. Gelb, D. P. Finegan, D. J. L. Brett, and P. R. Shearing, "Multi-scale 3D investigations of a commercial 18650 Li-ion battery with correlative electron- and X-ray microscopy," *J. Power Sources*, vol. 357, pp. 77–86, 2017.

[131] D. P. Finegan *et al.*, "Investigating lithium-ion battery materials during overcharge-induced thermal runaway: an *operando* and multi-scale X-ray CT study," *Phys. Chem. Chem. Phys.*, vol. 18, no. 45, pp. 30912–30919, 2016.

[132] V. Ruiz, A. Pfrang, A. Kriston, N. Omar, P. Van den Bossche, and L. Boon-Brett, "A review of international abuse testing standards and regulations for lithium ion batteries in electric and hybrid electric vehicles," *Renew. Sustain. Energy Rev.*, vol. 81, no. July 2017, pp. 1427–1452, 2018.

[133] Y. Chen *et al.*, "A review of lithium-ion battery safety concerns: The issues, strategies, and testing standards," *J. Energy Chem.*, vol. 59, pp. 83–99, 2021.

[134] D. Aurbach, E. Zinigrad, Y. Cohen, and H. Teller, "A short review of failure mechanisms of lithium metal and lithiated graphite anodes in liquid electrolyte solutions," in *Solid State Ionics*, 2002, vol. 148, no. 3–4, pp. 405–416.

[135] I. Epelboin, "Behavior of Secondary Lithium and Aluminum-Lithium Electrodes in Propylene Carbonate," *J. Electrochem. Soc.*, vol. 127, no. 10, p. 2100, 1980.

[136] R. Bhattacharyya, B. Key, H. Chen, A. S. Best, A. F. Hollenkamp, and C. P. Grey, "In situ NMR observation of the formation of metallic lithium microstructures in lithium batteries," *Nat. Mater.*, vol. 9, no. 6, pp. 504–510, 2010.

[137] F. Sun *et al.*, "Study of the Mechanisms of Internal Short Circuit in a Li/Li Cell by Synchrotron X-ray Phase Contrast Tomography," *ACS Energy Lett.*, vol. 2, no. 1, pp. 94–104, 2017.

[138] O. S. Mendoza-Hernandez, H. Ishikawa, Y. Nishikawa, Y. Maruyama, and M. Umeda, "Cathode material comparison of thermal runaway behavior of Li-ion cells at different state of charges including over charge," *J. Power Sources*, vol. 280, pp. 499–504, 2015.

[139] B. Mao, H. Chen, Z. Cui, T. Wu, and Q. Wang, "Failure mechanism of the lithium ion battery during nail penetration," *Int. J. Heat Mass Transf.*, vol. 122, pp. 1103–1115, 2018.

[140] H. Maleki, "Thermal Stability Studies of Li-Ion Cells and Components," *J. Electrochem. Soc.*, vol. 146, no. 9, p. 3224, 1999.

[141] E. P. Roth and D. H. Doughty, "Thermal abuse performance of high-power 18650 Li-ion cells," *J. Power Sources*, vol. 128, no. 2, pp. 308–318, 2004.

[142] P. J. Bugryniec, J. N. Davidson, D. J. Cumming, and S. F. Brown, "Pursuing safer batteries: Thermal abuse of LiFePO 4 cells," *J. Power Sources*, vol. 414, no. January, pp. 557–568, 2019.

[143] W. C. Chen, Y. W. Wang, and C. M. Shu, "Adiabatic calorimetry test of the reaction kinetics and self-heating model for 18650 Li-ion cells in various states of charge," *J. Power Sources*, vol. 318, pp. 200–209, 2016.

[144] M. N. Richard and J. R. Dahn, "Predicting electrical and thermal abuse

behaviours of practical lithium-ion cells from accelerating rate calorimeter studies on small samples in electrolyte," *J. Power Sources*, vol. 79, no. 2, pp. 135–142, 1999.

[145] C. F. Lopez, J. E. Soc, C. F. Lopez, J. A. Jeevarajan, and P. P. Mukherjee, "Characterization of Lithium-Ion Battery Thermal Abuse Behavior Using Experimental and Computational Analysis Characterization of Lithium-Ion Battery Thermal Abuse Behavior," 2015.

[146] J. Zhu, T. Wierzbicki, and W. Li, "Review article A review of safety-focused mechanical modeling of commercial lithium-ion batteries," *J. Power Sources*, vol. 378, no. November 2017, pp. 153–168, 2018.

[147] M. Ender, J. Joos, T. Carraro, and E. Ivers-Tiffée, "Three-dimensional reconstruction of a composite cathode for lithium-ion cells," *Electrochem. commun.*, vol. 13, no. 2, pp. 166–168, 2011.

[148] O. O. Taiwo, "3D and 4D Characterisation of Lithium Ion Battery Electrode Microstructures using X-ray Tomography," 2016.

[149] J. R. Wilson, J. S. Cronin, S. A. Barnett, and S. J. Harris, "Measurement of three-dimensional microstructure in a LiCoO2 positive electrode," *J. Power Sources*, vol. 196, no. 7, pp. 3443–3447, 2011.

[150] T. Waldmann *et al.*, "Review — Post-Mortem Analysis of Aged Lithium-Ion Batteries : Disassembly Methodology and Physico-Chemical Analysis Techniques," 2016.

[151] P. R. Shearing, L. E. Howard, P. S. Jørgensen, N. P. Brandon, and S. J. Harris, "Characterization of the 3-dimensional microstructure of a graphite negative electrode from a Li-ion battery," *Electrochem. commun.*, vol. 12, no. 3, pp. 374–377, 2010.

[152] R. T. DeHoff, J. Alkemper, and P. W. Voorhees, "Quantitative serial sectioning analysis," *J. Microsc.*, vol. 201, no. 3, pp. 388–394, 2001.

[153] M. D. Uchic, L. Holzer, B. J. Inkson, E. L. Principe, and P. Munroe, "T hree-Dimensional Microstructural Beam Tomography," vol. 32, no. January 2017, pp. 408–416, 2007.

[154] M. Ebner, F. Geldmacher, F. Marone, M. Stampanoni, and V. Wood, "X-Ray Tomography of Porous, Transition Metal Oxide Based Lithium Ion Battery Electrodes," *Adv. Energy Mater.*, vol. 3, no. 7, pp. 845–850, 2013.

[155] P. R. Shearing *et al.*, "Multi Length Scale Microstructural Investigations of a Commercially Available Li-Ion Battery Electrode," *J. Electrochem. Soc.*, vol. 159, no. 7, pp. 1023–1027, 2012.

[156] S. J. Cooper *et al.*, "Image based modelling of microstructural heterogeneity in LiFePO 4 electrodes for Li-ion batteries," *J. Power Sources*, vol. 247, pp. 1033–1039, 2014.

[157] P. J. Withers, "X-ray nanotomography," *Mater. Today*, vol. 10, no. 12, pp. 26–34, 2007.

[158] E. Maire and P. J. Withers, "Quantitative X-ray tomography," *Int. Mater. Rev.*, vol. 59, no. 1, pp. 1–43, 2014.

[159] O. O. Taiwo *et al.*, "Comparison of three-dimensional analysis and stereological techniques for quantifying lithium-ion battery electrode microstructures," *J. Microsc.*, vol. 263, no. 3, pp. 280–292, 2016.

[160] B. Song, T. Sui, S. Ying, L. Li, L. Lu, and A. M. Korsunsky, "Nano-structural changes in Li-ion battery cathodes during cycling revealed by FIB-SEM serial sectioning tomography," *J. Mater. Chem. A*, vol. 3, no. 35, pp. 18171–18179, 2015.

[161] M. Ebner, F. Marone, M. Stampanoni, and V. Wood, "Visualization and quantification of electrochemical and mechanical degradation in Li ion batteries," *Science (80-.).*, vol. 342, no. 6159, pp. 716–720, 2013.

[162] J. M. Paz-Garcia *et al.*, "4D analysis of the microstructural evolution of Si-based electrodes during lithiation: Time-lapse X-ray imaging and digital volume correlation," *J. Power Sources*, vol. 320, pp. 196–203, 2016.

[163] Y. Orikasa, K. Yamamoto, T. Shimizu, and Y. Uchimoto, "Multiscale and hierarchical reaction mechanism in a lithium-ion battery," *Chem. Phys.*

Rev., vol. 3, no. 1, p. 011305, 2022.

[164] P. Pietsch and V. Wood, "X-Ray Tomography for Lithium Ion Battery Research: A Practical Guide," *Annu. Rev. Mater. Res.*, vol. 47, no. 1, pp. 451–479, 2017.

[165] D. S. Eastwood *et al.*, "The application of phase contrast X-ray techniques for imaging Li-ion battery electrodes," *Nucl. Instruments Methods Phys. Res. Sect. B Beam Interact. with Mater. Atoms*, vol. 324, pp. 118–123, 2014.

[166] O. O. Taiwo, D. P. Finegan, J. Gelb, C. Holzner, D. J. L. Brett, and P. R. Shearing, "The use of contrast enhancement techniques in X-ray imaging of lithium–ion battery electrodes," *Chem. Eng. Sci.*, 2016.

[167] D.-W. Chung, P. R. Shearing, N. P. Brandon, S. J. Harris, and R. E. Garcia, "Particle Size Polydispersity in Li-Ion Batteries," *J. Electrochem. Soc.*, vol. 161, no. 3, pp. A422–A430, 2014.

[168] J. Geder, H. E. Hoster, A. Jossen, J. Garche, and D. Y. W. Yu, "Impact of active material surface area on thermal stability of LiCoO 2 cathode," *J. Power Sources*, vol. 257, pp. 286–292, 2014.

[169] S. Y. Lee *et al.*, "Revisiting Primary Particles in Layered Lithium Transition-Metal Oxides and Their Impact on Structural Degradation," *Adv. Sci.*, vol. 6, no. 6, 2019.

[170] M. S. Pan *et al.*, "Single-particle measurements of electrochemical kinetics in NMC and NCA cathodes for Li-ion batteries," *Energy Environ. Sci.*, vol. 11, no. 4, pp. 860–871, 2018.

[171] K. J. Park *et al.*, "Degradation Mechanism of Ni-Enriched NCA Cathode for Lithium Batteries: Are Microcracks Really Critical?," *ACS Energy Lett.*, vol. 4, no. 6, pp. 1394–1400, 2019.

[172] H. Quantification *et al.*, "Resolving Li-Ion Battery Electrode Particles Using Rapid Lab-Based X-Ray Nano-Computed Tomography for," vol. 2000362, pp. 1–8, 2020.

[173] I. V. Thorat, D. E. Stephenson, N. A. Zacharias, K. Zaghib, J. N. Harb,

and D. R. Wheeler, "Quantifying tortuosity in porous Li-ion battery materials," *J. Power Sources*, 2009.

[174] M. Ebner, D. W. Chung, R. E. García, and V. Wood, "Tortuosity anisotropy in lithium-ion battery electrodes," *Adv. Energy Mater.*, vol. 4, no. 5, pp. 1–6, 2014.

[175] B. Vijayaraghavan, D. R. Ely, Y.-M. Chiang, R. García-García, and R. E. García, "An Analytical Method to Determine Tortuosity in Rechargeable Battery Electrodes," *J. Electrochem. Soc.*, vol. 159, no. 5, p. A548, 2012.

[176] M. Smith, R. E. García, and Q. C. Horn, "The Effect of Microstructure on the Galvanostatic Discharge of Graphite Anode Electrodes in LiCoO[sub 2]-Based Rocking-Chair Rechargeable Batteries," *J. Electrochem. Soc.*, vol. 156, no. 11, p. A896, 2009.

[177] S. R. Daemi *et al.*, "4D visualisation of in situ nano-compression of Li-ion cathode materials to mimic early stage calendering," *Mater. Horizons*, pp. 612–617, 2019.

[178] D. E. Stephenson, B. C. Walker, C. B. Skelton, E. P. Gorzkowski, D. J. Rowenhorst, and D. R. Wheeler, "Modeling 3D Microstructure and Ion Transport in Porous Li-Ion Battery Electrodes," *J. Electrochem. Soc.*, vol. 158, no. 7, p. A781, 2011.

[179] L. Zielke *et al.*, "A combination of X-ray tomography and carbon binder modeling: Reconstructing the three phases of LiCoO2Li-ion battery cathodes," *Adv. Energy Mater.*, vol. 4, no. 8, pp. 2–7, 2014.

[180] S. Komini Babu, A. I. Mohamed, J. F. Whitacre, and S. Litster, "Multiple imaging mode X-ray computed tomography for distinguishing active and inactive phases in lithium-ion battery cathodes," *J. Power Sources*, vol. 283, pp. 314–319, 2015.

[181] S. R. Daemi *et al.*, "Visualizing the Carbon Binder Phase of Battery Electrodes in Three Dimensions," *ACS Appl. Energy Mater.*, vol. 1, no. 8, pp. 3702–3710, 2018.

[182] A. N. P. Radhakrishnan, M. Buckwell, M. Pham, D. P. Finegan, and A.

Rack, "Quantitative spatiotemporal mapping of thermal runaway propagation rates in lithium-ion cells using cross-correlated Gabor filtering," *ChemRxiv*, 2021.

[183] C. J. Mikolajczak, T. Hayes, D. Ph, M. V Megerle, M. Wu, and D. Ph, "A Scientific Methodology for Investigation of a Lithium Ion Battery Failure," pp. 8–13, 2007.

[184] N. Williard, B. Sood, M. Osterman, and M. Pecht, "Disassembly methodology for conducting failure analysis on lithium – ion batteries," pp. 1616–1630, 2011.

[185] D. P. Finegan *et al.*, "In-operando high-speed tomography of lithium-ion batteries during thermal runaway.," *Nat. Commun.*, vol. 6, p. 6924, 2015.

[186] D. P. Finegan *et al.*, "Tracking Internal Temperature and Structural Dynamics during Nail Penetration of Lithium-Ion Cells," *J. Electrochem. Soc.*, 2017.

[187] D. Patel, J. B. Robinson, S. Ball, D. J. L. Brett, and P. R. Shearing, "Thermal Runaway of a Li-Ion Battery Studied by Combined ARC and Multi-Length Scale X-ray CT," *J. Electrochem. Soc.*, vol. 167, no. 9, p. 090511, 2020.

[188] T. Yokoshima *et al.*, "Direct observation of internal state of thermal runaway in lithium ion battery during nail-penetration test," *J. Power Sources*, vol. 393, no. February, pp. 67–74, 2018.

[189] E. Sahraei, M. Kahn, J. Meier, and T. Wierzbicki, "Advances under mechanical loading," *RSC Adv.*, pp. 80369–80380, 2015.

[190] R. F. Ziesche *et al.*, "4D imaging of lithium-batteries using correlative neutron and X-ray tomography with a virtual unrolling technique," *Nat. Commun.*, no. III, pp. 1–11.

[191] V. Yufit, P. Shearing, R. W. Hamilton, P. D. Lee, M. Wu, and N. P. Brandon, "Investigation of lithium-ion polymer battery cell failure using X-ray computed tomography," *Electrochem. commun.*, vol. 13, no. 6, pp. 608–610, 2011.

[192] N. Zhang and H. Tang, "Dissecting anode swelling in commercial lithium-ion batteries," *J. Power Sources*, vol. 218, pp. 52–55, 2012.

[193] W. Wu, R. Ma, J. Liu, M. Liu, W. Wang, and Q. Wang, "Impact of low temperature and charge profile on the aging of lithium-ion battery: Non-invasive and post-mortem analysis," *Int. J. Heat Mass Transf.*, vol. 170, p. 121024, 2021.

[194] M. Tang, P. Albertus, and J. Newman, "Two-Dimensional Modeling of Lithium Deposition during Cell Charging," *J. Electrochem. Soc.*, vol. 156, no. 5, p. A390, 2009.

[195] L. A. Middlemiss, A. J. R. Rennie, R. Sayers, and A. R. West, "Characterisation of batteries by electrochemical impedance spectroscopy," *Energy Reports*, vol. 6, pp. 232–241, 2020.

[196] A. H. Wiedemann, G. M. Goldin, S. A. Barnett, H. Zhu, and R. J. Kee, "Effects of three-dimensional cathode microstructure on the performance of lithium-ion battery cathodes," *Electrochim. Acta*, vol. 88, pp. 580–588, 2013.

[197] C. S. Xu *et al.*, "Enhanced FIB-SEM systems for large-volume 3D imaging," *Elife*, vol. 6, pp. 1–36, 2017.

[198] M. Strobl, I. Manke, N. Kardjilov, A. Hilger, M. Dawson, and J. Banhart, "Advances in neutron radiography and tomography," *J. Phys. D. Appl. Phys.*, vol. 42, no. 24, 2009.

[199] J. H. Hubbell and S. M. Seltzer, "NIST: X-Ray Mass Attenuation Coefficients," *Physical Reference Data*. 1996.

[200] X. Pan, E. Y. Sidky, and M. Vannier, "Why do commercial CT scanners still employ traditional, filtered back-projection for image reconstruction?," *Inverse Problems*. 2009.

[201] P. R. Shearing, J. Gelb, and N. P. Brandon, "X-ray nano computerised tomography of SOFC electrodes using a focused ion beam sample-preparation technique," *J. Eur. Ceram. Soc.*, 2010.

[202] J. J. Bailey *et al.*, "Laser-preparation of geometrically optimised samples

for X-ray nano-CT," *J. Microsc.*, vol. 267, no. 3, pp. 384–396, 2017.

[203] H. Villarraga-Gómez and S. T. Smith, "Effect of the number of projections on dimensional measurements with X-ray computed tomography," *Precis. Eng.*, vol. 66, no. November, pp. 445–456, 2020.

[204] A. Buades, B. Coll, and J. M. Morel, "A non-local algorithm for image denoising," *Proc. - 2005 IEEE Comput. Soc. Conf. Comput. Vis. Pattern Recognition, CVPR 2005*, vol. II, no. 0, pp. 60–65, 2005.

[205] S. J. Cooper, A. Bertei, P. R. Shearing, J. A. Kilner, and N. P. Brandon, "TauFactor: An open-source application for calculating tortuosity factors from tomographic data," *SoftwareX*, vol. 5, pp. 203–210, 2016.

[206] Y. Xie, S. Shi, J. Tang, H. Wu, and J. Yu, "Experimental and analytical study on heat generation characteristics of a lithium-ion power battery," *Int. J. Heat Mass Transf.*, vol. 122, pp. 884–894, 2018.

[207] H. Giel, D. Henriques, G. Bourne, and T. Markus, "Investigation of the heat generation of a commercial 2032 (LiCoO2) coin cell with a novel differential scanning battery calorimeter," *J. Power Sources*, vol. 390, no. April, pp. 116–126, 2018.

[208] J. Zheng *et al.*, "Tuning of Thermal Stability in Layered Li(NixMnyCoz)O2," *J. Am. Chem. Soc.*, vol. 138, no. 40, pp. 13326–13334, 2016.

[209] S. S. Zhang, "A review on the separators of liquid electrolyte Li-ion batteries," *J. Power Sources*, vol. 164, no. 1, pp. 351–364, 2007.

[210] J. Hong, H. Maleki, S. Al Hallaj, L. Redey, and J. R. Selman, "Electrochemical-Calorimetric Studies of Lithium-Ion Cells," 1998.

[211] W. Zhao, M. Rohde, I. U. Mohsin, C. Ziebert, and H. J. Seifert, "Heat generation in NMC622 coin cells during electrochemical cycling: Separation of reversible and irreversible heat effects," *Batteries*, vol. 6, no. 4, pp. 1–12, 2020.

[212] J. R. Dahn, "Phase diagram of Li_xC_6," *Phys. Rev. B*, vol. 44, no. 17, pp. 9170–9177, 1991.

[213] S. Li, S. Tsutsumi, S. Shironita, and M. Umeda, "Peak Attribution of the Differential Capacity Profile of a LiCoO2-based Three-electrode Li-ion Laminate Cell," *Electrochemistry*, vol. 90, no. 3, pp. 63–67, 2022.

[214] J. Li, J. Harlow, N. Stakheiko, N. Zhang, J. Paulsen, and J. Dahn, "Dependence of Cell Failure on Cut-Off Voltage Ranges and Observation of Kinetic Hindrance in LiNi 0.8 Co 0.15 Al 0.05 O 2," *J. Electrochem. Soc.*, vol. 165, no. 11, pp. A2682–A2695, 2018.

[215] A. Van Der Ven, J. C. Thomas, Q. Xu, B. Swoboda, and D. Morgan, "Nondilute diffusion from first principles: Li diffusion in Lix TiS2," *Phys. Rev. B - Condens. Matter Mater. Phys.*, vol. 78, no. 10, pp. 1–12, 2008.

[216] A. J. Smith and J. R. Dahn, "Delta Differential Capacity Analysis," *J. Electrochem. Soc.*, vol. 159, no. 3, pp. A290–A293, 2012.

[217] Y. Hu, S. Y. Choe, and T. R. Garrick, "Measurement of heat generation rate and heat sources of pouch type Li-ion cells," *Appl. Therm. Eng.*, vol. 189, no. August 2020, p. 116709, 2021.

[218] M. Reiter *et al.*, "Evaluation of transmission based image quality optimisation for X-ray computed tomography," *Conf. Ind. Comput. Tomogr.*, pp. 241–250, 2012.

[219] R. Robert, C. Bunzli, E. J. Berg, and P. Novák, "Activation Mechanism of LiNi0.80Co0.15Al0.05O2: Surface and bulk operando electrochemical, differential electrochemical mass spectrometry, and x-ray diffraction analyses," *Chem. Mater.*, vol. 27, no. 2, pp. 526–536, 2015.

[220] L. de Biasi *et al.*, "Phase Transformation Behavior and Stability of LiNiO2 Cathode Material for Li-Ion Batteries Obtained from In Situ Gas Analysis and Operando X-Ray Diffraction," *ChemSusChem*, vol. 12, no. 10, pp. 2240–2250, 2019.

[221] H. Arai, S. Okada, H. Ohtsuka, M. Ichimura, and J. Yamaki, "Characterization and cathode performance of Li1 - xNi1 + xO2 prepared with the excess lithium method," *Solid State Ionics*, vol. 80, no. 3–4, pp.

261–269, 1995.

[222] C.-F. Chen, A. Verma, and P. P. Mukherjee, "Probing the Role of Electrode Microstructure in the Lithium-Ion Battery Thermal Behavior," *J. Electrochem. Soc.*, vol. 164, no. 11, pp. E3146–E3158, 2017.

[223] "Safety Requirements and Test Methods for Traction Battery of Electric Vehicle, GB/T 31485-2015," *General Administration of Quality Supervision Inspection and Quarantine of the People's Republic of China (AQSIQ),* 2015. [Online]. Available: https://www.chinesestandard.net/PDF.aspx/GBT31485-2015. [Accessed: 27-Nov-2022].

[224] M. T. M. Pham *et al.*, "Correlative acoustic time-of-flight spectroscopy and X-ray imaging to investigate gas-induced delamination in lithium-ion pouch cells during thermal runaway," *J. Power Sources*, vol. 470, no. June, p. 228039, 2020.

[225] J. B. Robinson *et al.*, "Non-uniform temperature distribution in Li-ion batteries during discharge: A combined thermal imaging , X-ray micro-tomography and electrochemical impedance approach," *J. Power Sources*, vol. 252, pp. 51–57, 2014.

[226] C. Zhang, J. Xu, L. Cao, Z. Wu, and S. Santhanagopalan, "Constitutive behavior and progressive mechanical failure of electrodes in lithium-ion batteries," *J. Power Sources*, vol. 357, pp. 126–137, 2017.

[227] X. Feng *et al.*, "Thermal runaway features of large format prismatic lithium ion battery using extended volume accelerating rate calorimetry," *J. Power Sources*, vol. 255, pp. 294–301, 2014.

[228] T. M. M. Heenan *et al.*, "Identifying the Origins of Microstructural Defects Such as Cracking within Ni-Rich NMC811 Cathode Particles for Lithium-Ion Batteries," *Adv. Energy Mater.*, vol. 10, no. 47, 2020.

[229] D. P. Abraham, E. P. Roth, R. Kostecki, K. McCarthy, S. MacLaren, and D. H. Doughty, "Diagnostic examination of thermally abused high-power lithium-ion cells," *J. Power Sources*, vol. 161, no. 1, pp. 648–657, 2006.

[230] F. Rçder, S. Sonntag, D. Schrçder, and U. Krewer, "Simulating the Impact of Particle Size Distribution on the Performance of Graphite Electrodes in Lithium-Ion Batteries," pp. 1588–1597, 2016.

[231] G. Zhang, X. Wei, X. Tang, J. Zhu, and S. Chen, "Internal short circuit mechanisms , experimental approaches and detection methods of lithium-ion batteries for electric vehicles : A review," *Renew. Sustain. Energy Rev.*, vol. 141, no. January, p. 110790, 2021.

[232] C. Y. Jhu, Y. W. Wang, C. Y. Wen, and C. M. Shu, "Thermal runaway potential of LiCoO2 and Li(Ni1/3Co1/3Mn1/3)O2 batteries determined with adiabatic calorimetry methodology," *Appl. Energy*, vol. 100, pp. 127–131, 2012.

[233] T. Y. Lu *et al.*, "Thermal hazard evaluations of 18650 lithium-ion batteries by an adiabatic calorimeter," *J. Therm. Anal. Calorim.*, vol. 114, no. 3, pp. 1083–1088, 2013.

[234] W. C. Chen, Y. W. Wang, and C. M. Shu, "Adiabatic calorimetry test of the reaction kinetics and self-heating model for 18650 Li-ion cells in various states of charge," *J. Power Sources*, vol. 318, pp. 200–209, 2016.

[235] B. Lei, W. Zhao, C. Ziebert, N. Uhlmann, M. Rohde, and H. J. Seifert, "Experimental Analysis of Thermal Runaway in 18650 Cylindrical Li-Ion Cells Using an Accelerating Rate Calorimeter," *Batteries*, vol. 3, no. 2, pp. 1–14, 2017.

[236] B. Sankur, "Survey over image thresholding techniques and quantitative performance evaluation," *J. Electron. Imaging*, vol. 13, no. 1, p. 146, 2004.

[237] G. Berckmans, M. Messagie, J. Smekens, N. Omar, L. Vanhaverbeke, and J. Van Mierlo, "Cost projection of state of the art lithium-ion batteries for electric vehicles up to 2030," *Energies*, vol. 10, no. 9, p. 1314, 2017.

[238] D. D. MacNeil and J. R. Dahn, "The Reaction of Charged Cathodes with Nonaqueous Solvents and Electrolytes: II. LiMn[sub 2]O[sub 4] charged

to 4.2 V," *J. Electrochem. Soc.*, vol. 148, no. 11, p. A1211, 2001.

[239] H. Yang, H. Bang, K. Amine, and J. Prakash, "Investigations of the Exothermic Reactions of Natural Graphite Anode for Li-Ion Batteries during Thermal Runaway," *J. Electrochem. Soc.*, vol. 152, no. 1, p. A73, 2005.

[240] K. Kumai, H. Miyashiro, Y. Kobayashi, K. Takei, and R. Ishikawa, "Gas generation mechanism due to electrolyte decomposition in commercial lithium-ion cell," *J. Power Sources*, vol. 81–82, pp. 715–719, 1999.

[241] Z. Li *et al.*, "Tri-layer nonwoven membrane with shutdown property and high robustness as a high-safety lithium ion battery separator," *J. Memb. Sci.*, vol. 565, no. August, pp. 50–60, 2018.

Chapter 10

10. Appendices

10.1. Publications and conference attendance

1. **Patel, D.**, Robinson, J. B., Ball, S., Brett, D. JL., Shearing, P. R. (2020). "Thermal runaway of a Li-Ion battery studied by combined ARC and multi-length scale X-ray CT". *Journal of the Electrochemical Society*, 167 (9), 090511.

2. (Accepted Manuscript) **Patel, D.**, Reid, H., Ball, S., Brett, D. JL., Shearing, P. R. (2022). "X-ray CT for Failure Mechanism Characterisation within Layered Pouch Cells: Part I, Lithium-ion battery safety." *Johnson Matthey Technology Review*.

3. (Accepted Manuscript) **Patel, D.**, Reid, H., Ball, S., Brett, D. JL., Shearing, P. R. (2022). "X-ray CT for Failure Mechanism Characterisation within Layered Pouch Cells: Part II, Post-mortem analysis of failed cells." *Johnson Matthey Technology Review*.

4. Hack, J., **Patel, D.**, Bailey, J. J., Iacoviello, F., Shearing, P. R., Brett, D. JL. (2021). "In situ x-ray computed tomography of zinc-air primary cells during discharge: correlating discharge rate to anode morphology". *Journal of Physics: Materials*, 5 (1), 014001.

5. Pham, M. TM., Darst, J. J., Walker, W. Q., Heenan, T. MM., **Patel, D.**, Iacoviello, F., Rack, A., Olbinado, M. P., Hinds, G., Brett, D. JL., Darcy, E., Finegan, D. P., Shearing, P. R. (2021). "Prevention of lithium-ion battery thermal runaway using polymer-substrate current collectors". *Cell Reports Physical Science*, 2 (3), 100360.

6. Sharp, M., Darst, J. J., Hughes, P., Billman, J., Pham, M., Petrushenko, D., Heenan, T. MM., Jervis, R., Owen, R., **Patel, D**., Du, W., Michael, H., Rack, A., Magdysyuk, O. V., Connolley, T., Brett, D. JL., Hinds, G., Keyser, M., Darcy, E., Shearing, P. R., Walker, W., Finegan, D. P. (2022). "Thermal Runaway of Li-Ion Cells: How Internal Dynamics, Mass Ejection, and Heat Vary with Cell Geometry and Abuse Type". *Journal of the Electrochemical Society*, 169 (2), 020526.

7. Abouelamaiem, D. I., Mostazo-López, MJ., He, G., **Patel, D.**, Neville, T. P., Parkin, I. P., Lozano-Castelló, D., Morallón, E., Cazorla-Amorós, D.,

Jorge, AB., Wang, R., Ji, S., Titirici, MM., Shearing, P. R., Brett, D. JL. (2018). "New insights into the electrochemical behaviour of porous carbon electrodes for supercapacitors". *Journal of Energy Storage*, 19, 337-347.

8.   Abouelamaiem, D. I., He, G., Neville, T. P., **Patel, D.**, Ji, S., Wang, R., Parkin, I. P., Jorge, AB., Titirici, MM., Shearing, P. R. (2018). "Correlating electrochemical impedance with hierarchical structure for porous carbon-based supercapacitors using a truncated transmission line model". *Electrochimica Acta*, 284, 597-608.

ORAL PRESENTATIONS

- *241st ECS Meeting, May/June 2022*
  Title: In-situ/operando X-ray CT characterisation of lithium-ion pouch cells during thermal failure

- *242nd ECS Meeting, online, May/June 2021*
  Title: Multi-Length Scale X-Ray CT and Thermal Analysis for Battery Safety Assessment

- *Johnson Matthey Academic Conference, March 2021*
  Title: Characterisation Techniques for Battery Safety Assessment

POSTER PRESENTATIONS

- *Johnson Matthey Academic Conference, April 2019*
  Title: X-ray Computed Tomography and Thermal Analysis of Lithium-Ion Battery Cathode Materials

- *STFC Batteries Early Career Researchers Conference, March 2019*
  Title: Multi-scale Safety Characterisation of Cathode Materials using X-ray CT and Calorimetry

- *Johnson Matthey Academic Conference, April 2018*
  Title: Characterisation Techniques for Battery Safety

- *UK Energy Storage Conference, March 2018*
  Title: *Calorimetry and X-ray CT to Understand Thermal Failure of Li-ion Batteries*

- *Industry Advisory Board at Dept. of Chemical Engineering, UCL, Feb 2018*
  Title: Advanced Characterisation Techniques to Understand Thermal Failure of Li-ion Batteries

10.2. Chapter 3 Appendix

Table 10.1 Single layer pouch cell design parameters.

| Cell design parameters	Cathode			Anode
	NMC111	NMC622	NMC811	
Material and composition	NEI Nanomyte BE-50E 90 wt% NMC, 5 wt% PVDF, 5 wt% Carbon black (Super P)			NEI Nanomyte BE-200E 90 wt% Graphite, 5 wt% PVDF, 5 wt% Carbon black (Super P)
Foil thickness, µm	16			10
Coating loading, mg cm^{-2}	12.55	10.63	9.77	6.57
Electrolyte	1 M LiPF$_6$ in a 1:1:1 by wt EC:EMC:DC and 1% VC			
Separator	Celgard 2500 (single layer)			
N:P ratio for 0.1 C	1.11	1.24	1.20	-
Active area, cm^2	13.19			14.71
Capacity, mAh	26.49	23.84	24.48	29.46

10.3. Chapter 5 Appendix
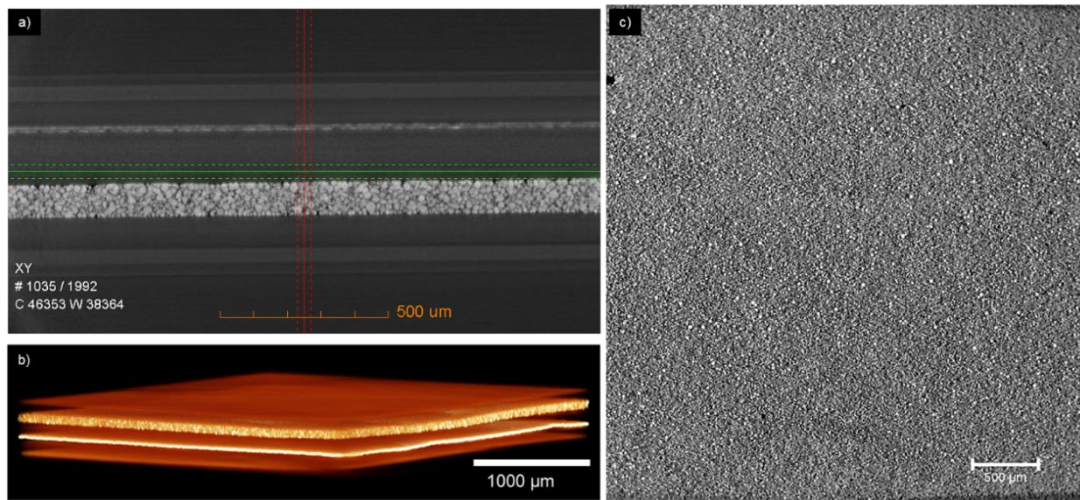
Figure 10.1 Orthoslices and volume renderings of a single-layer pouch cell scan (Sample 2).
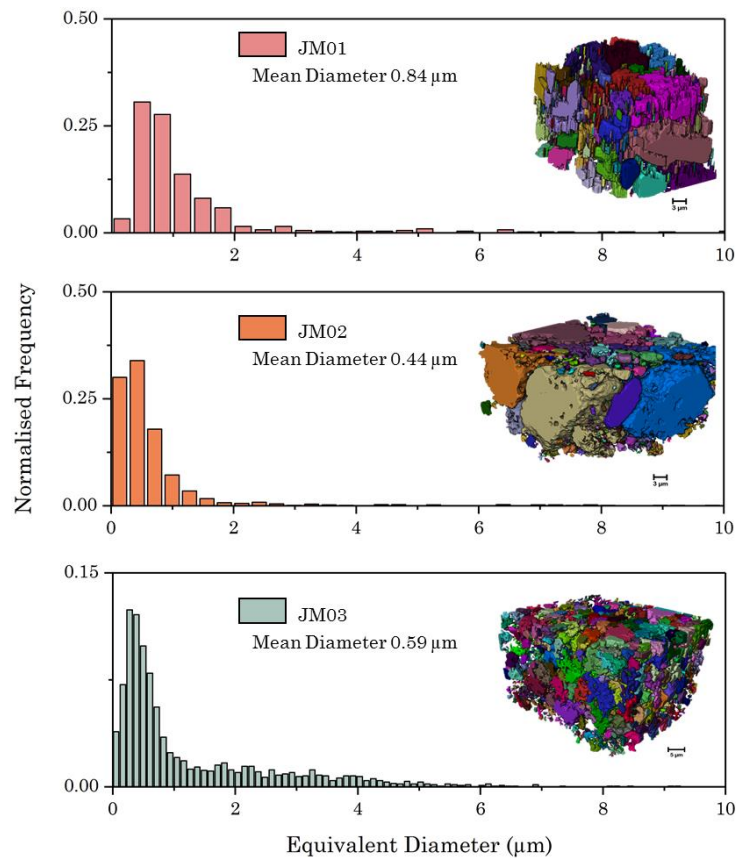

Figure 10.2 Particle size distribution results shown alongside the extracted sub-volume renderings using Avizo software (FEI VSG, France).
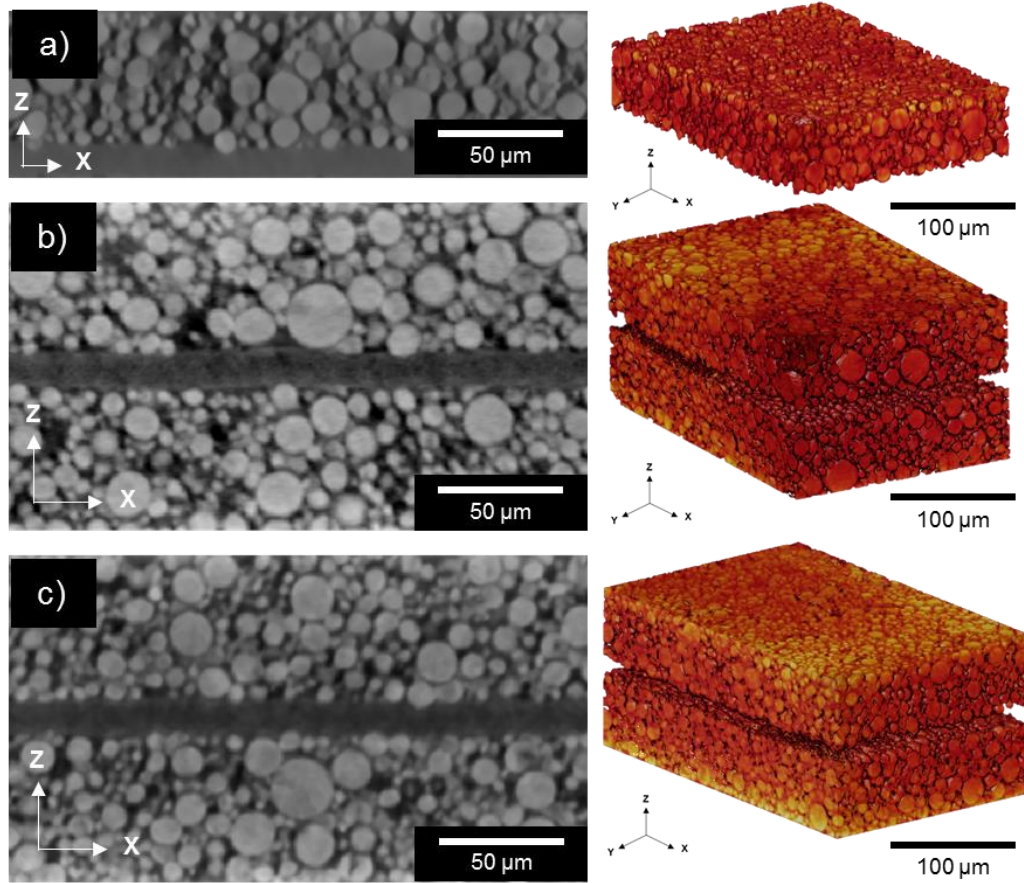
Figure 10.3 Orthoslice in the ZX plane and volume renderings of the (a) pristine, (b) thermally failed, and, (c) nail penetrated bulk cathode layers taken from scans 7, 9 and 11 with corresponding voxel sizes of 0.181, 0.387 and 0.387 µm.

Table 10.2 Summary of voxel sizes, in μm, achieved for all scans.

Imaging instrument	FOV	Cell 1: Pristine cell and materials (no failure mode)			Cell 2: External heating by accelerating rate calorimetry (ARC)			Cell 3: Internal short circuit by nail penetration			
		Whole cell	*Anode*	*Cathode*	*Whole cell*	*Anode*	*Cathode*	*Whole cell*	*Anode*	*Cathode*	
Nikon XT X 255		31.7 (#1)			33.6 (#2)			27.8 (#3)			Non-invasive / whole cell
ZEISS Xradia 520 Versa (4 X obj. lens)	3000 – 4000	1.83 (#4)			2.00 (#5)			1.70 (#6)			
ZEISS Xradia 520 Versa (40 X obj. lens)	384		−	0.181 (#7)		0.387 (#8)	0.387 (#9)		0.387 (#10)	0.387 (#11)	Invasive
ZEISS Xradia 810 Ultra (LFOV)	64		−	0.0631 (#12)		−	0.126 (#13)		−	0.126 (#14)	
ZEISS SEM EVO MA 10	N/A		−	0.035 – 0.090		0.035 – 0.090	0.035 – 0.090		0.035 – 0.090	0.035 – 0.090	

Table 10.3 Summary of parameters extracted from the invasive (bulk electrode layer and particle morphology) scans.

	Pristine cathode		Cathode after Thermal failure (TF)*		Cathode after Nail penetration (NP)**		Anode after TF*	Anode after NP**
Imagine instrument and (#scan number)	Versa (#7)	Ultra (#12)	Versa (#9)	Ultra (#13)	Versa (#11)	Ultra (#14)	Versa (#8)	Versa (#10)
Sample type/feature of interest	(I)	(II)	(I)	(II)	(I)	(II)	(I)	(I)
Voxel size (μm)	0.181	0.0631	0.387	0.126	0.387	0.126	0.387	0.387
Bounding box dimension (total voxels)	326 x 1475 x 1029	421 x 488 x 542	516 x 794 x 129	339 x 352 x 368	129 x 794 x 516	307 x 353 x 485	646 x 559 x 154	491 x 605 x 169
Mean particle diameter (μm)	5.39 ± 0.65	2.93 ± 0.51	4.76± 0.64	4.43± 0.50	6.10± 0.70	4.47± 0.42	16.99± 1.01	13.59± 0.76
Min. particle diameter (μm)	0.22	0.24	0.48	1.06	0.4	0.68	0.48	0.48
Max. particle diameter (μm)	23.20	20.49	26.40	26.38	24.26	15.27	32.16	27.15
Particle volume fraction	0.46	0.42	0.40	0.46	0.48	0.46	0.69	0.64
Tortuosity	1.29	1.51	1.33	1.53	1.43	1.62	2.97	3.19
Surface area per volume (μm $^{-1}$)	0.478	0.429	0.408	0.572	0.490	0.764	0.654	0.660

*Extracted from Cell 2, **Extracted from Cell 3

(I) Bulk electrode layer via micro-CT, (II) Particle via nano-CT